THE UNIVERSITY
of EDINBURGH

Exploring the Role of Central Nervous System Myelination in Circuit Function and Behaviour

Megan Madden

Doctor of Philosophy
University of Edinburgh
2020

Declaration

I declare that this thesis was composed by myself and that the work contained therein is my own, except where explicitly stated otherwise in the text. This thesis has been submitted exclusively to the University of Edinburgh for the degree of Doctor of Philosophy.

(*Megan Madden*)

To Tilly,

and all of the fish

Acknowledgements

I consider myself extremely lucky to have been part of the Lyons Lab for the past four years. In fact, the more time that passes since I finished working in the lab, the more I realise that I will always feel a part of it. As a group, you have covered all the bases for a holistic PhD experience: lots of science, lots of (inappropriate) laughter, abundant tea breaks, occasional BBQs and intermittent twister, karaoke, human pyramids and most recently, water slides – all while being completely teetotal. Much of this is down to my supervisor Dave's refined selection process, which has resulted in a collection of incredible and unique people to work with. In all honesty, I would have been lost without you all. I have learnt so much from you.

Particularly special thanks are due to Dave, for giving me the freedom and independence to explore new and sometimes rocky territory, while providing nothing but encouragement and support throughout. Additionally, I must thank him for giving me the opportunity to spend such a large part of my PhD at another institution - giving me exposure to a different field of neuroscience and expanding my horizons. This brings me to give a huge thank you to Isaac Bianco for welcoming me into his team at UCL, for being extremely generous with his time and providing me with an exceptional extended lab family. I feel very fortunate to have worked as part of his group and have made some great friends in the process. To the rest of the first floor: thank you for always pretending to be excited to see me when I kept coming back to do experiments and for making eating curry *every* Friday lunchtime a legitimate activity!

I would not have been able to complete my PhD without my lovely friends providing me with floors, sofas and beds to sleep on while I visited UCL. And in turn, for coming to visit me in Scotland and reminding me what's important in life. Thank you all for cheering me on to the end, even when it meant I was missing your infamous

birthday parties! On this note I need to thank my family, who also live at the opposite end of the country, for their constant support and commitment to visiting me regularly in Scotland – I'm sure the whisky, fishing, food and Fringe had no influence on this!

Most importantly, thank you to Rob for always having faith in my ability, and for keeping me laughing, fed and 'watered' during the writing process. You never question my endeavours but always support me through them.



Lay Summary

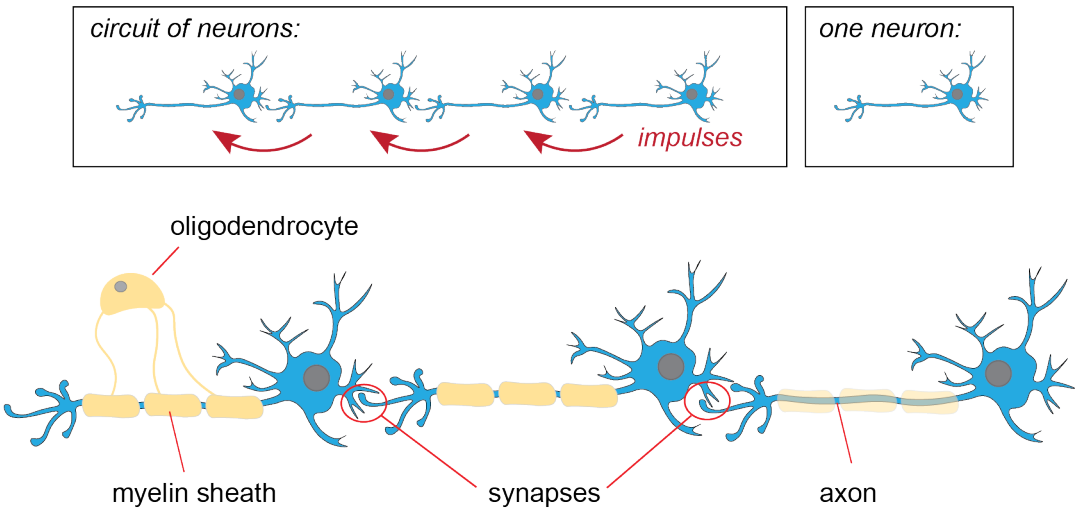

Figure 1: Structure of a neuron wrapped by myelin

Our nervous system is made up of billions of cells known as neurons. Neurons are specially designed to carry electrical messages or 'impulses' across our nervous system. They form connections with one another known as 'synapses' – this is where they receive and transmit impulses. They also have a long cable like structure known as the 'axon' which acts as a highway for impulses to travel along. In the central nervous system (brain and spinal cord), cells known as 'oligodendrocytes' produce a fatty layer, known as a myelin sheath, which wraps around and insulates the axon. Myelin not only increases the speed at which impulses can travel along an axon, but also provides nourishment and support. For impulses to travel across the central nervous system (CNS) they follow routes composed of multiple neurons – these are known as circuits. In general, each circuit of the CNS has its own function – from a simple blink reflex to more complex functions such as the formation of memories.

It has long been known that learning a new skill such as riding a bike, speaking a

new language or mastering a computer game requires specific patterns and timings of impulse arrival at the synapses along a circuit. More recently, evidence has emerged showing that the development of these skills may be associated with changes in the structure of the myelin, for example the length, thickness and number of myelin sheaths. However, the purpose of these changes is currently unclear. Given that myelin has the power to control the speed and thus timing of impulses, we think that these changes in myelin may be contributing to the development of new skills and behaviours. This would represent a completely new function of myelin and totally change our understanding of the processes that control brain function and behaviour.

To explore the role of myelin in circuit function and behaviour we used larval (young) zebrafish. Larval zebrafish are well suited for this purpose. Firstly, they are transparent which allows us to observe patterns of myelin in their CNS using specialised microscopes. Secondly, their circuits are much simpler than those found in mammals making it easier to measure the timing of impulses. Finally, larval zebrafish perform a wide range of behaviours which can be assessed using established behavioural tests.

In this thesis, I explored the effects of disrupting myelin in the CNS of larval zebrafish on the development of their swimming behaviour. By creating an error or 'mutation' in a gene required for the production of myelin in the CNS, I reduced the amount of myelin here by two thirds. To assess how this would affect behaviour, I used high-speed cameras and tracking software to monitor the movement of the larvae while they performed multiple types of behaviour. In doing so, I identified two specific behaviours which were disrupted by the loss of myelin: larvae took longer to perform an escape response following a loud noise, and they performed a higher number of fast swims while exploring their environment. Due to the loss of myelin in these fish, we predict that the delay to perform an escape response is caused by impulses travelling too slowly along the axon of the neuron which is responsible for this behaviour. The circuits controlling swim speed are much more complex and here we anticipate that the loss of myelin may be causing more widespread disruption to impulse timing. Interestingly, due to an unexpected but recognised genetic phenomenon, larvae that only carry one copy of the mutated gene had *more* myelin in their CNS. In these fish, the escape response was normal, but they too performed an increase in the number of fast swims. This suggests

that for some circuits of the CNS a balance of myelin is required; that is, too little or too much myelin can have a detrimental effect on impulse timing.

In summary, the findings of this project support a role for myelin in controlling impulse timing across specific circuits of the CNS during the development of larval zebrafish behaviours. Future experiments will use specialised techniques to measure impulse timing in these circuits to prove this theory. This will provide the basis for ongoing investigations into the effects of myelin on circuit function. Advancing our knowledge in this field of research will eventually inform our understanding of human brain function.

Abstract

Activity-mediated myelination, the adjustment of myelin morphology in response to neuronal activity, has been proposed as a novel mechanism of central nervous system (CNS) plasticity. As a key regulator of conduction velocity, adaptations in myelin structure have the potential to exert spatiotemporal control over action potentials across neurons of a given circuit, in turn influencing circuit function and behaviour. Despite a breadth of evidence supporting this hypothesis, a definitive conclusion has been hindered by the technical difficulties of assessing circuit activity in parallel with myelin morphology and behaviour *in vivo*.

Using larval zebrafish as a model, this study investigated the effect of disrupting the normal program of CNS myelination on the development of locomotor behaviour. CRISPR/Cas9 mutagenesis of Myelin Regulatory Factor (Myrf) gene, encoding for a transcription factor vital for CNS myelination, was used to create a CNS specific model of hypomyelination. Larvae from Myrf heterozygous in-crosses were then tested across a suite of behavioural assays, allowing the measurement of detailed kinematic parameters during spontaneous and stimulus-driven responses.

Myrf homozygous mutants displayed a 66% reduction in the number of myelinated axons in the spinal cord along with reduced gene expression of myelin basic protein (Mbp). Unexpectedly, heterozygous animals exhibited precocious myelination of small caliber axons, resulting in a 53% increase in the number of myelinated axons. This finding was associated with a subtle upregulation of Mbp gene expression. Subsequent behavioural analysis revealed that Myrf homozygous mutants demonstrated a significant delay in the latency to perform acoustic startle responses. Interestingly, both homozygous and heterozygous mutants exhibited an increase in the frequency of high velocity swim bouts performed during spontaneous swimming, driven by subtle adjust-

ments in tail kinematics.

The findings of this study support a role for myelination in the control of action potential timing across defined circuits of the CNS and suggest that a balance of myelination is important for the function of more complex circuits such as those controlling swim speed. Future work, using *in vivo* electrophysiology and functional imaging, will interrogate how neuronal activity is altered in the circuits underlying these behaviours. Together, these findings will advance our understanding of the role that CNS myelination plays in circuit function and behaviour.

Contents

Abbreviations

AMPA	alpha-amino-3-hydroxy-5-methyl-4-isoxazolepropionic acid
ABR	auditory brainstem response
ADP	adenosine diphosphate
AKT	protein kinase B
ATP	adenosine triphosphate
Bcl2	B-cell lymphoma 2
BDNF	brain derived neurotrophic factor
C14	carbon 14
CAP	compound action potential
Cas9	CRISPR associated protein 9
Caspr	contactin associated protein
CKO	conditional knockout
CiA	circumferential ascending (interneuron)
CiD	cirumferential descending (interneuron)
Cnp	2',3'-cyclic nucleotide 3'-phosphodiesterase
CNS	central nervous system
crRNA	CRISPR RNA
CoBl	commissural bifurcating longitudinal
CoPa	commissural primary ascending
CPG	central pattern generator
CreERT	tamoxifen-inducible Cre recombinase
CRN	cranial relay neuron
CV	conduction velocity
dpf	days post fertilisation
DRG	dorsal root ganglion
DTI	diffusion tensor imaging

EAE	experimental autoimmune encephalitis
EdU	5-Ethynyl-2'-deoxyuridine
eEPSCs	evoked excitatory post-synaptic currents
Enpp6	ectonucleotide pyrophosphatase/phosphodiesterase 6
ErbB	epidermal growth factor receptor
Erk	extracellular-signal-regulated kinase
FA	fractional anisotropy
FACS	fluorescent-activated cell sorting
GABA	gamma-aminobutyric acid
GECIs	genetically encoded calcium indicators
GLUT	glucose transporter
GS	glutamine synthetase
Kir	inwardly rectifying potassium channel
Kv	voltage gated potassium channel
LDH	lactate dehydrogenase
LES	Long Evans Shaker
LIF	leukemia inhibitory factor
LLC	long latency c-start
LTD	long term depression
LTP	long term potentiation
Mag	myelin associated glycoprotein
MAPK	mitogen activated protein kinase
Mbp	myelin basic protein
MCT	monocarboxylate transporter
MLR	mesencephalic locomotor region
Mog	myelin oligodendrocyte glycoprotein
mPFC	medial prefrontal cortex
MRI	magnetic resonance imaging
mRNA	messenger RNA
Mpz	myelin protein zero
mTOR	mammalian target of rapamycin
MTR	magnetization transfer ratio
MS	multiple sclerosis

Myrf	myelin regulatory factor
NF-155	neurofascin-155
NG2	neural/glial antigen 2
NMDA	N-methyl-D-aspartate
nMLF	nucleus of the medial longitudinal fasciculus
NoGo	neurite outgrowth inhibitor
NR	NMDA-receptor
OL	oligodendrocyte
OMgp	oligodendrocyte myelin glycoprotein
OMR	optomotor response
ORF	open reading frame
OT	optic tectum
OPC	oligodendrocyte precursor cell
P13K	phosphatidylinositol 3-kinase
PHP	passive hyperpolarising potential
Plp	proteolipid protein
PMN	primary motor neuron
PNS	peripheral nervous system
PPI	prepulse inhibition
Pten	phosphatase and tension homolog
PTZ	pentylenetetrazol
qRT-PCR	quantitative real time polymerase chain reaction
RB	Rohon-Beard (neuron)
RFLP	restriction fragment length polymorphism
RGCs	retinal ganglion cells
RS	reticulospinal
sgRNA	single guide RNA
Sox10	Sry-box 10
SLC	short latency c-start
STDP	spike timing dependent plasticity
TCA	tricarboxylic acid cycle
TEM	transmission electron microscopy
TL	Tupfel long-fin

TrkB	tropomyosin receptor kinase B
TTX	tetradotoxin
VEP	visually evoked potential
VGCC	voltage gated calcium channel
vSPNs	ventral spinal projection neurons

Chapter 1

Introduction

1.1 The central nervous system is adaptable

Our ability to exhibit complex behaviour relies on the diversity of our central nervous system (CNS). Consisting of 100 billion neurons in the brain alone, our nervous system is organised into complex three-dimensional circuits of neurons wired together to carry out specific functions. Nestled among these neuronal connections resides a roughly equal number of glial cells (von Bartheld et al., 2016), namely oligodendrocytes (OLs), oligodendrocyte precursor cells (OPCs), astrocytes, microglia and radial glial cells. Traditionally known as the 'supporting cells' of the brain, it has become increasingly recognised over the past decade that glia are able to exert their own control over neural circuit function and development (reviewed in Corty and Freeman (2013) and Allen and Lyons (2018)). Together, this myriad of cell types equips the nervous system with a unique ability to adapt its circuitry in response to external or internal physiological cues, a feature known as 'nervous system plasticity'.

Nervous system plasticity in humans is most prominent during early development when neural circuits undergo significant structural and functional reorganisation, coinciding with the manifestation of behavioural milestones such as learning to walk and talk. Critical periods of development define windows of time when this process is particularly vulnerable to external cues. However, the phenomenon of nervous system plasticity is not restricted to childhood. Pivotal human imaging studies from the early 2000s demonstrated structural brain plasticity in the grey matter of the brain during adulthood. Maguire et al. (2000) performed magnetic resonance imaging (MRI) of London

taxi drivers and found that the volume of their posterior hippocampus, a brain region specifically involved in spatial memory, was increased compared to control subjects (non-taxi drivers). Similarly, Draganski et al. (2004) published that subjects trained to juggle over three months demonstrated localised increases in grey matter volume which declined once physical training was discontinued.

These structural adaptations are no surprise given that the grey matter harbours the majority of synapses, where traditional forms of *functional* plasticity have been suggested to exist since Hebb's rule of synaptic plasticity was first proposed: when the firing patterns of two neurons are closely associated a process occurs to strengthen the causality between the two (Hebb, 1949). This theory is now established as a fundamental mechanism of synaptic plasticity known as 'spike timing dependent plasticity' (STDP) (Caporale and Dan, 2008). Similar forms of synaptic plasticity are also reliant on the timing of action potentials; *in vivo* and *in vitro* systems have been used to demonstrate that the timing of action potential arrival from a pre-synaptic neuron to its post-synaptic target, relative to the firing of the post-synaptic neuron, can either stabilise, known as long term potentiation (LTP), or weaken (long term depression, LTD) that synaptic connection (Bi and Poo, 1998; Markram et al., 1997). These mechanisms represent the most studied form of plasticity in the CNS to date, where they are of central importance to circuit development and learning.

Structural forms of synaptic plasticity also exist in the form of dendritic remodelling, synaptogenesis and synaptic pruning (Holtmaat and Svoboda, 2009). Indeed, *in vivo* two-photon microscopy of synaptic structures in the motor cortex of mice during periods of motor learning revealed rapid formation of new dendritic spines and selective spine elimination over time providing evidence of microstructural changes which may contribute to the findings in human imaging studies (Xu et al., 2009). Cortical neurogenesis has been reported in adult primates and could hypothetically contribute to grey matter plasticity, although this finding remains controversial to date (Gould et al., 1999). Furthermore, non-neuronal cell types such as microglia and astrocytes have been implicated in regulating synaptic function and could equally contribute to structural grey matter changes (Allen and Eroglu, 2017; Paolicelli et al., 2011).

Alongside the depth of knowledge surrounding synaptic plasticity and its importance in learning, a place for grey matter plasticity in the development of behaviour is well established. However, this synapse-centric approach does not take into account that the temporal control of action potential (spike timing) arrival at the synapse is facilitated by alternative aspects of the neuronal subunit. As a key regulator of action potential conduction velocity (CV) along an axon, myelin represents a potent mediator of this control. In this introduction, I will present evidence for a novel form of *structural* plasticity involving the myelinating cells of the CNS and review the potential for a *functional* role of myelination in exerting control over circuit function and behaviour.

1.2 White matter plasticity

1.2.1 Myelin puts the white into white matter

Myelinated axons make up a major component of white matter tracts in the CNS. In fact, the high lipid content (70 to 85%) of myelin sheaths provides white matter with its white colour and subsequent nomenclature (Morell and Quarles, 1999) (Figure 1.1). Myelin sheaths restrict water molecule movement across an axon providing white matter regions of the brain with unique water diffusion qualities which allow its structure to be assessed with advanced MRI techniques such as diffusion tensor imaging (DTI). The advent of these imaging techniques has provided researchers with the opportunity to investigate whether mechanisms of structural plasticity, as seen in the grey matter, also exists in the white matter of the CNS.

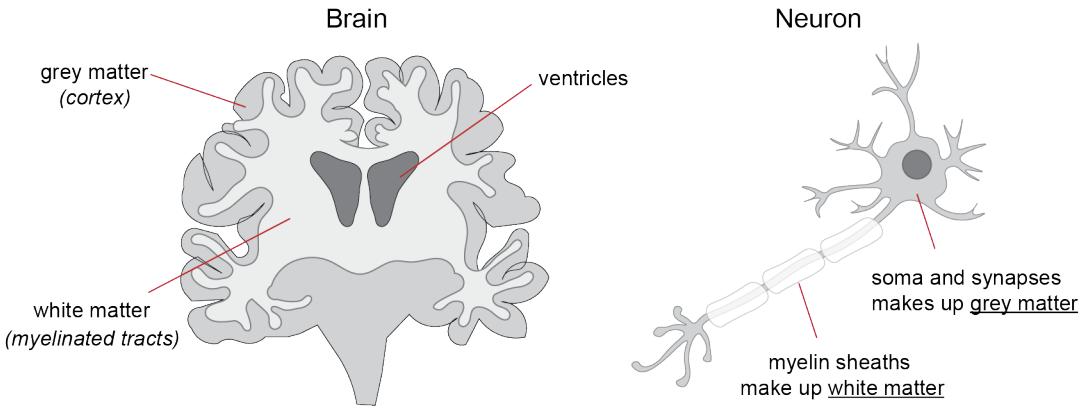

Figure 1.1: The CNS can be divided into regions of white and grey matter
Left: Schematic showing the location of white matter and grey matter regions of the brain on a coronal view. Right: Schematic of a myelinated neuron. In general, the myelinated axon spans the white matter tracts of the brain, whereas the soma and synapses make up the grey matter of the brain.

1.2.2 White matter plasticity during development

Human neonates are born with relatively few myelinated axons compared to other species (Miller et al., 2012). During post-natal development and adolescence, white matter tracts, as viewed using MRI, undergo significant development and reorganisation coinciding with critical periods of learning such as learning to walk or read (Deutsch et al., 2005; Schmithorst and Yuan, 2010). These findings correlate with post-mortem brain studies which demonstrate that in certain areas of the brain (i.e. the neocortex) the expansion of myelination continues throughout childhood and well into our third decade of life (Miller et al., 2012). This prolonged period of myelination has been proposed as a mechanism which may allow additional shaping of our circuitry to environmental cues, particularly during those critical periods of development, allowing humans the cognitive flexibility that few other species possess.

It is important to note that during development white matter changes do not occur independently of adaptations in the grey matter, in fact they show remarkably similar trajectories. For example, in the early post-natal period, synaptogenesis is closely followed by periods of myelinogenesis (Tau and Peterson, 2010). This temporal relationship continues into adolescence when grey matter undergoes significant shrinkage, due to processes such as synaptic pruning, in parallel to subcortical white matter expansion (Ziegler et al., 2019). Indeed, the process of synaptic pruning has been shown to peak at a similar timepoint as myelination in our third decade of life (Miller et al., 2012; Petanjek et al., 2011). These findings suggest that mechanisms of both white and grey matter plasticity are tightly correlated and together may contribute to a similar functional adaptation. This is not surprising given that many of the cell bodies and synapses which constitute the grey matter belong to neurons whose axons span white matter tracts (Figure 1.1).

1.2.3 White matter plasticity during adulthood

White matter structure and connectivity can also be assessed in humans using advanced MRI techniques such as DTI (Basser et al., 1994). DTI measures the directional diffusion properties of water within tissue. Within the axons of the brain, water is restricted by the cell membrane and will diffuse along an axon rather than across it (Takahashi et al., 2002). Using a diffusion tensor model, the diffusion of each voxel (the unit of

an MRI image) can be quantified along three axes to produce a value of 'fractional anisotropy' (FA) - the directional dependence of the diffusion signal. FA values can then be collated to form a diffusivity map representing the white matter structure of the brain (Basser et al., 1994). Most importantly, DTI allows quantification of white matter structure permitting comparison within and between individuals.

This imaging technique has allowed researchers to investigate whether structural features of the white matter can be correlated to behaviour. A seminal study by Bengtsson et al. (2005) found that measures of FA and fiber tract organisation in the white matter of adult professional pianists correlated strongly with the total number of hours practiced by each subject during childhood, adolescence and adulthood. Furthermore, changes in FA were found to be region specific according to which training period they were regressed with, suggesting that white matter tracts demonstrate susceptibility to plasticity at different time points. Indeed, early trained musicians have been found to exhibit greater connectivity on DTI, with FA values correlating more strongly with performance in auditory and visual sensorimotor synchronization task than late trained musicians (Steele et al., 2013). Away from expert populations, inter-individual variation in white matter has also been documented in the general population. For example, variation in FA values in the body of the corpus callosum can be correlated to a subject's ability to perform a bimanual motor coordination task (Johansen-Berg et al., 2007). Similar findings were found in healthy, aged individuals in which FA values of the splenium and parietal pericallosal white matter were positively associated with the ability to perform an alternate finger tapping task (Sullivan et al., 2001). Relationships between pathway specific FA and non-motor behaviours, such as visual reaction time (Madden et al., 2004), reading ability (Klingberg et al., 2000), spatio-visual attention (Tuch et al., 2005), playing Baduk (Lee et al., 2010), learning a new language (Schlegel et al., 2012) and meditating (Tang et al., 2010) have also been documented. One of the key questions raised from these cross-sectional studies, and those of the grey matter, is whether the structural differences observed at the timepoints tested were the result of true experience driven plasticity or whether they represented genetic variation in brain structure predisposing individuals to a variable skill level. Although the study by Bengtsson et al. (2005) attempted to tackle this by quantifying the number of hours each subject spent playing the piano, these numbers were self-reported and could still

indicate genetic factors that influence white matter structure as well as the inclination to train. To address this problem directly, it would be essential to perform longitudinal interventional studies to obtain baseline levels of white matter and monitor adaptations in response to skill development.

1.2.4 Evidence for training induced white matter plasticity

Fulfilling the requirement for a longitudinal study, Scholz et al. (2009) demonstrated that individuals trained in a complex visuomotor skill (juggling) for six weeks had a significant increase in fractional anisotropy in the white matter underlying the intraparietal sulcus, an area of the brain involved in motor-coordination, compared to their pre-training baseline and untrained controls. Structural adaptations in the grey matter overlying this region were also observed over a longer time frame - white matter levels peaked after six weeks of training and declined four weeks following cessation of training, whereas grey matter volume showed more modest density changes after six weeks and continued to rise at the final scan. This is an interesting finding as it suggests that the biological mechanisms underlying white and grey matter plasticity in adulthood occur over different timescales. Additionally, it implies that white matter changes precede and may influence grey matter adaptations during learning, although this remains to be investigated.

Examples of white matter plasticity are not restricted to motor training. Bridging the gap between human and rodent studies Hofstetter et al. (2013) identified structural changes in the fornix of both species within hours of training in a spatial learning task. However, measures of FA and mean diffusivity were reduced in learning groups compared to controls, in contrast to the findings of previous studies. The cellular changes underlying this discrepancy are open to interpretation but could reflect early adaptations of white matter to learning such as axon swelling in response to action potentials, changes in the extracellular volume or increase in glial cell volume. Alternatively, this inconsistency may imply that different white matter adaptations occur in response to different types of learning. Nevertheless, the structural white matter changes observed in this study correlated with improvement in the learning task over time and mean diffusion measurements in the hippocampus, supporting an association

between mechanisms of white and grey matter plasticity. Importantly, this study revealed the potential for conserved mechanisms of white matter plasticity in rodents and humans which was fundamental in establishing rodents as a model to study white matter plasticity and allowed us to start investigating the cellular mechanisms at play.

Conclusion

Together these studies unequivocally establish that the white matter in our brain exhibits structural plasticity in response to short and long-term experience and that this can be reliably correlated to behavioural performance. However, there are clear downfalls to voxel-based imaging techniques. Although DTI is considered to provide a more specific measure of white matter microstructure than other imaging modalities, the resolution is too limited to allow us any indication of the cellular phenomena underlying changes in diffusivity. For example, a voxel of 100μm x 100μm x 100μm from a rodent white matter tract can contain as many as 13,000 axons, 86 OLs, 22 astrocytes, 6.5 OPCs and 9.5 microglia (Walhovd et al., 2014). Furthermore, the extensive processes of OLs and astrocytes can span up to ∼48% of this volume. If these values are extrapolated to the size of a voxel from a human imaging study (2mm x 2mm x 2mm), the number of cells that could contribute to FA values becomes vast. Diffusivity parameters yielded by DTI could thus represent multiple changes at a cellular level, including: axon density, axon diameter, glial cell number and morphology, vasculature changes, myelin adaptations and fibre density/arrangement, to name but a few (Beaulieu, 2002) (Figure 1.2).As mentioned previously, myelinated axons make up a major component of white matter. Given the traditional understanding that myelin regulates action potential conduction speed along an axon, a favoured hypothesis is that the findings of the aforementioned studies are, at least in part, represented by adaptations in myelin morphology, such as myelin sheath thickness, length and number (Figure 1.2). While advancements in human imaging techniques are underway to optimise myelin-specific imaging techniques, such as Magnetic Transfer Ratio (MTR), researchers have sought to address this hypothesis using animal models. In Section 1.4.2, I will present our current understanding of how these parameters can influence CV along individual axons. Following this, I will introduce direct evidence that the white matter changes observed on brain imaging studies are due to adaptations in myelin (Section 1.5).

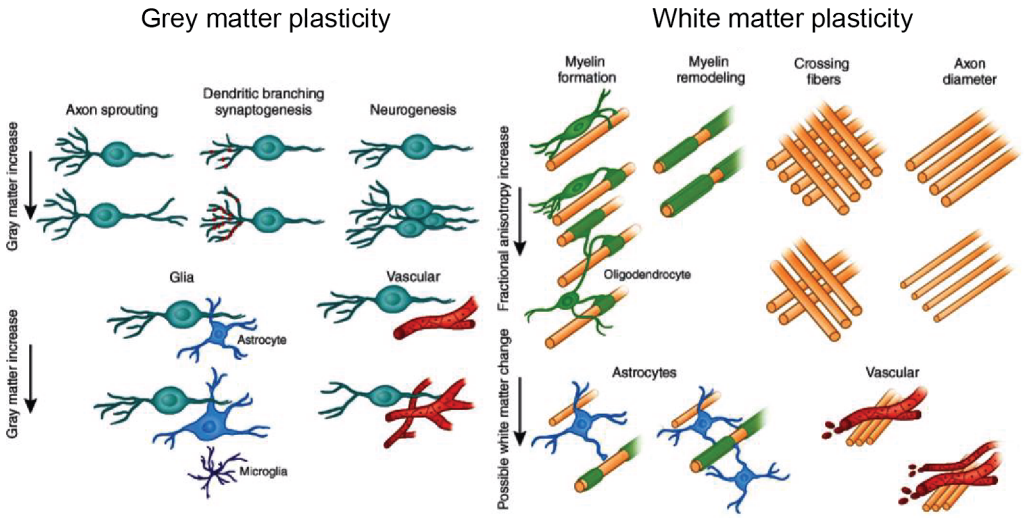

Figure 1.2: Potential cellular adaptations underlying white and grey matter structural plasticity
Image taken from (Zatorre et al., 2012). Left: Neuronal adaptations underlying grey matter plasticity can include axon sprouting, dendritic branching/synaptogenesis and neurogenesis. In addition, vascular and glial changes could contribute to changes in grey matter volume. Right: Myelin specific changes underlying white matter plasticity include myelination of unmyelinated axons and remodelling of existing myelin sheaths. In addition, changes to axon fiber caliber, density and orientation can also influence measures of FA. Changes in astrocyte number, morphology and angiogenesis may also contribute.

1.3 Myelin sheath structure and formation

Myelin sheaths are produced by OLs in the CNS and Schwann cells in the peripheral nervous system (PNS). OLs are capable of producing up to ∼30-60 myelin sheaths *in vivo* (Matthews and Duncan, 1971), whereas Schwann cells only form one myelin sheath on their chosen axon. In both the PNS and CNS, a single axon will be myelinated by multiple myelinating glia. The myelin sheath itself is a specialised extension of the OL plasma membrane. Remarkably, myelin sheaths in the CNS can consist of up to 150 myelin lamellae (layers) (Remahl and Hildebrand, 1990). During myelin sheath production, the inner tongue of the myelin sheath, which remains in contact with the axonal surface, is progressively surrounded by multiple wraps of lipid rich and protein-containing membrane which expand longitudinally along an axon where they form specialised axoglial junctions at the paranodal region (Snaidero et al., 2014) (Figure 1.3). Subsequent myelin sheath compaction occurs from the outer layers inwards, and relies on a balance of antagonism between myelin proteins myelin basic protein (Mbp) and 2'-3'-cyclic nucleotide-3'-phosphodiesterase (Cnp) (Snaidero et al., 2017). Paranodal junctions result from the interactions of axonal proteins Contactin

and Contactin-associated protein and glial Neurofascin 155 (Zonta et al., 2008) (Figure 1.3). The formation of these junctions serves to both cluster sodium channels at small (∼1 micron), unmyelinated gaps known as 'nodes of Ranvier' and to isolate them from potassium channels in the juxtaparanodal region (Rosenbluth, 2009). As I will go on to discuss in Section 1.4, it is this spatial segregation of ion channels that endows myelinated axons with their ability to perform saltatory conduction.

Myelin sheaths are often referred to as 'internodes', alluding to the distance between two nodes of Ranvier. The two terms are often used interchangeably, however, given that patterns of myelination are irregular along many axons where large unmyelinated gaps often exist between sheaths without nodal structures, this conflation is inaccurate. Thus, for consistency and clarity I will use the term 'myelin sheath' from here on. The common measure of myelin sheath thickness is computed as a 'g-ratio'. This represents the ratio between the diameter of the inner axon and the diameter of the axon including its myelin sheath i.e. larger g-ratio values represent thinner myelin sheaths. This term will be used frequently throughout this thesis.

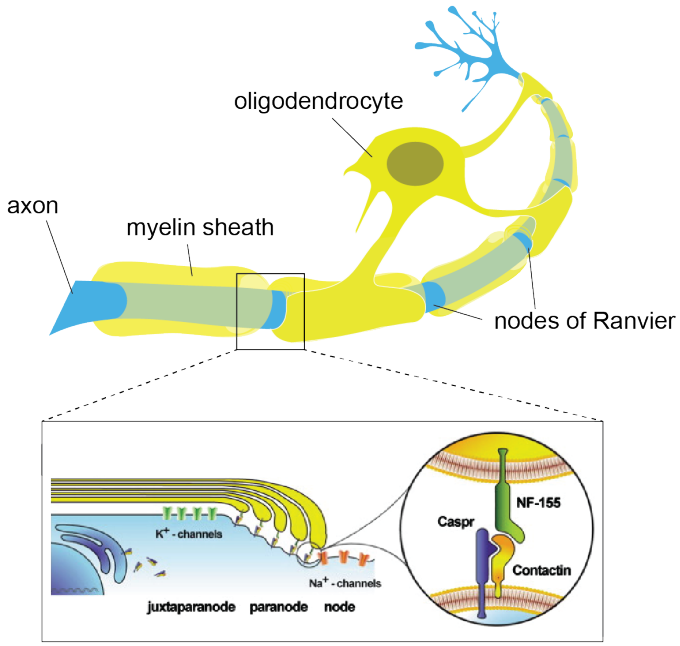

Figure 1.3: Structure of a myelinated axon and an associated oligodendrocyte Schematic demonstrating the structure of a myelinated axon and an associated oligodendrocyte. Schematic adapted from Wikimedia (LadyofHats). Insert: The structure of the juxtaparanode, paranode and node of Ranvier are illustrated. Paranodal junctions restrict potassium channels to the juxtaparanodal region and sodium channels to the node of Ranvier. Axoglial interactions at the paranodal junction form between OL expressed NF-155 and axonal expressed Caspr and Contactin. Figure taken from Boyle et al. (2001).

1.4 The influence of myelination on neuronal physiology

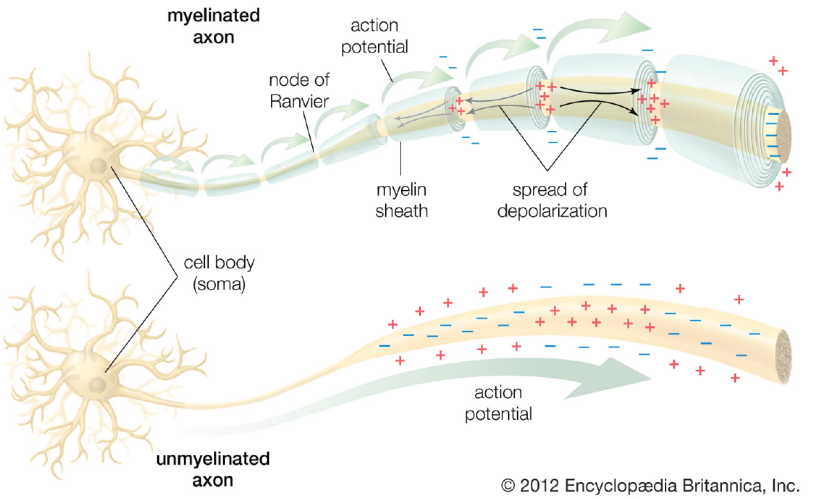

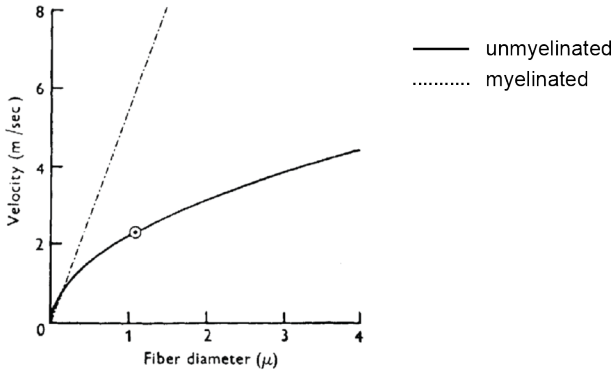

Figure 1.4: Myelination allows saltatory conduction
Top: Schematic demonstrating the propagation of an action potential along a myelinated (top) and unmyelinated (bottom) axon via saltatory conduction and continuous conduction respectively. Bottom: Graph from Waxman (1980) demonstrating the theoretical relationship between conduction velocity and diameter for myelinated (dashed line) and unmyelinated (solid line) axons. Myelinated axons exhibit a linear relationship between velocity and fiber diameter. Note how myelination only exerts a functional advantage to an axon over the size of approximately 0.2μm.

1.4.1 Myelination provides unique biophysical properties to the underlying axon

In general, OLs (in mammals) preferentially myelinate axons over a caliber of approximately 0.2 microns (Remahl and Hildebrand, 1982; Waxman and Bennett, 1972) which is the size threshold at which myelination is predicted to confer an advantage to the speed of CV (Waxman, 1980) (Figure 1.4). The structural features of the myelin sheath endow the underlying axon with multiple electrophysiological specialisations required

for saltatory conduction, i.e. rapid action potential propagation, to occur. Firstly, the density of sodium channels at the nodes of Ranvier causes rapid depolarisation and large sodium influx upon action potential arrival. Secondly, the presence of myelin membrane around the axon at internodal regions increases resistance (i.e. isolates extracellular cations from anions inside the axoplasm) and reduces capacitance (i.e. the amount of stored charge on both sides of the membrane). These biophysical properties result in the rapid diffusion of cations longitudinally along the axon to the next node of Ranvier, where propagation of the action potential will occur. These localised regions of ion exchange provide saltatory conduction its name, from 'saltate' which means to leap. In unmyelinated axons, whose ion channels are dispersed diffusely across the axolemma, the propagation of action potentials is slower due to the sequential opening of sodium and potassium channels along the entire length of an axon, a process known as 'continuous conduction' (Figure 1.4).

In addition to permitting saltatory conduction, the biophysical properties of myelination are integral to maintain other aspects of neuronal physiology, for example, the ability to sustain high rates of action potential firing i.e. the excitability of the neuron, and reduce temporal jitter i.e. fluctuations in the timing of single action potentials on repeat stimulation (Kim et al., 2013). Theoretically, myelination is also thought to act as a physical barrier to ephaptic communication. Ephaptic coupling between neurons occurs when the electric field produced by one neuron can polarise the membrane of another via current flow through extracellular space - known as 'field effects'. This non-synaptic form of communication promotes synchronous firing and timing of action potentials among groups of neurons and is thought to play a functional role in rhythmogenesis in the CNS (Weiss, 2010).

In summary, the ability of myelin to influence multiple aspects of neuronal physiology can be attributed to its structural enforcement of ion channels to the nodal and paranodal regions. Ultimately, it is the spatial distribution of ion channels which determines the speed of action potential CV and the excitability of an axon. In the following sections, I will discuss how individual parameters of a myelin sheath along a single axon can alter this distribution and the resulting effects this incurs on action potential CV. A detailed review on this subject is available in the review by Suminaite et al. (2019).

1.4.2 Individual parameters of myelin sheath morphology and conduction velocity

Myelin sheath length:

Myelin sheaths in the CNS exhibit significant variation in their length, number and distribution along an axon in comparison to the PNS (Auer et al., 2018; Hill et al., 2018; Hughes et al., 2018; Tomassy et al., 2014). It has long been predicted from modelling studies that changes in myelin sheath length can influence CV along an axon (Brill et al., 1977; Huxley and Stämpeli, 1949; Moore et al., 1978; Waxman, 1980). Concrete evidence for this effect in the CNS is sparse but it has been well demonstrated in PNS models (Court et al., 2004; Simpson et al., 2013; Wu et al., 2012). For example, in periaxin-null mice which exhibit impaired elongation of myelin sheaths in the PNS, action potential CV was reduced by 50% (Wu et al., 2012). In comparison, enhancing the elongation of myelin sheaths by a third of their length - by physical extension of a rabbits hindlimb – had no effect on CV measurements, suggesting that past a certain point myelin sheath length does not influence CV (Simpson et al., 2013). In support of this, measurements of CV during development *in vivo* have been shown to reach a flat maximum when myelin sheaths reach a certain length (Figure 1.5b) (Wu et al., 2012).

Few have investigated the effects of myelin sheath length on CV in the CNS. In a recent study by Etxeberria et al. (2016), reducing neuronal activity by monocular deprivation resulted in shorter myelin sheaths along fibers of the optic nerve. This finding was associated with delays in CV detectable as widened compound action potential (CAP) waveforms. This is the first example from the CNS that changes in myelin sheath length affect conduction properties. However, this particular experimental manipulation resulted in oligodendrogenesis and increase in node of Ranvier numbers, making it difficult to ascribe the given conduction properties to myelin sheath length alone. Similar changes in myelin sheath length have been observed upon aging in the CNS, where adult born OLs produce shorter myelin sheaths along fibers of the optic nerve than those born earlier in development (Young et al., 2013). Using established computer models, the authors predicted that this would cause a reduction in CV under certain conditions.

In summary, CV demonstrates sensitivity to myelin sheath length. In general, shortening of myelin sheaths slows CV, while lengthening myelin sheaths can increase CV to

a physiological maximum. However, in the presence of other myelin adaptations differential effects may be observed. Evidence for a direct effect of myelin sheath length on CV along CNS axons is less abundant than in the PNS, but predicted to follow similar patterns. However, it is reasoned that the additional variability in sheath length in the CNS may represent a requirement for more complex control of CV timing across circuits in this region of the nervous system. This will be discussed in depth in the next section concerning myelin and circuit function (Section 1.8).

Myelin sheath thickness:

Myelin sheath thickness is closely correlated to axon caliber in the CNS, where larger axons will generally possess thicker myelin sheaths (Blakemore, 1973; Hildebrand and Hahn, 1978; Moore et al., 1978; Rushton, 1951). However, this relationship slows down with increasing axon size suggesting that there is a limit to myelin thickness *in vivo* (Hildebrand and Hahn, 1978). Historical modelling studies predicted that for axons of a certain diameter, speed of CV is optimal at a g-ratio of 0.6 (Rushton, 1951). However, when variable conditions and space restrictions of the CNS are taken into account, this value is closer to 0.77 (Chomiak and Hu, 2009). In reality, g-ratios are extremely variable across the CNS and even along single axons (Gao et al., 2019). Remarkably, other than the predictions made by these modelling studies, our understanding of how variations in myelin sheath thickness affect CV *in vivo* remains limited.

It is generally well recognised that significant decreases in myelin thickness result in delayed CV. Much of the supporting evidence for this comes from studies of human models of demyelinating neuropathies for which conduction delays are often diagnostic (Verhoeven et al., 2003). Additionally, functional conduction delays are a common feature in many animal models with hypomyelination (Bilbool et al., 1983; Kim et al., 2013; Lehman and Harrison, 2002; Roy et al., 2007). However, the assignment of slowed conduction velocities to myelin sheath thickness specifically is problematic due to concurrent pathophysiology in many of these models. Providing more definitive evidence, cell type specific overexpression of an ERK1/2 upstream kinase in mature OLs drove the production of thicker sheaths which were associated with reductions in latency (i.e. increased CV) on auditory brainstem response (ABR) recordings (Jeffries et al., 2016). However, the differences in latency were within hundreds of microseconds suggesting

only a modest contribution of increases in myelin sheath thickness to conduction speeds *in vivo*. Indeed, in models of remyelination, improvements in CV are detected prior to the development of mature myelin sheaths at the early stages of myelin ensheathment. Furthermore, conduction speeds largely return to normal despite remyelinated sheaths being thinner and shorter (Smith et al., 1979; Smith and Hall, 1980). Finally, although not a change in myelin thickness per se, the loss of tight junctions between myelin lamellae can be enough to induce a 50% decrease in CV in small caliber axons (Devaux and Gow, 2008; Gow et al., 1999). Thus, maintaining the integrity of the myelin sheath, and appropriate localisation of ion channels, is equally as important for the control of CV.

Importantly, changes in myelin sheath thickness are achieved by the addition or removal of myelin lamellae and their junctions at the paranode (Snaidero et al., 2014). Because of this, changes in myelin thickness are usually associated with altered myelin sheath and nodal distances (Ibrahim et al., 1995; Jeffries et al., 2016). Thus, it is problematic to isolate the effects of these parameters on CV from each other.

Nodal properties:

As nodal length is in part determined by myelin sheath thickness it is included here as an indirect parameter of myelination. As the main site of sodium channel densities, nodal parameters can exert large effects on action potential CV speeds. Modelling studies have demonstrated that increasing nodal length while holding the sodium channel number constant leads to reductions in CV by increasing the membrane capacitance and resistance (Arancibia-Cárcamo et al., 2017) (Figure 1.5C). Nodal diameter has also been shown to influence timing of conduction in anatomically informed modelling studies of the auditory brainstem circuit in rodents (Ford et al., 2015).

Examples where nodal length is disrupted in the absence of other changes to myelinating cells are limited. Both conditional ablation of cohesion regulatory protein Esco2 from the OL lineage (Schneider et al., 2016) and overexpression of Anosmin-1 in mice (Murcia-Belmonte et al., 2016) result in lengthening of nodes of Ranvier. However, in these studies differing effects on action potential CV were obtained from *in vivo* stimulation and recording in the corpus callosum. This discrepancy could be accounted for

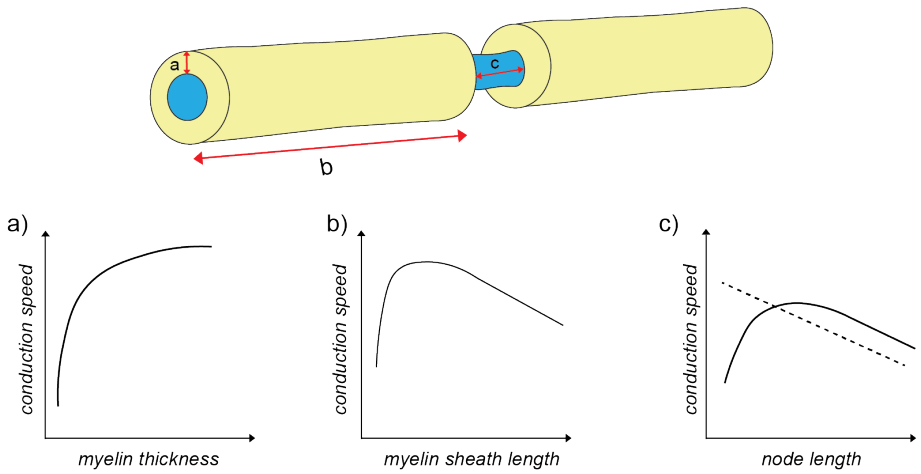

Figure 1.5: Individual parameters of the myelin sheath exert different effects on conduction velocity
Schematics representing the approximate relationships between individual parameters of the myelin sheath with conduction velocity along an axon. **a) Myelin sheath thickness:** Schematic based on predictions by Waxman (1980). For a fiber with a fixed diameter, conduction velocity increases monotonically with increasing myelin sheath thickness. **b) Myelin sheath length:** Schematic based on predictions by Brill et al. (1977). Conduction velocity increases with increasing myelin sheath length but reaches a flat maximum at a certain value. **c) Node length:** Schematic based on modelling estimations by Arancibia-Cárcamo et al. (2017). Conduction velocity decreases if node length increases due to a reduction in the sodium channel density (dashed line). However, if sodium channel density is held constant, conduction velocity increases linearly with nodal length to a maximum value, past which conduction velocity decreases due to increased nodal capacitance and axial resistance.

by the presence of thicker myelin sheaths with overexpression of Anosmin-1, whereas no differences in myelination were observed with Esco2 knockdown. Additionally, the interventions had differential effects on OPC proliferation and OL differentiation which could exert their own effect on conduction speeds.

It is important to note that clustering of sodium channels at the nodes of Ranvier can occur independently of intact axoglial junctions at the paranodal regions (Zonta et al., 2008). Furthermore, during development the early clustering of sodium channels or 'pre-nodes' can occur along specific axons prior to myelination, but remains dependent upon the presence of OL signals (Freeman et al., 2015). Remarkably, the assembly of these pre-nodes is already sufficient to increase the speed of action potentials conduction prior to myelination. Additionally, the timing of node formation depends on the presence of axonal cytoskeletal proteins which permit anchorage of axoglial adhesion complexes (Brivio et al., 2017). Thus, structural nodal changes can be driven by the axon as well as by myelin sheath length.

Conclusion

In summary, there is strong evidence from electrophysiological and computer modelling studies that multiple parameters of myelin sheath morphology can influence action potential CV along individual axons. With the observation that the white matter of our brain exhibits structural plasticity during development and adulthood, correlating with behavioural performance, it is tempting to hypothesise that adaptations in myelin sheath morphology represent a major cellular component of white matter plasticity and play a functional role in promoting circuit function and the development of behaviour. In the following sections, I will strengthen this hypothesis by presenting evidence that adaptations in myelin underlie changes in white matter structure observed in imaging studies, and discuss activity-mediated myelination as a mechanism by which these adaptations could occur.

1.5 Linking white matter plasticity to changes in myelination

1.5.1 Evidence for myelin adaptations in response to learning

DTI imaging of fixed spinal cords from myelin-deficient rats and wild type controls has shown that the presence or absence of myelin is enough to modulate the values of diffusion anisotropy (Gulani et al., 2001). Further studies set out to corroborate this relationship in the context of learning induced plasticity. In a similar spatial-navigation learning paradigm to Hofstetter et al. (2013), Blumenfeld-Katzir et al. (2011) found regional differences in FA in the grey and white matter of rats following five days of using the Morris Water Maze. Within the white matter, an increase in FA was identified in the corpus callosum. Subsequent histological examination of this region revealed an increase in myelin basic protein (Mbp) immunoreactivity following immunohistochemical staining. Similar results were observed in a study by Sampaio-Baptista et al. (2013) which quantified FA and immunohistochemical Mbp staining following 11 days of learning a skilled-reaching task. Circuit specific increases in FA were identified in the subcortical white matter underlying the contralateral motor cortex along with increased intensity of Mbp staining in the same region. Each of these parameters correlated with the learning rate of individual animals however no direct relationship between Mbp intensity and FA values was found. Together these results provide evidence that learning

can induce changes in myelination, however, it is likely that other structural changes alongside myelination are required to contribute to changes in FA.

Further suggestion for a role of myelinating cells in motor learning came from McKenzie et al. (2014). Using cell-type specific conditional knockout (CKO) of myelin gene regulatory factor (Myrf), which is required for OL differentiation and myelination, from OPCs the authors were able to block the production of new myelin in adult mice and investigate how this affected their ability to perform a novel motor learning task. Mice were assessed on their ability to learn to run on a 'complex running wheel', where rungs of the wheel have been removed at irregular intervals, over eight days. Although both groups of mice demonstrated improvement in this task over the experiment duration, homozygous CKO mice exhibited reduced performance on each day of using the wheel quantified as lower average speeds and irregular locomotor patterns compared to their heterozygous littermates. Whether this study truly represents a motor learning paradigm is controversial given that the rate of improvement over time is very similar between groups and the complex running wheel was initially designed to detect subtle motor deficits rather than to test motor learning (Schalomon and Wahlsten, 2002). Furthermore, no attempts were made to assess levels of myelination in this study, leaving a large question mark hanging over the mechanism underlying this phenotype.

In the same study, OL lineage cell dynamics were assessed in the wild type cohort alone during the motor learning paradigm. Using 5-Ethyl-2'-deoxyuridine (EdU) staining to label differentiating cells, McKenzie et al. (2014) found that running on the complex running wheel induced OPC proliferation within six days. By eleven days these cells were detectable as mature OLs. However, this delayed effect on OL number does not match the timing of behavioural impairment observed in Myrf CKO mutants, in which OL differentiation is blocked, which occurs 2 days after introduction to the running wheel. This raises the question as to whether a lack of newly formed OLs is really driving the suggested motor learning impairment observed in the Myrf CKO mice. However, using a novel marker of newly differentiated OLs, ectonucleotide pyrophosphatase/phosphodiesterase 6 (enpp6), the follow up study from Xiao et al. (2016) showed that OLs can differentiate as early 2 to 3 hours following the introduction to this complex running wheel and CKO of Myrf from OPCs impaired motor learning

within the same timeframe. Although these studies propose an intriguing role of OL differentiation in motor learning, there is no direct evidence from these studies that these behavioural changes are due to a lack of myelination per se. Furthermore, a lack of Myrf in OLs has been shown to result in apoptosis (Emery et al., 2009). With this knowledge, it would be important to confirm that the behavioural phenotype observed in these studies is not due to microglial activation, a phenomena that is observed in other models of disrupted myelination (Janova et al., 2017). Further investigations using this model are currently underway, aiming to directly correlate changes in myelin to performance on the complex running wheel. This would provide stronger evidence for a role of myelin adaptations in this particular behavioural paradigm.

1.5.2 Evidence for myelin adaptations in response to experience

Outside the context of learning and/or motor activity, evidence exists that myelinating cells respond to social and sensory experience. Two weeks of social isolation in mice following weaning is associated with abnormal myelination of the medial prefrontal cortex (mPFC) and deficits in social behaviour and working memory when tested four weeks later (Makinodan et al., 2012). On examination of the mPFC, OL number was stable however OLs exhibited abnormal morphology such as shorter and less ramified processes with fewer myelin sheaths per OL. Evaluation of the mPFC using electron microscopy revealed increased g-ratios consistent with thinner myelin sheaths. Tissue expression of myelin specific proteins such as Mbp and Mag were also reduced. Interestingly, only mice isolated between post-natal days 21 and 35 displayed these abnormalities, suggesting the existence of a critical period during which the mPFC is responsive to experience. A parallel study asked whether these findings would persist upon social isolation of adult mice (Liu et al., 2012). Indeed, the findings of social withdrawal and reductions in myelin sheath thickness in the mPFC were found in adult mice but required an extended duration of social isolation (8 weeks). The behavioural effects of social isolation in younger mice were phenocopied by OL specific knockdown of erbB3, supporting an OL specific effect of social isolation on myelination and behaviour (Makinodan et al., 2012). Additionally, treatment with clemastine, a pro-myelinating, antimuscarinic compound for two weeks following social isolation rescued the social interaction phenotypes and g-ratios in the mPFC of adult mice, although these effects may not be limited to the action of the drug on myelin alone (Liu et al., 2016).

In mice, the somatosensory pathway from whiskers to the barrel cortex has proven a useful model to study the effects of sensory deprivation and stimulation on myelinating cells. An innovative experiment by Hughes et al. (2018) hung strings of beads from the lids of the animals' enclosures. Enriching their environment in this way allowed investigation into the effects of excessive sensory stimulation. Using two photon imaging over an extended time course, the authors were able to demonstrate that this manipulation led to an increase in the number of OLs in the somatosensory cortex. Similarly, training rats in a texture detection task (involving exposure of their paws to smooth and textured surfaces) resulted in higher fractional anisotropy values on DTI and upregulation of Mbp transcript expression in the somatosensory cortex (Sampaio-Baptista et al., 2020). As one might anticipate, eliminating sensory input to the barrel cortex by removing whiskers at an early age led to a reduction in the number of OLs due to impaired survival of early-stage OLs (Hill et al., 2014). However, sensory deprivation in this way has also been shown to cause altered distribution and an increased proliferation of OPCs in the barrel cortex, pointing towards differential effects of sensory experience on different stages of the OL lineage (Mangin et al., 2012).

Conclusion

In summary there is direct evidence for alterations in myelination and OL lineage dynamics in response to different types of experience. These studies raise the question: by what mechanisms are these changes in myelinating cells induced? During learning or sensory stimulation, it is reasonable to suggest that the level of electrical activity in the corresponding neural circuits will increase. In support of this, increases in the immediate early gene cfos expression were higher in the somatosensory cortex of rats exposed to the texture discrimination task (Sampaio-Baptista et al., 2020). In contrast, the effects of social and sensory deprivation on OL lineage cells and myelination are predicted to be caused by reductions in neuronal circuit activity. For example, a lack of glutamatergic input from thalamocortical neurons was associated with the OPC proliferation and distribution observed in the barrel cortex of sensory deprived mice (Mangin et al., 2012). Indeed, a large body of evidence exists to support the role of neuronal activity in shaping myelination *in vivo*, a mechanism referred to as 'activity-mediated myelination'. In the following sections, I will describe the capacity of the

CNS to produce myelin throughout life and present evidence that this process can be influenced by neuronal activity.

1.6 The CNS possesses a lifelong capacity for myelination

OPCs originate from neural stem cells located within the ventricular zones of the brain and spinal cord, from where they migrate to occupy diverse regions of the CNS during development (Richardson et al., 2006). From here, they persist into adulthood where they represent around 5% of the cells in the brain (Dawson, 2003; Trotter et al., 2010). Newly differentiated OLs are initially overproduced, with the majority undergoing cell death before committing to myelination (Barres et al., 1992; Hughes et al., 2018). This program of cell death has been shown to be important to establish the correct spatiotemporal pattern of myelination within the CNS (Sun et al., 2018). Despite this, a reservoir of OPCs persists in the CNS throughout life where they not only exist as a source of OLs but may also contribute to circuit maintenance (Chang et al., 2000; Sakry et al., 2014) - this will be discussed in further detail in Section 1.9. Indeed, the very nature of protracted myelination in humans demonstrates an ongoing ability for OL differentiation (Miller et al., 2012). Carbon dating studies have demonstrated that the levels of carbon 14 (c14) in purified myelin fractions from human brains corresponded to atmospheric c14 concentrations at the time of death, suggesting that myelin is continuously replenished in humans. However, the majority of OLs in the corpus callosum are born during childhood (up until 5 years of age), with turnover continuing at a low (<1%) but stable rate throughout adulthood (Yeung et al., 2014). In contrast, production of OLs was more protracted in the cortex and exhibited higher turnover rates of 2.5%. These levels of OL differentiation are in stark contrast to rodents which maintain much higher (>30%) rates of differentiation in adulthood (Young et al., 2013). This dichotomy in differentiation rates may be a species or region specific finding, or, may be explained by the chosen methodology: a major caveat of the carbon dating technique is that the integration of c14 occurs at the time of OPC division. This does not necessarily correlate with the time of differentiation of an OL, given that OPCs are capable of differentiating directly into OLs without undergoing cell division (Hughes et al., 2013). Therefore, the low turnover rate of OLs in the study by Yeung et al. (2014) should be taken as a bare minimum.

Zebrafish studies have shown that once an OL commits to myelination, new sheaths are formed within a matter of hours (Czopka et al., 2013). The length and patterns of myelin sheath are established within a matter of days, after which they remain largely stable (Auer et al., 2018). Complementary rodent studies have demonstrated that the myelin sheaths of mature OLs are indeed extremely stable across different regions of the brain and exhibit little change in the number or length of their myelin sheaths over protracted periods of time (Hill et al., 2018; Hughes et al., 2018; Tripathi et al., 2017). Young et al. (2013) revealed that even in the heavily myelinated optic nerve, adult born OLs continue to form new myelin sheaths throughout life without the loss of pre-existing sheaths. In other regions of the CNS (such as the cortex), unmyelinated gaps exist along individual axons which are slowly filled with new sheaths over a prolonged period (years) of a rodent's life (Hill et al., 2018; Hughes et al., 2018). Thus, adult born OLs are present and able to produce new myelin sheaths contributing to patterns of myelination. Evidently, the role of this population of OLs would be different in the presence of disease, when their role in replacing lost sheaths would be integral. Interestingly, zebrafish studies have revealed that during development, the loss of a single myelin sheath along an axon can be rescued by the remodelling and extension of a neighbouring sheath (Auer et al., 2018). Whether similar mechanisms are present in mammalian or adult systems has not yet been tested.

This lifelong capacity for myelination in the CNS provides multiple routes by which exposure to experience and altered levels of neuronal activity could influence myelin morphology. The presence of adult-born OLs and the availability of unmyelinated regions along axons in some parts of the CNS suggests that 'de novo' myelination exists as one form of myelination recruitable for the purposes of plasticity. Contrastingly, it is also possible that myelin plasticity results from remodelling of existing myelin sheaths. The exceptional stability of myelin sheaths suggests that this form of remodelling is not a common finding in adulthood. However, a caveat to these studies is that they only documented myelin sheath length dynamics, not myelin sheath thickness. Indeed, activation of the PI3K/AKT/mTOR pathway in OLs has been shown to reinitiate myelin sheath growth in adulthood through the addition of myelin wraps (Snaidero et al., 2014). Although this has not been documented under physiological conditions, it is remains a possibility that remodelling can occur in a radial direction throughout life.

OLs possess an intrinsic ability to myelinate

It is important from the outset to appreciate that in contrast to the Schwann cells of the peripheral nervous system (Birchmeier and Nave, 2008), axonal signals are not essential for the induction of myelination by OLs. When OPCs are cultured in the presence of inert, synthetic nanofibers with diameters equivalent to those of axons found *in vivo* (1-2μm), they follow a program of differentiation and myelination including the production of compact myelin membrane (Bechler et al., 2015). Furthermore, examples exist whereby the absence of neuronal activity has little to no effect on myelination (Etxeberria et al., 2016; Lundgaard et al., 2013; Stevens et al., 1998). I mention these findings to clarify that innate, activity-*independent* mechanisms of myelination exist in the CNS in addition to the activity-mediated mechanisms which will be covered in the next section.

1.7 Evidence for activity-mediated myelination

1.7.1 OL lineage cells respond to neuronal activity

It has long been known that neuronal activity plays a role in OL lineage cell dynamics and myelination. This relationship was first established by pivotal studies using the developing rat optic nerve. Transection of the optic nerve was shown to cause reductions in OPC proliferation (Barres et al., 1993) and OL survival (Barres and Raff, 1993), which could be prevented by delivering growth factors to the nerves prior to transection. This provided the first evidence that axonal signals may mediate OL dynamics and survival *in vivo*. Shortly after, researchers demonstrated that these signals can be mediated by neuronal activity (Demerens et al., 1996; Stevens et al., 2002, 1998). Using neurotoxins such as TTX to block action potential firing in the optic nerve *in vivo* resulted in a reduction in the number of mature OLs and myelinogenesis, while stimulating activity *in vitro* using alpha-scorpion toxin had the opposite effect (Demerens et al., 1996). However, the role of neuronal activity on myelination has been shown to be quite variable according to the developmental time point and conditions in which they are assessed (reviewd by Zalc and Douglas Fields (2000)).

Neuronal activity involves the release of signalling molecules via synaptic and non-synaptic mechanisms (Gallo et al., 1996; Stevens et al., 2002; Wake et al., 2011). In-

deed, OL lineage cells express a variety of receptors sensitive to neurotransmitters e.g. glutamate and GABA (Káradóttir and Attwell, 2007), as well as secreted factors e.g. growth factors (Barres et al., 1992; Lundgaard et al., 2013), cytokines e.g. leukaemia inhibitory factor (LIF) (Ishibashi et al., 2006) and extracellular adenosine (Stevens et al., 2002; Zhang et al., 2014), all of which have been implicated in mediating aspects of OL lineage cell survival and myelination. Additionally, voltage gated ion channels such as sodium, calcium and potassium channels are expressed throughout the OL lineage (Larson et al., 2018). Thus, they are well equipped to receive and integrate a multitude of signals. With advancements in *in vivo* imaging techniques, cell-type specific genetic manipulations and the discovery of stage-specific OL cell lineage markers, we have been able to further our understanding of how neuronal activity shapes OL lineage cell behaviour and myelination *in vivo*. Here I will review evidence that myelinating glia are responsive to changes in neuronal activity and discuss cellular and signalling mechanisms that have been implicated in activity-mediated myelination.

1.7.2 Neuronal activity induces OPC proliferation

OPCs represent the only cells of the OL lineage which are able to form direct synapses onto neurons, allowing monitoring and response to neuronal activity (Bergles et al., 2000). Pivotal experiments using patch clamp recordings directly from OPCs in the hippocampus (Bergles et al., 2000) and white matter of the cerebellum (Káradóttir et al., 2005) demonstrated that the majority of excitatory activity in OL lineage cells is mediated by AMPA and NMDA receptors, stimulated by glutamate release at synaptic sites. Glutamatergic synaptic input to OPCs can induce calcium transients in their soma, although how these transients guide OPC cell dynamics is unclear at present (Sun et al., 2016). Both synaptic input and glutamate signalling have been shown to regulate OPC proliferation in *in vitro* and *in vivo* systems (Gallo et al., 1996; Mangin et al., 2012). OPCs also express functional GABA receptors *in vivo* which have been shown to mediate OPC depolarisation in response to hippocampal interneuron firing (Lin and Bergles, 2004; Serrano-Regal et al., 2019). Loss of GABAergic input to OPCs has been demonstrated to drive excessive proliferation and delayed differentiation of OLs resulting in dysmyelination (Zonouzi et al., 2015).

Evidence for a direct response of OPCs to neuronal activity *in vivo* comes from Gib-

son et al. (2014). Using optogenetic techniques to stimulate neurons in the premotor cortex of awake, freely behaving mice, the authors were able to study the subsequent effects on OL lineage dynamics and myelination. Stimulation of channel-rhodopsin 2 expressing neurons at physiologically relevant levels for only thirty minutes caused re-entry of OPCs into the cell cycle, detectable as robust increases in OPC number in the premotor cortex and subcortical white matter three hours later. Extending the stimulation paradigm over seven days resulted in a burst in oligodendrogenesis four weeks later. These findings were accompanied by the presence of thicker myelin sheaths in the white matter tracts containing the axons of the stimulated neurons, and subtle behavioural motor adaptations. Interestingly, a recent study using electrode stimulation in the corpus callosum of adult mice, found that OPC proliferation and differentiation were dependent on the frequency of activity (Nagy et al., 2017). Lower frequency (5Hz) stimulation promoted differentiation into early OLs, whereas higher frequency (25Hz and 300Hz) stimulation resulted in OPC proliferation. Together, these studies provide evidence for robust OPC proliferation in response to neuronal activity *in vivo*, with potential for subsequent downstream effects on myelination. Importantly, it has been recently demonstrated that OPC expression of voltage-gated ion channels and glutamate receptors is heterogenous with age and throughout brain regions, suggesting that the effects of neuronal activity on OPC dynamics are likely region and time point specific (Spitzer et al., 2019). This could contribute to variability in the susceptibility of specific regions of the brain to mechanisms of activity-regulated myelination.

1.7.3 Effects of neuronal activity on OL differentiation and survival

Despite the lack of a traditional synapse, mature OLs remain responsive to glutamatergic signalling via both AMPA and NMDA receptors (Káradóttir et al., 2005), although the level of receptor expression is reduced relative to their OPC form (De Biase et al., 2010). Genetic manipulations of glutamatergic receptors have expanded our understanding of their role in myelination. Triple knockdown of OPC glutamate subunits 2,3,4 - using cell-type specific techniques for subunits 2 and 4, in combination with constitutive knockdown for subunit 3 - resulted in reduced survival of OLs and a subsequent reduction in the number of myelinated axons *in vivo* (Kougioumtzidou et al., 2017). This suggests that AMPA signalling predominantly drives myelination via the promotion of OL survival and differentiation. Developing OLs also maintain GABA

receptor expression during their lineage progression, where GABAergic input promotes OL differentiation and maturation (Serrano-Regal et al., 2019; Zonouzi et al., 2015). In summary, both glutamatergic signalling via AMPA receptors and GABAergic signalling have been shown to promote the differentiation and maturation of OLs from their precursor form. *In vitro*, GABA-mediated upregulation of Mbp expression is mediated by Src-family kinase signalling (Serrano-Regal et al., 2019), however, our understanding of the molecular mechanisms driving OL dynamics in response to GABA and glutamatergic signalling *in vivo* is limited.

1.7.4 Neuronal activity mediates axonal selection and sheath formation

Exploiting the power of larval zebrafish for imaging the dynamics of myelination, intricate studies have shown that neuronal activity can influence axonal selection and subsequent myelin production by OLs (Hines et al., 2015; Mensch et al., 2015). Global inhibition of synaptic vesicle release during the onset of myelination reduced OL number and the number of sheaths formed per OL while increasing neuronal activity using PTZ, a GABA antagonist, resulted in an increase in the number of myelin sheaths made per OL (Mensch et al., 2015). A parallel study followed myelin sheath formation from the perspective of the axon: inhibiting synaptic vesicle release from a subset of neurons reduced the selection of those axons for myelination and resulted in a reduction in the length of nascent (new) myelin sheaths formed (Hines et al., 2015). However, increasing neuronal activity in this study had no observable effect on myelin sheath length which may be due to the techniques or subset of neurons targeted. Despite this discrepancy, these studies provided resounding evidence that neuronal activity can influence myelin sheath dynamics *in vivo*. Koudelka et al. (2016) took this further to demonstrate that activity-mediated myelination is specific to neuronal subtypes in the spinal cord of zebrafish, suggesting that this mechanism is not a global feature of the CNS.

Further evidence exists to support a role for neuronal activity in axonal selection. During the initial stages of myelination *in vivo*, OPCs extensively survey their environment by extending and retracting their processes to sample potential targets for myelination. Providing a mix of 'active' neurons and silenced neurons (treated with

botulinum toxin to prevent vesicular release) to OL lineage cells *in vitro* resulted in the preferential myelination of the active population (Wake et al., 2015). Using a similar competitive approach *in vivo*, chemogenetic activation of somatosensory neurons in the cortex biased myelination in the corpus callosum towards the axons of activated cells (Mitew et al., 2018). The stimulation paradigm in this study also induced OPC proliferation and differentiation and production of thicker myelin sheaths. Thus, the choice of an OL to myelinate an axon appears to be partly regulated by the level of neuronal activity. Time course imaging in zebrafish suggests that this preferential selection of active neurons is mediated at the level of sheath stabilisation (Hines et al., 2015). OPCs demonstrated normal 'sampling' of tetanus-expressing inactive axons but fail to stabilise sheaths on these axons following their initial formation. In support of this role for neuronal activity in sheath stabilisation, complementary functional imaging studies in zebrafish have demonstrated that the patterns of calcium transients in nascent (newly formed) myelin sheaths can predict the likelihood of their stabilisation and subsequent elongation (Baraban et al., 2018; Krasnow et al., 2018).

1.7.5 Effects of neuronal activity on myelin sheath growth

Studies in developmental models also support a role for the activity-mediated regulation of myelin sheath length (Etxeberria et al., 2016; Koudelka et al., 2016). Blocking neuronal vesicular release causes fewer and shorter myelin sheaths to be produced along the length of individual axons in larval zebrafish (Koudelka et al., 2016). Similarly, monocular deprivation during active myelination of the visual system results in a subtle reduction in the length of myelin sheaths along fibers of the optic nerve (Etxeberria et al., 2016). Furthermore, inhibiting release of glutamate from retinal ganglion cells using conditional ablation of vesicular glutamate transporter replicated these findings. However, in contrast to the finding that removing sensory input to the somatosensory cortex reduces OL number (Hill et al., 2014), loss of glutamate signalling in this model was associated with an increase in the number of OLs, which may imply circuit specific responses to neuronal activity. Two recent studies have shown that the extent of myelin sheath growth can be predicted from the pattern of calcium transients observed in myelin sheaths (Baraban et al., 2018; Krasnow et al., 2018). Exploiting the suitability of zebrafish for non-invasive, longitudinal imaging, these studies set out to correlate the dynamics and fate of newly forming myelin sheaths to calcium dynamics

in developing OLs. Sheath elongation was associated with a high frequency of low amplitude, short duration calcium transients, whereas high amplitude calcium transients were associated with sheath shortening and retraction (Baraban et al., 2018; Krasnow et al., 2018).

Myelin sheath thickness represents another parameter which may be regulated by neuronal activity. In juvenile and adult mice, optogenetic and chemogenetic stimulation of neurons leads to increased myelin sheath thickness in corresponding white matter tracts (Gibson et al., 2014; Mitew et al., 2018). However, our current understanding of the molecular mechanisms by which neuronal activity can regulate myelin sheath thickness and growth are primitive. It is known that mature OLs express NMDA receptors on the inner myelin membrane, adjacent to the axonal surface, suggesting that glutamatergic signalling may play a role in local myelin remodelling (Káradóttir et al., 2005). In support of this, local calcium transients in the myelin sheath have been shown to be predominantly driven by NMDA receptors (Micu et al., 2006). However, the role of OL NMDA receptors in myelination is controversial, given that genetic knockout of the NR1 subunit (required for functional NMDA receptor formation) from OL lineage cells causes no discernible effect on developmental myelination *in vivo* (De Biase et al., 2011).

The pathways through which calcium mediates myelin sheath dynamics are not clear. It has been proposed that calcium signalling may act to regulate actin cytoskeleton dynamics involved in myelin sheath growth (Nawaz et al., 2015) or induce the local translation of Mbp via fyn kinase signalling (Wake et al., 2011). Recently, stimulation of the P13K/AKT/mTor and MAPK/ERK signalling pathways has been shown to trigger the production of thicker myelin sheaths (Jeffries et al., 2016; Snaidero et al., 2014). However, whether any of these pathways allow myelin sheath remodelling in response to neuronal activity *in vivo* is yet to be proven.

1.7.6 Non-synaptic mechanisms of activity-mediated myelination

Purinergic signalling

OL lineage cells express receptors to ATP and its products adenosine and ADP (Welsh and Kucenas, 2018). ATP transporters are used to package neurotransmitters into synaptic vesicles. Consequently, ATP is released alongside other neurotransmitters

such as glutamate upon exocytosis (Abbracchio et al., 2009). It is also possible for neurons to release ATP extrasynaptically although the mechanisms for this are less clear (Stevens et al., 2002). Providing adenosine receptor antagonists to co-cultures of DRG neurons and OPCs prevents neuronal activity induced proliferation and differentiation of OPCs, confirming a direct adenosine mediated effect of activity-mediated ATP release on OPC dynamics (Stevens et al., 2002). Intriguingly, astrocytes have been shown to secrete a pro-myelinatory cytokine, LIF, in response to ATP release from axons following electrical stimulation, providing a model for multiple cell type involvement in activity-mediated myelination (Ishibashi et al., 2006). However, despite clear evidence for a role of ATP in activity-mediated myelination *in vitro*, these mechanisms are yet to be demonstrated *in vivo*.

Neurotrophins and growth factors

Neurotrophins, such as brain derived neurotrophic factor (BDNF), are known to regulate cell survival in the CNS. Furthermore, their neuronal expression levels can be influenced by neuronal activity (Ghosh et al., 1994). TrkB, the receptor for BDNF, is expressed by OL lineage cells *in vivo*, however, it is also highly expressed by astrocytes and neurons (Vondran et al., 2010; Zhang et al., 2014). BDNF heterozygous mice, which possess a 40% reduction in BDNF levels, exhibitted reduced numbers of OPCs and downregulation of myelin protein genes in the presence of normal axon density (Vondran et al., 2010). However, given the range of cell types that express TrkB receptors it is difficult to determine which cell type facilitated this effect. Subsequent cell type specific knockout of TrkB from OLs resulted in a specific reduction in myelin sheath thickness during development, a phenotype which was not maintained into adulthood suggesting that BDNF is required during periods of active myelin sheath production (Wong et al., 2013). Providing intriguing evidence for a role for BDNF in activity-mediated myelination, Lundgaard et al. (2013) demonstrated that the addition of BDNF to co-cultures enhanced myelination of DRG neurons via NMDA receptor dependent activation of the P13K-Akt pathway. Whether such a mechanism exists *in vivo* is currently unknown. Finally, recent work by Geraghty et al. (2019) has shown that activity-mediated myelination *in vivo*, using the optogenetic stimulation paradigm described in previous work from the same lab (Gibson et al., 2014), is dependent on BDNF-TrkB signalling. Expressing an inactive triple site mutant knockin of BDNF

in neurons or inducing OPC specific conditional knockout of TrkB receptor resulted in a failure of induction of OPC proliferation, OL differentiation and myelin sheath thickness following optogenetic stimulation. This appears to be conclusive evidence for a role of BDNF in activity-mediated myelination, at least in response to this experimental paradigm.

Neuregulin, another growth factor, has also been shown to enhance NMDA-receptor mediated modes of myelination *in vitro* (Lundgaard et al., 2013). A neuregulin receptor, Erbb3, has been implicated in activity-mediated myelination *in vivo*, where OL specific knockdown of ErbB3 phenocopies the effects of social isolation on myelination i.e. reduced myelin thickness in the mPFC and deficits in social behaviour and working memory (Makinodan et al., 2012). However, this role for neuregulin-erbb3 signalling appears to be either region specific or only applicable to later stages of myelination, as neither CKO of NRG1 from forebrain neurons nor cell type specific knockdown of ErbB receptors from OLs had an effect on OL number or CNS myelination during development (Brinkmann et al., 2008; Michailov, 2004). However, transgenic overexpression of NRG1 caused significant hypermyelination, with lower g-ratios (thicker myelin) and a higher density of myelinated axons on EM (Brinkmann et al., 2008). In contrast, (Roy et al., 2007) found that blocking erbB signalling in OLs caused an increase in OL number and altered myelin morphology including reduced myelin sheath thickness and a reduction in the number of myelin sheaths per cell. The cause of the discrepant effects between studies is unclear but may be due to the genetic approaches employed. Regardless, there is potential for activity-mediated myelination to be mediated by neuregulin and further work should aim to establish the relevant circuitry and developmental time points at which this occurs.

Conclusion on activity-mediated mechanisms of myelination

In this section I have focussed on the core activity-regulated synaptic and non-synaptic neuronal signalling molecules shown to mediate myelination. However, it is important to note that there are many other candidate molecules that are likely to be involved, including activity-mediated expression of neuronal adhesion molecules (Itoh et al., 1995; Laursen et al., 2009; Stevens et al., 2002) in addition to non-neuronal signals such as vasoactive peptides (Swire et al., 2019), which are beyond the remit of this introduc-

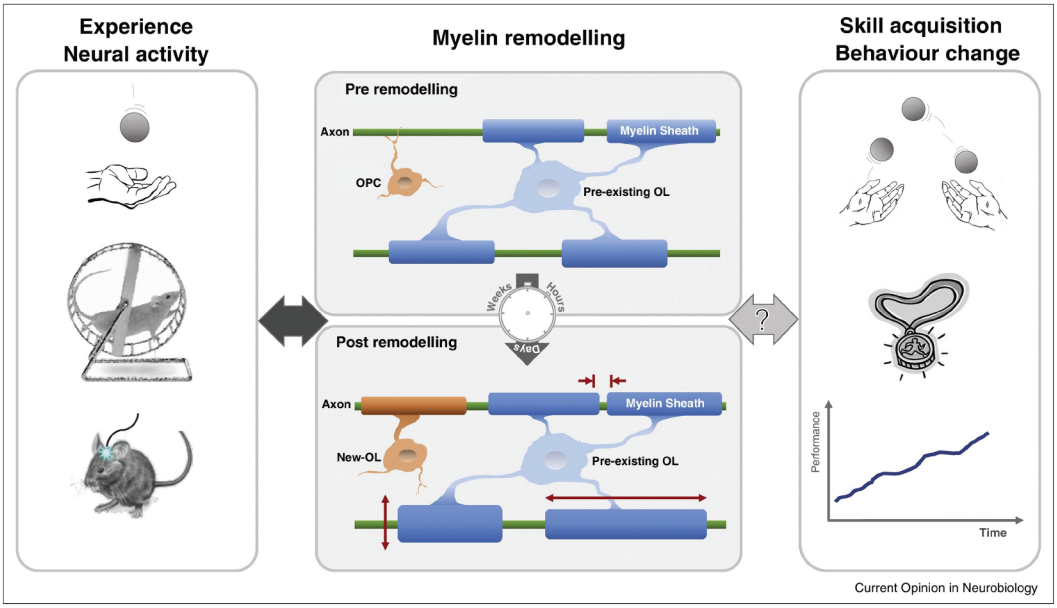

Figure 1.6: Summary of the effects of experience and neuronal activity on myelin remodelling
Figure taken from Kaller et al. (2017). Changes in myelination in response to neuronal activity, such as learning to juggle or using a complex running wheel, may include 'de novo' myelination by newly differentiated OLs or adaptations to the length or thickness of pre-existing sheaths. These changes may provide a functional effect to the underlying circuit allowing subsequent skill acquisition and behaviour to develop.

tion. Evidence presented so far demonstrates that OL lineage cells are fully equipped with a variety of receptors enabling them to detect and integrate a multitude of activity dependent signals from surrounding cells which can influence their progression through the OL lineage, choice of target for myelination and resulting myelin sheath morphology. The evidence for myelin remodelling in response to activity at later stages of development is limited, but may occur through changes in myelin sheath thickness and/or length mediated by intracellular signalling cascades such as P13K/Akt/mTor pathways (Gibson et al., 2014; Snaidero et al., 2014).

The main question resulting from these studies is whether activity-mediated myelination confers a functional advantage to the underlying circuitry. Only two studies assessed the functional output of activity-induced myelination: increases in myelin thickness in response to optogenetic stimulation were associated with subtle adaptations on gait analysis i.e. an increased swing speed of the limb contralateral to the stimulated motor cortex (Gibson et al., 2014), and altered myelin sheath length in

response to monocular sensory deprivation reduced conduction speeds by 22% (Etxeberria et al., 2016). Given the nature of these interventions it is problematic to assign these functional adaptations to changes in myelin alone - stimulation or inhibition of neuronal activity will influence other aspects of the neuronal subunit, including synaptic structure and function, in addition to non-neuronal cell types such as astrocytes and microglia. However, with our current understanding that different parameters of myelin influences action potential CV (Section 1.4.2), it is tempting and logical to hypothesise that activity-mediated myelination will exert a functional effect onto the underlying circuitry. In the following sections, I will strengthen this hypothesis by presenting known roles for myelination in controlling circuit function *in vivo*.

1.8 Evidence for a role of central nervous system myelination in circuit function

1.8.1 Patterns of myelination exist throughout the CNS *in vivo*

Under physiological conditions, morphological parameters of myelination are heterogenous throughout the CNS. For instance, variability in myelin sheath thickness, length and nodal length can be found along individual axons (Arancibia-Cárcamo et al., 2017; Auer et al., 2018; Gao et al., 2019). In addition, specific patterns of myelination have been documented across brain regions and neuronal subtypes. For example, in mice the optic nerve is almost completely myelinated by adulthood, while sparsely myelinated axons persist in the cortex (Hill et al., 2018; Hughes et al., 2018). Nodal length has also been shown to fluctuate across brain regions, with larger variation observed in the cortex than the white matter (Arancibia-Cárcamo et al., 2017). Furthermore, unique and reproducible patterns of myelination have been demonstrated in the visual cortex. In a rigorous effort, Tomassy et al. (2014) reviewed high-throughput serial electron microscopy datasets and performed myelin tracing of pyramidal neurons in this region. In doing so, they identified a highly unusual pattern of myelination in layer II/III descending excitatory pyramidal neurons of the visual cortex, characterised by intermittent myelin sheaths separated by long unmyelinated gaps. A subset of neurons also possessed extremely long, unmyelinated proximal regions prior to the location of the first myelin sheath. Similar patterns of myelination have been observed along parval-

bumin positive inhibitory neurons in rodent and human cortical brain tissue (Micheva et al., 2016; Stedehouder et al., 2017; Zonouzi et al., 2019). These examples support the argument that specific parameters of myelin sheath morphology could provide a functional advantage to the underlying axons and relevant circuitry – otherwise, why would such patterns exist? In this section, I will strengthen this argument by providing *in vivo* examples where distinct patterns of myelination are associated with modifications in action potential timing across circuits of the CNS.

Are patterns of myelination *in vivo* functional or developmental?

The presence of different patterns of myelination along specific neuronal populations in the CNS supports the argument that specific parameters of myelin provide a functional advantage to the underlying neurons and circuitry. On the contrary, it could be argued that the unique myelination patterns observed in the cortex reflect the protracted nature of myelination in this region. Indeed, time course imaging of myelin sheaths in the somatosensory cortex of mice showed that unmyelinated regions get filled slowly over time (Hill et al., 2018). However, the finding that certain patterns appear to be specific to neurons with particular molecular identities would argue against that rationale (Micheva et al., 2016; Stedehouder et al., 2017). An incredible study by Gao et al. (2019) used expansion microscopy combined with lattice light-sheet microscopy to image the cortical column of mice. In a similar manner to Tomassy et al. (2014), they performed neuronal tracing and compared myelination patterns in the somatosensory and visual cortex at nanoscale resolution. In support of a functional, over developmental, adaptation of myelination patterns, the authors found that neurons in layer VI of the visual cortex display intermittent patterns of myelination, whereas neurons in the equivalent layer of the sensory cortex are fully myelinated. Similarly, the finding that certain neuronal subtypes in the spinal cord of zebrafish establish different patterns of myelination in response to neuronal activity points towards a diversity in their function (Koudelka et al., 2016). For example, reticulospinal (RS) neurons which mediate locomotor behaviour myelinate via activity-mediated mechanisms, whereas commissural primary ascending (CoPa) interneurons which relay sensory information across the spinal cord do not myelinate in this way. However, evidence to support the theory that defined patterns of myelination exert a functional effect over circuit function is limited, mainly due to the technical difficulties of imaging myelination and recording

activity across entire neuronal circuits *in vivo*. In the next section, I will review the limited electrophysiological evidence we have that myelination exerts control over circuit function.

1.8.2 A role for myelin in controlling action potential arrival over different timescales

The degree of control that myelin exerts over the timing of action potentials across entire circuits and the circuit mechanisms that this may be most relevant to are not well understood. At the start of this chapter I highlighted the importance of spike timing in forms of synaptic plasticity. Having discussed the multiple parameters of myelin which can influence the speed of action potential propagation, hereby lies a fundamental mechanism by which myelin could contribute to circuit function. However, there is a broader requirement for timing across larger and more complex networks of the CNS, on an order of magnitude above the millisecond precision required for e.g. STDP. For example, synaptic mechanisms such as spatial summation require synchronous action potential arrival from multiple presynaptic neurons to a common target to allow an action potential to be initiated. Take, for example, the three presynaptic neurons in Figure 1.7 which have similar axon calibers and constant conduction velocities, but their length is variable i.e. the axon of neuron A is longer than B, which is longer than C. Assuming that they fire simultaneously, in the unmyelinated condition the conduction delay will vary across axons resulting in non-synchronous activation of excitatory post-synaptic potentials. In contrast, if these axons are myelinated in such a way that speed of CV is increased along the axons of neuron A and B, this could allow for synchronous spike timing arrival, synaptic summation and altering firing properties in the post synaptic neuron. Furthermore, if these arrival timings were further adjusted to allow submillisecond precision, this could exert an effect on STDP. In this section, I will provide evidence for a role of myelination at both levels and conclude with my thoughts on the degree of timing precision that myelin can provide.

Myelin and network function

At a broader network level, myelin has been implicated in isochronicity of the CNS: a feature of certain networks in the brain whereby conduction velocities along axons with

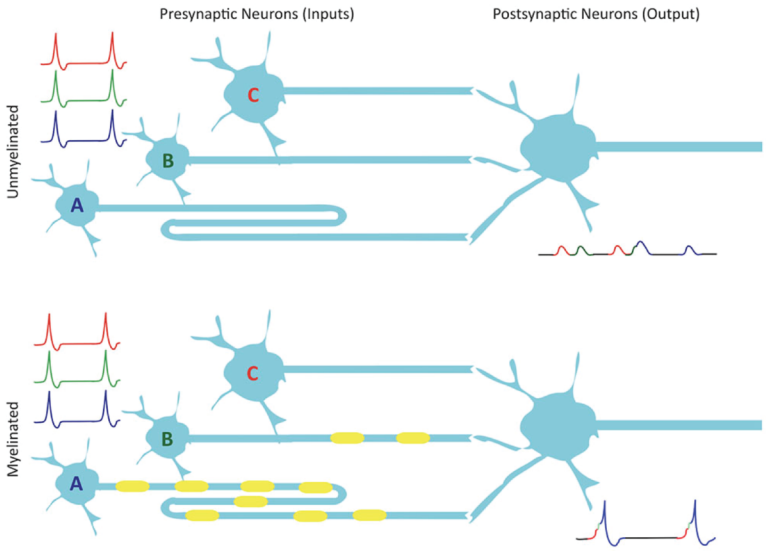

Figure 1.7: Patterns of myelination exert control over action potential timing across circuits
Figure taken from Chorghay et al. (2018). The schematic demonstrates a hypothetical circuit in which three neurons (A-C) with axons of different length input onto a common postsynaptic target. In the top example, axons belonging to all three neurons are unmyelinated. Under this condition, even if the neurons fire simultaneously their action potentials travel at different speeds along their axons resulting in non-synchronous activation of excitatory postsynaptic potentials. In the bottom example, myelination modulates conduction velocities along the axons of A and B such that action potentials arrive in synchrony at their target allow summation in the postynaptic neuron and initiation of action potentials.

different lengths and trajectories are tuned to arrive at their targets in synchrony. For example, thalamocortical neurons exhibit a high degree of variability in their trajectory from the ventral body of the thalamus to their cortical inputs. Despite this, the latency of excitatory postsynaptic currents (EPSCs) following stimulation of the thalamus is similar across all cortical regions. This is in part due to regional myelination which allows a ten-fold increase in CV along axons between the thalamus and the subcortical white matter (Salami et al., 2003). Similar findings have been observed in layer V pyramidal neurons which extend multiple axonal projections to proximal and distant regions of the brain yet exhibit remarkable isochronicity in spike conduction along their ipsilateral projections. Modelling predictions based on anatomically derived data showed that the isochronicity observed could be accounted for by incorporating partial myelination (Chomiak et al., 2008). Another example is found in the olivocerebellar tract. In adult rats, activation of the inferior olive leads to constant latency values across multiple regions of the cerebellum despite broad distances covered by the axons. The onset of isochronicity in the cerebellum correlates with myelination of the olivo-

cerebellar pathway, from postnatal day 14 onwards. In myelin deficient rats, similarities in conduction timing across the cerebellum were never achieved suggesting myelination as the contributing factor to achieving isochronicity. Moreover, the uniform conduction timings in wild type rats was shown to allow a higher degree of synchronous activity across the cerebellum, as detected using electrode arrays (Lang and Rosenbluth, 2003). Although no attempts were made to characterise myelin structure, these studies provide correlative evidence that myelination may coordinate timing of action potential propagation across widespread regions of the brain.

Synchronicity of neural firing is also important for the generation of oscillatory brain rhythms which are fundamental for healthy nervous system function such as attention, arousal, sleep, memory formation and consciousness (Buzsaki, 2006; Uhlhaas, 2009). As such, activity-mediated changes in myelin have been suggested to play a role in regulating oscillatory functions although this area is largely unexplored (Pajevic et al., 2014).

Myelin and circuit function

The avian and mammalian auditory brainstem circuits have served as an excellent model of an *in vivo* circuit that rely on the temporal precision of action potentials at defined synaptic terminals. Computation of interaural time differences, required for sound localisation, relies on integration of information from ipsilateral and contralateral pathways at coincidence detector nuclei: the medial superior olive in mammals, and the nuclear laminis in birds, with submillisecond precision. Despite contralateral fibers travelling over twice the distance to their common target, inputs from both pathways arrive at their target in remarkable synchrony (Ford et al., 2015; Seidl et al., 2010). Furthermore, in mammals a subset of these fibers must first pass through a giant synaptic terminal: the calyx of Held. Combining measurements of axonal and myelin sheath parameters of axons in this pathway with modelling approaches, differences in axon diameter and myelin sheath length have been demonstrated as mechanisms which compensate for the extra distance travelled by these fibers by increasing CV (Ford et al., 2015; Seidl et al., 2010). In addition, Ford et al. (2015) identified a unique pattern of shortening myelin sheath lengths and increasing nodal diameter in a subset of fibers on their approach to the Calyx of Held, which accelerated CV by

33% (from 4.4m/s to 11.3m/s) compared to the axons which bypass this synapse, allowing the rapid and timely depolarisation of their common target. The modelling simulations and *ex vivo* recordings suggest that the difference in action potential timing achieved by these adjustments is in the order of microseconds. Similar findings have been observed in this system *in vivo*. Measurement of auditory brainstem responses (ABRs) in Claudin11 null mice, which fail to assemble tight junctions in CNS myelin, demonstrate delays in conduction and a loss of synchronicity at the level of the lateral superior olive. Meanwhile, in a mouse model of hypermyelination, action potential conduction velocities through the auditory brainstem are increased by fractions of a millisecond (Jeffries et al., 2016). Together, these studies present a role of myelin in the control of action potential timing across *in vivo* circuits, at least in the context of the auditory brainstem.

Conclusion

In conclusion, there is evidence to support a role for myelin in controlling timing across networks and local circuits of neurons. However, the advantage of myelination conferred across the wide-spanning circuits of the cortex is of a magnitude higher than those within the auditory circuit of rodents. Examples from the auditory system provide the only direct evidence so far of a circuitry that gains a functional advantage from specific patterns of myelination. With the modelling simulations employed, it appears that these patterns are able to offer the submillisecond precision required for the computation of interaural time differences. Mechanisms of STDP occur over a similar timescale, therefore patterns of myelination may hold the potential to influence synaptic plasticity, although demonstrating this would be technically challenging. Our current understanding of myelin in circuit function has been limited to circuits which are accessible for non-invasive recordings (such as the auditory brain stem) or *ex vivo* preparations. This is largely due to the technical difficulties of assessing myelin morphology and neuronal activity simultaneously in current models. In order to expand our knowledge of *in vivo* circuits in which patterns of myelination are required for optimal function, and whether established patterns of myelination along axons in a circuit can adapt in response to neuronal activity, a suitable *in vivo* model is required. This forms an aim of this thesis and will be discussed at the end of this discussion.

1.9 Alternative functions for oligodendrocyte lineage cells in the control of circuit function

In addition to a role for myelin in controlling CV and timing across circuits, OL lineage cells possess alternative mechanisms of maintaining neuronal physiology which may also contribute to circuit function following activity-mediated changes in myelin morphology and OL lineage cell number. The potential for these mechanisms should be acknowledged and explored in the event that future investigations do not identify a specific role of activity-mediated myelination in controlling timing across circuits *in vivo*.

1.9.1 Oligodendrocytes provide metabolic support to the neuron

Saltatory conduction demands large amounts of energy in the form of axonal ATP for the active transport of sodium and potassium ions back across the axolemma following repolarisation. In neurons, ATP can be produced as a by-product of aerobic glycolysis, the conversion of glucose to pyruvate and lactate within the cytoplasm. However, this form of ATP production alone is not sufficient for neuronal survival (Fünfschilling et al., 2012) and neurons rely heavily on oxidative phosphorylation in which pyruvate enters the TCA cycle to produce large quantities ATP. In the absence of glucose, lactate acts as a very efficient energy substrate for neuronal metabolism through its conversion into pyruvate by the enzyme lactate dehydrogenase (LDH) (Bélanger et al., 2011). During periods of high activity, internal glucose supplies are often depleted rendering these non-glycolytic pathways preferable.

Neurons express GLUT3 (glucose) and MCT2 (lactate) channels on their surface allowing uptake of metabolites from the extracellular space (Maher and Simpson, 1994; Rinholm et al., 2011). Emerging evidence suggests that in myelinated axons, pyruvate and lactate are shuttled into the neuron directly from glial cells, via glial expressed MCT1 channels. Originally this was considered to be an astrocyte-neuron specific phenomena (Barros and Weber, 2018) but recent, seminal studies have revealed that OLs can also provide support to the axon in this way (Fünfschilling et al., 2012; Lee et al., 2012). MCT1 transporters are highly expressed in OLs, where they are localised to the inner tongue - in direct contact with the adaxonal space (Lee et al., 2012; Saab et al.,

2016). This is a convenient location to permit metabolite transport to the neuron via MCT2 channels. Blocking lactate transport from OLs to axons using cell-type specific knockdown of MCT1 resulted in axonal degeneration highlighting the importance of OL MCT1 expression for axonal support *in vitro*, although this remains to be validated *in vivo* (Lee et al., 2012). Furthermore, there is evidence to suggest that metabolic support from OLs may also be mediated by neuronal activity. Using a combination of *in vitro* and *in vivo* techniques, Saab et al. (2016) demonstrated that NMDA receptor activation can promote GLUT1 surface expression in OLs, providing a conduit for glucose influx and glycolytic metabolism in periods of high neuronal demand. To test the role of this pathway in axonal support, the authors examined *ex-vivo* optic nerve function from OL specific NR1 knockdown mice following periods of metabolic stress. Following oxygen glucose deprivation, nerves from NR1 knockout mice exhibited reduced axonal recovery, as determined by CAP measurements. However, nerve function could be recovered by reperfusion with lactate containing medium, further supporting the notion that OL production of lactate is required for axon integrity.

A role for myelinating cells in the trophic support of neuronal metabolism is unsurprising given that many neurodegenerative diseases are accompanied by a loss of myelin e.g. multiple sclerosis. However, the finding that OLs may provide metabolic support via activity-mediated mechanisms provides an alternative hypothesis for the role of activity-mediated myelination in maintaining axonal integrity and circuit function.

1.9.2 Potassium homeostasis

During repolarisation, potassium accumulates in the periaxonal space via axonal expressed Kv1 channels located underneath the myelin sheath in the juxtaparanode (Wang et al., 1993). During the refractory period which follows, ion balance must be restored across the axolemmal membrane in preparation for the next action potential. This is extremely important to maintain normal excitability and function of neurons (Bellinger et al., 2008; Bostock et al., 1991; Brazhe et al., 2011). This can be achieved via 3Na+/2K+ ATPase pumps located along the axon or via glial uptake through inwardly rectifying potassium (Kir) 4.1 channels. The presence of a glial buffer of extracellular potassium is advantageous in periods of high neuronal activity, as maintaining Na+/K+ ATPase pumps is costly to the axon. Indeed, the importance of

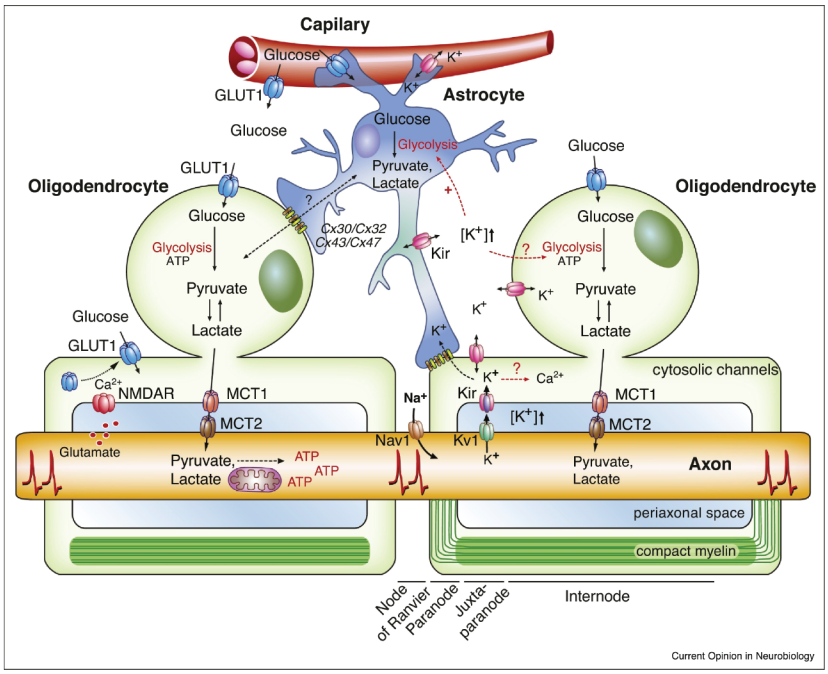

Figure 1.8: Model of activity-regulated metabolic support
Figure taken from Saab and Nave (2017). Oligodendrocytes (green) take up glucose from the extracellular space and perform glycolysis to produce pyruvate and lactate, which are delivered to the axon via MCT1 (OL) and MCT2 (axon) transporters. Glucose and pyruvate can be exchanged between OLs and astrocytes (blue) via gap junctions. Neuronal activity releases glutamate into the periaxonal space activating NMDA receptors on the myelin membrane. In turn, this induces GLUT1 expression in the OL membrane permitting increased glucose uptake and subsequent delivery of metabolites to the axon. OLs and astrocytes also express inwardly rectifying potassium channels which allow for potassium buffering during periods of high neuronal activity. Extracellular elevations in potassium stimulate glycolysis in astrocytes.

Kir4.1 channel expression in glial cells is highlighted by the severe neurological phenotypes that are observed in glial specific or null mutations (Djukic et al., 2007; Neusch et al., 2001). In these models, failures of OL maturation and myelination result in ataxia, seizures and premature death by postnatal day 25. However, it is difficult to distinguish cell type contribution to these phenotypes given that Kir4.1 channels are highly expressed in astrocytes and OLs, as well as microglia and neurons to a lesser degree (Zhang et al., 2014). Using CKO techniques, recent studies have established that OLs play very specific roles in controlling potassium homeostasis and by proxy, the excitability of neurons (Larson et al., 2018; Schirmer et al., 2018).

Subcellular localisation of Kir4.1 channels has been observed in the soma, proximal processes and inner tongue of the myelin sheath in mature OLs (Brasko et al., 2017; Schirmer et al., 2018). Thus, these channels are perfectly placed to facilitate K+ re-

uptake from the adaxonal space following action potential propagation. Indeed, CKO of Kir4.1 from OLs results in reduced potassium clearance in white matter tracts and prolonged depolarisation and recovery of OLs following repetitive stimulation (Larson et al., 2018). Although mice lacking OL Kir4.1 are normal in the early stages of development, they proceed to develop spontaneous seizures and increased seizure susceptibility consistent with altered neuronal excitability. Reminiscent of the study by McKenzie et al. (2014), these mice also fail to achieve similar performance levels to their wild type siblings after multiple days of using a running wheel. Similar functional deficits were present in older mice in which cKO of Kir4.1 was driven in OPCs or mature OLs (Schirmer et al., 2018). These lines exhibited seizures, reduced motor performance using a rotarod and delayed latency of visually evoked potentials (VEPs). In contrast to Larson et al. (2018), loss of OL Kir4.1 was associated with myelin pathology and axonal degeneration, suggesting a potentially important role for OL potassium buffering in the long-term support of axonal health. This finding represents a core discrepancy between the two studies, which could be ascribed to the use of different cre-driver lines i.e. Cnp-cre versus Mog-iCre, or the brain regions examined i.e. the optic nerve versus the spinal cord.

1.9.3 Support of synaptic glutamatergic signalling

An unexpected role for OL lineage cells in control of synaptic function has also been documented, suggesting that axo-glial signalling of neuronal activity is not just a one-way system. Neuronal activity can drive the cleavage of OPC membrane protein NG2 *in vivo*. Loss of NG2 proteoglycan from OPCs resulted in functional deficits at the neuronal synapse in the form of impaired NMDAR-dependent LTP (Sakry et al., 2014). Motor function and tests of learning and memory were normal in these mice, however they displayed consistent sensorimotor gating phenotypes in the form of reduced prepulse inhibition (PPI) and reduced response to olfactory stimuli. Further evidence for a role of mature OLs in glutamatergic signalling is the recent confirmation that OLs express the enzyme glutamine synthase (GS), implying that they may be involved in the uptake and breakdown of extrasynaptic spillover of glutamate into glutamine (Xin et al., 2019). OL specific knockdown of GS resulted in impaired glutamatergic synaptic transmission indicated by reduced evoked EPSCs and increased cocaine-induced locomotor sensitisation. The ability of OL lineage cells to regulate glutamatergic sig-

nalling provides another myelin-independent mechanism of control over circuit activity to consider.

1.9.4 Myelin and synaptogenesis

The processes of myelination and synaptic formation/maturation temporally overlap during development, supporting a close relationship between the two. For example, during the post-natal period, synaptogenesis overlaps with periods of myelinogenesis (Tau and Peterson, 2010). Similarly, in adolescence the process of synaptic pruning and cortical thinning occurs in synchrony with expansion of subcortical white matter (Ziegler et al., 2019). Despite a clear association between these processes, evidence for a causal role of myelination in synaptic formation *in vivo* is sparse.

Myelin proteins such as NogoA, MAG and OMgp have been found to act as inhibitors to axonal regrowth and neurite sprouting, important processes for synaptogenesis, *in vitro* (Fields, 2008). However, these effects were mainly observed in models of axonal injury and regeneration. *In vivo*, myelin proteins have been implicated in defining the critical periods of plasticity within certain circuits. In a model of ocular dominance of the visual cortex, a form of plasticity in which mice up to the age of post-natal day 19 to 32 can switch cortical preference to the visual input from the contralateral eye during monocular deprivation, genetic knockdown of Nogo receptor or its ligand Nogo-A extends the period of plasticity. This suggests that myelination and upregulation of myelin proteins may act to strengthen neuronal circuitry during development by contributing to the closure of critical periods (McGee, 2005).

Direct evidence for a role of myelination in synaptogenesis came from a rodent model of neonatal hypoxia, where hypomyelination was associated with reduced labelling of pre- and postsynaptic markers and glutamatergic puncta (Wang et al., 2018). Electrophysiological recordings demonstrated a lower frequency of miniature EPSCs consistent with reduced excitatory synaptic function. The authors were able to attribute the synaptic changes in this model specifically to the loss of myelination by performing OL specific loss and gain of function studies. Specifically, conditional deletion of Olig2 from OPCs caused hypomyelination and phenocopied the synaptic changes, whereas accelerating myelination by performing cell-type specific deletion of muscarinic receptors in OPCs

rescued synaptic and functional deficits in hypoxic mice. In summary, there is emerging evidence to support a role for OPCs and the production of myelin proteins in controlling synapse formation and circuit strenghtening. Given the effects of neuronal activity on OPC proliferation, it seems pertinent to consider the potential for these cells to exert control at the synapse in isolation from the effects of myelination on circuit function.

Conclusion

Here I have highlighted that the capacity for OL lineage cells to support circuit function is not specific to the control of action potential timing exerted by their myelin sheath. Of course, the role of myelination in facilitating saltatory conduction is well established and the effects of activity-mediated myelination on action potential timing should remain the leading candidate for providing functional adaptations to a given circuit. However, given the influence of neuronal activity on multiple stages of the OL lineage, particularly OPC proliferation, these novel myelin-independent mechanisms of circuit support must be considered as simultaneous or alternative functions of activity-mediated myelination on circuit function and behaviour.

1.10 Myelin, circuit dysfunction and behaviour

Maintaining appropriate timing of action potentials across circuits is fundamental to healthy nervous system function and behaviour. Away from the specific examples presented Section 1.8, the importance of myelin in circuit function *in vivo* can be inferred from the observed consequences of its disruption in a number of neuropathological and psychological human diseases (Fields, 2008). A common cause of myelin disruption in humans is Multiple Sclerosis (MS). MS is an immune-mediated disease of the CNS which causes inflammatory demyelination and secondary axonal pathology. Neuropathological features of MS display considerable heterogeneity: demyelinated lesions can vary in shape, size and number and occupy multiple regions of the CNS, namely the cerebral cortex, cerebellar white matter, brain stem, optic pathways and spinal cord (Love, 2006). This can result in a variety of symptoms involving the sensory, motor and cognitive systems. Using MS as an example, I will approach these systems in turn and present evidence from other human syndromes and animal models to demonstrate that disruptions in myelin cause aberrant circuit function and behaviour.

1.10.1 Disorders of connectivity/cognition

The presence of myelination has been associated with the establishment of isochronicity of conduction timing across brain regions and is suggested to play a role in maintaining oscillatory brain rhythms required for normal cognition, mood and memory (Buzsaki, 2006; Pajevic et al., 2014). In support of this, 40-60% of MS patients display cognitive deficits associated with speed of information processing, memory and attention (Politte and Stern, 2008). Psychiatric symptoms are also highly prevalent, ranging from major depressive disorders to dysphoria, agitation, anxiety, and psychosis. These symptoms are often associated with demyelinating lesions in the temporal and frontal lobes, areas that also display white matter abnormalities in patients with schizophrenia, suggesting a shared circuit-disrupting mechanism (Davis et al., 2003). A loss of myelin is common to both disorders, with disruption in the expression of myelin-related genes – such as Cnp and Mag – and loss of OLs forming a common hallmark of pathology in schizophrenic patients (Barley et al., 2009; Hakak et al., 2001; Mccullumsmith et al., 2007).

Cognitive dysfunction is also present in animal models with disruption to myelin-specific genes. Overexpression of proteolipid protein (Plp), a core myelin protein, causes myelin thinning and subtle changes to paranodal structure (Tanaka et al., 2009). In the absence of any motor dysfunction phenotypes, mice exhibited behaviours consistent with schizophrenia-like symptoms e.g. altered anxiety, reduction in PPI, spatial learning and working memory deficits. PPI acts as a sensory gating mechanism and is a sensitive diagnostic test in humans with schizophrenia, who commonly display deficits in this behaviour (Tkachev et al., 2003). Interestingly, heterozygous shiverer mice, which possess a much milder hypomyelination phenotype than their homozygous counterparts, also exhibit a PPI deficit and develop a catatonic phenotype into old age consistent with progressive network dysfunction (Poggi et al., 2016).

Genetic linkage studies have proven a rich source of evidence for the relationship between myelin gene dysfunction and psychiatric disease (Takahashi et al., 2011). In particular, defects in the genes encoding Neuregulin-1 and one of its receptors, erbB3, have been genetically linked to the risk of developing schizophrenia (Corfas et al., 2004). In addition to myelination, this signalling pathway has been implicated in a number

of aspects of neural development, such as neurotransmission and synaptic plasticity. However, cell type specific ablation of ErbB signalling in OLs has been shown to cause hypomyelination, abnormal anxiety behaviour and deficits in working memory (Makinodan et al., 2012; Roy et al., 2007). Intriguingly, mice expressing a dominant negative form of erbB4, which effectively ablates all erbB signalling, in mature OLs exhibited alters levels of dopamine receptors and transporters in the cortex, nucleus accumbens and striatum of their brains, supporting an emerging relationship between myelin dysfunction and neuromodulatory signalling in psychiatric disorders (Roy et al., 2007; Takahashi et al., 2011). Similar neuromodulatory effects have been observed with an OL specific conditional knockdown of Olig2, which display reduced numbers of mature OLs in the cerebral cortex, elevated glutamate expression and anxiety like behaviours (Chen et al., 2015).

The potential for a myelin-independent role for glial function in schizophrenia has also been described. The major myelin protein Cnp1 is involved in regulating myelin compaction, however its presence is not essential for myelin assembly (Lappe-Siefke et al., 2003; Snaidero et al., 2014). Indeed, loss of Cnp results in the early compaction of the myelin lamellae due to a lack of its antagonistic function against Mbp (Snaidero et al., 2014). Partial loss of Cnp has been associated with catatonia-depressive like symptoms in mice as well as humans with single nucleotide polymorphisms in the gene locus (Hagemeyer et al., 2012; Janova et al., 2017). However, as I will describe later, these phenotypes are associated with axonal degeneration and low-grade inflammation in the absence of overt changes to myelin sheath morphology, suggesting an unknown role for Cnp1 function in OLs.

People suffering from MS are also three to six times more likely to suffer from seizures (Lund et al., 2014; Marrie et al., 2015), another symptom of altered brain connectivity commonly associated with loss of white matter on MRI (Gross, 2011). Given that epileptiform activity is caused by neuronal hyperactivity and hypersynchronisation, aberrant OL function and myelination are well placed to contribute to its initiation. Indeed, seizures are a classic phenotype in rodent models of hypomyelination (Delaney et al., 1995; Emery et al., 2009; Koenning et al., 2012; Lang and Rosenbluth, 2003) and have been recently associated with a reduced OL potassium buffering capacity

(Larson et al., 2018; Schirmer et al., 2018). Post mortem assessment of brain tissue from patients who suffered seizures alongside MS identified a selective loss of cortical layer IV and VI GABAergic interneurons (Nicholas et al., 2016). Similarly, mice models of cuprizone induced chronic demyelination display seizures and specific loss of parvalbumin positive interneurons (Lapato et al., 2017). This is interesting given our knowledge that these neuronal subtypes exhibit unique patterns of myelination under healthy conditions (Micheva et al., 2016; Stedehouder et al., 2017). However, alongside demyelination and interneuron loss, cuprizone administration induces reactive astrocytes which are a key player in regulating epileptogenesis. Despite these confounding features, the specific loss of inhibitory interneurons supports a functional role of the patterns of myelination along these neurons. Finally, white matter integrity has also been shown to deteriorate during the aging of the healthy population, raising the question as to whether myelin loss also contributes to general cognitive decline (Cox et al., 2016).

1.10.2 Sensory and motor dysfunction

The vast distances spanned by motor and sensory neurons render their function particularly susceptible to conduction delays caused by hypomyelination. An early symptom of MS is a loss of visual acuity, which can be assessed using visually evoked potentials to measure the latency of conduction timing between the retina and cortical regions in response to alternating visual stimuli (Regan and Neima, 1984). Similar delays in VEP have been demonstrated in rodent models of hypomyelination and dysmyelination (Bilbool et al., 1983; Dutta et al., 2018; Lehman and Harrison, 2002). MS patients also suffer significant motor impairment manifesting as muscle weakness, ataxia and tremors (Trapp and Nave, 2008). Ataxia and tremors are hallmark phenotypes of CNS hypomyelination in rodent models and are most likely related to hypomyelination of the cerebellum. Homozygous shiverer mice, which almost completely lack CNS myelin, develop generalised tremors from a few weeks of age, followed by ataxia and spontaneous seizures - phenotypes that are replicated across many rodent models of hypomyelination (Delaney et al., 1995; Emery et al., 2009; Koenning et al., 2012; Lang and Rosenbluth, 2003). Deterioration in motor function and coordination are also the inevitable behavioural phenotypes of demyelination in rodent models of MS such as the experimental autoimmune encephalomyelitis (EAE) model (Stromnes and Goverman,

2006; Tripathi et al., 2010). However, these models are complicated by the presence of neuronal damage, which may actually precede demyelination. Despite this, it is clear that a lack of myelin contributes to significant motor and sensory deficits. Interestingly, motor function seems largely resistant to models of mild myelin disruption. Heterozygous parents of the shiverer mice exhibit thinning of the corpus callosum on MRI and subtle reductions in myelin sheath thickness, particularly of small caliber axons, without an overall change to the number of myelinated axons (Poggi et al., 2016). Despite behavioural phenotyping across a battery of tests, minimal motor phenotypes were detected apart from a decreased startle response to auditory stimuli. All tests of motor coordination and strength were completely normal. In fact, mild myelin disruption appears to be more significant to cognitive than motor function, as demonstrated by the findings of a significant PPI and catatonia-like phenotype in this study.

1.10.3 What about too much myelin?

If a role for myelin in the control of action potential timing across circuits is correct, then too much myelin could be equally disruptive to circuit function. The evidence for this is sparse; there are few human diseases where generalised or regional hypermyelination is a feature. Furthermore, of the handful of animal models with hypermyelination that exist, few have examined behaviour. Hypermyelination can be induced by activating the P13k/Akt/mTor pathway, either by overexpression of Akt (Flores et al., 2008) or knockdown of a P13K antagonist Pten (Harrington et al., 2010) in myelinating glia, which results in increased myelin production by individual cells without influencing OL number. Hypermyelination in these mice is CNS specific and manifests as reduced g-ratios and gross enlargement of white matter tracts in the brain and spinal cord. Surprisingly, there is no evidence in the literature to suggest that the behaviour of these mice has been fully assessed. However, it is noted that the hypermyelination eventually results in a progressive neuropathy characterised by myelin abnormalities e.g. splitting of myelin lamellae, axonal degeneration and nodal disorganisation (Harrington et al., 2010) and premature death by approximately fourteen months of age (Flores et al., 2008). It would certainly be interesting to address whether these mice demonstrate any behavioural phenotypes at earlier stages of testing, before neuronal pathology becomes a confounding factor.

Sustained activation of ERK1/2 in OLs appears to drive increased myelin thickness in existing myelin sheaths in the absence of neuronal pathology, providing an excellent model to study the effects of hypermyelination in isolation (Jeffries et al., 2016). Predicted increases in CV were detected in these mice upon measurement of ABRs. Interestingly, hypermyelination did not appear to disrupt motor behaviours and tests of memory, such as novel object recognition. However, mice displayed significantly increased freezing behaviour following conditioned fear testing indicative of increased hippocampal dependent learning. This could imply that certain circuits of the CNS are more sensitive to the effects of hypermyelination than others.

A second study identified that OL specific knockdown of transcriptional factor EB (TFEB) enabled OL survival by suppressing cell-death pathways that would normally maintain appropriate spatio-temporal control of myelination in the brain (Sun et al., 2018). This resulted in elevated numbers of mature OLs and precocious myelination in the white and grey matter; including ectopic myelination of layer I of the cortex and the molecular layer of the cerebellum which are usually devoid of myelin. Specifically, TFEB CKO mice exhibit a 50% increase in the number of myelinated axons in the corpus callosum and thicker myelin sheaths. Surprisingly, this degree of enhanced myelination had no overt physiological consequences for the mice. However, only a limited number of sensory and motor performance assays were performed, in which the only significant finding was a subtle improvement in performance on the first day of testing on the accelerated rotarod.

In summary, extensive behavioural characterisation of models of precocious or hypermyelination is lacking, perhaps due to the absence of a directly translatable clinical syndrome in humans. However, further investigation into the effects of hypermyelination on circuit function would be enlightening, not only to advance our fundamental understanding of myelin function but also in the context of developing safe remyelinating therapies. Remarkably, it seems that the CNS is more tolerant to increases in myelin sheath thickness than it is to decreases, with only subtle effects on behaviour noted in the cited studies. This raises the question as to how much activity-mediated increases in myelination, at least sheath thickness, actually contribute to circuit function and behaviour (Gibson et al., 2014).

Conclusion

The requirement for appropriate levels of myelination for circuit function in the CNS is exemplified by the diversity of symptoms, or behavioural phenotypes, that appear when myelination is disrupted. However, as is the nature of human disease - and many *in vivo* models - changes in myelination do not occur in isolation of other pathophysiological processes. This has made it difficult to tease out the direct contribution of myelin in maintaining normal circuit function in these contexts. However, with the development of cell-type specific genetic manipulations, we are quickly beginning to overcome this problem and strengthen the argument for a fundamental role of myelinating cells in circuit dysfunction.

1.11 Conclusion

To summarise, human and rodent imaging studies have provided concrete evidence that the white matter of the CNS, in addition to the grey matter, demonstrates structural plasticity in response to experience e.g. motor learning. There is extensive literature to support the argument that these structural changes are due, at least in part, to changes in myelin morphology and OL lineage cell number, likely via activity-mediated mechanisms. The obvious question to arise from these findings is whether activity-mediated effects on myelinating cells and myelination plays a causal role in modifying circuit function and permitting the manifestation of novel behaviour in response to specific experiences. Furthermore, uncovering the specific mechanisms of how myelinating cells may exert their control of circuit function *in vivo* is of fundamental importance to advancing our understanding of nervous system plasticity, and brain function in general.

Considerations with *in vivo* models

Assigning behavioural and circuit adaptations to changes in myelination alone are fraught with difficulty in the context of *in vivo* models, due to the presence of multiple other cell types which could also be dynamically regulated by the chosen experimental manipulation. For instance, astrocytes are receptive to neuronal activity and play a crucial role in synapse formation and function as well as providing metabolic support to the axons (Allen, 2014; Stobart and Anderson, 2013). Gap junctions exist between

OLs and astrocytes, providing a conduit for inter cellular signalling and transfer of, e.g. metabolic, function during periods of activity (Nagy et al., 2004). Although changes are observed in myelin morphology in response to activity, there is limited evidence *in vivo* that it is these exact adaptations that are responsible for the functional effect in the underlying circuit. The use of cell-type specific manipulations has helped to circumvent this problem to a degree; however, until this approach is coupled to a full elucidation of the molecular mechanisms mediating adaptive myelination specifically in OLs, the confounding effect of other cell types, as well as myelin-independent mechanisms, must be held to consideration in the interpretation of results.

An example of such an interpretation can be gained from the study by Xiao et al. (2016), in which the differentiation of new OLs was blocked by cell type specific CKO of Myrf gene function. This manipulation is specific to myelinating OLs and removes the ability of adult mice to produce new myelin while exposed to a novel motor learning task. Myrf CKO mice displayed behavioural divergence in their performance, defined as their average speed, to perform complex wheel running as early as 2 hours after introduction to the task. The timing of this deficit is likely too soon to be mediated by a lack of new myelination and, away from a myelin-independent OL role, could indicate an effect mediated by other cell types, for example: the persistence of OPCs, imbalance of OL-astrocytic communication or infiltration of microglia in response to OL apoptosis. Indeed, hypomyelination is often associated with low grade inflammation, either induced by OL apoptosis or the presence of myelin debris (Janova et al., 2017; Poggi et al., 2016). Janova et al. (2017) found that mutation of the myelin protein gene Cnp resulted in a catatonia phenotype which was reversed by depletion of microglia, further exemplifying the importance of considering other cell types in seemingly myelin-specific interventions. Given the extent of communication between glial cells in the healthy nervous system, it seems naïve to imagine that these events can be truly isolated from each other during investigations into activity-mediated myelination. Thus, efforts should be made to document the dynamics and interrogate the influence of other cell types wherever possible.

A specific role for myelination in the manifestation behaviour?

Having discussed the problem of confounding factors *in vivo*, I will select the studies that I believe provide us with the best evidence that changes in myelin/myelinating cells could permit a functional advantage during activity-mediated myelination *in vivo*. Few of the studies presented thus far have performed the integrative analysis of myelin morphology, circuit function and behaviour required to address this directly. The closest evidence in the context of activity-mediated myelination comes from Gibson et al. (2014), who demonstrated subtle increases in myelin thickness and functional adaptations detectable as gait modification in response to optogenetic stimulation of the motor cortex. These particular effects of optogenetic stimulation were inhibited upon treatment with epigenetic modifiers to block OL differentiation. However, neither the intervention nor the rescue is specific to changes in myelinating cells and as such does not confirm that the behavioural advantage was permitted by activity induced changes in myelin thickness. Using cell type specific genetic manipulations, Makinodan et al. (2012) demonstrated that OL specific knockdown of ErbB3 signalling effectively phenocopied the effects of social isolation characterised by hypomyelination of the mPFC and working memory deficits. OL specific upregulation of ERK/MAPK signalling, a pathway that may be recruitable in response to activity, resulted in hypermyelination and increased conduction velocities detectable on ABRs (Jeffries et al., 2016). Furthermore, the finding that seizures can be induced by cell type specific ablation of Kir4.1 channels from OLs, which are known to increase in number in response to neuronal stimulation, reminds us that behaviour can be mediated by these cells in a myelin-independent manner (Larson et al., 2018). These studies provide more definitive substantiation for a causal role of myelin and myelinating cells in behaviour.

With our knowledge of the biophysical effect of myelin sheaths along single axons, it would be reasonable to assume that changes to a myelin sheath will in turn influence CV and timing across circuits, and this should be considered the top candidate for the functional role of adaptive myelination. However, as I discussed previously, there are plenty of other ways in which myelinating cells support axonal physiology, such as potassium buffering, metabolic support and even maintenance of synaptic function. This forms the alternative hypothesis that activity-mediated changes in myelination are homeostatic responses to meet the new demands of the frequently firing neurons,

and not to exert control over timing across the circuit. The truth is that we have little idea which of these hypotheses is true. To answer this, we need a model in which we can document cellular resolution changes in myelination and functional assessment of circuit activity alongside relevant behaviour phenotyping over time. Then, we can begin to focus on testing these hypotheses.

To what degree does myelin contribute to circuit function?

It is clear that a large spectrum of behavioural phenotypes exists across the many animal models of hypomyelination and dysmyelination. Partly this is down to the severity of each myelination phenotype: severely hypomyelinated animals, such as shiverer mice, display serious neurological phenotypes such as seizures and death, whereas models with more subtle myelin phenotypes display milder, often cognitive, phenotypes (Makinodan et al., 2012; Poggi et al., 2016; Tanaka et al., 2009). Thus far in animal models, the documented adaptations in myelin induced by neuronal activity have been very subtle e.g. a change in g-ratio from 0.76 to 0.70, and their associated behavioural output mild e.g. an increase in limb swing speed (Gibson et al., 2014). However, the behavioural adaptations observed in human imaging studies presented in Section 1.2, such as learning to juggle or being a professional musician, are very robust. It appears to me that there may be a mismatch in the level of behavioural adaptation that can be accomplished with experimentally induced activity-mediated myelination and the degree of performance observed in the human studies. Of course, it is not anticipated that activity-mediated myelination is responsible for the entirety of white matter changes observed on DTI, but this observation highlights the likelihood that other mechanisms of white matter plasticity are at play during these behavioural paradigms. For this reason, it would be interesting to quantify the direct contribution of myelin adaptation to circuit function. Given the subtleties of behavioural phenotypes observed with only mild changes to myelin morphology, I would predict that perhaps activity-mediated changes in myelination serve to provide an element of finesse to a given behaviour rather than the ability to perform the behaviour. As a crude example, activity-mediated adaptations in myelination may provide the difference between the ability to maintain a standard juggling sequence and the ability to perform the sequence quickly with an extra ball, rather than providing the ability to juggle or not.

Which adaptations in myelination are required to control circuit function?

The effects of neuronal activity on myelin morphology are variable across the multiple models and manipulations described in this chapter. It is currently unknown which of these are recruited under physiologically driven conditions of activity-mediated myelination, for example during motor learning. To test this would require temporal assessment of myelination along individual axons of a given circuit and correlation with electrophysiological or behavioural readouts. *In vivo* imaging techniques suitable for this aim are established for the cortical regions of mice (Hill et al., 2018), however current limitations in rodent imaging techniques would limit the depth and span of circuits that could be assessed. Larval zebrafish represent an attractive organism for this experimental purpose, given their transparency, size and established repository of transgenic reporters for imaging myelination along single axons (Auer et al., 2018; Koudelka et al., 2016).

The temporal relationship between synaptic plasticity and activity-mediated myelination

Circuit function, and subsequently behaviour, is ultimately determined by synaptic function. Throughout this introduction I have alluded to the close temporal relationship between gross white and grey matter changes during development, as well as the additional roles of myelinating cells in regulating synapse formation and function. To place activity-mediated myelination as a mechanism which precedes and consolidates synaptic plasticity during circuit development and learning, it will be integral to document adaptations in myelination in parallel to synaptic structure and function over time. Unravelling the relationship between myelination and synaptic plasticity further could lead to a paradigm shift in our understanding of the mechanisms underlying learning and behaviour.

Zebrafish as a candidate model organism for investigating the role of myelination on circuit function and behaviour

To address these questions experimentally would not only require (sub)cellular resolution imaging to assess multiple components of the neuronal unit in synchrony: from the synapses to myelin sheaths; monitoring of behavioural performance; measurements

of circuit activity and the ability to manipulate individual properties of myelin sheaths, but they would all need to be achievable *in vivo* and repeatable over time. Establishing a model that meets these requirements would provide the opportunity to yield more direct evidence for a functional role of myelination on circuit function *in vivo*. Once this has been achieved, the model would be recruitable for specific investigations into the *function* of activity-mediated myelination.

We propose zebrafish as a model that meet these criteria. As an extremely well established *in vivo* model for the study of myelination, a plethora of transgenic reporters exist to allow super resolution imaging of the entire axonal unit, from the myelin sheath structure to the release of vesicles at the synapse, allowing non-invasive documentation of these parameters over time (Auer et al., 2018; Koudelka et al., 2016). Indeed, imaging capabilities in larval zebrafish are second to none; their transparency and size allows optical penetration of the entire CNS, allowing access to all aspects of the circuitry underlying specific behaviours. For this reason, zebrafish have become a popular and recognised model for the study of neuronal circuit function, resulting in the generation and validation of a large number of optogenetic constructs and genetically encoded calcium indicators. Finally, multiple zebrafish models and mutants exist in which specific parameters of myelin sheath have been defined: from models of demyelination (Karttunen et al., 2017) and developmental myelin plasticity (Williamson et al. *in preparation* to mutants with increased sheath number (Czopka et al., 2013) and abnormal sheath formation (Klingseisen et al., 2019). Techniques have also been developed to allow laser ablation of single OLs and their myelin sheaths providing a means to disrupt patterns of myelin across chosen circuits (Auer et al., 2018). Together, the qualities of the larval zebrafish render it an almost ideal organism to investigate the effects of myelination on circuit function and behaviour *in vivo*. However, given the potential subtleties of activity-regulated myelination on circuit function, we first need to establish that differences in circuit function and behaviour can be reliably detected in this model organism in response to more robust manipulations of myelination.

1.12 Project aims

The overarching aim of this PhD thesis is to establish larval zebrafish as a model organism for investigations into the role of CNS myelination on circuit function and behaviour. This project will form the first attempt to combine and correlate *in vivo* imaging of myelination, circuit activity and measurements of behaviour in larval zebrafish.

The specific aims of this thesis are to:

- Develop a larval zebrafish model of CNS hypomyelination **(Chapter 3)**
- Identify behaviours that are disrupted by a loss of CNS myelin **(Chapter 4)**
- Identify candidate circuitry for investigations into the functional effects of myelin loss **(Chapter 4)**

Chapter 2

Materials and Methods

2.1 Animals and transgenic tools

Adult zebrafish were maintained in accordance with UK Home Office regulations and kept at adequate numbers to allow provision of embryos for experimental purposes. Adult zebrafish were kept in a dedicated aquatic facility in the Queen's Medical Research Institute (Edinburgh, UK) at 26.5°C degrees under a 14 hour light and 10 hour dark cycle. Ethical approval for all experiments was obtained from the Home Office UK under the Animal Scientific Procedures Act 1986.

2.1.1 Zebrafish lines

Table 2.1 lists the mutant and transgenic zebrafish lines used throughout this project. Myrf$^{+/-}$mutants were crossed into these transgenic lines at the beginning of the project to provide heterozygous mutants carrying the transgenic reporters necessary for experimental aims. The Myrf line was outcrossed to Tupfel long fin (TL) wild type zebrafish line every other generation to maintain a healthy genetic background. Unless otherwise stated, all cellular and behavioural experiments were performed on third generation or younger Myrf mutant lines.

2.1.2 Transgenic tools

Transgenic tools utilised during this project are listed in Table 2.2.

Table 2.1: Mutant and transgenic lines

Line name	Description	Reference
$Myrf^{UE70}$ mutant allele	Model of CNS specific hypomyelination	This study
Tg(mbp:nls-eGFP)	Labels oligodendrocyte and Schwann cell nuclei	Karttunen et al. (2017)
Tg(mbp:EGFP-CAAX)	Labels myelin sheaths	Almeida et al. (2011))
Tg(hb9:gal4)	Motor neuron driver line	Wyart et al. (2009)
Tg(UAS:Gcamp6s)	Reporter line for GCamp6s	Chen et al. (2013)
Tg(nefma:KalTA4)	Driver line for reticulospinal and motor neurons	Unpublished

Table 2.2: Transgenic tools

Trangenic tool	Description	Reference
mbp:mCherry-CAAX	labels membrane of myelinating cells	unpublished

2.1.3 Acquisition of fertilised eggs

Fertilised eggs were obtained by natural spawning through pair matings of adult zebrafish. Embryos were kept at a maximum stocking density of 50 per petri dishes (Corning 10cm petri dishes, Sigma-Aldrich Company Ltd, Gillingham, UK) containing embryo medium (10mm HEPES-buffered E3 embryo medium; 500PM NaCL, 170 KCl PM, 330 PM CaCl2, 330PM MgSO4) or 0.000001% methylene blue conditioned aquarium water in a 28.5°C incubator on a 14hour light 10hr dark cycle. Unless otherwise stated, $Myrf^{+/-}$ adult in-crosses were performed in order to provide Myrf wild type, heterozygous and homozygous mutant embryos at a mendelian frequency for all experiments. Clutches from multiple parents were combined to prevent random clutch effects.

2.1.4 Microinjections

Microinjections of zebrafish embryos were performed following published protocols (Rosen et al., 2009) using an IM 300 Microinjector (Narishige International Limited, London, UK) and a Micromanipulator M3301R (World Precision Instruments Ltd, Hertfordshire, UK). Needles were pulled using a P-97 Flaming/Brown Micropipette Puller (Sutter Instrument, Novato, CA, USA).

2.2 Molecular Biology

2.2.1 Genotyping for Myrf

Adult zebrafish were anaesthetised with tricaine/MS222 (ethyl 3-aminobenzoate methanesulfonate, Sigma-Aldrich Company Ltd) (see Stocks and Buffers for dose). A microsurgical blade (Performance Microsurgical Blades, Katena, Stockport, UK) used to excise a small piece of the tail fin tissue. Fish were recovered in standard fish system water and the tissue placed into a PCR tube containing 50μL of 50mM sodium hydroxide. Tissue from larval zebrafish was obtained either by placing the entire larvae in the same volume of sodium hydroxide following a terminal anaesthetic or via larval fin clips (see next section). Adult fin clips and whole larval tissue samples were denatured at 98°C for 10 to 20 minutes. Following tissue lysis, DNA samples are neutralised by the addition of 1M tris-base hydrochloride (Hydroxymethyl-aminomethane, Sigma-Aldrich Company Ltd, Gillingham, UK) (pH 8) to a final concentration of 0.1M.

Restriction fragment length polymorphism (RFLP) was utilised to develop a genotyping assay specific to the Myrf mutagenesis site allowing confirmation of genotype based on the size of digestion product. Primers were designed to amplify Myrf genomic DNA spanning the mutagenesis site using NCBI Primer Blast. Primers were purchased from Integrated DNA Technologies and kept at stocks of 100mM (Table 2.3). The DNA fragment was amplified using standard protocols with OneTaq (New England Biolabs, Hertfordshire, UK) DNA polymerase. Digestion of the PCR fragment was performed with restriction enzyme PSP GI (New England Biolabs). The PSP GI recognition site is absent on the mutant allele as a result of targeted CRISPR/Cas9 mutagenesis to this site, therefore mutant PCR product remains uncleaved. The wild type PCR product is digested into two fragments of similar size (131bp and 157bp). Heterozygous PCR product consists of all three fragments. Gel electrophoresis is performed to visualise the digested fragments using a 2% gel containing 5% ethidium bromide run at 180V for 30 minutes and imaged using a UV gel doc (Uvitec, Cambridge UK). See Figure 2.1 as an example. N.B. when the gel is run at this speed, the two wild type fragments can appear as one band.

Larval fin clips

If larval tissue was required for downstream uses (e.g. TEM processing, RNA ex-

Table 2.3: Primer sequences

Primer	Sequence
Myrf F Primer	5'- AACTGTGCGTAGGAACACGATA -3'
Myrf R Primer	5'- TGGACCTCCGTGAAACAACTG -3'

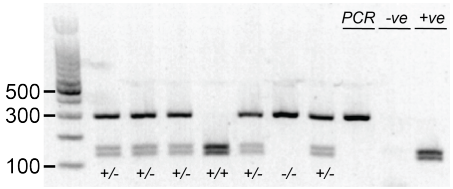

Figure 2.1: Gel image demonstrating PCR fragment sizes for each genotype following PCR amplification and restriction enzyme digestion.
The first seven lanes are labelled with their respective genotypes. Last three lanes are labelled as PCR control (undigested), negative control (no DNA) and positive control (digested, wild type DNA)

traction) then entire larval tissue could not be used for genotyping. In this instance, genotyping was performed on fin clip biopsies collected using an adapted protocol from Wilkinson et al. (2013). This technique involves anaesthetising the larvae in embryo media using tricaine and arraying them on a petri dish lid lined with autoclave tape. Using a dissecting microscope and a surgical microblade, a small piece of the tail fin is removed as far distal to the caudal vasculature as possible and transferred into 10μL of 50mM sodium hydroxide using fine-tipped forceps. Larval fin clip samples are denatured at 98° for 2 minutes. Following tissue lysis, samples are neutralised by the addition of 1M tris-base hydrochloride (pH 8) to a final concentration of 0.1M tris-base hydrochloride in sodium hydroxide.

2.2.2 Morpholino injections

Morpholino antisense oligos (Table 2.4) targeted to the ATG start site of all six known Myrf mRNA transcripts were ordered from Gene tools (Gene Tools, LLC, Philomath, OR, USA). Morpholinos were diluted to a stock concentration of 1mM and stored in the dark at room temperature in a sealed container (as per manufacturers instructions). A working solution of 2ng/nL morpholino was made by diluting in nuclease free water (Qiagen, Manchester, UK). Injections solutions were heated at 65°for 5 minutes to activate and stored at room temperature prior to use. Morpholino was injected into the yolk sac of tg(mbp:eGFP-caax) transgenic embryos at the 1-4 cell stage at concentrations ranging from 2 to 6ng. Standard control morpholino was used as a control at

each concentration (also purchased from Gene Tools). The highest morpholino concentration in which toxicity was not observed (2ng) was utilised for ongoing experiments.

Table 2.4: Morpholino sequences

Morpholino	Transcripts targeted	Sequence
Myrf 1	1,2,3,5,6	5'-CCGTTTCATCAATCACGGTTTCCAT-3'
Myrf 2	4	5'-GACCTGCTCGAAGCCACAGCATT-3'
Standard control	No target in zebrafish	5-CCTCTTACCTCAGTTACAATTTATA-3

2.2.3 RNA extraction protocol

RNA extraction was performed using a modified Trizol RNA extraction protocol. RNA was extracted from pools or 10-40 larvae or 1-2 adult brains per group. Tissue was homogenised in 250μL TriReagent solution (Ambion) and incubated for three minutes at room temperature. 50μL of chloroform (Sigma-Aldrich, Missouri, USA) was added to each sample which was mixed gently by inversion and incubated for a further three minutes at room temperature. Samples were then centrifuged for 15 minutes at 16,000rcf at 4°C. The aqueous layer was removed and placed into a new eppendorf and an equal volume of isopropanol (Sigma-Aldrich) added to the sample. Samples were inverted gently to mix and incubated at room temperature for 10 minutes. Centrifugation for 15 minutes at 16,000rcf at 4°C was performed to collect the RNA pellet. The supernatant was removed and discarded and 150μL ice cold 70% ethanol added to the sample which was subsequently centrifuged for a further 5 minutes at 7000rcf in order to wash the pellet. Ethanol was removed and a short centrifugation step repeated. Residual ethanol was removed and samples airdried for a few minutes prior to resuspension of RNA pellet in 15μL nuclease free water. Total RNA concentration and quality was measured using nanodrop. RNA samples with a 260/280 ratio more than 1.8 and a 260/230 ratio more than 1.8 were deemed acceptable. If the 260/280 ratio was less than 1.8 an RNA clean-up protocol was performed. Samples were stored immediately at -80°C.

Brain dissection for RNA extraction

Adult zebrafish were terminally anaesthetised using tricaine and a scalpel blade was

used to severe the spinal cord via decapitation. The sample was stabilised using insect pins and blunt forceps were used to pierce and remove the skull. Optic nerves were transected prior to removing the brain in its entirety. The brain was placed into an RNAse free 1.5ml eppendorf and stored on ice. RNA extraction was performed immediately after dissection before RNA degradation occured.

RNA cleanup

Total RNA cleanup was performed by adding 1/10th volume 5M ammonium acetate to each sample alongside 2 volumes of ice cold 100% ethanol. Samples were mixed gently by pipetting and stored at -20°C for 20 minutes. Samples were spun for 15 minutes at 16,000rcf and the supernatant removed. A brief centrifugation step was repeated and any remaining ethanol was removed. Samples were air dried for a few minutes prior to resuspension in 10μL nuclease free water.

2.2.4 cDNA synthesis

cDNA synthesis was performed using Accuscript Hi Fidelity First Strand Synthesis kit and oligo d(T) primers or random primers (Agilent Technologoies, Santa Clara, CA, USA) (protocol page 4-5). The amount of RNA entered into the reaction was normalised between samples (500-1000ng per sample for qRT-PCR).

2.2.5 Assessment for alternative splice sites

cDNA was synthesised from wild type, heterozygous and homozygous mutant total RNA. Primers were designed to amplify the entire Myrf coding sequence (Table 2.5). PCR amplification was performed using Phusion Hi-Fidelity DNA polymerase (New England Biolabs, Hertfordshire, UK). The size of the product was checked by gel electrophoresis (approximately 3000bp). The band was excised from the gel and DNA extracted using Monarch DNA gel extraction kit (New England Biolabs, Hertfordshire, UK). The Zero Blunt TOPO PCR Cloning Kit (Invitrogen, CA, USA) was used to insert the fragment of DNA into the pCRII-Blunt-TOPO vector. Plasmid was transformed into One Shot Top 10 Competent Cells (page 16 TOPO TA Cloning Kit protocol, Invitrogen, CA, USA). Following transformation, cells were cultured on kanamycin selective agar plates overnight. Three individual colonies per genotype were picked and grown in 4ml LB media containing kanamycin antibiotic (concentration 1:1000) overnight.

Plasmids were extracted the following day using PEQlab miniprep cleanup (VWR life-science, Leuven, Belgium) and sent for sequencing using commercially available M13 forward and reverse primers which recognise plasmid DNA surrounding the cloned Myrf coding sequence.

Table 2.5: Primer sequences for amplification of entire Myrf coding sequence. Lower case letters represent the coding sequence.

Gene name	Primer sequences
Myrf	F 5'-GGAGCCGCTAGAatggaaaccgtg-3' R 5'-CGTGATGCTCTttagcatgtgctg3'

2.2.6 RT-PCR

Semi-quantiative RT-PCR

For semi-quantitative assessment of Myrf transcript at different stages of development, cDNA samples were entered into routine PCR reactions using OneTaq polymerase (New England Biolab) and transcript specific primers (Table 2.6). EF1-alpha was used as a loading control.

Table 2.6: Semi-quantiative RT-PCR primer sequences

Gene name	Primer sequence
Myrf	F 5'-AATCGTTCTGGGGAACTCGG-3' R 5'-GATCGTTAGCTTGCTGGGGT3'
EF1-alpha	F 5'-TGGTACTTCTCAGGCTGACT-3' R 5'-TGACTCCAACGATCAGCTGT-3

Quantiative RT-PCR

Primers were designed using NCBI Primer-blast or Primer 3 (http://bioinfo.ut.ee/primer3-0.4.0/) to amplify 80-150bp regions of the genes of interest (Table 2.7). Primers were tested for specificity using wild type cDNA and routine PCR using standard protocol for oneTaq DNA polymerase (New England Biolabs). Standard curves were calculated for each primer using a 1:2 or 1:5 wild type cDNA dilution series and SYBR Green qPCR (Brilliant III Ultra-Fast SYBR Green QPCR Master mix, Agilent Technologies, California, USA) run on a Roche LightCycler 96 (Roche, Indiana, USA). Each sample was run in triplicate. Melting curve, amplification curve and linear efficiency was

assessed for each primer pair using Light Cycler 96 software (Roche, Indiana, USA). Primers with a single product amplification and efficiency values of more than 90%, QT error less than 0.5 and negative no template controls were chosen for downstream qRT-PCR experiments. qRT-PCR experiments were run in triplicate for each sample with a minimum of three samples per condition. House keeping gene ef1a was chosen as a reference gene (McCurley and Callard, 2008). The delta-delta CT method was used to perform relative quantification of the gene of interest, with the average CT of wild type samples used as a calibrator. Values were normalised to wild type values in order to provide the relative expression of the gene of interest.

Table 2.7: qRT-PCR primer sequences

Gene name	Primer sequence
Myrf	F 5'-AGCGAGACCACCGCTAATAA-3' R 5'-CTGACGATGATCCTCTCGGA-3'
Myrf-like	F 5'-GCGAAACCACTGCCAATAAC-3' R 5' CAGACCCACCACCATCATAA-3'
Myelin basic protein	F 5'-ACAGAGACCCCACCACTCTT-3' R 5'-TCCCAGGCCCAATAGTTCTC-3'
ef1-alpha	F 5'-TGGTACTTCTCAGGCTGACT-3' R 5'-TGACTCCAACGATCAGCTGT-3'

2.2.7 Plasmid preparation

Remnant or stored glycerol plasmid stocks were entered into a TOPO cloning reaction (Page 12, TOPO TA Cloning Kit protocol, Invitrogen) and subsequently transformed into One Shot TOP10 Chemically Competent E. coli (Page 16, TOPO TA Cloning Kit protocol, Invitrogen). Following transformation, bacteria were cultured overnight on agarose plates containing kanamycin. Isolated bacterial colonies were picked and propagated in 4ml LB broth (LB-AGAR Medium (capsules), MP Biomedicals, LLC, UK) containing kanamycin antibiotic (1:1000) on a shaker at 37°C overnight. Plasmid DNA was extracted the following day using the PEQlab miniprep protocol (VWR lifescience, Leuven, Belgium). The concentration of plasmid was determined using a nanodrop spectrophotometer (NanoDrop one, ThermoScientific, MA, USA).

2.2.8 Myrf-like Crispant strategy

With CRISPr/Cas9 mutagenesis, guide RNAs are used to transport Cas9 nuclease to the targeted genomic region for mutagenesis. Commercially available Cas9 can only edit at a PAM (NGG) site. Therefore, guide RNAs were designed such that the 20bp sequence ended in a PAM site and spanned a commercially available restriction enzyme recognition site within a coding exon of the Myrf-Like gene (Table 2.8). Subsequently, PCR amplification of a fragment surrounding the target site, followed by digestion with the specific restriction enzyme can confirm the mutagenesis efficiency of the guide. Random insertions and deletions at the target site will only result in a bi-allelic frame shift in 33% of cells. Thus, injecting two guides is suggested to increase the likelihood of biallellic frame shift in the coding sequence and subsequent loss of function. Guides were designed against four different exons and ordered as synthetic CRISPR RNA (crRNA) from Sigma-Aldrich Company Ltd. (Gillingham, UK). crRNAs and tracer RNA (also Sigma-Aldrich) were co-injected in combination with Cas9 protein (20μM, NEB) into the yolk sac of wild type fertilised embryos at the single cell stage. Injection solutions contained 1μl each crRNA, 1μl tracer (250ng/μL), 1μl Cas9 protein, 1μl RNAse free water and 1μl fluorescent dextran. At 2dpf, larvae were screened for toxic effects and DNA was extracted from a subset of larvae to test the efficiency of each guide. Primers were designed to span 150-300bp region of genomic DNA around each individual mutagenesis site. PCR amplification was performed using BioMix 2x reaction mix containing Taq DNA polymerase (Bioline, Meridian Life Science Inc., Tennessee, USA) following standard protocol. Restriction enzyme digestion was then performed and the efficiency of mutagenesis assessed using gel electrophoresis (Figure 2.2). The two guides which demonstrated the highest (>90%) efficiency were chosen for subsequent experiments. Efficiency was quantified using the gel analyser tool in ImageJ to measure the area of the peaks produced by the cut and uncut fragments.

Table 2.8: Myrf-like guide sequences

Exon targetted	crRNA sequence
Exon 6	5' GCAGTCCACAGACCCAGTA*TGGG-3'
Exon 8	5' GGTGACGGTTCACATAGGCATGG-3'

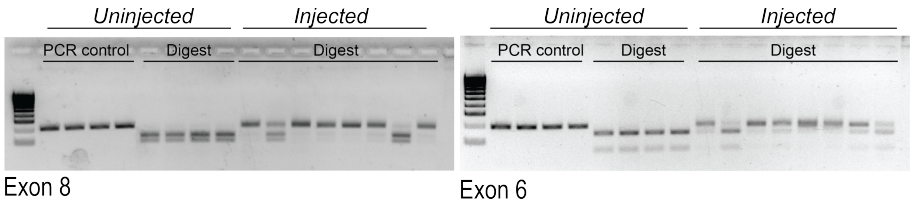

Figure 2.2: Testing the efficiency of Myrf-Like guide RNAs
The first four lanes of each image contain the undigested PCR control (uninjected embryos). The next four lanes are digested controls (uninjected embryos). The final eight lanes contain the digestion product of injected embryos. Note how many of the lanes retain undigested product of an equivalent size to PCR control. This suggests efficient mutagenesis at the restriction enzyome recognition site and subsequent failure of digestion.

2.3 Transmission electron microscopy (TEM)

2.3.1 Perfusion fixation of adult zebrafish

Adult zebrafish were terminally anaesthetised in tricaine and slowly perfused via the heart with PBS (to exclude all blood from the vasculature), followed by cooled primary fixative solution (4% paraformaldehyde (EM grade, 16%, Ted Pella Inc., Redding, USA), 2.5% glutaraldehyde (EM grade, 25%, also Ted Pella Inc.) in 0.1M Sodium Cacodylate (Agar Scientific, Stansted, UK)). The sample is appropriately fixed when the tissue becomes stiff and pale. Samples were incubated in fresh fixative solution for 24 hours at 4°C. The following day, the brain and spinal cord were extracted and placed into eppendorfs containing fresh primary fixative solution and processed for electron microscopy following the microwave fixation protocol for larval zebrafish (see below).

2.3.2 Microwave-assisted larval zebrafish tissue processing for TEM

Larval zebrafish were terminally anaesthetised. Their heads and tails were removed and transferred into 50μL sodium hydroxide solution for DNA extraction and genotyping. The larval bodies were transferred into individual 0.5μL PCR strip tubes containing 200μL primary fixative:4% PFA (EM grade, 16%), 2.5% glutaraldehyde (EM grade, 25%, both Ted Pella Inc., Redding, USA) in 0.1M Sodium Cacodylate (Agar Scientific, Stansted, UK) and processed for EM following the detailed protocol provided by Czopka and Lyons (2011).

2.3.3 Microtome sectioning

Resin blocks containing larvae embedded in polymerized EPON were trimmed such that the body of the larva was within the centre of a small trapezoid shape and trimmed close to the level of somite 15 (identified by the cloaca). Samples were sectioned using a microtome (Reichert Jung Ultracut Microtome, Leica, Wetzlar, Germany) and histo jumbo knife (Diatome, Philadelphia, USA). Transverse sections were cut at 80nm thickness and ribbons collected in the knife boat filled with distilled water. Sections were smoothed using chloroform vapour, picked up using a perfect loop (Perfect Loop, Leica EM accessory eM UC7, Leica, Wetzlar, Germany) and transferred onto electron microscopy grids (300 hexagonal grid holes, TAAB, Berkshire, UK), which were placed on Whatman chromatography paper to dry (Thermo Fisher Scientific, Waltham, USA).

2.3.4 Section staining

Grids underwent two staining protocols prior to imaging. Firstly, equal amounts of saturated uranyl acetate and absolute EM grade ethanol were mixed. One 50-100ul drop per grid was placed onto a square of fresh parafilm inside a plastic petri dish. Grids were placed face down onto a drop. The petri dish was covered with foil and grids were left to stain for five minutes then gently washed with 50% ethanol. Grids were dried on Whatman paper prior to the next staining process. The procedure was repeated using Sato's lead stain. Sodium hydroxide pellets were placed around the perimeter of the petri dish during this stain to reduce levels of carbon dioxide and avoid precipitation of the lead stain. For this reason, it is imperative to avoid breathing onto the samples during the staining process. Samples are incubated for 5 minutes then washed using distilled water. Grids were dried on Whatman paper and stored in a grid case (TAAB) at room temperature.

2.3.5 TEM image acquisition and processing

Transmission electron microscopy (TEM) images were obtained using a JEOL JEM-1400 Plus Electron Microscope located at the University of Edinburgh Electron Microscopy facility in the Daniel Rutherford building located at King's Buildings. Overviews of the entire spinal or hemispinal cord were obtained at 3.4-7.1Kx magnification. Myelinated regions were imaged at a minimum of 11.2Kx magnification. Images were obtained in .dm3 format and subsequently converted into 8 bit TIFF format using the

batch-convert tool in Image J (National Institute of Health, Bethesda, MD, USA). Images were tiled using Adobe Photoshop 2019 (Creative cloud) automated photomerge tool (using reposition setting) and analysed using Fiji/ImageJ. Images of the peripheral lateral line were also obtained using 7.1Kx-11.2Kx magnification.

2.3.6 TEM image analysis

The number of myelinated axons was counted in one hemispinal cord per animal (labelled in Figure 2.3A) using the cell counter tool in ImageJ (NIH). Axons were considered myelinated if more than one dark staining membrane (i.e. myelin) was observed surrounding the axon. Subsequent analysis compared the number of myelinated axons in the dorsal and ventral region of the spinal cord (also labelled in 2.3A). Axon perimeter and area were measured for the 30 largest axons present in the hemispinal cord (magenta dashed line, 2.3B) and all myelinated axons. The external perimeter and area of myelinated axons (axon + myelin sheath) was measured for all myelinated axons (green solid line, 2.3B). Diameter was extrapolated from perimeter measurements using the calculation:

$$c = 2\pi r$$

g-ratios are typically determined using the following equation:

$$g - ratio = \frac{diameter\ of\ axon}{diameter\ of\ myelinated\ axon}$$

However, this equation assumes circularity of axons which is often not true in larval zebrafish TEM preparations. Thus, g-ratio was calculated using *area* in place of *diameter*. G-ratios were only calculated for axons which displayed clearly demarcated myelin sheath outlines. Axons which appeared to be cut longitinudinally, as determined by the appearance of the neurofilament staining inside the axon, were also excluded so as not to distort g-ratio values.

2.4 Confocal Microscopy

2.4.1 Mounting fish for imaging

To prepare larvae for imaging they are anaesthetized in embryo medium with 1x tricaine (3-amino benzoic acid ethyl ester, Sigma) and embedded in small droplets of 1.3-

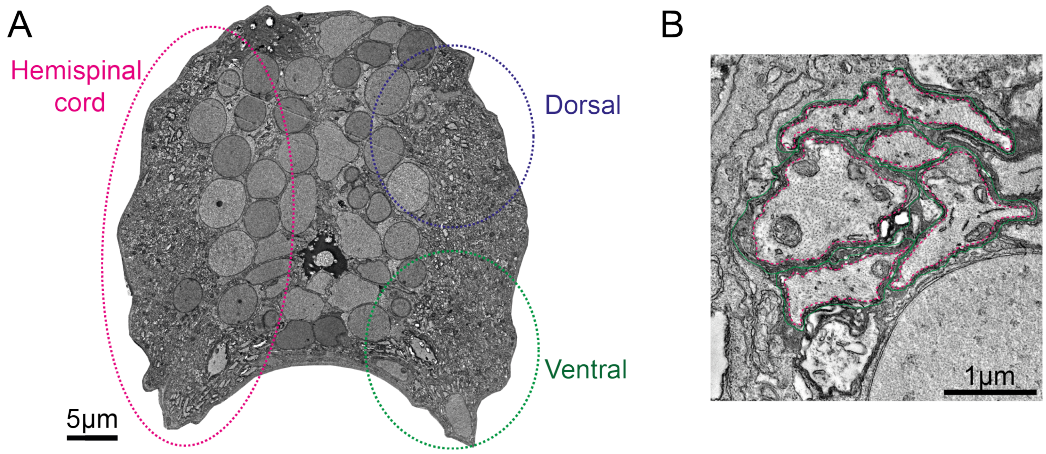

Figure 2.3: Analysis of TEM images
(A.) Overview of an entire spinal cord with the regions used for analysis marked as hemispinal cord (pink), dorsal (blue) and ventral (green). **(B.)** Examples of myelinated axons where the axon (magenta dashed line) and myelinated diameter (green solid line) have been traced. These areas within these perimeters are used for subsequent g-ratio calculation.

1.5% low melting point agarose (Ultrapur LMP Agarose, Invitrogen, Carlbad, USA) on a glass coverslip (Menzel-Glaeser, 22x22mm, no. 1 thickness (0.13-0.16mm), Braunschweig, Germany). Forceps are used to place the larvae in a lateral position and carefully press along the length of their body to keep them as flat to the coverslip as possible. Once the agarose had polymerised, silicon grease (Dow Corning high-vacuum silicone grease, Sigma-Aldrich Company Ltd, Gillingham, UK) was placed around the perimeter of a standard microscope slide (Super Premium Microscope slides, VWR International, Leuven, Belgium) and filled with a small amount of embryo medium containing tricaine. The coverslip is then inverted and pressed lightly towards the slide to create a seal with the paraffin wax and bring the agarose into contact with the embryo medium allowing maintenance of anaesthesia throughout the imaging period. Following image acquisition, larvae are removed from the agarose using microsurgical blades (Performance Microsurgical Blades, Katena, Stockport, UK) and transferred into fresh embryo medium to recover from anaesthetic or culled using a Home Office approved Schedule 1 method.

2.4.2 Image acquisition and processing

Confocal images were acquired with the Zen software on a Zeiss LSM 880 confocal microscope (Carl Zeiss Microscopy GmbH, Jena, Germany) using a 20x objective (Zeiss Plan-Apochromat 20x dry, NA=0.8, Carl Zeiss Microscopy). With the exception of sin-

gle cell imaging, the visual field was always centred over the urogenital opening (roughly somite 15) and a z-stack obtained of the entire spinal cord. Bright field overview images were obtained using a Zeiss Axio Imager 2 combined with an Apotome.2 system and processed using Zen 2.2 software (Carl Zeiss Microscopy). Unless otherwise stated, all images presented in this thesis represent a lateral view of the zebrafish spinal cord, with anterior to the left and posterior to the right with dorsal on top and ventral on bottom. Within experiments, images were obtained using similar laser intensity and optical gain settings. Images were processed using ImageJ (National Institute of Health, Bethesda, MD, USA) and maximal intensity projections created using the Z-project function for figure images. Figure panels for this thesis were formed using Adobe Illustrator CC2019 and Adobe Photoshop CC2019 (Adobe, San Jose, CA, USA)

2.4.3 Single cell imaging and analysis

Oligodendrocytes were mosaically labelled by injecting DNA plasmid encoding tg(mbp: mCherry-CAAX) into embryos at the single cell stage. Plasmid was injected into the yolk sac or single cell at concentrations between 2.5-10ngμL alongside 25ng/μL transposase mRNA, nuclease free water and phenol red (1 in 10 dilution) using a Pneumatic PicoPump PV830 (World Precision Instruments Ltd, Hertfordshire, UK) and a Micromanipulator M3301R (World Precision Instruments Ltd, Hertfordshire, UK). Immediately prior to imaging, larvae were mounted and screened on a Zeiss AxioImager A1 microscope (Carl Zeiss Microscopy) for fluorescent expression in isolated cells. The tg(mbp:mCherry-CAAX) construct drives expression of the fluorescent protein mCherry in the membrane of myelinating oligodendrocytes allowing visualisation of individual myelin sheaths. Only cells from the dorsal spinal cord were selected for imaging in order to minimise variability. Larvae were imaged at either 4 or 6dpf on a Zeiss LSM 880 confocal microscope (Carl Zeiss Microscopy) using a 20x objective (Zeiss C-Apochromat 20x dry, NA = 0.8, Carl Zeiss Ltd) using the RFP channel (561nm laser). Confocal z-stacks were obtained of the entire cell and its myelin sheaths. Raw stacks were then airyscan processed. Images were opened in ImageJ (NIH) and myelin sheath length was measured using the freehand measure tool. Cells were excluded from analysis if it was not deemed possible to obtain accurate measurements for each myelin sheath. Abnormal sheaths were defined as sheaths with abnormal elongation,

incomplete wrapping or membrane blebbing. Abnormal sheaths were only counted for a single cell if all sheaths were measurable, providing an accurate proportion of abnormal myelin sheaths per cell.

2.4.4 Time course imaging

Using the procedure above, the same single cell was imaged at 4 and 6dpf with recovery of the larvae in between imaging sessions. The length of individual sheaths was compared at 4 and 6dpf, with the change in growth being calculated as the length at 6dpf minus the length at 4dpf. Net growth was calculated by taking the average change in length across all sheaths per cell. Where possible, all sheaths per cell were analysed. In instances where measurement of all myelin sheaths was no longer possible (due to overcrowding of sheaths), only isolated myelin sheaths were measured. Sheath retractions were defined as myelin sheaths which were present at 4dpf but absent by 6dpf. Retracted sheaths were excluded from sheath growth analysis. Cells used in time course analysis were also included in the individual 4 and 6dpf datasets.

2.4.5 Vertebrate Automated Screening Technology

Larval zebrafish were arrayed into individual wells of a 96 well plate in embryo media and anaesthetised with tricaine. Larvae were automatically dispensed into the corresponding well of a receiving 96 well plate using an automated dispenser (Union Biometrica, Holliston, MA, USA), allowing genotyping following imaging. Fish were loaded and oriented for imaging using a Large Particle (LP) Sampler and VAST BioImager system fitted with a 600μm capillary (both Union Biometrica, Holliston, MA, USA). The imaging system consisted of an AxioCam 506m CCD Camera (Carl Zeiss Ltd), a CSU-X1 spinning confocal scanner (Yokogawa, Tokyo, Japan), a 527/54+645/60nm double bandpass emission filter, 1.6x C-Mount adapter (Carl Zeiss Ltd), a PIFOC P-725.4CD piezo objective scanner (Physik Instrumente, Karlsruhe, Germany), C-Plan-Apochromat 10x 0.5NA objective (Carl Zeiss Ltd, Cambridge, UK) and an Axio Examiner D1 (Carl Zeiss Ltd). Established by Dr. Jason Early, this system allows fully automated image acquisition of the spinal cord and peripheral lateral line with semi-automated analysis of myelinating glia number (Early et al., 2018). Z-stacks covering the depth of the capillary (600μm) were acquired using a 4μm z-interval, 3 x 3 binning and 60ms exposure. Images were processed using Zen software and cus-

tom written macros. Semi-automated cell counts of the dorsal and ventral spinal cord were subsequently performed using custom written macros. All code is available in the supplementary materials of Early et al. (2018).

Analysis of developmental morphometrics

Bright field images (Figure 2.4) were obtained of larvae as they passed through the capillary tube of the VAST BioImager system. Images were batch processed in ImageJ (NIH) and measurements made of the ocular diameter, swim bladder height and body length of the each larval zebrafish using the measure tool.

Figure 2.4: Measurement of developmental features in larval zebrafish
Ocular diameter (magenta line), swim bladder height (green line) and body length (blue line) were measured for Myrf larvae at 6dpf.

2.4.6 Additional Image analysis

Fluorescent intensity measurements

In the transgenic line 'tg(mbp:eGFP-caax)', GFP is targeted to the membrane of myelinating oligodendrocytes. When constitutively expressed, this reporter gives an excellent representation of the gross level of myelination in the CNS and PNS. In order to quantify reductions in myelination in the spinal cord in response to different interventions i.e. during morpholino and crispant experiments, an Image-J macro written by Dr. Jason Early was used to calculate the average intensity of myelinated areas. In short, this script takes z-stack images of the spinal cord or posterior lateral line (PNS), forms a maximal intensity projection and performs autothresholding (Huang method (Huang and Wang, Mao-Jiun J, 1995)) to delineate regions of fluorescent intensity. A mask is built around these areas which are subsequently designated as ROIS. The area and fluorescent intensity within each ROI is calculated and totalled across the whole image providing quantification of the overall area of GFP expression and the total fluorescent intensity. Average fluorescent intensity (total fluorescent intensity / area) values were used for comparison between groups.

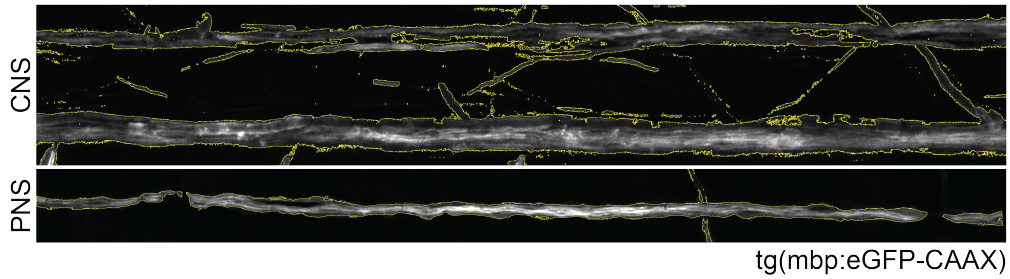

Figure 2.5: Quantifying fluorescence intensity of tg(mbp:eGFP-CAAX) expression in the spinal cord. Representative image of the regions of interest detected using the custom written ImageJ macro. Good delineation of the ventral and dorsal spinal cord (top panel), and posterior lateral line (bottom panel), is obtained using this method.

Manual oligodendrocytes counts

Z-stack images of the spinal cord from Myrf tg(mbp:nls-eGFP) fish, in which the nuclei of myelinating oligodendroglia are labelled with green fluorescent protein, were opened in ImageJ (NIH). The cell counter tool was used to manually count oligodendrocyte cell bodies throughout the entire z-stack.

2.5 Statistics

Data was assessed for Gaussian distribution using a D'agostino Pearson omnibus normality test (Prism 7). If all data groups were normally distributed then a parametric test was performed. If data consisted of two groups then a t-test was performed, if analysis was to be performed on more than two groups then a one-way ANOVA was chosen. If data was not normally distributed then an appropriate non-parametric test was performed such as a Mann-Whitney or Kruskal-Wallis test according to the number of groups to be analysed. If the number of values in any group was too small to assess for normality it was assumed that the data was not normally distributed. All data were averaged per biological replicate (larva), so in every case N represents the number of larvae.

2.6 Buffers and stocks

General buffers and stocks

25x Tricaine stock (100ml solution)

Larvae and adults are anaesthetised by adding tricaine to conditioned fish water or embryo media to a final concentration of 0.16mg/ml, i.e. 4.2ml tricaine (25x) per 100ml embryo medium.

MS222	0.4g
distilled H2O	98ml
Tris buffer (1M, pH 9)	2ml

10mM HEPES buffered E3 embryo medium (2L)

distilled H2O (15MW)	1920ml
50x HEPES	40ml
50x E3 medium	40ml
Adjust to pH 7.2 with 5M NaOH	

50x HEPES buffer stock (500mM)

HEPES crystals	95.58g
distilled H2O (18MW)	500ml

50x E3 stock solution (1L)

NaCl (250mM)	14.61g
KCl (8.5mM)	0.63g
CaCl2 (16.5mM)	1.83g
MgSO4 (16.5mM)	4.07g
Make up to 1L with distilled H2O (18MW)	

HEPES crystals (N-(2-Hydroxyethyl)piperazine-N'-2-ethanesulfonic Acid) are sourced from Thermo Fisher Scientific, Waltham, MA, USA. All other chemicals were sourced from Sigma-Aldrich Company Ltd, Gillingham, UK.

Solutions required for TEM microwave fixation and processing

All chemicals were sourced from Sigma-Aldrich Company Ltd, Gillingham, UK.

Primary fixative (10ml)

Paraformaldehyde (EM grade, 16%)	2.5ml
Glutaraldehyde (EM grade, 25%)	0.8ml
Sodium cacodylate buffer (0.1M)	6.7ml

Secondary fixative (10ml)

Osmium textroxide (4%)	5ml
Sodium cacodylate buffer (0.1M)	2.5ml
Imidazole buffer (0.1M)	2.5ml

Imidazole 0.1M (50ml)

Imidazole	350mg
distilled H2O	50ml

Sodium cacodylate buffer (1M, 40ml)

Sodium cacodylate	8.56g
Distilled H2O	40ml

Uranyl acetate saturated solution (8%))

Uranyl acetate	8g
Distilled H2O	100ml

EMBED with benzyldimethylamine (BDMA)

EMBED	100ml
Dodecenyl succinic anhydride (DDSA)	45ml
Methyl-5-norbonene-2,3-dicarboxylic anhydride (NMA)	60ml
Benzyldimethylamine (BDMA)	6.15ml

Sato's lead stain

Lead citrate	0.2g
Lead nitrate	0.15g
Lead acetate	0.15g
Sodium citrate	1g
NaOH (5M)	1.8ml
Boiled and coiled distilled H2O	48.2ml

Chapter 3

Establishing a larval zebrafish model of CNS specific hypomyelination

3.1 Introduction

In my general introduction I laid out the evidence supporting activity-mediated myelination as a novel form of plasticity in the central nervous system. Findings from several systems and levels of investigation have been pieced together to form a complex picture of how adaptations in myelin may influence circuit function and subsequent behaviour. However, the difficulties in bridging these levels of analyses – from studies of cellular morphology to whole organism behaviour – in the same model organism *in vivo* have hindered our ability to demonstrate that these mechanisms are functionally relevant. The aim of this chapter is to develop a larval zebrafish model to address this problem.

Zebrafish as a model to study CNS myelination and behaviour

Larval zebrafish are a popular and long-established model organism for the study of myelination (D'Rozario et al., 2017). Their transparency at early stages of development, when myelination is robust, confers them advantages over other model organisms: predominantly their suitability for longitudinal *in vivo* imaging. Combining this feature with their amenability to genetic manipulation e.g. Tol2 transgenesis (Kwan et al., 2007), a plethora of transgenic tools have been developed that allow us to monitor the dynamics of myelination at remarkable cellular resolution *in vivo* (Almeida et al., 2011;

Baraban et al., 2018; Czopka et al., 2013; Koudelka et al., 2016; Mensch et al., 2015). For example, driving expression of fluorescent protein under the promotion of glial-specific genes such as myelin basic protein (Mbp) allows detailed visualisation of the morphology of myelin sheaths belonging to individual oligodendrocytes (OLs) (Almeida et al., 2011). From the perspective of individual axons, patterns of myelination can be accurately inferred by driving fluorescent protein expression alongside axolemmal proteins which are extruded from the membrane upon myelination (Koudelka et al., 2016). Combining these tools with the small size of larvae (∼3.5mm long) it is possible to image patterns of myelin sheath morphology along the length of individual axons, and potentially across circuits, over time (Auer et al., 2018; Koudelka et al., 2016). A feat that is not yet achievable in other *in vivo* systems.

Using these tools, Koudelka et al. (2016) made the pivotal discovery that subsets of axons in the zebrafish spinal cord can myelinate via activity-mediated mechanisms. Using tetanus toxin expression to block synaptic vesicle release from single neurons, Koudelka et al. (2016) demonstrated that patterns of myelination i.e. number and length of myelin sheaths along an axons, were disrupted in reticulospinal (RS) neurons but not commissural primary ascending (CoPa) neurons of the spinal cord. This was an important finding in the context of placing zebrafish as a model to study mechanisms of myelin mediated plasticity as it provided evidence that, in larval zebrafish, different mechanisms of myelination may be tuned to to the function of the underlying circuit. For example, CoPa neurons are interneurons which relay sensory signals to the contralateral spinal cord, whereas the RS neurons command the generation of multiple motor behaviours.

At least 27 distinct types of RS neuron exist, the cell bodies of which reside in the midbrain and hindbrain, and large caliber axons extend along the ventral spinal cord where they synapse with their targets which include motor neurons (Kimmel et al., 1974). Functional studies of RS neurons have identified roles for the different subtypes of RS neuron in specific behaviours which will be discussed in further detail in Chapter 4. Of particular importance is the Mauthner axon, the largest and most readily identifiably RS neuron whose principal role is to drive the escape response, a stereotypical behaviour that is essential for larval zebrafish survival in the face of threatening

stimuli (Korn and Faber, 2005). The anterior portion of the Mauthner axon is the first to be myelinated in the spinal cord at 60 hours post fertilisation, possibly reflecting the importance of Mauthner's function in addition to its large size (Almeida et al., 2011). From here, myelination progresses in an anterior and posterior direction with extensive myelination of RS system over the next few days. Intriguingly, this timeline of myelination coincides with the onset and refinement of RS driven behaviours (Figure 3.1). For example, the escape response emerges at 2 days post fertilisation (dpf) corresponding with the timing of the myelination of Mauthner (Eaton et al., 1977). However, more complex behaviours such as hunting routines do not become established until 5dpf (Bianco et al., 2011), at which the RS system is extensively myelinated. Although many aspects of circuit development feature in this time window, one could hypothesise that myelination plays a critical role in the development of such behaviours.

The entire nervous system of a larval zebrafish consists of approximately 100,000 neurons which has served them as a popular organism for the study of circuit neuroscience over the past decades, with the objective of understanding circuit function in a reductionist system before pursuing more complex models (Hill, 2003). Traditionally, the role of specific neurons in larval zebrafish has been meticulously examined by ablating neurons and studying the subsequent effect on behaviour – indeed, this is how the Mauthner neuron was first found to be implicated in the performance of the escape response (Liu and Fetcho, 1999). In addition, the ongoing development of genetically encoded calcium indicators (GECIs) in combination with high speed volumetric imaging techniques has advanced our ability to monitor large populations of neurons in living, and even freely behaving, larvae during spontaneous and stimulus-driven behaviour (Ahrens et al., 2012; Kim et al., 2017). These techniques have drastically evolved our understanding of the individual neurons and circuits which mediate specific behaviours in larval zebrafish (Huang et al., 2013; Liu and Fetcho, 1999; Orger et al., 2008; Severi et al., 2014).

Similarly, our knowledge of myelinated neurons in the spinal cord of zebrafish is extensive. Research from our own laboratory group has established much of what we know from the timings of myelination, to which neurons are myelinated and the mechanisms controlling their myelination (Almeida, 2018; Almeida et al., 2011; Baraban

et al., 2018; Koudelka et al., 2016; Mensch et al., 2015). Furthermore, serial section electron microscopy has been performed across the CNS of larval zebrafish providing us with unprecedented detail regarding the myelination status of the majority of axons in the brain and spinal cord (Hildebrand et al., 2017; Svara et al., 2018). Given their extensive use in both the fields of circuits neuroscience and myelin biology, zebrafish are well poised to bridge the gap in our knowledge concerning the effects of myelination on circuit function and behaviour *in vivo*.

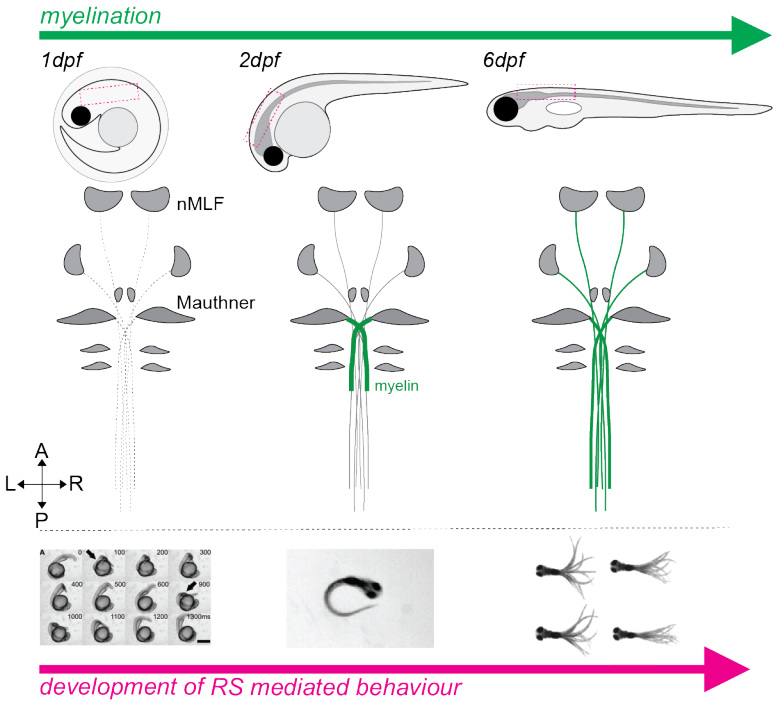

Figure 3.1: Schematic illustrating the development of behaviour in parallel with myelination of the reticulospinal system.// Top: developmental stage, middle: myelination status of the RS system, bottom: examples of behaviour present at these stages. At 1dpf, larvae remain in the chorion. At this stage the RS system is still developing and no myelination is present, however spontaneous activity within the developing CNS results in spontaneous coiling (image taken from Cui (2005)). At 2dpf, larvae have hatched from their chorion and myelination has begun in the anterior portion of the Mauthner axon - involved in the escape response (image taken from McClenahan et al. (2012)). 6dpf: The majority of the length of RS axons are myelinated and the behavioural repertoire has expanded to include complex swimming behaviour such as hunting. Image shows an overlay of larval zebrafish performing swimming responses while head-fixed in agarose gel (image taken from Wyart et al. (2009)).

Hypothesis and aims

The overarching hypothesis of this thesis is that myelination of the RS axons refines circuit function and locomotor behaviour during development.

The aims of this thesis are as follows:

1. To establish a larval zebrafish model of CNS specific hypomyelination (**this chapter**)

2. Investigate how disruption to the normal program of myelination affects RS-mediated locomotor behaviours (**Chapter 4**)

3. Identify candidate neural circuits for future assessment of the effects of hypomyelination on circuit function *in vivo* (**Chapter 4**)

Zebrafish models of CNS specific hypomyelination

Many core myelin genes – such as proteolipid protein (Plp), myelin basic protein (Mbp) and myelin protein zero (Mpz) - are functionally conserved across zebrafish and mammals. However, some key differences exist in their expression patterns (Brösamle and Halpern, 2002). For example, Mpz is present in the CNS and PNS in zebrafish, whereas its ortholog remains exclusive to the PNS in mammals (Bai et al., 2011). Current models of hypomyelination in zebrafish are either not exclusive to the CNS, or disrupt additional cell types which would confound interpretation of behavioural phenotypes. For example, disruption of SRY-Box 10 (Sox10) – an early onset transcription factor expressed in OL lineage cells - causes failure of OL survival and myelin gene expression in *colourless* mutants (Takada and Appel, 2010), however it is also expressed in interneurons, neural crest cells and Schwann cells (Dutton, 2001). Disruption of Neuregulin-ErbB signalling, through mutations in Erbb2 and Erbb3 receptors reduces Mbp expression in the PNS but leaves the CNS largely intact, although CNS myelination in this model has not been extensively studied (Lyons et al., 2005). Alternatively, larval zebrafish models of CNS demyelination exist, for example the transgenic zebrafish line which expresses bacterial enzyme nitroreductase in myelinating glia. Exposure of these fish to the drug metronidazole causes toxicity in cells expressing nitroreductase and subsequent cell death in two-thirds of OLs. However, this model also experiences cell death in half of the Schwann cell population and causes significant immune cell infiltration into the spinal cord (Karttunen et al., 2017).

The purpose of this project is to study the contribution of CNS myelination to circuit function and behaviour. Thus, the ideal zebrafish model to recruit to this study should have CNS **specific** hypomyelination with minimal disruption to other cell types. Using a developmental model such as the larval zebrafish could pose a challenge in this regard as many mechanisms of nervous system development are tightly interlinked. For example, axon caliber and myelination can directly regulate each other (Blakemore, 1973). Thus it will be prudent to characterise these parameters alongside reduced myelination to enable confidence in assigning behavioural phenotypes solely to myelin deficits. In addition, our model should have a strong enough reduction in CNS myelin for us to detect a behavioural phenotype, yet not so severe that the fish are impaired and unable to perform in behavioural assays. This is particularly important if this model is to be enrolled into plasticity based assays in the future.

Myelin regulatory factor as a candidate gene target for CNS specific perturbation of myelin

The Myelin Regulatory Factor (Myrf) gene represents a target for manipulation which could meet the requirements of a CNS specific phenotype. Myrf has been identified in transcriptome studies to be exclusively expressed by post-mitotic oligodendrocytes within the mouse forebrain (Cahoy et al., 2008) (Figure 3.2). Complementary transcriptome databases have confirmed a restricted expression pattern to OL lineage cells over other cells in the rodent cortex (Zhang et al., 2014). Although these databases have only studied specific regions of CNS tissue, there is no evidence that Myrf is expressed in the PNS. In fact, in the mouse conditional knockout (CKO) Myrf model, which I will go on to discuss further, myelination of the PNS remains intact (Emery et al., 2009). As far as we know, Myrf expression follows a similar pattern in larval zebrafish. Data provided in Appendix 1 (Figure 5.1) includes in-situ hybridisation and semi-quantitative RT-PCR data demonstrating that Myrf expression is restricted to OLs of the CNS (data provided by the group of Dr. Kelly Monk (The Vollum Institute, OHSU) and Dr. Anna Klingseisen (University of Edinburgh)).

Emery et al. (2009) were the first to characterise Myrf (gene model 98) function in mice. Using the cre-recombinase system, they performed cell-type specific ablation of Myrf

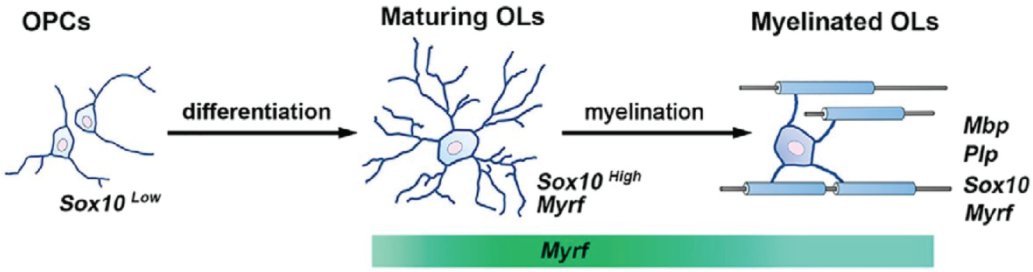

Figure 3.2: Schematic of Myrf expression during the OL lineage Myrf expression is largely restricted to newly formed OLs (here labelled as maturing OLS) and myelinating OLs (Zhang et al., 2014). Myrf functions as a transcription factor alongside other genes such as Sox10 to regulate the expression of core myelin genes such as Mbp and Plp. Image taken from (Huang et al., 2018)

in OL lineage cells by crossing olig2-cre mice to mice carrying floxed alleles in exon 8 of Myrf ($Myrf^{fl/fl}$). By post-natal day 11 these mice develop tremors, ataxia and seizures, and eventually die in their third postnatal week. These severe behavioural phenotypes were associated with a drastic reduction in the level of Mbp staining and number of OLs in brain and spinal cord, with corresponding loss of myelin protein levels on western blot analysis. Despite a normal number of oligodendrocyte precursor cells (OPCs), mature OLs underwent an increased rate of apoptosis in CKO mice which was proposed as a potential mechanism for the failure of myelination in this model. Subsequently blocking apoptosis using adenovirus expression of BCL-2 in OPCs demonstrated that Myrf CKO OPCs failed to upregulate myelin protein genes despite their survival suggesting an intrinsic failure to myelinate rather than failure of myelination due to premature cell death. From this study, it appears that Myrf expression in OL lineage cells is essential for the switch from a premyelinating to a myelinating OL and subsequent onset of CNS myelination during development.

Koenning et al. (2012) asked whether a similar requirement for Myrf expression was found in the adult mouse. To test this, they utilised an inducible CKO strategy by expressing CreERT under a PLP-promotor. In doing so, recombination is not only restricted to the mature OL population when crossed to the $Myrf^{fl/fl}$ line, but Myrf function will be retained during development until the administration of tamoxifen at 8 weeks of age. In this model, CKO of Myrf caused severe demyelination throughout the CNS with progressive motor deficits developing from 5 weeks post tamoxifen administration. Recombination was associated with downregulation of mature OL markers and increased rates of apoptosis, however, rebound OPC proliferation and differentiation

preserved OL number permitting remyelination and improved behavioural phenotypes 8 months following tamoxifen administration. Analysis of single recombined OLs in the cerebral cortex and striatum demonstrated that although some cells were associated with myelin, many displayed multiple fine processes with loss of associated myelin sheaths. In contrast, inducible CKO of Myrf from OPCs in adult mice using a pdgfra-creERT2 driver line results in a 90% reduction in OLs without affecting pre-existing myelin (McKenzie et al., 2014). Together these studies demonstrate that Myrf plays a critical role in all stages of the OL lineage, allowing the differentiation of myelinating OLs and maintenance of existing myelin in the developing and adult CNS.

The function of Myrf outside of its expression in OL lineage cells of the CNS has received little attention in mammals. However, constitutive deletion of Myrf in mice results in embryonic death suggesting it may play an important role in developmental processes and not just in myelination. Although gene function is not directly comparable between species, this notion is supported by studies investigating the role of Myrf orthologs in invertebrates. Dictyostelium species lacking mrfA display a progressive delay in development (Senoo et al., 2013) and MYRF-1 mutations in C. elegans cause developmental arrest by the L2 stage (Meng et al., 2017; Russel et al., 2011). Interestingly, MYRF-1, alongside its paralog MYRF-2, has been implicated in motor circuit remodelling during development in C. elegans, where absence of both paralogs results in a specific failure of synaptic rewiring in dorsal d (DD) GABAergic motor neurons (Meng et al., 2017). These studies suggest that Myrf's role as regulator of differentiation is likely conserved across species and, outside of its expression in OLs, may play an additional role in organism development in mammalian species.

Myelin regulatory factor gene function

Myrf is a membrane bound transcription factor which, in mammals, acts in the CNS to promote terminal differentiation of OLs and the production of myelin via the upregulation of myelin specific genes (Bujalka et al., 2013; Emery et al., 2009). The function of Myrf and its orthologs relies on the presence of unique, conserved functional domains: an intramolecular chaperone domain, DNA binding domain (N-terminus), transmembrane domain and a Myrf domain (C-terminus) (Bujalka et al., 2013; Li et al., 2013; Meng et al., 2017; Senoo et al., 2013) (Figure 3.3). The presence of the intramolecular

chaperone domain – conserved from endosialidases, the tail spike proteins of bacteriophages (Stummeyer et al., 2006) – allows Myrf to undergo auto-proteolytic cleavage in the endoplasmic reticulum resulting in retention of the C-terminus fragment (including transmembrane domain) in the cytoplasm and translocation of the N-terminus into the nucleus where it can fulfil its transcriptional role (Bujalka et al., 2013; Li et al., 2013; Meng et al., 2017; Senoo et al., 2013). The ability to auto-proteolytically cleave appears to be unique to Myrf and its homolog Myrf-like among membrane bound transcription factors, and essential for their function (Bujalka et al., 2013; Meng et al., 2017; Senoo et al., 2013). Myrf gene function has been most extensively characterised in the context of myelination. However, as I revealed earlier it also plays an interesting role in the developmental processes of invertebrates. I will first discuss how the functional domains of Myrf are known to regulate myelination, then I will return to their intriguing role in invertebrates and explain how this could be relevant in the context of myelination in vertebrates.

Following cleavage, the N-terminus localises to the nucleus where it directly binds to DNA enhancer regions of OL specific and myelin genes. Considerable overlap exists between binding sites for Myrf and key OL lineage transcription factors Sox10 and Olig1 suggesting interactions between these transcription factors during OL development and myelination (Bujalka et al., 2013). Emery et al. (2009) previously found that transfection of OPCs with Myrf *in vitro* drove expression of myelin genes such as Mbp and Mog in 80% of cells. While *in vivo*, equivalent levels of Mbp expression required co-transfection of Sox10 alongside Myrf. Using biochemical assays, Hornig et al. (2013) discovered that Myrf is a direct target of Sox10, which is able to drive Myrf expression by binding directly to an enhancer region in an intronic sequence adjacent to the Myrf gene. Additionally, the authors demonstrated that Sox10 and Myrf can act synergistically on regulatory elements of other myelin genes, corroborating the findings of Bujalka et al. (2013). Although these studies show that Myrf expression is downstream of Sox10 function in the OL differentiation program, its restriction to late-OL stages suggest that Sox10 – which is present in all stages of OL lineage – is not the sole driver.

Although the transcriptional regulatory function of Myrf has been well characterised, *in vitro* expression of the N-terminus alone in a glial cell line was observed to be less

competent at driving OL maturation than the presence of full-length wild type Myrf (Li et al., 2013). This suggests that the C-terminal domain which remains in the ER may play an additional role in regulating the differentiation program of OLs. Indeed, it has been speculated that the C-terminus may function to prepare the ER for the imminent flux of myelin components through secretory pathways. The surface area of a single OL has been documented to cover 1-20 x 10^3 microns^2, exemplifying the huge demands for lipid biogenesis during myelination (Pfeiffer et al., 1993). Given the temporal restriction of Myrf to myelinating oligodendrocytes, it is feasible that the C-terminus plays a currently unidentified role in regulating myelin protein secretion in vertebrates. In support of this, the C. elegans protein PQN47 – orthologous to Myrf – is involved in regulating secretion of the cuticle during larval molting cycles (Russel et al., 2011). Additionally, beyond the CNS, Myrf is expressed in a number of secretory tissues such as the gonads, gastrointestinal tract, lungs, hepatobiliary system (*EMBL-EBI Expression Atlas*, n.d.; *The Human Protein Atlas*, n.d.).

Myrf function in humans

Given high sequence homology we can reasonably extrapolate from mouse data that Myrf is likely to play a similar role in the regulation of myelination in humans. The scant literature which is available in humans comes from exome sequencing studies identifying *de novo* mutations of Myrf which have arisen in individuals. Of particular relevance is a study that identified a heterozygous single nucleotide variant mutation in the coding region of the Myrf gene in members of the same family. Individuals developed a transient encephalopathy with associated white matter abnormalities observed on diffusion weighted MRI, potentially indicating myelin pathology (Kurahashi et al., 2018). Other than this, many of the reported human phenotypes associated with Myrf mutations involve cardiac, urogenital, ocular and sex development abnormalities (Garnai et al., 2019; Hamanaka et al., 2019; Pinz et al., 2018; Rossetti et al., 2019). The majority of these mutations are located in coding regions of DNA and predicted to cause loss of function. However, given that these mutations are naturally occurring and heterozygous in nature it is not surprising that phenotypes are less severe than those which are observed in mice. Additionally, many of these studies are performed in individuals with medical syndromes that are likely to be associated with multiple genetic variants.

Conclusion

In summary, a wealth of information supports the choice of Myrf gene as a genetic target for the production of a zebrafish model of CNS specific hypomyelination. In the following sections, I will present our approach to creating a Myrf zebrafish mutant alongside extensive characterisation of its myelination phenotype, with the predominant aim of establishing a suitable model system for recruitment into behavioural assays (Chapter 4).

3.2 Materials and Methods

3.2.1 Generation of a stable Myelin Regulatory Factor mutant line

Generation of the Myrf zebrafish mutant line was performed by Dr. Jason Early (Lyons Lab) prior to the start of this project. The materials and methods described here were performed by Dr. Jason Early. **The results presented in this chapter were derived from experiments primarily performed by myself using the Myrf zebrafish mutant line**.

CRISPR/Cas9 technology has evolved as an extremely useful tool to achieve high efficiency mutagenesis in zebrafish (Chang et al., 2013; Li et al., 2016). The aim of targeted mutagenesis is to alter the coding sequence in a critical region of the gene such that no, or at least non-functional, protein is produced. Following the introduction of Cas9-RNA complex formation and double strand breaks into the DNA sequence, repair mechanisms will result in random insertions and deletions of nucleotides at the mutagenesis site. Ideally, a non-sense mutation or change to the open reading frame (ORF) will occur resulting in a premature stop codon, non-sense mediated decay of the transcript and lack of functional protein. Alternatively, protein may still be formed but a key residue has been altered such that its function is suboptimal. However, the genome is adaptable and intrinsic mechanisms exist that are equipped to protect a gene against a function disrupting mutation, for example the presence of alternative splice sites. It is important to consider these mechanisms during selection of sgRNA target sites and characterisation of the mutant alleles produced.

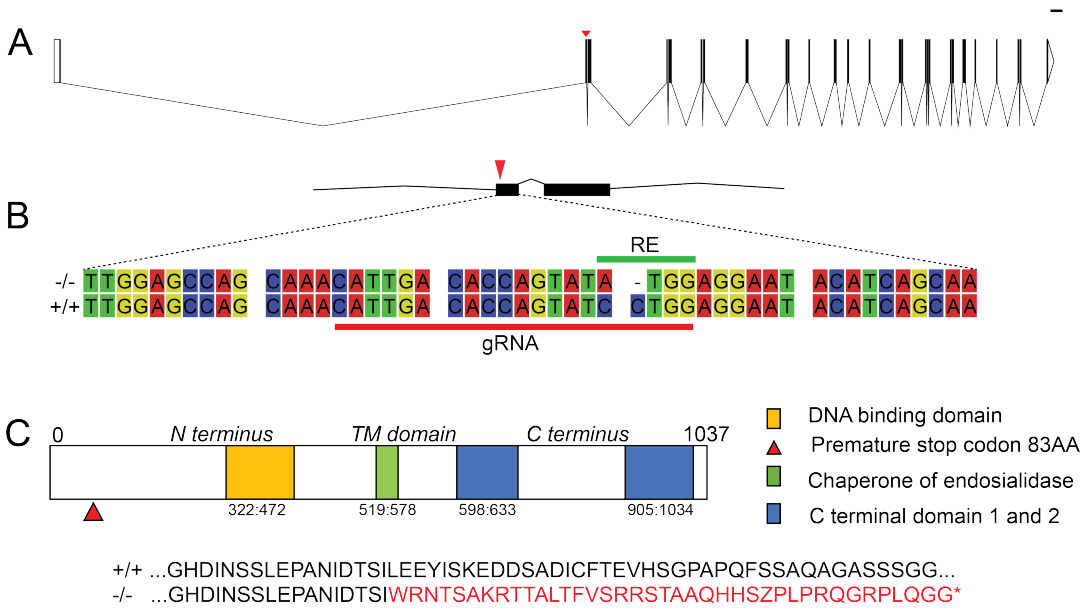

Figure 3.3: Overview of Myrf gene and protein structure
(A.) Myrf gene structure consisting of 27 exons. Scale bar (top right) represents 1000bp. Red arrowhead marks the location of the mutation in exon 2. Schematic made using Wormweb.org. **(B.)** Nucleotide sequence of a region of exon 2 spanning the mutagenesis site. Wild type and homozygous mutant sequences are provided. The gRNA target site is marked with a red line. The restriction enzyme recognition site is marked with a green line. **(C.)** Myrf protein structure and the amino acid sequence for wild type and homozygous mutants. The red arrow head marks the location of the premature stop codon at AA 73.

Myelin Regulatory Factor gene

Myrf is the zebrafish ortholog of the human and mouse Myrf coding genes known as c11orf9 and gm98 respectively. The zebrafish Myrf protein has approximately 64.92% and 64.49% homology with these orthologs respectively. In zebrafish, the Myrf gene is made up of 27 exons with 6 predicted splice isoforms (NCBI gene ID: 570792). All 6 isoforms are broadly similar except for a small number (<12bp) of nucleotide discrepancies, except for isoform x5 and x6 which lack exon 19. The first predicted isoform of Myrf closely resembles the Ensembl database APPRIS1 sequence. I will use this isoform for subsequent figures and examples (Figure 3.3). Zebrafish orthologs exist for 71.4% of human genes with many (65%) of these orthologs demonstrating a one-to-one relationship. However, for 21% of these genes there exist two or more orthologous genes in zebrafish due to teleost specific genome duplication (Howe et al., 2013). This is an important feature of the zebrafish genome to be aware of when performing genetic knockdown studies. Although this is not the case for Myrf, a *homologous* zebrafish gene does exist named 'Myelin Regulatory Factor Like', from here on referred to as 'Myrf-like' (NCBI Gene ID: 100329855). Myrf-like protein consists of 942 amino acids and shares

approximately 43% sequence homology with Myrf, with areas of sequence identity being conserved predominantly in the regions of the DNA binding and transmembrane domain (Appendix 1, Figure 5.4). The Myrf-like gene is also found in mammals where its function is relatively unknown.

CRISPR/Cas9 targeted mutagenesis of Myrf

Freely available guide selection tools (http://crispr.mit.edu) were used to select sgRNAs against the second exon of the Myrf gene. The sgRNA guide sequence is provided in Table 3.1. This exon was selected as it is the first conserved exon across the six known splice variants. Additionally, exon 2 is located prior to the DNA binding domain which is critical for transcription factor function. The guide was selected based on its predicted efficiency and the presence of a commercially available restriction enzyme recognition sequence within the target sequence. In this way, restriction fragment length polymorphism (RFLP) could be used to confirm efficient mutagenesis of the target site.

Table 3.1: sgRNA target sequence and template dsDNA
Target sequence for Myrf exon 2 guide RNA and the corresponding DNA oligonucleotide template sequences used to synthesise sgRNA. Italics denote the T7 promotor used for RNA synthesis. Nucleotides in bold are the reverse complement of the target. All nucleotides 5' of the target sequence is template for the sgRNA scaffold.

Target	Target Sequence	Template DNA for sgRNA 5' to 3'
Myrf exon 2	CATTGACACCAGTATCCTGG	AAAGCACCGACTCGGTGCCACTTTTT-CAAGTTGATAACGGACTAGCCTTATTT-TAACTTGCTATTTCTAGCTCTAAAAC-**CCAGGATACTGGTGTCAATG***CTA-TAGTGAGTCGTATTACGC*

Information on sgRNA and nCas9n synthesis can be found in the thesis of Dr. Jason Early (Early, 2016) (pg.54). Cas9 mRNA and sgRNA were injected into wild type embryos at the single cell stage to produce F0 animals. Injection at the single cell stage produces a mosaic pattern of genotypes and mutations at the targeted allele. RNA can persist for hours following injection allowing for the integration of mutations into different cell types during early stages of development. Consequently, individual gametes of adult F0 animals will possess a combination of unique mutant, as well as wild type, alleles. The efficiency of mutagenesis can be established by extracting DNA from injected and uninjected cohorts of wild type F0 animals, isolating a fragment around the mutation site and performing restriction enzyme digestion (i.e. RFLP) (Figure 3.4).

For example, a guide with very low efficiency will result in few mutagenised cells at the restriction enzyme recognition site. Thus, following digest of the PCR product a large proportion of the fragment will be digested. However, a highly efficient guide induces mutagenesis and ablation of restriction enzyme recognition site in a larger number of cells which will result in minimal digestion of the amplified fragment.

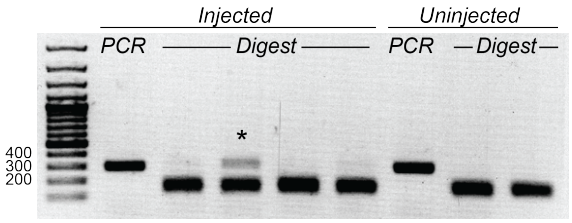

Figure 3.4: Testing mutagenesis efficiency using RFLP
Gel electrophoresis following PCR and digest of 291bp fragment spanning the Myrf mutagenesis site. The fragment is fully digested in the uninjected controls (final two lanes) in which the restriction enzyme recognition site is in tact. Incomplete digestion is present in only one of the injected F0 fish (*).

Founder identification and selection

Injected F0 animals were grown to adulthood and outcrossed to wild type animals to create F1 offspring. F0 founders were identified by genotyping their F1 offspring and identifying heterozygous carriers of the mutant allele (see genotyping protocol in Materials and Methods). Clutches of embryos from identified founders were raised to adulthood and DNA from twenty-four heterozygous F1 animals was sequenced to identify function disrupting mutant alleles. Given that F1 offspring will have incorporated the specific mutation present in a single F0 gamete into each cell during development, these fish will become stable carriers of a single, and unique, mutant allele. Multiple mutant alleles were identified, three of which I took forward for preliminary characterisation (Table 3.2).

Table 3.2: Myrf mutant alleles

Allele	Sequence
Wild type	CCAGTATCCTGGAGGAATA
ΔTCC	CCAGTA—TGGAGGAATA
+11bp	CCAGTATCC**AGACACCAGTA**TGGAGGAATA
ΔCC+A	CCAGTAT**A**TGGAGGAATA

3.3 Results

3.3.1 Characterisation of Myrf mutant alleles

To confirm that Myrf knockdown caused a myelin-disrupting phenotype I performed *in vivo* imaging of the candidate mutant allele lines (listed in Table 3.2) between 4 and 5dpf. Using the transgenic reporter tg(mbp:nls-eGFP), which labels nuclei of myelinating oligodendroglia, I quantified the total number of oligodendrocytes in the dorsal and ventral spinal cord. As described in Section 2.4, Chapter 2, all images for analysis were obtained and analysed at the same laser intensity and image brightness. We predicted that the allele 'ΔTCC', which is a three base pair deletion, would not alter the ORF and should not display a phenotype. However, mutant alleles +11bp and ΔCC+A alter the ORF are were therefore predicted to result in a premature stop codon and loss of protein function. Therefore we expected these lines to recapitulate the phenotype seen in Myrf CKO mice which exhibit an almost complete absence of OLs (Emery et al., 2009). Indeed, OL numbers were significantly reduced by 46% and 69% in mutant alleles +11bp ($p = 0.002$, one-way ANOVA with Tukey's multiple comparisons) and ΔCC+A ($p = <0.0001$, one-way ANOVA with Tukey's multiple comparisons) respectively, compared to wild type siblings (Figure 3.5). As expected, no difference was observed in the ΔTCC allelic line ($p = 0.83$, one-way ANOVA). Given the robust reduction in OL number in the ΔCC+A mutant allele, I took this line forward for extensive characterisation. All data presented in the rest of this chapter is collected from the stable ΔCC+A mutant allelic line (third generation onwards). Importantly, although a 69% reduction in OL number is marked, it does not match the severity observed in the aforementioned mouse model. This led me to question why the larval zebrafish model displays a less severe phenotype. Before progressing with extensive characterisation of this mutant line, it was pertinent to establish the efficiency of the gene knockdown and rule out common mechanisms of genetic compensation which might be at play. This will be addressed in the following sections.

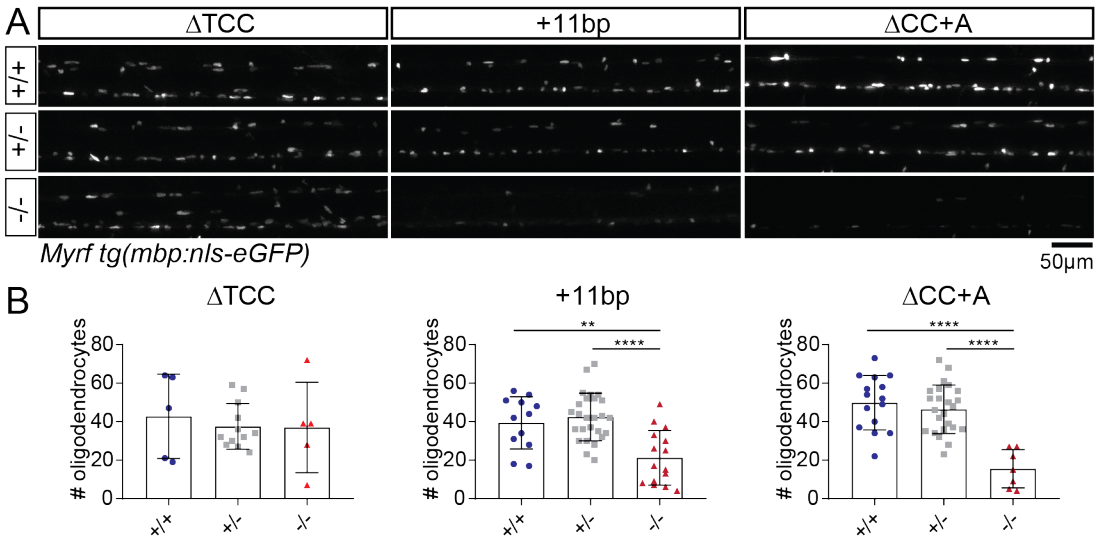

Figure 3.5: Quantification of oligodendrocyte number in different Myrf mutant alleles

(A.) Lateral images of the spinal cord of tg(mbp:nls-eGFP) expressing Myrf larval zerbafish at 4-5dpf. Oligodendrocytes in the dorsal (top) and ventral (bottom) spinal cord can be observed. Images are provided for wild type, heterozygous and homozygous mutants (top to bottom) for each allele (left to right). **(B.)** L-R **ΔTCC** No difference in oligodendrocyte number is observed between genotypes in the ΔTCC mutant line (42.80 ±21.89 oligodendrocytes in wild types, 37.58 ± 11.80 oligodendrocytes in heterozygotes and 37.00 ± 23.53 oligodendrocytes in homozygous mutants) (F (2,19) = 0.19, p = 0.83, one-way ANOVA). N = 5 wild type, N = 12 heterozygotes, N = 5 homozygous mutants. **+11bp** Myrf +11bp homozygous mutants display a significant reduction in the number of oligodendrocytes in the spinal cord (39.42 ± 13.57 oligodendrocytes in wild types, 42.42 ± 12.40 oligodendrocytes in heterozygotes, 21.27 ± 14.15 oligodendrocytes in homozygous mutants) (F (2,50) = 12.87, p = <0.0001, one-way ANOVA. Tukey's multiple comparisons: WT-Het = 0.79, WT-Hom = 0.002, Het-Hom = <0.0001). N = 12 wild type, N = 26 heterozygotes, N = 15 homozygous mutants. **ΔCC+A** Myrf ΔCC+A homozygous mutants display a significant reduction in the number of oligodendrocytes in the spinal cord (49.87 ± 14.14 oligodendrocytes in wild type, 46.42 ± 12.60 oligodendrocytes in heterozygotes, 15.57 ± 9.93 oligodendrocytes in homozygous mutants) (F (2,43) = 19.09, p = <0.0001, one-way ANOVA. Tukey's multiple comparisons: WT-Het = 0.69, WT-Hom = <0.0001, Het-Hom = <0.0001) N = 15 wild type, N = 24 heterozygotes, N = 7 homozygous mutants. Values and error bars represent mean ± standard deviation.

3.3.2 Myrf$^{-/-}$ mutants exhibit a gross CNS hypomyelination and dysmyelination phenotype

To perform an initial assessment of the level of myelination in the spinal cord I used the transgenic line tg(mbp:eGFP-CAAX) which drives expression of eGFP tethered to the membrane of myelinating cells, therefore labelling all myelin sheaths in the CNS and PNS (Figure 3.6A). Simply screening this line using an epifluorescence screening microscope it was possible to identify mutants with a 66% success rate (confirmed by

genotyping, data not shown) due to a robust reduction in GFP fluorescence in the spinal cord. This phenotype was confirmed using confocal microscopy to image the spinal cord at the level of the cloaca (Figure 3.6B). At this developmental time point (6pdf), myelination in the spinal cord of wild type and heterozygous siblings was robust. In contrast, Myrf$^{-/-}$ mutants exhibited reduced GFP expression in the myelinated tracts with patchy, incomplete myelination of the Mauthner axon consistent with a general hypomyelination and dysmyelination phenotype. Although this transgenic reporter gives us an excellent impression of the gross level of myelination in the spinal cord, it is not yet possible to determine myelin thickness accurately using this imaging technique. However, I would predict that the reduced membrane GFP expression observed in mutants is a result of thinner myelin sheaths alongside reduced Mbp expression. These predictions will be tested with transmission electron microscopy (TEM) and quantitative real time-polymerase chain reaction (qRT-PCR) in results to come.

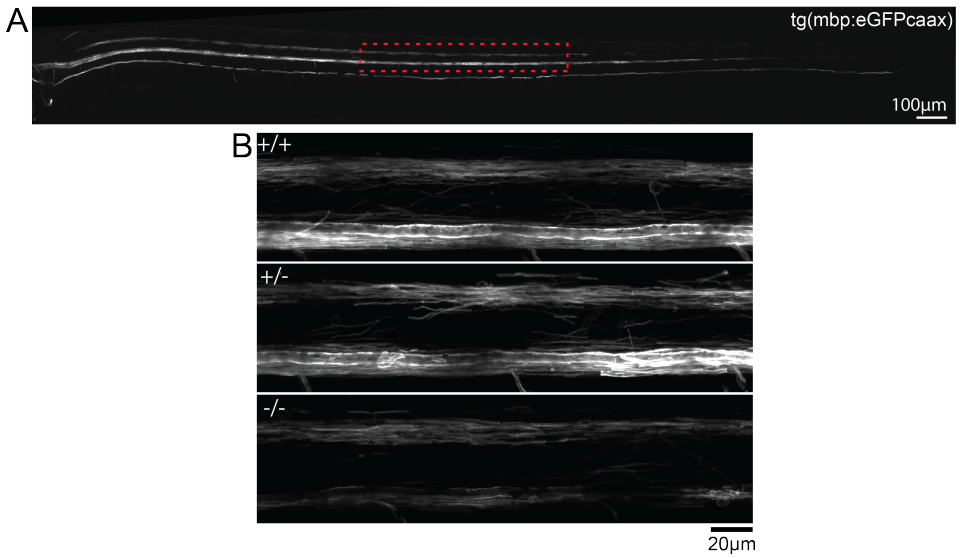

Figure 3.6: Myrf$^{-/-}$ mutants exhibit reduced myelin membrane GFP expression and dysmyelination in the spinal cord
(A.) Overview of transgene expression in a wild type tg(mbp:eGFP-CAAX) larvae at 5dpf. Lateral maximum intensity projection with the head of the larvae to the left of the image. **(B.)** Maximal intensity projections (1 x gain) of the myelinated tracts in the spinal cord of Myrf wild type, heterozygous and homozygous mutant siblings at 6dpf. 20x objective.

3.3.3 Myelin basic protein transcript levels are significantly reduced in Myrf$^{-/-}$ mutants

The Myrf$^{-/-}$ mutant DNA sequence contains a frameshift mutation within exon 2 which is predicted to result in a truncated protein prior to the DNA binding domain, a critical region for the gene's transcriptional activity (Figure 3.3). The presence of a premature stop codon prior to the last exon should initiate RNA surveillance mechanisms to induce non-sense mediated decay of transcript levels. qRT-PCR was performed in triplicate on whole brains extracted from adult Myrf zebrafish. Quantitative Myrf mRNA levels in homozygous and wild type siblings were compared to the housekeeper gene EF1-alpha which is constitutively expressed at all ages. Levels of Myrf mRNA were very low in all samples (similar finding in adult and larval tissue, data not shown), requiring a large number of cycles to amplify PCR fragments. This led to variable relative expression values for Myrf between wild type and mutant siblings with no significant difference detected between the samples (Figure 3.7B). Levels of Myrf-like transcript, a zebrafish homolog of the Myrf gene, were also assessed as part of ongoing investigations into genetic compensatory mechanisms (see next section). Similar variability in the levels of Myrf-like transcript were found (Figure 3.7C). Due to the low expression level of these transcripts across samples, in controls as well as mutants, I do not believe that these results reflect true differences in expression but a shortcoming of the current qPCR protocol. Due to the specificity of Myrf expression to OL lineage cells, one whole brain (as was used per fish in this experiment) may not provide enough OLs for detectable differences to be observed. In future, it would be necessary to perform FACS sorting of multiple brains or larvae to isolate large enough numbers of OL to be able to draw reliable comparisons from. Similarly, Myrf-like is expressed at very low levels in the CNS, so the use of an alternative tissue type (such as whole larvae) could be beneficial in future.

Conveniently, Mbp is expressed abundantly in the CNS. Given that Myrf directly regulates Mbp expression (Bujalka et al., 2013), I opted to test Mbp transcript levels as an indirect readout of Myrf function. Indeed, when I compared quantitative levels of Mbp between wild type, heterozygous and mutant siblings, significant changes in Mbp transcript levels were present across groups ($p = 0.0002$, one-way ANOVA) with a 95% reduction in mutant Mbp levels when compared to wild type siblings ($p = 0.0017$,

Tukey's multiple comparisons) (Figure 3.7A). This is in keeping with the mouse model which demonstrates an almost complete loss of Mbp immunostaining in the brain and spinal cord (Emery et al., 2009). Intriguingly, heterozygous siblings demonstrated a non-significant increase in the relative concentration of Mbp compared to wild type siblings (p = 0.06, one-way ANOVA followed by Tukey's multiple comparisons test). In summary, given the difficulties experienced in reliably quantifying Myrf transcript levels, I cannot confirm that non-sense mediated decay is occurring in this mutant line. However, Mbp transcripts are reliably abolished in Myrf$^{-/-}$ samples confirming a functional deficit in Myrf protein function in adult homozygous mutant brain tissue. This finding will need to be considered in the the assessment of subsequent live-imaging microscopy results, where transgenic lines using the mbp promotor are utilised (see Section 3.4).

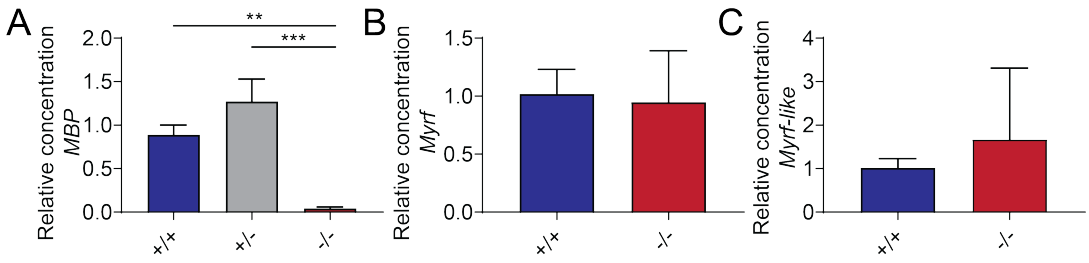

Figure 3.7: Relative expression levels of myelin genes across Myrf genotypes **(A.)** Relative concentration of MBP (0.88 ± 0.11 in wild types, 1.27 ± 0.26 in heterozygotes and 0.04 ± 0.02 in homozygous mutants (F(2, 6) = 44.81, p = 0.0002 one-way ANOVA. Tukeys multiple comparisons WT-Het p = 0.06, Het-Hom p = 0.002, WT-Hom p = 0.0002)). **(B.)** Relative concentration of Myrf (1.017 ± 0.21 wild type, 0.95 ± 0.44 mutants (p = 0.82, unpaired t-test). **(C.)** Relative concentration of Myrf-like (1.01 ± 0.21 wild type, 1.67 ± 1.64 mutant (p = 0.53, unpaired t-test). EF1-alpha was used as a housekeeper gene for all experiments. N = 3 brains per group. Samples run in triplicate.

3.3.4 Investigating mechanisms of genetic compensation in Myrf$^{-/-}$ mutants

Using Mbp expression in adult brain tissue as an indirect readout of Myrf gene function, I have shown that Myrf function is sufficiently disrupted in our mutant line. However, this does not explain the discrepancy in phenotypes between the Myrf$^{-/-}$ larval zebrafish in comparison to equivalent mouse models. Not only are mature OL numbers less severely effected, but Myrf$^{-/-}$ zebrafish mutants also survive into adulthood which is in stark contrast to the mouse model which displays premature death (Emery et al.,

2009). Given that larval zebrafish are known to display multiple modes of genetic compensation (El-Brolosy et al., 2019; Rossi et al., 2015), it was important to rule out the existence of genetic compensation mechanisms in the Myrf$^{-/-}$ mutant that may be providing a partial rescue in the larval stages. Importantly, if such a mechanism were to be identified it could provide a target for intervention and exacerbation of the myelin phenotype in Myrf$^{-/-}$ mutants if required.

Table 3.3: Summary of investigations into genetic compensatory mechanisms

Intervention	Rationale	Findings
Injection of Myrf antisense morpholino into Myrf$^{-/-}$ embryos	To assess for residual zygotic or maternal gene function	Myelin phenotype unaltered in Myrf$^{-/-}$ morpholino injected mutants (Appendix 1, Figure 5.3A)
Measurement of Myrf transcript in unfertilised eggs of Myrf$^{+/-}$ females	To detect the presence of maternal Myrf mRNA	No detectable transcript (Appendix 1, Figure 5.3B)
Knockdown of Myrf-like gene function in Myrf$^{-/-}$ embryos	To test the contribution of the homolog gene Myrf-like	Myelin phenotype unaltered in Myrf$^{-/-}$/Myrf-like$^{\text{CRISPANT}}$ mutants (Appendix 1, Figure 5.5)
Quantification of Myrf-like transcript levels	To assess for upregulated transcription of paralogous genes	Inconclusive due to low transcript levels in brain tissue (Figure 3.7)
Sequencing of Myrf$^{-/-}$ mRNA	To assess for alternative splicing	No evidence of alternative splicing (Appendix 1, Figure 5.7)

I predicted two mechanisms of genetic compensation that may be occurring. Firstly, as maternal heterozygotes were used to produce clutches of embryos for all experiments, there exists the possibility for wild type mRNA transfer to the fertilised embryo which would compensate for loss of zygotic gene function (Jimenez and Campos-Ortega, 1982; Perrimon et al., 1984). Secondly, non-sense mediated decay of the mutant transcript has been shown to cause upregulation of genes with a homologous DNA sequence (El-Brolosy et al., 2019). For Myrf, the most likely candidate gene for this function would be Myrf-Like which bears a 43% sequence similarity to Myrf. Although non-sense mediated decay of Myrf was not detectable on qRT-PCR, it is likely that this is a false negative finding given the disruption to Mbp levels. To test these core hypotheses I performed further assessment of gene expression and utilised different genetic knockdown techniques to target potential pathways. A summary of these interventions and their findings are presented in Table 3.3. The details of these experiments can be found

in Appendix 1. In short, targeting these candidate mechanisms provided no evidence to support a role of genetic compensation in the Myrf$^{-/-}$ mutants.

3.3.5 Myrf$^{-/-}$ mutants exhibit normal development up to 6dpf

Genetic knockdown in zebrafish is often associated with developmental delay which can be detected as morphological abnormalities, such as the absence of a swim bladder. It was important to ensure that no such characteristics were present in the Myrf$^{-/-}$ mutants as this would interfere with behavioural phenotyping in Chapter 4. Using bright field images of 6dpf Myrf larvae, I assessed the following morphological features: body length, ocular diameter and swim bladder diameter (see Materials and Methods, Figure 2.4). No significant difference in these features was observed between groups at 6dpf suggesting that development is normal until this timepoint (Figure 3.8). Myrf$^{-/-}$ mutants are viable into adulthood. However, at this point they display phenotypes consistent with a global loss of Myrf function, for example, they are often smaller in size, possess a lack of pigmentation of the ventral abdomen and are infertile (Appendix 1, Figure 5.6).

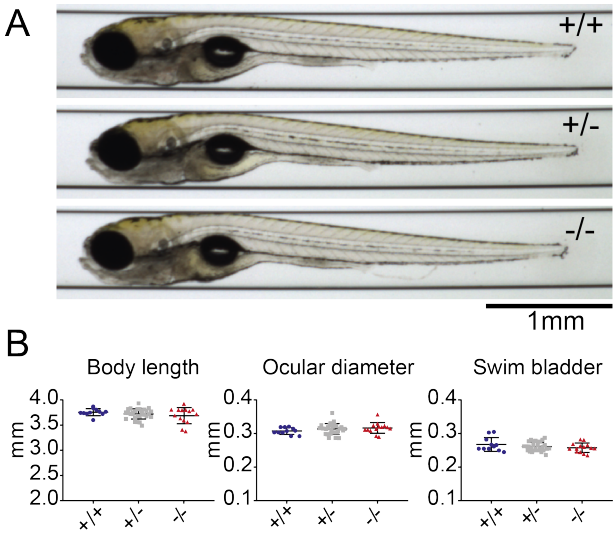

Figure 3.8: Assessment of developmental morphological features
(A.) Brightfield images of Myrf wild type, heterozygous and homozygous mutants at 6dpf. **(B.)** Body length: 3.76 ± 0.07mm wild types, 3.72 ± 0.1mm heterozygotes and 3.69 ± 0.16 homozygous mutants (F (2,51) = 0.99, p = 0.38, one-way ANOVA. Ocular diameter: 0.31 ± 0.01mm wild types, 0.31 ± 0.02mm heterozygotes and 0.32 ± 0.02mm homozygous mutants (F (2,51) = 1.19, p = 0.31, one-way ANOVA). Swim bladder height: 0.27 ± 0.02mm wild types, 0.26 ± 0.01mm heterozygotes and 0.26 ± 0.01mm in homozygous mutants (F (2,51) = 1.277, P = 0.29, one-way ANOVA) Bars represent mean ± standard deviation

3.3.6 Myrf$^{-/-}$ mutants exhibit a reduction in the number of oligodendrocytes in the spinal cord

***In vivo* imaging of oligodendrocyte number in the spinal cord**

In mice, CKO of Myrf from OL lineage cells using an olig2-cre driver line results in almost complete loss of mature OLs while leaving the OPC population in tact. Early pre-myelinating OLs are still detectable suggesting that differentiation can still take place, however these cells rapidly undergo apoptosis before reaching the capacity to myelinate (Emery et al., 2009). Data collected at the beginning of my project, presented in Figure 3.5, revealed that the Myrf$^{-/-}$ ΔCC+A mutants exhibited a 68% decrease in the number of mature OLs compared to wild type and heterozygous siblings at 4/5dpf (one-way ANOVA with Tukey's multiple comparisons, p = <0.0001). To investigate whether OL numbers remained low at later time points (particularly 6dpf when behavioural characterisation would be performed), I repeated this experiment and extended the analysis from 4 to 7dpf. *In vivo* confocal microscopy was performed using the transgenic line 'tg(mbp:nls-eGFP)' which labels the nuclei of myelinating glia.

The field of view was centred at the level of the cloaca, providing a consistent region of imaging roughly midway between anterior and posterior spinal cord. The total number of OL cell nuclei in the ventral and dorsal spinal cord within the field of view were quantified for each image and compared between genotypes at each timepoint. OL numbers were significantly reduced by 42% at 4dpf (p = 0.01, Kruskal-Wallis test with Dunn's multiple comparisons test) and 25% at 5dpf (p = 0.02. one-way ANOVA with Tukey's multiple comparisons) in Myrf$^{-/-}$ mutants compared to wild type siblings. Numbers of OLs appeared to recover between 6 and 7dpf although they remained lower than that of their siblings at all time points tested. Other than the obvious effect on OL number, the intensity of OL nuclei expressing GFP was visibly reduced in mutants compared to siblings (see homozygous panel in Figure 3.9) consistent with downregulation of Mbp (the promotor of which is used to drive GFP expression) in these myelinating OLs. The implications of using this transgenic line will be discussed at the end of this chapter.

This experiment demonstrated that Myrf$^{-/-}$ mutants display a reduction in the number of mature OLs in the spinal cord at early larval stages, corroborating early findings (Figure 3.5). However, OL number appear to recover by 7dpf. Additionally, the effect

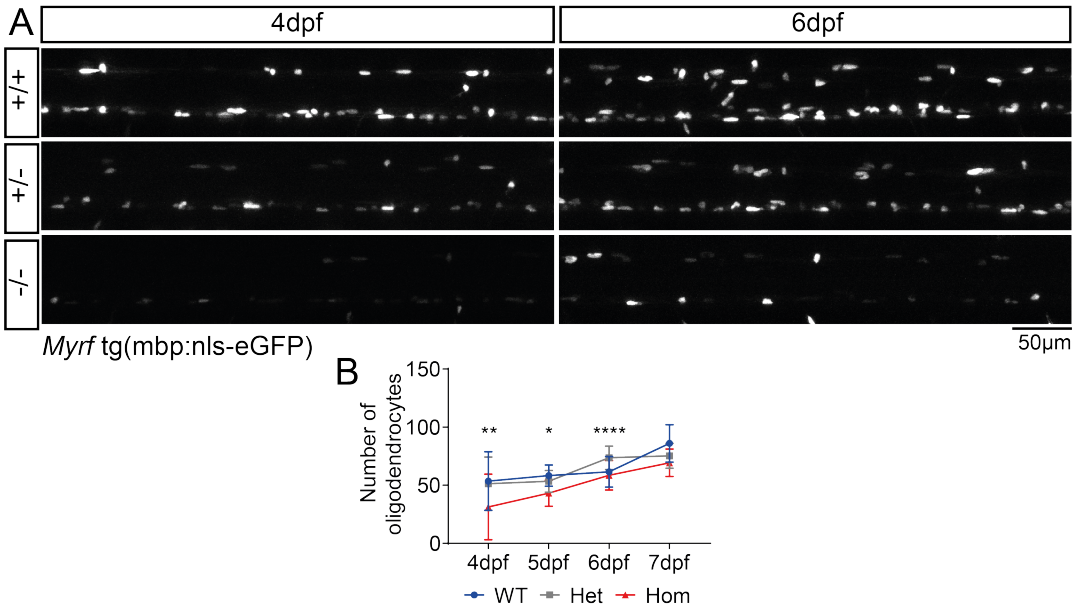

Figure 3.9: Quantification of oligodendrocyte number in the spinal cord from 4-7dpf
(A.) Confocal images showing a lateral view of the spinal cord at 4 and 6dpf across genotypes in the Myrf tg(mbp:nls-eGFP) transgenic line. **(B.)** Number and intensity of OLs is reduced at 4 and 5dpf, with recovery by 7dpf. At 4dpf numbers of OLs are 48.50 (34 to 62.50) in wild types, 40.09 (40.00 to 56.00) in heterozygotes and 26.00 (15.75 to 33.75) in homozygous mutants (p = 0.002, Kruskal-Wallis test. Dunn's multiple comparisons: WT-Het p = >0.99, WT-Hom p = 0.01, Het-Hom p = 0.003). At 5dpf number of OLs are: 58.33 ± 9.15 in wild types, 53.43 ± 9.32 in heterozygotes, 43.20 ± 11.38 in homozygous mutants (F (2,25) = 4.00, p = 0.03, one-way ANOVA. Tukey's multiple comparisons: WT-Het p = 0.47, WT-Hom p = 0.02, Het-Hom p= 0.1). At 6dpf number of OLs are: 58.88 ± 14.39 in wild types, 68.61 ± 12.48 in heterozygotes and 50.11 ± 15.50 in homozygous mutants (F (2,54) = 10.47, p = 0.0001, one-way ANOVA. Tukey's multiple comparisons: WT-Het p = 0.18, WT-Hom p = 0.30, Het-Hom p = <0.0001). Numbers of OLs at 7dpf are: 86.00 ± 16.02 in wild types, 75.33 ± 10.70 in heterozygotes and 69.33 ± 11.79 in homozygous mutants (F (2,21) = 3.12, p = 0.07, one-way ANOVA). N = 10 WT, N = 15 Het, N = 12 Hom at 4dpf; N = 9 WT, N = 14 Het, N = 5 Hom at 5dpf; N = 8 WT, N = 31 Het, N = 18 Hom at 6dpf, N = 9 WT, N = 9 Het, N = 6 Hom at 7dpf. Images obtained using a 20x objective. Asterisks indicate the results of a one-way ANOVA between groups prior to multiple comparisons.

size at 4 and 5dpf in this dataset is lower than that observed on initial characterisation of this mutant allele (69% reduction in OL number). This may be explained by loss of phenotype severity with subsequent generations of mutant fish, as the initial allele characterisation data (Section 3.3.1) was collected at early generational stages of the mutant line. Targeted mutagenesis using CRISPr/Cas9 technology can lead to additional undetectable off-target mutations which may have a synergistic effect on the observed phenotype. Over time, as these initial lines are outbred these off-target mutations should be lost. **For this reason, all subsequent experiments were performed on offspring from third generation (at least) parents**.

Following completion of this experiment, a Vertebrate Automated Screening Technology (VAST) system was established in the laboratory (Early et al., 2018). This imaging system allows automated, high throughput imaging and semi-automated analysis of myelination across the entire spinal cord. I took advantage of this system to corroborate the current findings and assess OL distribution throughout the spinal cord.

Automated imaging of the entire spinal cord

The VAST system allows fully automated imaging of an entire 96 well plate of larvae, permitting high throughput and uniform experiments. Ninety-six larvae (one per well) were imaged at each timepoint (4, 5 and 6dpf) and their tissue retained for genotyping. Semi-automated cell counts of the entire dorsal spinal cord were performed using published custom written scripts (Early et al., 2018). Initially, only the dorsal spinal cord cell numbers were compared between groups as cells are more sparse and easier to distinguish from each other at this level. At 4dpf, the number of OLs was reduced in Myrf$^{-/-}$ mutants by approximately 38% compared to wild type siblings ($p = <0.0001$, one-way ANOVA followed by Tukey's multiple comparisons test) (Figure 3.10). A similar reduction (35%) in OL number was maintained at 5dpf ($p = 0.006$, one-way ANOVA followed by Tukey's multiple comparisons), but started to recover by 6dpf when only a 12% reduction in OL number was present ($p = 0.05$, one-way ANOVA). At each time point heterozygous siblings displayed similar numbers of OLs to wild type siblings. There is a large degree of variability in OL number within groups, however the standard deviation values are broadly similar across groups at each time point.

During the analysis of TEM data, which will be presented in a subsequent sections (see Section 3.3.8), a dorsal/ventral difference in the severity of hypomyelination in the spinal cord was identified in 6dpf larvae: in the ventral spinal cord, a 73% reduction in the number of myelinated axons was observed compared to a 45% reduction in the dorsal tract. Knowing this, I returned to the current imaging datasets to establish whether a similar difference in OL number existed between the dorsal and ventral tracts of the spinal cord, which could contribute to the observed hypomyelination phenotype. OL numbers were counted in the ventral spinal cord of animals using the 6dpf cohort. In agreement with the TEM data, the effect size in the ventral spinal cord (27% reduction

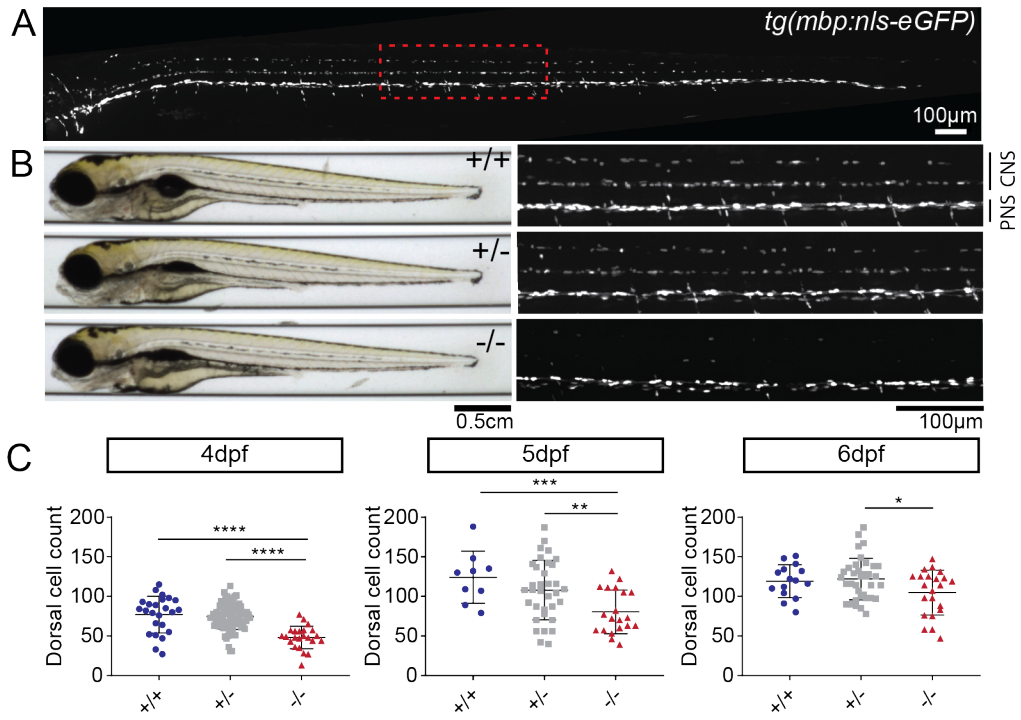

Figure 3.10: Automated imaging of the entire spinal cord using VAST
(A.) Overview of transgenic line tg(mbp:nls-eGFP). Red dashed box outlines the region of the spinal cord shown in (B.), roughly half way along its length. **(B.)** Left: Bright field images of wild type, heterozygous and homozygous mutant larvae at 4dpf. Right: region delineated by red dashed box in (A.). **(C.)** Quantification of OL number in the dorsal spinal cord only. **4dpf**: OL number was reduced by 38% from 77.08 ± 23.15 OLs in wild types, 74.69 ± 16.24 OLs in heterozygotes to 48.17 ± 14.27 OLs in homozygous mutants (F (2,129), p = <0.0001, one-way ANOVA. Tukey's multiple comparisons: WT-Het ns, WT-Hom p = <0.0001, Het-Hom p = <0.0001). N = 24 WT, N = 85 Het, N = 23 Hom at 4dpf. **5dpf:** OL numbers were reduced by 35% from 124.1 ± 32.9 in wild types, 107.9 ± 37.46 OLs in heterozygotes to 80.5 ± 27.61 OLs in homozygous mutants (F (2,60) = 6.40, p = 0.003, one-way ANOVA. Tukey's multiple comparisons: WT-Het ns, WT-Hom p = 0.006, Het-Hom p = 0.02). N = 9 WT, N = 34 Het, N = 20 Hom at 5dpf. **6dpf:** OL numbers were reduced by 12% from 119.2 ± 20.75 OLs in wild types, 121.9 ± 26.16 in heterozygotes to 104.7 ± 28.35 in homozygous mutants (F (2,70) = 3.13, p = 0.05, one-way ANOVA. Tukey's multiple comparisons: WT-Het ns, WT-Hom ns, Het-Hom p = 0.04). N = 15 WT, N = 36 Het, N= 22 Hom. Percentage reductions are calculated between wild type and homozygous values. Values and error bars represent mean ± standard deviation.

in OLs) was more than double that of the dorsal spinal cord (12% reduction in OL number) (Figure 3.11). When cell counts for the dorsal and ventral tracts were combined, a 21% significant reduction was achieved in Myrf$^{-/-}$ mutants compared to wild type siblings (p = <0.0001, one-way ANOVA followed by Tukey's multiple comparisons). In summary of these results, Myrf$^{-/-}$ mutants demonstrate a reduction in OL number relative to wild type siblings across all time points tested, with a more severe reduction in OL number observed in the ventral spinal cord at 6dpf.

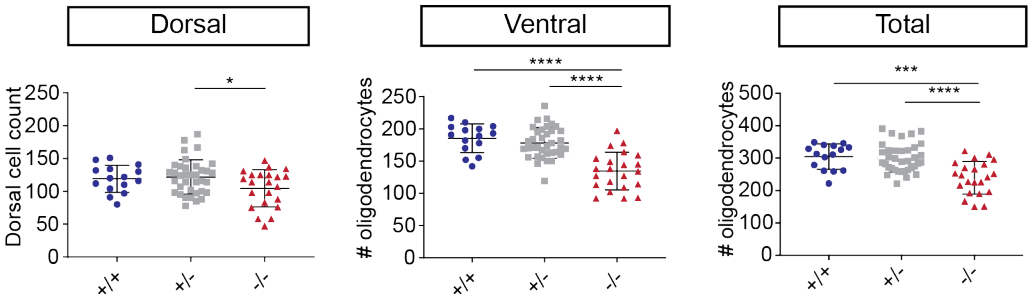

Figure 3.11: Quantification of oligodendrocyte number in the dorsal and ventral tract at 6dpf
Dorsal: Data presented here is the same as 6dpf data in Figure 3.10C. **Ventral:** Myrf$^{-/-}$ mutants possess 27% fewer OLs in the ventral spinal cord than wild type and heterozygous siblings (185.6 ± 22.3 OLs in wild type, 178.3 ± 23.78 OLs in heterozygotes, 134.6 ± 29.24 OLs in homozygous mutants. F (2,70) = 25.75, p = <0.0001, one-way ANOVA. Tukey's multiple comparisons: WT-Het p = 0.62, WT-Hom p = <0.0001, Het-Hom p = <0.0001). **Total:** The sum of ventral and dorsal oligodendrocyte numbers equates to 304.8 ± 39.07 OLs in wild types, 300.2 ± 43.43 OLs in heterozygotes and 239.3 ± 50.48 OLs in homozygous mutants (F(2,70) = 14.83, p = <0.0001, one-way ANOVA. Tukey's multiple comparisons: WT-Het ns, WT-Hom p = 0.0001, Het-Hom p = <0.0001). N = 15 WT, N = 36 Hets, N = 22 Hom for dorsal and ventral OL counts

3.3.7 The number of Schwann cells in the peripheral nervous system is maintained in Myrf$^{-/-}$ mutants

There is no evidence of Myrf expression in the PNS of larval zebrafish as detected by in-situ hybridisation (Appendix 1, Figure 5.1C, provided by Kelly Monk's laboratory, Vollum institute, OHSU) or imaging of transgenic tg(myrf-eGFP) larvae (Treichel and Hines, 2018). However, given our core aim to establish a CNS *specific* model of hypomyelination, it was integral to ensure that the PNS was not affected by our genetic manipulation. As Mbp is expressed in Schwann cells of the PNS, our transgenic reporter tg(mbp:nls-eGFP) conveniently labels nuclei of Schwann cells in addition to OLs (Figure 3.12A). Using the VAST imaging data for the 6dpf cohort, I performed semi-automated cell counts of the posterior lateral line (PLL) which constitutes the PNS of zebrafish. No significant difference in Schwann cell number was detected across genotypes at this time point (Figure 3.12C). In addition, the fluorescent intensity of cell nuclei in the PLL was never observed to be reduced, in contrast to OLs in the spinal cord (Figure 3.12B), although this is a subjective observation that should be quantified in future.

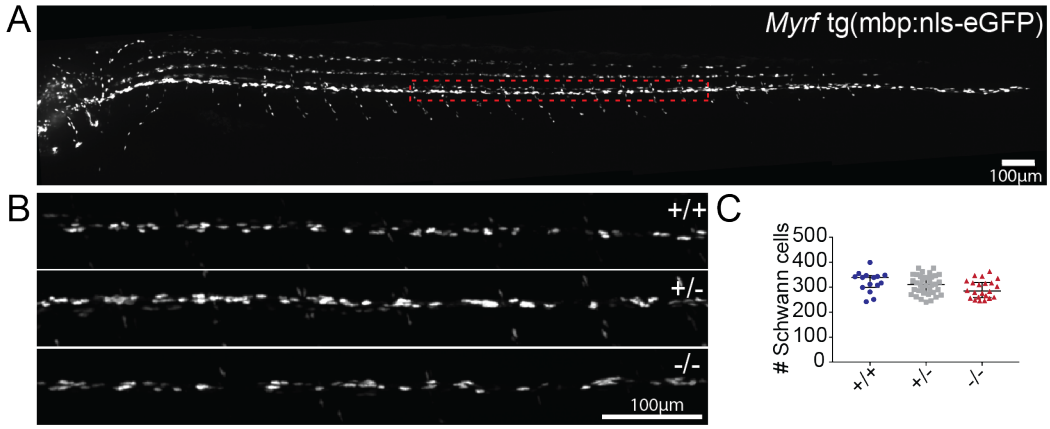

Figure 3.12: Quantification of myelinating Schwann cells in the PNS
(A.) Maximal intensity projection of a larval zebrafish expressing transgene tg(mbp:nls-eGFP) which labels nuclei of myelinating glia in the CNS and PNS. Red dashed box defines regions of PLL presented in (B). **(B.)** Posterior lateral line (PNS) at the level of somite 16 for wild type, heterozygous and homozygous siblings. **(C.)** Quantification of Schwann cell numbers along the the length of PLL in (A): 321.5 ± 41.15 Schwann cells in wild types, 310.1 ± 38.11 Schwann cells in heterozygotes, 292.6 ± 36.53 Schwann cells in homozygous mutants (mean ± standard deviation) ($F(2,70) = 2.74$, $p = 0.07$, one-way ANOVA). N = 15 WT, N = 36 Het, N = 22 Hom.

3.3.8 Myrf$^{-/-}$ mutants display a reduction in the number of myelinated axons in the spinal cord

The current gold standard for the assessment of the number of myelinated axons and myelin sheath thickness/compaction in the CNS is Transmission Electron Microscopy (TEM) (Czopka and Lyons, 2011). Behavioural characterisation in Chapter 4 was performed at 6dpf, when the majority of complex RS-mediated behaviours are present or inducible. By this timepoint, the majority of the RS system is myelinated under normal conditions (Figure 3.1). Thus, to allow direct correlation between the degree of myelination in Myrf$^{-/-}$ mutants and future behavioural phenotypes, TEM was performed on 6dpf larvae. Given that myelin thickness is a key regulator of conduction velocity (Waxman, 1980), I could then use parameters extracted from TEM data to predict how the myelination status of RS neurons might affect behaviour e.g. the thickness of myelin around the Mauthner axon and the latency of the escape response.

Larvae were terminally anaesthetised and processed for TEM at 6dpf (see Materials and Methods). The number of myelinated axons in a single hemi-spinal cord per animal were counted and compared between genotypes. Examples of tiled, hemispinal cord images are provided in Figure 3.13. Myelinated axons are typically found in the

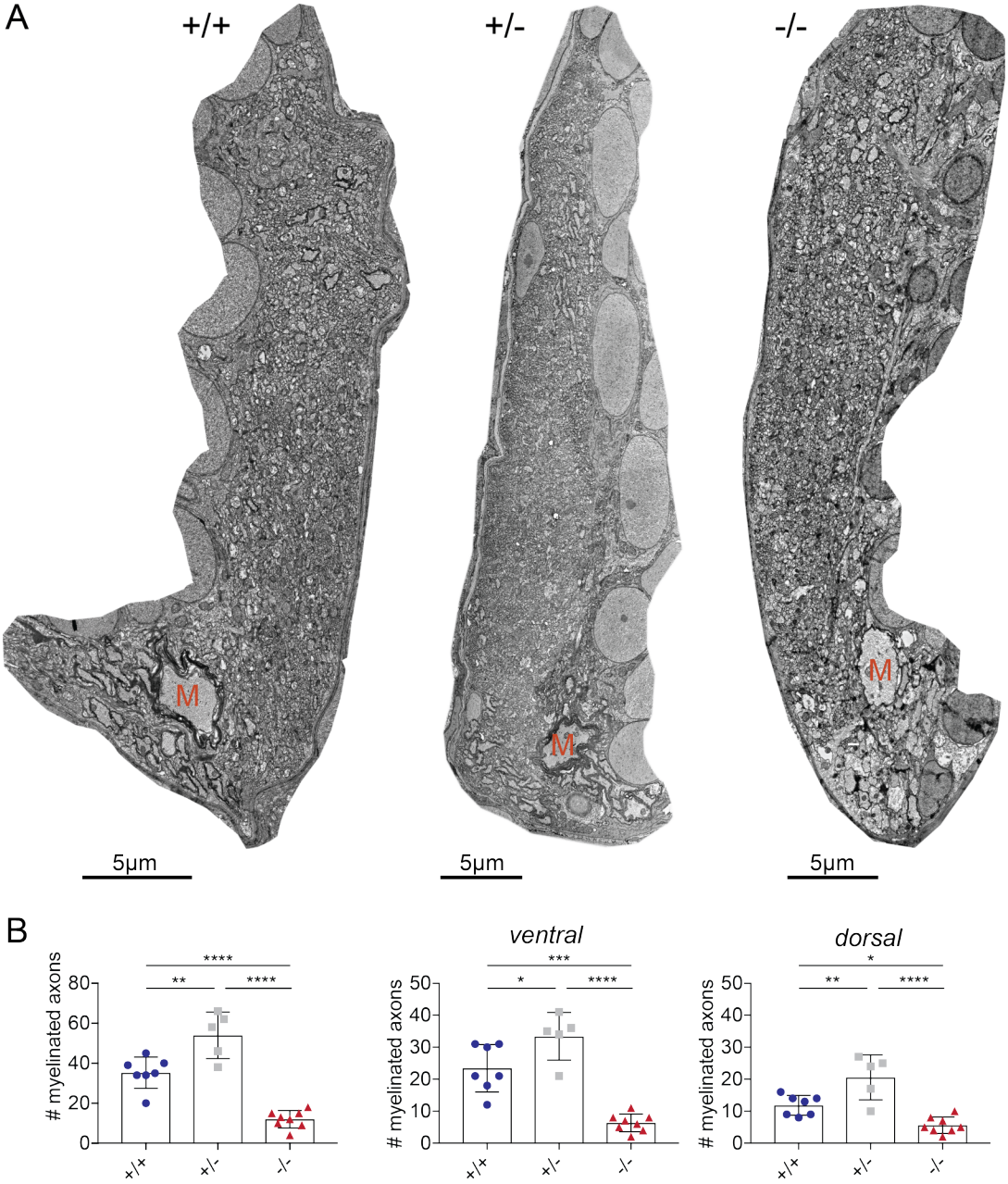

Figure 3.13: Transmission electron microscope images of hemispinal cords. **(A.)** Example images of a hemispinal cord from a wild type, heterozygous and homozygous mutant. M = Mauthner axon. **(B.)** L-R: Total number of myelinated axons per hemispinal cord: 35.29 ± 7.83 wild type, 54.00 ±11.66 in heterozygotes, 12.00 ± 4.34 in homozygous mutants (F (2,17) = 46.10, p = <0.0001, one-way ANOVA. Tukey's multiple comparisons test: WT-Hom p = 0.0021, WT vs Het p = <0.0001, Het-Hom p = <0.0001). **Ventral myelinated axons per hemispinal cord:** 23.43 ± 7.41 wild type, 33.40 ± 4.44 heterozygotes, 6.38 ± 2.77 in homozygous mutants (F (2,17) = 34.42, p = <0.0001, one-way ANOVA. Tukey's multiple comparisons: WT-Het p = 0.03, WT-Hom p = 0.0001, Het vs Hom p = <0.0001). **Dorsal myelinated axons per hemispinal cord:** 11.86 ± 3.13 wild type, 20.6 ± 7.02 heterozygotes, 6.62 ± 2.56 homozygous mutants (F (2,17) = 19.45, p = ¡0.0001, one-way ANOVA. Tukey's multiple comparisons: WT-Het p = 0.007, WT-Hom = 0.03, Het-Hom p = <0.0001). N = 7 WT, N = 5 Het, N = 8 Hom.

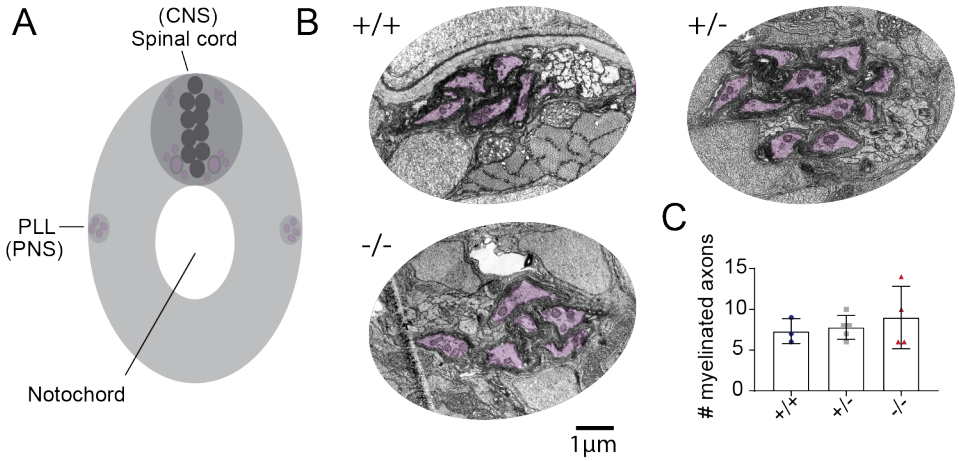

Figure 3.14: Transmission electron microscope images of the PNS
(A.) Schematic of a transverse section across a larval zebrafish at the level of the cloaca demonstrating the location of the posterior lateral line (PNS) relative to the spinal cord (CNS) **(B.)** Transverse TEM images of the posterior lateral line. Myelinated axons are highlighted in purple. **(C.)** Quantification of the number of myelinated axons present in the PLL. 7.33 ± 1.53 myelinated axons in wild type, 7.80 ± 1.48 myelinated axons in heterozygotes and 9.00 ± 3.83 myelinated axons in homozygous mutants (mean ± standard deviation) ($F(2,9) = 0.43$, $p = 0.67$, one-way ANOVA). N = 3 WT, N = 5 Het, N = 4 Hom. All data collected at 6dpf. Error bars for figures represent mean ± standard deviation.

reticulospinal tracts of the dorsal and ventral spinal cord. It is important to note that the majority of large caliber axons in the ventral spinal cord belong to RS neurons - those which mediate the behaviours I will assess in Chapter 4. Quantification of all myelinated axons in a hemispinal cord revealed that $Myrf^{-/-}$ mutants displayed a 66% reduction in myelinated axons compared to wild type siblings ($p = <0.0001$, one-way ANOVA followed by Tukey's multiple comparisons test). Surprisingly, $Myrf^{+/-}$ mutants possessed 53% more myelinated axons than their wild type siblings ($p = 0.0021$, one-way ANOVA followed by Tukey's multiple comparisons), and an even greater increase (78%) when compared to $Myrf^{-/-}$ siblings ($p = <0.0001$, Tukey's multiple comparisons). This difference cannot be explained by a batch effect because animals from the same clutch span all genotype groups. This finding was specific to the CNS, as the numbers of myelinated axons in the PNS were similar across groups (Figure 3.14C) ($p = 0.67$, one-way ANOVA). Interestingly, Mbp transcript levels were previously found to be mildly elevated (non significant) in $Myrf^{+/-}$ mutants relative to wild type siblings (Figure 3.7). This raised the intriguing question as to whether a gain of function mechanism could be at play in the heterozygous group.

The effect of hypomyelination is more severe in the ventral tract of the spinal cord

When analysis was split between dorsal and ventral regions of the spinal cord an unexpected finding was revealed. The effect size of the reduction in myelinated axon number was almost doubled in the ventral spinal cord, where mutants possess a 73% reduction in the number of myelinated axons relative to wild type siblings ($p = 0.0001$, one-way ANOVA with Tukey's multiple comparisons). In comparison, homozygous mutants exhibit a 45% reduction in myelinated axons in the dorsal spinal cord relative to wild types ($p = 0.03$, one way ANOVA with Tukey's multiple comparisons). Thus, the number of OLs (Figure 3.11) and number of myelinated axons (Figure 3.13B) are reduced in Myrf$^{-/-}$ mutants, with the *ventral* spinal cord more severely affected than the dorsal. Interestingly, this regional effect appears to be reversed for heterozygous mutants which possess 74% more myelinated axons than their wild type siblings in the *dorsal* spinal cord ($p = 0.007$, one-way ANOVA followed by Tukey's multiple comparisons). In the ventral spinal cord, a 43% increase in the number of myelinated axons is observed in heterozygotes compared to wild types ($p = 0.03$, one-way ANOVA followed by Tukey's multiple comparisons). This regional difference was surprising given that at the same timepoint the number of myelinating OLs is constant between heterozygous and wild type siblings (Figure 3.11). For an increase in the number of myelinated axons to be observed on TEM without a corresponding change in the number of myelinating OLs, the myelinating capacity of individual oligodendrocytes has to be greater. This could be achieved by increasing the length or number of myelin sheaths produced by each OL. This will be assessed in Section 3.3.12.

3.3.9 The large caliber Mauthner axons are hypomyelinated in Myrf$^{-/-}$ mutants

On initial assessment of TEM images, myelin sheaths generally appeared thinner in Myrf$^{-/-}$ mutants with a small minority of axons demonstrating preserved myelin thickness (see Figure 3.16). To quantify myelin thickness I calculated the g-ratio for myelinated axons on a subset of TEM images that I deemed to have optimal tissue preservation. G-ratio is normally determined using axon diameter, however this assumes circularity of axons which if often not the case in fixed larval zebrafish tissue. Therefore, g-ratio was calculated using the following equation, in which diameter has been replaced with area:

$$g - ratio = \frac{area\ of\ axon}{area\ of\ myelinated\ axon}$$

To determine g-ratio, the perimeter of the axon (inside the myelin sheath) and the perimeter of the myelinated axon (including the myelin sheath) were traced and the area calculated using ImageJ (NIH, Bethesda, USA) measure tool (see Materials and Methods, Figure 2.3). Area values were then input into the equation above and g-ratio calculated for each myelinated axon. As the Mauthner axon is unique in its morphology - it has a very large axon caliber - from other axons in the ventral spinal cord, I have segmented the analysis of myelin thickness and axon caliber for Mauthner and non-Mauthner axons (Mauthner analysis: Figure 3.15; non-Mauthner axons: Figure 3.16 and 3.17). Myrf$^{-/-}$ Mauthner axons displayed a striking reduction in the thickness of their surrounding myelin (Figure 3.15A): the average g-ratio was 67% and 77% higher than that for wild type and heterozygous siblings respectively ($p = 0.0001$, one-way ANOVA) (Figure 3.15B, g-ratio). This finding was supported by the calculation of myelin thickness as the area of the myelinated axon minus the area of the axon. Here, Myrf$^{-/-}$ mutants demonstrated a 83% decrease in myelin sheath thickness relative to wild type sibligns ($p = <0.0001$, one-way ANOVA followed by Tukey's multiple comparisons) (Figure 3.15B, myelin thickness). Interestingly, in this analysis heterozygotes displayed a subtle yet significant 20% reduction in myelin sheath thickness in comparison to wild type siblings ($p = 0.02$, one-way ANOVA followed by Tukey's multiple comparisons). Despite severe hypomyelination of the Mauthner axons in Myrf$^{-/-}$ mutants, axon calibers (area) were not significantly different across groups. However,

the degree of variability in axon caliber in the homozygous group could reflect a subtle effect of hypomyelination on the regulation of axon caliber (Figure 3.15B, axon caliber).

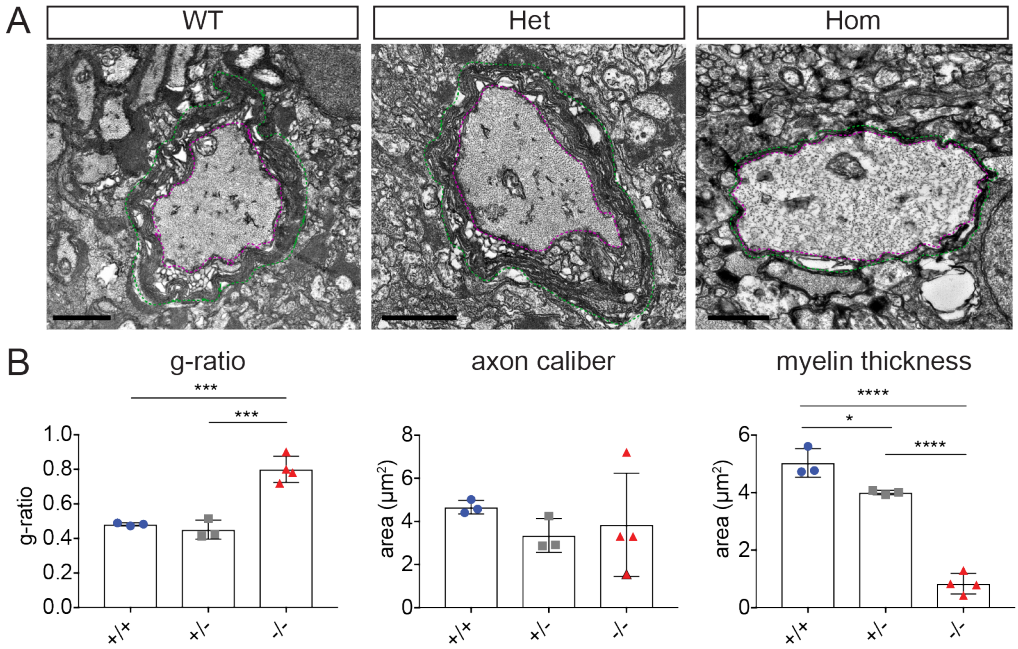

Figure 3.15: Large caliber Mauthner axons exhibit reduced myelin thickness **(A.)** High magnification images of the Mauthner axon from a wild type, heterozygous and homozygous mutant. The magenta line delineates the perimeter of the axon. Green dashed line delineated the perimeter of the myelinated axon. Scale bar = 1 micron. **(B.) G-ratio:** The average g-ratios for Mauthner are 0.48 ± 0.009 in wild types, 0.45 ± 0.06 in heterozygotes and 0.80 ± 0.08 in homozygous mutants (F (2,7) = 39.96, p = 0.0001, one-way ANOVA. Tukey's multiple comparisons: WT-Het ns, WT-Hom p = 0.0004, Het-Hom p = 0.0003). **Axon caliber:** Average axon calibers presented as the area of the axon are 4.67 ± 0.31μm^2 in wild types, 3.35 ± 0.78μm^2 in heterozygotes and 3.84 ± 2.40μm^2 in homozygous mutants (F (2,7) = 0.50, p = 0.63, one-way ANOVA). **Myelin sheath thickness:** The average thickness of myelin sheaths surrounding Mauthner are 5.03 ± 0.50μm^2 in wild types, 4.00 ± 0.08μm^2 in heterozygotes and 0.84 ± 0.36μm^2 in homozygous mutants (F (2,7) = 135.2, p = <0.0001, one-way ANOVA. Tukey's multiple comparisons: WT-Het p = 0.02, WT-Hom p = <0.0001, Het-Hom p = <0.0001). **(C.)** G-ratio plotted against axon area (μm^2) for the Mauthner axons from each genotype. One Mauthner axon per fish, N = 3 WT, N = 3 Het, N = 4 Hom. Values and error bars represent mean ± standard deviation.

3.3.10 Myelination of non-Mauthner axons is compromised in Myrf$^{-/-}$ mutants

Performing the same assessment on the remainder of myelinated axons in the spinal cord did not reveal such striking differences. Here, Myrf$^{-/-}$ mutants display a modest but non-significant increase in the average g-ratio ($p = 0.19$, one-way ANOVA) and reduction in myelin sheath thickness (area) ($p = 0.17$, one-way ANOVA) (both Figure 3.16D). To assess distribution of g-ratio data, g-ratios were plotted as a function of axon area (Figure 3.16B). When plotted in this way, the distribution of g-ratios is similar between groups, with homozygous data nestled within sibling values. However, when linear regression is performed there is a slightly steeper relationship between the increase in g-ratio with axon area in Myrf$^{-/-}$ mutants ($R^2 = 0.25$ homozygous mutants, $R^2 = 0.21$ in heterozygous siblings, $R^2 = 0.02$ in wild type siblings), indicating that larger caliber axons possess thinner myelin sheaths. This would be consistent with the finding from the Mauthner axon analysis (Figure 3.15). To test this, I split the data into small caliber ($<0.3\mu$m) and large caliber ($>0.3\mu$m) axons and compared their respective g-ratios between groups. Remarkably, segmenting the data in this way revealed a significant increase in g-ratio in large caliber axons in Myrf$^{-/-}$ mutants relative to wild type ($p = <0.0001$, one-way ANOVA followed by Tukey's multiple comparisons) and heterozygous ($p = <0.003$, one-way ANOVA followed by Tukey's multiple comparisons) siblings (Figure 3.16C). Interestingly, although there was no significant difference between g-ratios in the small caliber axons ($p = 0.52$, Kruskal-Wallis test), a proportion of axons within the heterozygous group display lower g-ratios consistent with thicker myelin sheaths.

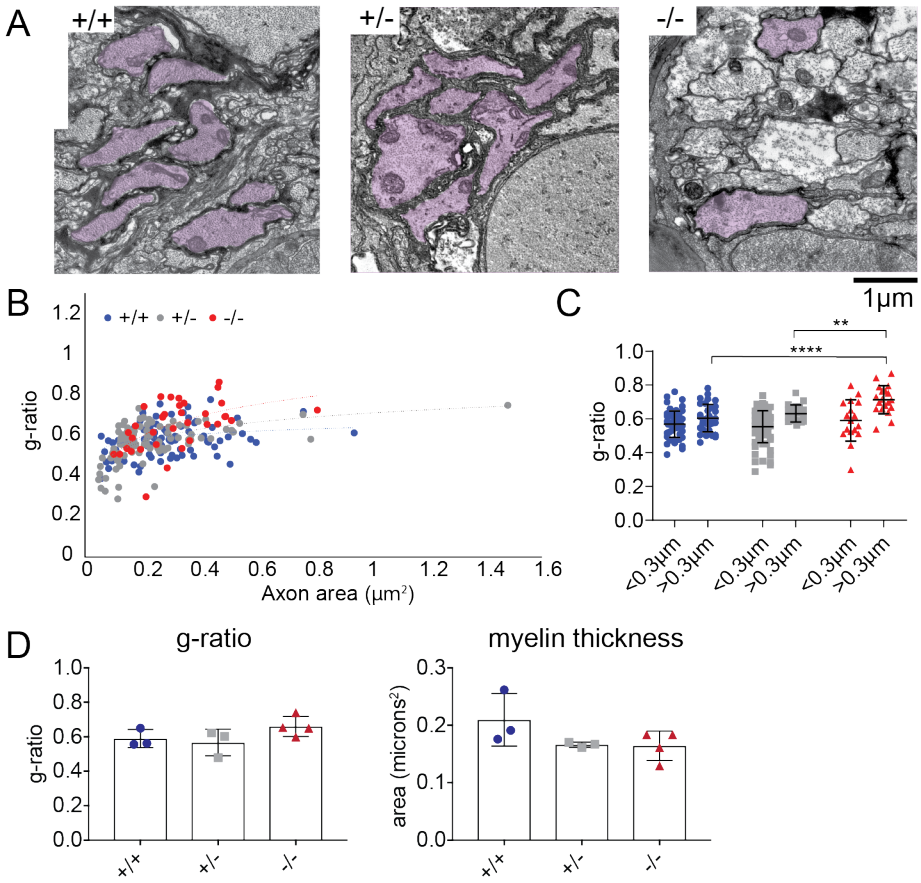

Figure 3.16: Quantification of non-Mauthner myelin sheath thickness
(A.) Example TEM images of non-Mauthner axons in a region of the ventral spinal cord. Myelinated axons are highlighted in purple. **(B.)** G-ratio plotted against axon caliber (not including Mauthner). Wild type: n = 86 myelinated axons, N = 3; Heterozygotes: n = 92 myelinated axons, N = 3; Homozygous mutants: n= 36 myelinated axons, N = 4. **(C.)** Comparison of g-ratios for small (<0.3μm) and large caliber (>0.3μm) axons. No significant difference in the g-ratio of small caliber axons is detected (median (IQR): 0.57 ± (0.52 to 0.62) in wild types, 0.56 (0.51 to 0.62) in heterozygotes, 0.59 (0.52 to 0.70) in homozygous mutants. p = 0.52, Kruskal-Wallis test). G-ratio for larger caliber axons is significantly larger in homozygous mutants (mean ± standard deviation: 0.60 ± 0.08 in wild types, 0.63 ± 0.05 in heterozygotes and 0.71 ± 0.08 in homozygous mutants. F (2,69) = 12.99, p = <0.0001. Tukey's multiple comparisons: WT-Het ns, WT-Hom p = <0.0001, Het-Hom p = 0.003). **(D.) Average g-ratio**: 0.59 ± 0.05 wild type, 0.57 ± 0.08 heterozygotes, 0.66 ± 0.06 homozygous mutants (F (2,7) = 2.14, p = 0.19, one-way ANOVA). **Myelin thickness:** 0.21 ± 0.05 microns^2 in wild type, 0.17 ± 0.005 microns^2 in heterozygotes, 0.16 ± 0.03 microns^2 in homozygous mutants. (F (2,7) = 2.35, p = 0.17, one-way ANOVA). Values and error bars represent mean ± standard deviation. N = 3 WT N = 3 Het, N = 4 Hom.

3.3.11 Axon caliber and myelination status in non-Mauthner axons

Axon caliber growth and myelination are tightly linked mechanisms in the CNS. As much as axon caliber can influence the degree of myelination (Blakemore, 1973), trophic support from the sheath during radial axon growth may also influence the axon caliber. Given the severely reduced levels of myelination in homozygous mutants it was vital to inspect the axons for morphological defects which could act as a confounding factor in future behavioural analysis.The perimeters of the 30 largest axons ("top 30") in one hemispinal cord, regardless of myelination status, were traced and the axonal area (caliber) calculated as before. The distribution of all axon areas was similar across genotypes (Figure 3.17A) and no difference was observed when comparing mean axon caliber between groups (Figure 3.17B, Top 30) ($p = 0.93$, one-way ANOVA). There was no significant difference in the caliber of *myelinated axons* when plotted as an average per fish ($p = 0.45$, one-way ANOVA) (Figure 3.17C, myelinated), however, this is a crude analysis given the variability in axon caliber observed in the CNS. Indeed, when the caliber of all myelinated axons was plotted as a cumulative sum distribution plot (Figure 3.17B) it was surprising to see that the frequency of small caliber axons that were myelinated was significantly increased in heterozygous mutants compared to wild type and homozygous siblings (both $p = <0.0001$, Kolmogorov-Smirnov test). In contrast, no difference in the caliber of myelinated axons was observed between wild types and homozygous mutants ($p = 0.12$, Kolmogorov-Smirnov test). The discovery that heterozygous mutants myelinate a larger frequency of small caliber axons, alongside a higher overall number of myelinated axons (Figure 3.13), particularly in the dorsal spinal cord, is consistent with precocious (excessive) myelination. This notion is supported by the finding that 100% of the "top 30" axons are myelinated in heterozygotes, suggesting that they finish myelinating all the large caliber axons in the spinal cord and then turn their attention to the smaller ones. In contrast, the proportion of "top 30" axons that are myelinated is reduced by 58% in Myrf$^{-/-}$ mutants (Figure 3.17C, top 30 myelinated).

In summary of the TEM analysis, Myrf$^{-/-}$ mutants exhibit a striking reduction in the number of the myelinated axons in the spinal cord, with a larger effect in the ventral spinal cord where the axons of RS neurons are located. Among the remaining myelinated axons, large caliber axons including the Mauthner axons, are more severely

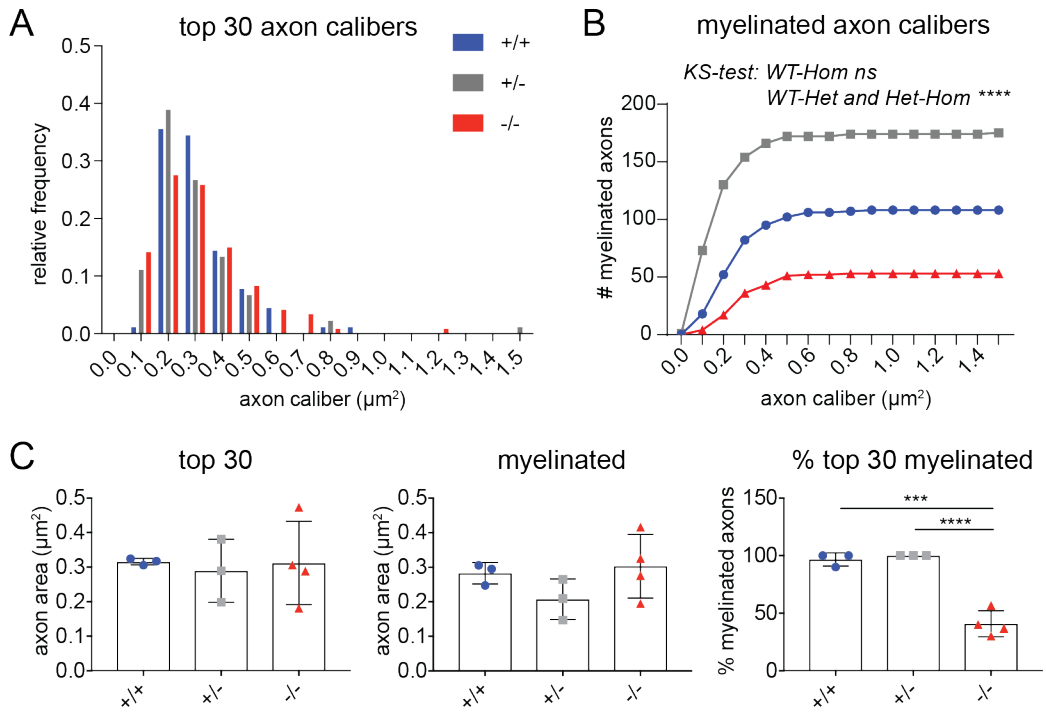

Figure 3.17: Axon caliber and myelination status of non-Mauthner axons **(A.)** Histogram displaying the relative frequency of axon diameters for the top 30 largest axons in the hemispinal cord. Wild type: n = 90 axons from N = 3 larvae, heterozygotes: n = 90 axons from N = 3 larvae, homozygous mutants: n = 120 axons from N = 4 larvae. **(B.)** Cumulative sum of the number of myelinated axons across axon calibers (includes myelinated axons excluded from g-ratio analysis due to poorly preserved / misshapen myelin). Wild type: n = 108 axons from N = 3 larvae, Heterozygotes: n = 175 axons from N = 3 larvae, Homozygotes: n = 53 axons from N = 4 larvae (p = <0.0001 WT-Het, p = 0.12 WT-Hom, Kolmogorov-Smirnov test). **(C.) Top 30**: The average caliber of the top 30 largest axons in one hemispinal cord was 0.32 ± 0.01 μm^2 in wild types, 0.29 ± 0.09 μm^2 in heterozygotes and 0.31 ± 0.12 μm^2 in homozygous mutants (F (2,7) = 0.07, p = 0.93, one-way ANOVA). **Myelinated**: The average caliber of all myelinated axons in the hemispinal cord was 0.29 ± 0.03 μm^2 in wild types, 0.21 ± 0.06 μm^2 in heterozygotes and 0.30 ± 0.09 μm^2 in homozygous mutants (F (2,7) = 1.69, p = 0.25, one-way ANOVA). **Top 30 axons myelinated**: The percentage of the "top 30" largest axons the hemispinal cord which are myelinated is 96.67 ± 5.77% wild type, 100.0 ± 0% in heterozygotes and 40.83 ± 11.34% in homozygous mutants (F (2,7) = 61.47, p = <0.0001, one-way ANOVA. Tukey's multiple comparisons: WT-Het ns, WT-HOM = 0.0001, Het-Hom p = <0.0001). Values and error bars represent mean ± standard deviation

hypomyelinated than their smaller counterparts. Importantly, axon caliber on the whole appeared to be unaffected by the hypomyelination phenotype. The unexpected finding that heterozygous mutants possess a higher number of myelinated axons, due to the precocious myelination of smaller caliber axons, is intriguing to say the least. Assessment of single cell myelinating capacity will be important to reveal the potential mechanism responsible for this phenotype.

3.3.12 Assessment of the myelinating capacity of individual oligodendrocytes

The disparity between the 66% reduction in the number of myelinated axons and the 21% reduction in total OL number in the spinal cord at 6dpf suggests that the myelinating capacity of OLs must be compromised in Myrf$^{-/-}$ mutants. To explore this idea, single OL morphologies were first assessed in the dorsal spinal cord. Here, it is more feasible to image cells in isolation of one another and quantify myelin sheath length and number per cell with confidence. However, given the severity of phenotype in the ventral spinal cord it will be necessary to perform equivalent experiments in the ventral spinal cord in future. To image single OLs, the DNA construct tg(mbp:mCherry-caax) was injected into the single cell stage of embryos, providing mosaic labelling of individual OLs in the spinal cord. Using *in vivo* confocal imaging at two time points, 4dpf (early myelination) and 6dpf (established myelination), OLs were assessed for their number, length and quality of sheaths.

Myelinating capacity is reduced in Myrf$^{-/-}$ mutants at 4dpf

When the number and length of myelin sheaths per OL were compared between genotypes at 4dpf no significant difference was observed. However, when total myelin per cell (sheath length x sheath number) was calculated, a 35% reduction was observed in Myrf$^{-/-}$ mutant OLs relative to wild types ($p = 0.04$, one-way ANOVA followed by Tukey's multiple comparisons)(Figure 3.18C). Interestingly, at this timepoint single OLs from heterozygous siblings produced 32% more myelin than their wild type siblings ($p = 0.05$, one-way ANOVA followed by Tukey's multiple comparisons). Although this data was collected an earlier developmental timepoint, it supports the precocious myelination phenotype observed on TEM at 6dpf. As a high degree of heterogeneity in sheath length can exist within the same OL (Czopka et al., 2013), an alternative approach to assessing sheath length data is to plot all sheaths from every cell in a frequency distribution histogram as seen in Figure 3.18B. When data was displayed in this way the distribution of myelin sheath lengths was shifted towards lower values in Myrf$^{-/-}$ mutants, consistent with a larger proportion of shorter sheaths. In summary of this data, subtle reductions in myelin sheath number and length contribute to a significant reduction in the total amount of myelin produced per OL in Myrf$^{-/-}$ mutants at 4dpf. At this timepoint, heterozygous mutants began to show signs of an increased ca-

pacity for myelination, evident as a trend towards an increase in the number of sheaths formed and a significant increase in the total myelin produced per cell.

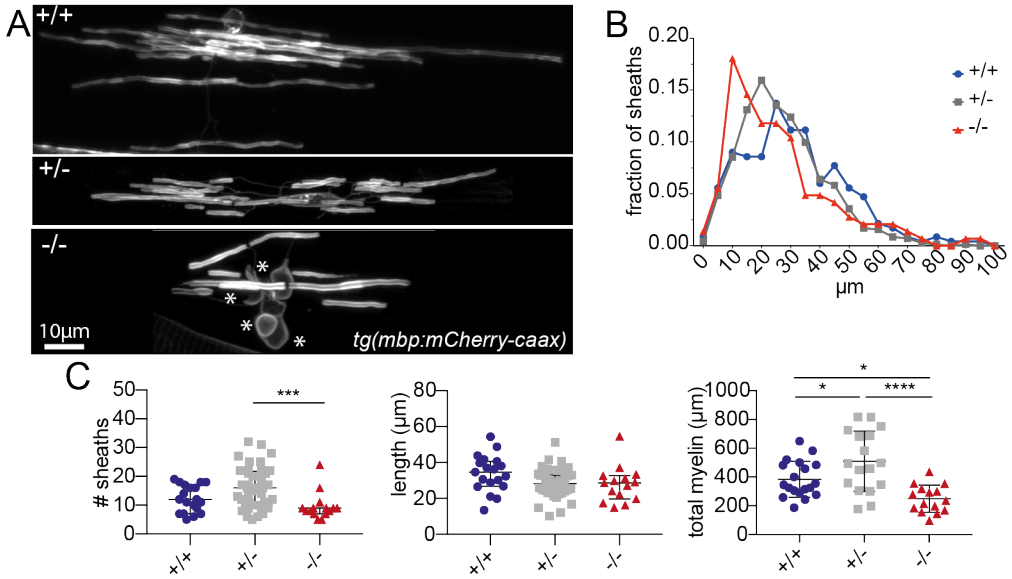

Figure 3.18: Morphology of single oligodendrocytes at 4dpf
(A.) Representative images of wild type, heterozygous and homozygous single oligodendrocytes mosaically labelled with tg(mbp:mCherry-caax). Asterisks in the homozygous image label myelinated profiles which are occasionally observed in homozygous cells. **(B.)** Histogram displaying relative frequency of sheath lengths. n = 233 wild type myelin sheaths, n = 702 heterozygote myelin sheaths, n = 144 homozygous myelin sheaths. **(C.)** L-R **Myelin sheath number:** Number of myelin sheaths is significantly different across groups (p = 0.0009, Kruskal-Wallis test. Dunn's multiple comparisons test: WT-Het p = 0.18, WT-Hom p = 0.30, Het-Hom p = 0.0008). Wild type, heterozygous and homozygous mutants possess 12 (7 to 17), 16 (10.25 to 21.75), 9 (7 to 9) myelin sheaths per cell respectively. **Myelin sheath length:** Average sheath length per cell is not significantly different across groups (p = 0.07, Kruskal-Wallis test). Average sheath length reaches 34.62 (26.78 to 40.55) in wild types, 28.64 (24.12 to 32.93) in heterozygotes and 28.56 (19.68 to 32.6) microns in homozygous mutants. Values and error bars represent median (IQR) for myelin sheath number and length. **Total myelin:** The average total of myelin produced per cell equated to 384.7 ± 124.8 in wild types, 509.1 ± 210.4 in heterozygotes, 250 ± 94.22 in homozygous mutants (F (2,48) = 11.55, p = <0.0001, one-way ANOVA. Tukey's multiple comparisons: WT-Het p = 0.05, WT-Hom p = 0.04, Het-Hom p = <0.0001). Values and error bars represent mean ± standard deviation for total myelin. N = 19 WT, N = 44 Het, N = 15 Hom.

Myelinating capacity is reduced in Myrf$^{-/-}$ mutants at 6dpf

Similar patterns of myelin sheath morphology were observed at the 6dpf timepoint. Myrf$^{-/-}$ mutants possessed significantly fewer myelin sheaths than heterozygous mutants ($p = 0.0014$, one-way ANOVA followed by Dunn's multiple comparisons) and trended towards a significant reduction in sheath number when compared to wild type siblings ($p = 0.09$, one-way ANOVA followed by Dunn's multiple comparisons) (Figure 3.19C). At this time point single OLs in Myrf$^{-/-}$ mutants displayed a statistically significant 25% reduction in myelin sheath length compared to wild type siblings ($p = 0.0016$, Kruskal-Wallis test followed by Dunn's multiple comparison test). Remarkably, total myelin produced per cell was reduced by 47% in Myrf$^{-/-}$ mutants relative to wild type siblings ($p = 0.0004$, one-way ANOVA followed by Tukey's multiple comparisons) (Figure 3.19C). However, in contrast to single OLs at 4dpf, the difference in myelinating capacity between wild type and heterozygous cells was indistinct. This could suggest that the gain of function observed in heterozygotes is transient, and the effect is diminished by 6dpf by which timepoint wild type cells have reached a similar capacity for myelination. Interestingly, the robust reduction in myelinating capacity in homozygous OLs (47%) is remarkably similar to the reduction in the number of myelinated axons observed in the equivalent (dorsal) tract of the spinal cord on TEM (45%) reduction. Therefore, for the effect size observed in the ventral spinal cord on TEM (73%), I would predict the total myelinating capacity to be more severely affected in homozygous OLs occupying the ventral spinal cord.

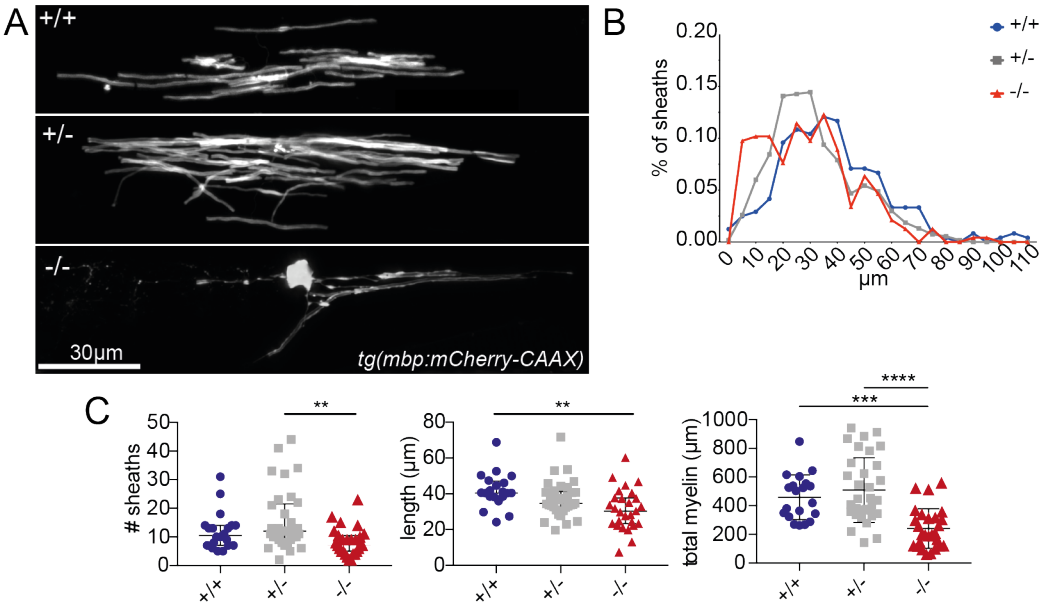

Figure 3.19: Morphology of single oligodendrocytes at 6dpf
(A.) Representative images of wild type, heterozygous and homozygous single oligodendrocytes mosaically labelled with tg(mbp:mCherry-caax). **(B.)** Histogram displaying the relative frequency of sheath lengths. n = 240 wild type myelin sheaths, n = 533 heterozygote myelin shaths, n = 236 homozygous myelin sheaths.**(C.)** L-R **Myelin sheath number:** Myelin sheath numbers are significantly different across groups (p = 0.0019, Kruskal-Wallis test followed by Dunn's multiple comparisons: WT- Het p = >0.999, WT-Hom p = 0.09, Het-Hom p = 0.0014). Wild type, heterozygous and homozygous mutants possess 10.5 (7 to 14), 12 (9 to 21.5) and 7 (5 to 10.5) myelin sheaths per cell respectively. **Myelin sheath length:** The average myelin sheath length per cell differs across groups (p=0.0024, Kruskal-Wallis test followed by Dunn's multiple comparisons: WT-Het p = 0.19, WT-Hom p = 0.0016, Het-Hom p = 0.16). Average sheath lengths are 40.51 (38.23 to 47.01), 34.74 (31.71 to 41.21), 30.37 (23.36 to 37.65) microns in wild type, heterozygous and homozygous mutants respectively. **Total myelin:** The average total myelin produced per cell equated to 458.2 ± 156.4 microns in wild type, 508.6 ± 226.4 microns in heterozygotes and 241.1 ± 138.6 microns in homozygous mutants (F (2,77) = 16.79, p = <0.0001, one-way ANOVA. Tukey's multiple comparisons: WT-Het ns, WT-Hom p = 0.0004, Het-Hom p = <0.0001) N = 20 WT, N = 33 Het, N = 27 Hom.

Myrf$^{-/-}$ oligodendrocytes display abnormal morphology

A number of abnormal sheaths were observed on the blinded assessment of single cell images. Thus, in addition to myelin sheath length and number, I quantified the number of abnormal sheaths per OL and compared these numbers across genotypes at both time points. Abnormal sheaths were defined as sheaths which displayed membrane blebbing, abnormal sheath elongation profiles or patchy GFP expression (suggestive of incomplete wrapping) (Figure 3.20). Abnormal sheaths were occasionally present at 4dpf across all genotypes, but appeared to be more common by 6dpf when on average, Myrf$^{-/-}$ mutants possessed two (median (IQR): 2 (0 to 3)) abnormal sheaths per cell, compared to wild types who possessed zero (median (IQR): 0 (0 to 0)) (Figure 3.20). A two-way ANOVA was used to compare the number of abnormal sheath lengths between genotypes at 4 and 6dpf. No significant effect of age on the number of abnormal sheaths was found ($p = 0.08$) but there is a significant effect of genotype ($p = 0.0003$) with a significant interaction between genotype and age ($p=0.0034$). Following multiple comparisons, this interaction was caused by an increase in the number of abnormal sheaths in homozygous mutants at 6dpf relative to wild type ($p =<0.0001$, Sidak's multiple comparisons test) and heterozygous siblings ($p = <0.0001$, Sidak's multiple comparisons test) at the same age.

Along with the presence of a reduced myelinating capacity at this timepoint (Figure 3.19C), this data suggest that appropriate myelin morphology is not maintained in Myrf$^{-/-}$ mutants over time. However, as different cells were imaged at each time point it is difficult to distinguish whether these cells are formed normally and proceed to degenerate, or whether more abnormal cells are produced at this later stage of myelination. With this in mind, I decided to repeat this experiment but follow the same cells over time and assess their ability to maintain myelin sheaths.

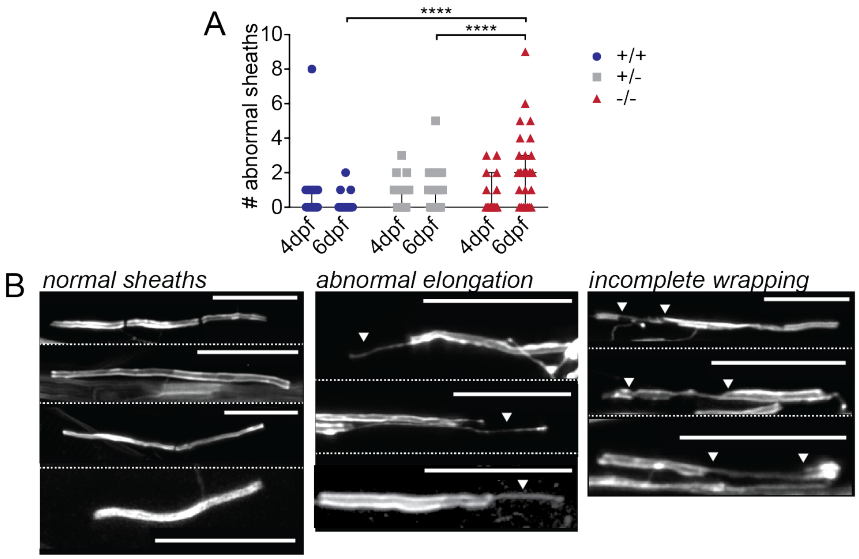

Figure 3.20: Quantification of abnormal myelin sheaths
(A.) Scatter plot displaying the number of abnormal sheaths per genotype at 4 and 6dpf. A two-way ANOVA was performed to compare the number of abnormal sheaths across genotypes at 4 and 6dpf. No significant effect of age was detected ($F(1,152) = 3.10$, $p = 0.08$), a significant effect of genotype ($F(2,152)$, $p = 0.0003$) and an interaction of age and genotype were found ($F(2, 152) = 5.91$, $p = 0.003$). Sidak's multiple comparisons: WT-Hom $p = <0.0001$, Het-Hom $p = <0.0001$ at 6dpf. All other comparisons ns. **Number of abnormal sheaths at 4dpf:** On average, the number of abnormal sheaths per cell reached 0 (0 to 1) in wild types, 0 (0 to 1) in heterozygotes and 0 (0 to 2) in homozygous mutants. N = 19 WT, N = 44 Het, N = 15 Hom. **Number of abnormal sheaths at 6dpf:** On average, the number of abnormal sheaths per cell reached 0 (0 to 0) in wild types, 0 (0 to 1) in heterozygotes and 2 (0 to 3) in homozygous mutants. N = 20 WT, N = 33 Het, N = 27 Hom. Values and error bars represent median and interquartile range. **(B.)** Examples of normal myelin sheaths (left) and abnormal sheaths (middle and right). Scale bars = 20μm. Arrow heads mark regions of abnormality.

3.3.13 Myrf$^{-/-}$ mutant oligodendrocytes exhibit reduced myelin sheath stability

Myrf is known to directly regulate Mbp expression (Bujalka et al., 2013). In agreement with this, I have demonstrated a reduction in Mbp transcript levels (Figure 3.7) and highlighted a reduction in the expression levels of fluorescent protein using the Mbp promotor (Figure 3.10 and 3.6) in the Myrf$^{-/-}$ mutants. Mbp is a core myelin protein which is essential for the compaction of the myelin lamellae and ongoing sheath maintenance (Aggarwal et al., 2013; Snaidero et al., 2017). This is exemplified by Mbp$^{-/-}$ 'Shiverer' mice which exhibit severe CNS hypomyelination and poorly compacted myelin sheaths (Readhead and Hood, L, 1990). Given this information and the over representation of abnormal myelin sheaths observed in Myrf$^{-/-}$ at 6dpf (Figure 3.20), I wanted to estab-

lish whether OLs were able to maintain their myelin sheaths by imaging the same cell over time. To test this I performed time course imaging of the same OL at 4dpf and 6dpf. Under normal conditions, myelin sheaths belonging to OLs imaged at 4dpf may undergo a few retractions or slight changes in length before repeat imaging at 6dpf, but should otherwise remain largely stable (Auer et al., 2018; Czopka et al., 2013). OLs were selected if they demonstrated a dorsal spinal cord location and lacked typical early oligodendrocyte morphology (i.e. many short, nascent myelin sheaths) in order to minimise variability. Sheath length was measured at each time point and used to calculate a growth or shrinkage value for each sheath. These values were then averaged across all sheaths per cell to provide a net growth or shrinkage value per cell. Between 4 and 6dpf, Myrf$^{-/-}$ mutants demonstrated a significant net *shrinkage* of myelin sheath length (mean ± standard deviation: -0.31 ± 4.79 microns) compared to wild type (6.34 ± 3.426 microns, p = 0.0006, Kruskal-Wallis test followed by Dunn's multiple comparisons) and heterozygous siblings (5.17 ± 3.92 microns, p = 0.0019, Kruskal-Wallis test followed by Dunn's multiple comparisons) which demonstrated net *growth* (Figure 3.21D). Homozygous mutants also displayed significantly more sheath retractions per cell than wild type (p = 0.006, one-way ANOVA followed by Tukey's multiple comparisons) and heterozygous siblings (p = 0.004, one-way ANOVA followed by Tukey's multiple comparisons) suggesting that they are unable to maintain their sheaths over time (Figure 3.21D).

In summary of the single cell analysis, Myrf$^{-/-}$ mutant OLs exhibit a reduced capacity to form myelin at 4 and 6dpf and fail to maintain their myelin sheaths between these timepoints, as demonstrated by the abnormal myelin sheath morphology, net shrinkage of myelin sheaths and an increase in the number of sheath retractions. Together with a reduced myelinating capacity of OLs, these findings account for the reduction in myelinated axons observed in the dorsal spinal cord on TEM analysis. Future experiments are required to assess the myelinating capacity of OLs in the ventral spinal cord where we predict the phenotype will be more severe.

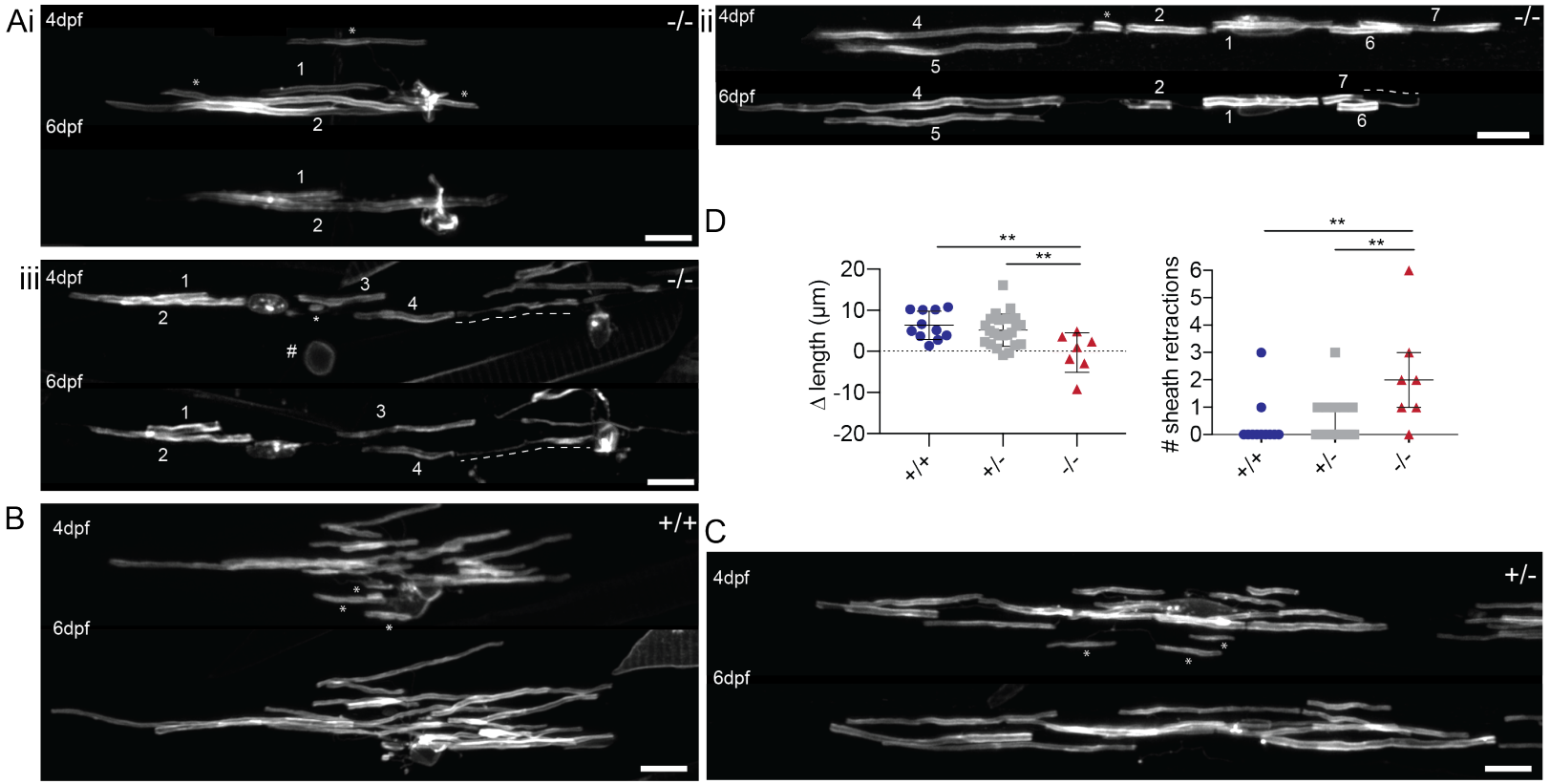

Figure 3.21: Timecourse analysis of single cells between 4 and 6dpf
(A.) Three examples of single oligodendrocytes in homozygous mutants mosaically labelled with tg(mbp:mCherry-CAAX) imaged at 4dpf (upper) and 6dpf (lower). **(B.)** Example oligodendrocyte from a wild type sibling. **(C.)** Example oligodendrocyte from a heterozygous sibling. **(D.)** L-R: **Mean change in sheath length per cell:** Homozygous mutants exhibit a significant net shrinkage in sheath length of -0.31 ± 4.79 microns compared to wild type and heterozygous siblings which retain stable sheath length with an average net growth of 6.33 ± 3.4 microns and 5.17 ± 3.9 microns respectively (values and error bars represent mean ± standard deviation) (F, 2,38) = 6.70, p = 0.003 one-way ANOVA. Tukey's multiple comparisons: WT-Het p =0.70, WT-Hom p = 0.004, Het-Hom p = 0.007). Sheaths must be present at both timepoints to be included in this analysis. **Average number of retractions:** Homozygous mutants retract on average 2 (1 to 3) sheaths between 4 and 6dpf. Significantly more than their wild type and heterozygous siblings which exhibit 0 (0 to 0) and 0 (0 to 1) retracts over the same time period, respectively (values and error bars represent median and interquartile range) (p = 0.003, Kruskal-Wallis test. Dunn's multiple comparisons: WT-Het p = >0.99, WT-Hom p = 0.006, Het-Hom p = 0.004). One cell was imaged per larva. N = 11 WT, N = 23 Het and N = 7 Hom. (*) mark retracted sheaths, dashed lines identify sheaths with abnormal morphology, numbers mark sheath identity. Values for individual sheath lengths can be found in the Appendix 1 Figure 5.8.

3.3.14 Hypomyelination is maintained into adulthood

The inability to maintain myelin sheaths led me to question whether adult Myrf$^{-/-}$ mutants display a more severe myelin phenotype than at the larval stages. To investigate this I perfused adult (approximately 1 year old) Myrf zebrafish and extracted their spinal cords to process for TEM. Preliminary data suggests that the hypomyelination phenotype observed in Myrf$^{-/-}$ larvae extends into adulthood and appears to be more severe, with the majority of large caliber axons in the regions observed displaying a robust lack of any detectable myelin (Figure 3.22B) compared to heterozygous siblings at the same timepoint. These are preliminary images from the first round of TEM with adult samples. Quantification of this TEM data should be performed as for the larval TEM data, once sample numbers have been increased. Despite the low N numbers, the images are indicative of a persistent and potentially more severe hypomyelination phenotype in adult homozygous mutants.

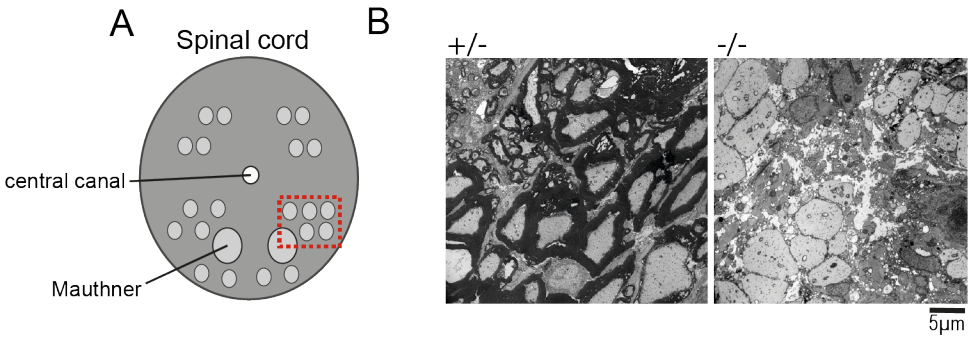

Figure 3.22: Transmission electron microscopy images of adult spinal cords **(A.)** Schematic demonstrating the location of TEM images. **(B.)** A region of the spinal cord from an adult Myrf heterozygous and homozygous mutant. Note the apparent hypomyelination in homozygous mutants relative to heterozygous siblings.

3.4 Discussion

The aim of this chapter was to produce a larval zebrafish model with CNS specific hypomyelination. This model would then be recruited into a suite of behavioural assays to identify RS-mediated, locomotor behaviours that are disrupted by aberrant myelination. In this discussion, I will describe how I have successfully achieved this aim through the generation of a Myrf larval zebrafish mutant line and raise suggestions for further characterisation of this mutant in the context of results to date. I will conclude this chapter by making predictions as to how this manipulation may affect subsequent circuit function and behaviour.

Myrf$^{-/-}$ mutants possess a third of the normal number of myelinated axons at 6dpf

Using TEM, I demonstrated that Myrf$^{-/-}$ mutants are afflicted by a 66% reduction in the total number of myelinated axons in the spinal cord at 6dpf. This time point was chosen for analysis to allow direct comparison with future behavioural phenotypes, which would be assessed at 6dpf when the majority of RS mediated behaviours are present or inducible. The finding that the ventral tract of spinal cord was more severely affected (73% reduction in myelinated axon number) than the dorsal tract (45% reduction in myelinated axon number) was a surprising yet advantageous discovery, for the ventral tract harbours the axons belonging to RS neurons – those responsible for the behaviours we would subsequently be testing. The axons of RS neurons are the largest in the spinal cord, with the Mauthner axon being the largest of all. In general, larger axons tend to possess thicker and longer myelin sheaths (Hildebrand et al., 1993; Matthews and Duncan, 1971; Murray and Blakemore, 1980), thus typically this tract is densely myelinated. As such, the regional diversity in this phenotype suggests an inability of Myrf$^{-/-}$ mutant OLs to myelinate large caliber targets. This notion is best supported by the data showing that the proportion of large caliber axons (i.e. the "top 30"), predominantly located in the ventral spinal cord, that are myelinated is reduced by 58% in Myrf$^{-/-}$ mutants in the absence of any change to axon caliber. Although the Mauthner axon is myelinated in the majority of Myrf$^{-/-}$ mutant larvae, myelin thickness around this axon is severely compromised. The early myelination of Mauthner and its functional significance during development may make myelination of this axon a priority in Myrf$^{-/-}$ mutants. Importantly, the myelination status of the

PNS was unaffected by disruption of Myrf, confirming that our model was CNS specific.

To avoid confounding findings in subsequent behavioural analysis, it was important to establish that axonal health was not compromised by the hypomyelination status of homozygous mutants. Measurement of axonal caliber was used as an initial marker of axonal health given that hypomyelination may impede axonal growth due to lack of trophic support. Furthermore, axonal degeneration is often associated with axonal swelling, although this is more typical following primary axonal damage and subsequent Wallerian degeneration. No difference was observed in axon caliber between genotypes (Figure 3.17 and 3.15). In hindsight, axon caliber could be seen as a primitive assessment of axonal health and further analysis could be performed to ensure that axonal health is not affected. Such analysis could be performed on the existing TEM dataset, including: quantification of mitochondrial size, number and localisation, neurofilament and microtubule orientation, density and spatial distribution, and axonal discoloration. For example, increased numbers of mitochondria have been observed in axons belonging to patients with MS than equivalent axons in healthy controls (Mahad et al., 2009), as well as experimentally demyelinated axons in cats (Mutsaers and Carroll, 1998) and larval zebrafish (Karttunen, 2017). Furthermore, measurement of cytoskeletal morphological properties using TEM images is an established readout of axonal degeneration during development (Lyons et al., 2005) and following injury (Fournier et al., 2015; Pettus and Povlishock, 1996). The described analysis should be performed prior to assigning future behavioural phenotypes solely to the absence of myelination.

To understand the morphological changes to myelinating OLs that were occurring to cause a reduction in the number of myelinated axons I performed *in vivo* imaging of single OLs in the spinal cord. At the time of executing these experiments I was not aware of the dorsal/ventral phenotype and investigations had been focused on the dorsal spinal cord for the entirety of this experiment. For this reason, I will discuss the single cell findings in relation to the dorsal tract phenotype and then return to a description of our experimental plans to characterise the ventral tract. The total number of myelinating OLs in the spinal cord of $Myrf^{-/-}$ mutants was reduced by 21% at 6dpf, with the dorsal component exhibiting a modest reduction of 12%. This effect size was not enough by itself to explain the 45% reduction in the number of myelinated axons

in the dorsal spinal cord. We postulated that the myelinating capacity of OLs must be reduced: either they produce shorter and/or fewer sheaths. Indeed, Myrf$^{-/-}$ mutant single OLs produced 47% less myelin overall, due to a combination of shorter and fewer sheaths. This is a remarkably similar number to the reduction in myelinated axons (45%) in the same tract. However, combining the reduction in OL number (12%) with reduced myelinated capacity (47%), I would expect the number of myelinated axons in the dorsal tract to be more severely affected i.e. 59% reduction. One explanation for this may be that the analysis of single OLs in the spinal cord is not spatially restricted to the same area analysed for TEM. To analyse single OLs in isolation from the multitude of other cells and myelin in the spinal cord, we perform injection of a DNA construct encoding our transgenic reporter, e.g. tg(mbp:mCherry-CAAX), into the single cell stage embryo to provide mosaic integration of the transgene into myelinating cells. The very nature of mosaicism means that cells available to image in the spinal cord are sparse and may occupy further anterior and posterior regions from the cloaca, which was the anatomical landmark for sections obtained for TEM. This is important to note as heterogeneity can be found in the morphology of oligodendrocytes and their myelinating sheaths according to the number of local targets (axons) to myelinate, which varies in an anterior to posterior direction (Almeida et al., 2011). Another explanation for the discrepancy between TEM and live imaging data may lie in the choice of promotor region in the transgenic line used for *in vivo* imaging experiments. This will be discussed in the following section.

Potential for confounding effects using the myelin basic protein promotor for *in vivo* live imaging experiments

The live-imaging experiments reported in this thesis were performed using transgenic lines which drive a fluorescent protein expression using the Mbp promotor region. These transgenic lines are well established in our laboratory and are commonly used as first line reporters of myelination *in vivo*. Data from this chapter and supporting literature (Bujalka et al., 2013) conclude that Mbp is under the direct transcriptional regulation of Myrf, thus introducing a potential confounding effect in the interpretation of our cellular data. One could argue that current data regarding OL numbers in the Myrf homozygous mutants represents those cells which express enough myelin basic protein, and subsequent fluorescent protein, to be detectable, rather than the true number of

OLs present. This would lead to the true number of oligodendrocytes being underestimated, which could explain the discrepancy between the reduction in the number of myelinated axons in the dorsal spinal cord as assessed by TEM (45%), and the predicted reduction (59%) in myelinated axon number in the same tract when combining OL number (12%) with reduced myelinating capacity (47%), as discussed previously. However, this would not explain the discrepancy between larval zebrafish and rodent Myrf mutants, where OL numbers are apparently *less* severely affected in larval zebrafish than mice (see later section). Furthermore, for assessment of cell morphology, unconscious bias may have lead to the selection of cells possessing better fluorescent protein expression (and thus Mbp) expression which may confound results further. To circumvent such confounding issues in future, the use of a transgenic line with a different promotor should be considered. The selection of a suitable promotor region is difficult as Myrf is a transcriptional regulator of the majority of myelin proteins (Emery et al., 2009). Additionally, other transcription factors such as Olig2 and Sox10, which are commonly used as pan-oligodendroglial lineage markers, form functional networks with Myrf, thus subsequent myelin expression may still be influenced by Myrf knockdown (Bujalka et al., 2013; Hornig et al., 2013). A potential candidate is Olig1, an early stage marker of differentiated OLs which appears prior to the onset of myelin protein expression (Auer et al., 2018; Schebesta and Serluca, 2009). The use of such a promotor may improve the accuracy of OL cell counts without the aforementioned confounding features. Morphological assessment of *mature* myelin sheaths belonging to individual OLs is limited to transgenic lines using myelin protein gene promotors. To overcome this, myelination patterns could be assessed using the experimental approach detailed in the next section.

Experimental approach to quantify myelin sheath morphology in the *ventral* spinal cord

The severity of hypomyelination in the Myrf$^{-/-}$ mutants is almost doubled in the ventral spinal cord, where there is a 73% reduction in the number of myelinated axons and a 27% reduction in the number of OLs. Given these findings, I would predict that the myelinating capacity of OLs will also be more drastically affected in this region. To test this hypothesis, it will be important to carry out the single cell imaging at 6dpf selecting for ventral cells. An additional approach would be to measure myelin sheath length and

number from the perspective of individual RS axons (Koudelka et al., 2016). Koudelka et al. (2016) developed a transgenic reporter in which membrane GFP is tagged to the axonal membrane protein contactin1a, to form the construct tg(GFP-cntn1a). Upon myelination, contactin1a is extruded from the axolemma and observed as a loss of GFP fluorescence. From this, you can infer myelin sheath length and number along the entire length of an axon. This construct has now been modified such that the coding sequence for GFP-cntn1a, alongside a second fluorescent structural reporter, is downstream of an upstream activating sequence. Taking advantage of the UAS:GAL4 system, we can inject this construct into fertilised embryos of fish expressing KalTA4 - the zebrafish optimised Gal4 sequence (Distel et al., 2009) - under a RS-specific promotor (provided by Dr. Isaac Bianco). The benefit of this particular technique is that it allows us to quantify myelin sheath number and length along the entire length of individual RS axons. In the context of our long-term aim to image myelination across circuits, this is certainly an elite approach and would provide us with physiologically relevant parameters of myelination. As described in my general introduction, multiple parameters and patterns of myelin sheaths along individual axons can influence the speed of action potential conduction velocity. Using this technique, we could collect data that would allow us to compute predictions of conduction speeds along neurons and correlate these to behavioural phenotypes identified in Chapter 4.

Myrf$^{+/-}$ mutants display precocious myelination

Perhaps the most intriguing result from this chapter is the discovery that Myrf$^{+/-}$ mutants appear to display precocious myelination at the age of behavioural testing. Analysis of TEM images was integral to this finding. Here, Myrf$^{+/-}$ mutants displayed a 53% increase in the total number of myelinated axons in the spinal cord relative to wild type siblings. This difference was even more striking on analysis of the ventral and dorsal sub-regions, where the effect sizes are the reverse of that seen in the homozygous mutants. In the dorsal spinal cord, a 73% increase in the number of myelinated axons is observed, in contrast to a 43% increase in the ventral spinal cord. Remarkably, this effect appears to be driven by an increase in the number of small caliber axons that are myelinated, as demonstrated by the cumulative sum graph in Figure 3.17. This result, in the presence of normal g-ratios of these axons, is consistent with precocious myelination. This is supported by the morphological data obtained in the single cell

imaging experiments, in which Myrf$^{+/-}$ OLs demonstrated an increased (32%) myelinating capacity, in the form of total myelin produced per cell, at the earlier timepoint assessed (4dpf). This increase in myelinating capacity appears to be achieved by the non-significant increase in the number of sheaths produced per OL, given the presence of normal myelin sheath length. However, by 6dpf the average myelinating capacity is only elevated by 11%, which cannot account for dramatic effect on myelinated axon number in the dorsal tract at this timepoint. Again, this may be explained by the inconsistency in the location of the spinal cord at which single cells are imaged compared to TEM analysis. It is also possible that this precocious myelination is a regional or transient effect. To investigate this, one could perform TEM at earlier time points (e.g. 4dpf) and at multiple locations along the anterior to posterior axis. Importantly, the experiments I proposed earlier to characterise myelin sheath morphology along entire axons in Myrf$^{-/-}$ mutants should also be employed in heterozygotes. In addition to analysing single cells in the ventral spinal cord, one could classify OLs based on their location along the anterior to posterior gradient and perform analyses to compare myelinating capacity in different regions of the spinal cord.

By what mechanism could heterozygotes be achieving precocious myelination? When a mutation in the genetic code occurs, it can leads to loss-of-function (null mutation) or a reduction in the protein's ability to work (hypomorph). Equally, a random mutation may result in an increase in the protein's function (gain-of-function), production of a protein that interferes with the wild-type protein's function (dominant negative), or even the acquisition of a new function (neomorph). An interesting example of such a gain-of-function mutation can be seen in the human disease sickle cell anaemia. A simple point mutation in the haemoglobin beta (HBB) gene leads to a single nucleotide change subsequently altering the amino acid sequence. This causes the production of a different form of haemoglobin protein which causes red blood cells to acquire an abnormal (sickle) shape and cause disease. The *recessive* nature of this gain-of-function allele results in interesting phenotypic variation between heterozygous carriers and homozygous individuals. Homozygous individuals become affected by sickle cell anaemia, while heterozygous carriers, in which only 50% circulating red blood cells are 'sickle' shaped, the mutation confers a dominant inheritance of resistance to malaria. An example of a *dominant* gain-of-function mutation can be found in Huntington's disease, where the

mutant allele confers a toxic gain of function of the mutant protein which interferes with the wild type protein, resulting in heterozygous individuals being as severely affected as homozygous individuals. Although gain-of-function mutations are well described phenomena, the opposing myelination phenotypes in heterozygous and homozygous Myrf larval zebrafish mutants make this an unlikely mechanism. A recent study by El-Brolosy et al. (2019) provides a more tempting hypothesis. Previous studies using zebrafish have shown that the genetic knockdown of a target gene can trigger transcriptional adaptation of homologous genes (Rossi et al., 2015). El-Brolosy et al. (2019) continued this work to establish the molecular mechanisms by which this can occur. Transcriptional adaptation of some mutant alleles is reliant upon the initiation of RNA-surveillance mechanisms during mRNA decay. This leads to transcriptional upregulation of genes with high sequence similarity, as found in gene homologs and paralogs. Most relevant however, is the finding that a subset of heterozygous mutants tested demonstrated an *increase* in the level of transcript from the wild type allele of the same gene (extended data Fig2c, (El-Brolosy et al., 2019)). Although this results in a gain-of-function, the adaptation is driven by adaptive transcriptional mechanisms rather than the genetic mutation itself. An indication that such transcriptional adaptation may be occurring in the Myrf$^{+/-}$ mutant comes from my quantitative RT-PCR data which shows a subtle but non-significant increase in the relative expression levels of Mbp. If transcription of the wild type Myrf allele is being driven by transcriptional adaptation in this model, then the expression of Mbp would be driven consequentially. It would be interesting to prove this hypothesis by performing quantitative RT-PCR analysis of mutant and wild type Myrf transcript expression, using allele specific primers. Additionally, an excess of Mbp expression could be confirmed by comparing the fluorescent intensity of OL nuclei (tg(mbp:nls-eGFP)) or myelinated tracts (tg(mbp:eGFP-CAAX) between wild type and heterozygous siblings from transgenic Myrf lines.

Myrf$^{-/-}$ mutants display abnormal myelin sheath morphology and retractions

Interestingly, the myelinating capacity of single OLs in Myrf$^{-/-}$ mutants was already reduced at 4dpf. Yet at this point, the majority of myelin sheaths exhibitted normal morphology. In contrast, by 6dpf myelin sheaths displayed significantly abnormal morphology. Using time course imaging I demonstrated that this was due to an inability of

Myrf$^{-/-}$ mutant OLs to maintain their sheaths over time, with OLs exhibiting retractions and overall net shrinkage of their myelin sheaths between the two timepoints. This suggests that there may be a combination of an intrinsic failure to myelinate (reduced myelinating capacity) and a demyelination phenotype (sheath shrinkage/retraction). These findings can be explained by the known function of Myrf, predominantly its role as a transcription factor to regulate the expression of core myelin genes such as Mbp (Bujalka et al., 2013). Indeed, I have shown that the transcription of Mbp is effectively abolished in Myrf$^{-/-}$ mutants. Mbp is a major myelin protein and functions within the myelin sheath to mediate myelin membrane compaction and establish cytoplasmic channels that are required to shuttle metabolites and allow signal transduction between the OL and underlying axon (Aggarwal et al., 2013; Snaidero et al., 2014). Mbp$^{-/-}$ shiverer mice display a reduction in the number of myelinated axons with thinner myelin sheaths which display variable levels of compaction (Bird et al., 1978; Rosenbluth, 1980). Interestingly, while extensively characterising the myelin phenotype of shiverer mouse, Rosenbluth (1980) occasionally observed evidence of myelin damage in the form of axonal and glial myelin inclusions and vacuolation. This is consistent with myelin sheath breakdown and fits with the inability of Myrf$^{-/-}$ mutants to maintain myelin sheath integrity. An additional hypothesis, that I touched upon in my introduction, is that Myrf may play an, as of yet, unidentified role in regulating the secretion of myelin membrane components. The transcriptional aspects of Myrf's function are solely driven by the N-terminus of the protein. However, the C-terminus has been shown to play a role in regulating larval molt (a highly secretory process) of C. elegans (Russel et al., 2011). Additionally, outside of the CNS, Myrf expression is found in a number of secretory tissues such as the lungs and intestine. This role of Myrf has never been investigated in vertebrate OLs and as such, a function for Myrf in regulating the secretion of myelin proteins remains a conjecture at present. In summary, the inability of Myrf$^{-/-}$ mutants to maintain myelin sheaths is most likely due to the lack of the major myelin protein Mbp. However, an undetermined role of Myrf in the secretion of myelin products could also be at play.

Discrepancy between rodent and larval zebrafish Myrf homozygous mutants

A challenge during the course of this project was trying to understand the discrepancy in phenotypes between the Myrf CKO rodent model and this larval Myrf KO model. The main discrepancy is that our own genetic manipulation of Myrf in zebrafish resulted in a less severe phenotype than that observed in the mouse CKO model. To illustrate this point, in the optic nerve of Myrf CKO mice at age post-natal day 13 there exists an almost 100% reduction in the number of myelinated axons and number of mature OLs Emery et al. (2009). In contrast, our model displays a 21% reduction in OL cell number and a 66% reduction in myelinated axons in the spinal cord at 6dpf. Importantly, a greater reduction in OL cell number was seen in early experiments (Figure 3.5) when earlier generations of the Myrf zebrafish line were used. In Section 3.3.6 I explain how this phenomenon may arise with the introduction of off-target mutations during the initial mutagenesis which could act synergistically with the Myrf mutation to exacerbate the cellular phenotype, although this is purely conjecture. Any potential off-target mutations would have been outbred with subsequent generations; behavioural and cellular data were collected on third generation or younger lines and a generational drift in phenotype is not noted to have occurred. However, more complex statistical analysis such as mixed-modelling could be used to address whether this is was a confounding factor of the analysis. It is possible that the disparity between species could result from regional differences i.e. the density of myelinated fibers is higher in the optic nerve than the spinal cord. In support of this, my results demonstrate that a regional difference exists within the spinal cord, so it is not far-fetched to suggest that regional differences may exist further across the CNS. However, the fact that Myrf CKO mice develop severe neurological phenotypes and die by post-natal day 21 suggests that severe hypomyelination is likely to be widespread in the mouse model. This, along with the fact that Myrf KO larval zebrafish survive into adulthood represents yet another inconsistency. Interestingly, the finding that adult Myrf$^{-/-}$ mutants appear to be severely hypomyelinated is more consistent with rodent models and may imply the presence of a protective developmental or size effect in the early larval stages.

Taken together, the differences between the two models suggest that alternative mechanisms must be at play. Either Myrf is not as critical for OL function in larval zebrafish

as it is in mammals, the larval zebrafish model is experiencing genetic compensation, or the genetic manipulations in the two models are incomparable. The latter is less likely as both genetic techniques targeted early exons in the Myrf gene and were shown to cause reduced expression levels of myelin proteins (Emery et al., 2009), and adult zebrafish were severely hypomyelinated on initial assessment. However, the failure to reliably detect differences in Myrf transcript levels in my own experiments leaves open the possibility that the mutation in our zebrafish model is hypomorphic. This could be discounted by performing FACs sorting and RNA extraction of large numbers of OLs to amplify the amount of Myrf transcript available to assay, allowing more reliable estimation of transcript levels using qRT-PCR. The fact that hypomyelination appears to be more severe in adult zebrafish, on the small number of samples available, could suggest the presence of genetic compensatory mechanisms at early stages that are 'worn out' by adulthood. We reasoned that this compensation may derive from maternal wild type RNA, or upregulation of paralogous gene function. However, I am confident that I excluded the most likely candidate compensatory mechanisms during my early characterisation of the Myrf$^{-/-}$ mutant. Firstly, no Myrf transcript was detected in unfertilised heterozygous eggs suggesting that maternal transfer of this gene does not exist at detectable levels. Secondly, the injection of Myrf morpholino, which should prevent transcription of maternal Myrf RNA if present, did not worsen the Myrf$^{-/-}$ phenotype. Finally, targeting the Myrf-like gene, which bears high sequence homology to Myrf, using CRISPr/Cas9 targeted mutagenesis, did not exacerbate the phenotype of Myrf$^{-/-}$ mutants. However, the possibility that another unidentified gene can compensate for Myrf function has not been excluded. An obvious distinction between rodent and zebrafish models which could explain the difference in myelin phenotypes between the species-specific mutants resides in the constituents of CNS myelin. In mammals, CNS myelin is composed of myelin proteins Plp and Mbp, while Mbp and P0 form PNS myelin. However, the zebrafish ortholog of P0 (Mpz) is present in the CNS, co-expressed alongside Plp and Mbp (Brösamle and Halpern, 2002). Furthermore, Mpz is known to be upregulated in OLs following CNS injury in larval zebrafish (Schweitzer et al., 2003). Thus, it is possible that Mpz may compensate for the lack of Mbp seen in Myrf-/- larval zebrafish mutants, while the absence of P0 in the CNS of mice allows a more severe hypomyelination phenotype when Myrf function is disrupted. To prove this hypothesis, quantification of Mpz transcript levels should be included in subse-

quent qRT-PCR experiments.

If genetic compensatory mechanisms are not at play, then what is accounting for the severity of hypomyelination observed in adult zebrafish and postnatal mice in comparison to larval zebrafish? Perhaps the answer lies in OL heterogeneity. It is possible that the population of OLs present during early larval stages are transcriptionally, and potentially functionally, different to those found at later time points of development, or in mammals. Indeed, considerable OL heterogeneity has been identified in transcriptomic studies of rodents and humans (Jäkel et al., 2019; Marques et al., 2016) with recent reports of a similar heterogeneity existing in zebrafish too (Marisca et al., 2020). For currently unknown reasons, it is possible that a lack of Myrf in OL lineage cells is less likely to trigger an apoptotic response in larval zebrafish than in mammalian systems. For example, OPCs from Myrf-deficient mice differentiate but undergo apoptosis prior to upregulating myelin genes *in vitro* (Emery et al., 2009). It would be interesting to assess levels of OL apoptosis in Myrf$^{-/-}$ mutants relative to their siblings and establish whether general levels of apoptosis are indeed much lower than that observed in rodent models. This could be performed using *in vivo* markers of apoptosis such as acridine-orange staining (Hammerschmidt et al., 1996). Furthermore, it is apparent from my own data that OL numbers appear to be more significantly reduced at earlier timepoints i.e. a 38% reduction in OL number was observed in the dorsal spinal cord at 4dpf, compared to a 12% reduction in OL number in the same tract at 6dpf. This could suggest a delay in OL differentiation or, perhaps, a rebound proliferation and differentiation of OPCs in response to low levels of apoptosis. In any case, monitoring the dynamics of OPC number and rates of apoptosis during the larval stages will be enlightening. OPC numbers could be assessed *in vivo* using established Sox10 (OPC/OL specific) and/or Olig1 (OPC specific) reporter lines.

In summary, the biological mechanism allowing the deviation in phenotypes between rodent and larval zebrafish Myrf mutants is yet to be identified. The presence of a severe phenotype in adults confirms that the ability of zebrafish to tolerate loss of Myrf function varies with age. It seems reasonable to propose that the degree of protection present in larval zebrafish may be due to developmental stage-specific differences in OL subtype. However, as discussed, it is also possible that an unidentified compensatory

mechanism is at play. Regardless, the hypomyelination achieved in the larval zebrafish model remains robust and is deemed adequate for future investigations.

Adult Myrf$^{-/-}$ mutants exhibit severe hypomyelination

Preliminary TEM data demonstrates that there is a severe lack of myelination in the spinal cord of adult Myrf$^{-/-}$ mutants compared to their wild type and heterozygous siblings. At first glance, this phenotype appears to be worse than that observed in larval zebrafish, although sample numbers must be increased and further quantification performed to state this with confidence. As I alluded to in the previous section, this difference may be accounted for by stage-specific susceptibility to loss of Myrf function. It was interesting to observe that although OLs in the spinal cord of Myrf$^{-/-}$ larval zebrafish were able to produce myelin initially, they were unable to maintain their myelin sheaths between 4 and 6dpf. This is consistent with a degenerative process, and under normal circumstances we would predict that these OLs would undergo apoptosis due to a lack of axonal support. Thus, although OL numbers appear to recover between 4 and 6dpf, it is unlikely that these cells will go on to produce stable myelin. It is possible that past this time point, the intrinsic ability of newly differentiated OLs to function without Myrf is exhausted and cell apoptosis, and subsequently, hypomyelination worsens. As mentioned earlier, it will be integral to assess apoptosis in this model and extend the analysis to later, juvenile stages to confirm this prediction.

If significant apoptosis is found to occur in the Myrf$^{-/-}$ zebrafish model, it will be vital to establish whether this initiates an inflammatory response at the time of behavioural testing, for this could confound our interpretation of behavioural phenotypes. At these time points, innate immune cells, namely microglia and macrophages are present in CNS and periphery of larvae respectively (Herbomel et al., 2001). Resident microglia and invading macrophages are known to be activated by OL death and demyelination in the larval zebrafish spinal cord where they are required to phagocytose and clear myelin debris (Karttunen et al., 2017). To assess for an inflammatory response we can perform live imaging using transgenic zebrafish lines such as tg(mpeg:GFP), which drives expression of GFP in macrophages and microglia, and quantify the number of these cells present in the spinal cord of Myrf$^{-/-}$ mutants at 6dpf.

Another possible explanation for the degree of hypomyelination in the adult Myrf$^{-/-}$ mutants could be due to an inability of OLs to myelinate larger caliber axons. At the larval stages, I documented a 56% reduction in the proportion of the largest caliber axons that are myelinated in Myrf$^{-/-}$ mutants and reported a significantly increased g-ratio value (i.e. thinner myelin) for those large caliber axons that were myelinated (Mauthner and non-Mauthner axons >0.3μm). Although total myelinating capacity per OL was reduced at these stages, perhaps enough myelinating capacity exists to be able to maintain the third of myelinated axons that are observed. However, during development axon caliber increases dramatically; many of the axons present in the adult spinal cord exhibit larger calibers than that of the Mauthner axon at larval stages. Under normal conditions, larger caliber axons possess thicker and longer sheaths thus demanding additional myelin biogenesis and maintenance which may exceed the capacity of OLs present at these later stages.

Conclusion

By genetically targetting the Myrf gene in larval zebrafish we have successfully established a CNS specific model of hypomyelination. Through the characterisation of this model, I have shown that Myrf mutants possess a third of the number of myelinating axons normally present in the spinal cord at 6dpf, in the absence of an overt effect on axonal development. In this model, larger caliber axons of the ventral spinal cord are less likely to be myelinated than their smaller, dorsal counterparts. This effect is advantageous to our aims, given that these axons belong to those RS neurons which mediate the majority of locomotor behaviours that we plan to study in Chapter 4.

With the presence of unmyelinated axons that are usually myelinated, and reduced myelin sheath thickness around those myelinated axons that remain in Myrf$^{-/-}$ mutants, we can make predictions about the behavioural phenotypes that may arise in the following chapter. Having established the role of myelination along single axons in my general introduction, we could predict that these findings will influence the speed of action potential conduction velocity along affected axons and the ability of neurons to sustain high frequency firing. Given the widespread nature of hypomyelination across RS neurons in this model, this could influence behaviour in a number of ways. As I will present in the next chapter, locomotor behaviours in larval zebrafish are diverse

and can involve distributed activity across multiple RS neurons. However, in some instances specific aspects of a behaviour are mediated by individual RS neurons. For example, the Mauthner axon is chiefly responsible for allowing a *fast* performance of escape responses. Thus, we can make some preliminary predictions of how these behaviours may be affected. For example, in Myrf$^{-/-}$ mutants the thickness of myelin sheath surrounding the Mauthner axon is reduced by 83% relative to wild type siblings. Given the known relationship between myelin sheath thickness and conduction velocity (Waxman, 1980) we would predict that conduction velocity will be slower and the latency to escape response will be longer in Myrf$^{-/-}$ mutants compared to their siblings. The most relevant data available to allow prediction of the delay in latency comes from electrophysiological recordings of the Mauthner axon in larval zebrafish in the presence and absence of myelin (courtesy of Dr. Dau Suminaite). Using an Olig2 morpholino to prevent myelination of the Mauthner axon, antidromic measurement of conduction velocity was reduced by ∼43% from ∼1.75m/s in uninjected larvae to ∼1m/s in morpholino injected larvae. From these values, we can predict that in Myrf$^{-/-}$ mutants, which exhibit a severe reduction in the thickness of myelin around the Mauthner axon, that action potential conduction velocity – and thus latency to response – would not be prolonged by more than 43% compared to wild types. However, the effect of dysmyelination along this axon in the Myrf$^{-/-}$ may differentially influence conduction velocity and it would be important to correlate a behavioural phenotype in this response to *in vivo* electrophysiological recordings.

Chapter 4

Investigating the effects of CNS hypomyelination on locomotor behaviours

4.1 Introduction

Larval zebrafish have become a robust and popular model organism in the field of circuit and behavioural neuroscience. The main advantage that larval zebrafish offer is their remarkable tractability for non-invasive *in vivo* imaging. This is exemplified by regular publications performing *in vivo* imaging of neuronal activity while driving a spectrum of behaviours in awake and sometimes freely moving animals (Ahrens et al., 2013, 2012; Chen et al., 2018; Cong et al., 2017; Haesemeyer et al., 2018; Kim et al., 2017). Although significant advancements in technology e.g. head mounted epifluorescence microscopes (Ghosh et al., 2011; Ziv and Ghosh, 2015) and miniaturised laser scanning and two-photon coupled microscopes (Flusberg et al., 2008; Helmchen et al., 2001; Ozbay et al., 2018) now allow for the imaging of neuronal populations in rodents during similar scenarios, the capacity for imaging large volumes and function across distributed circuits at cellular resolution remains limited. In zebrafish larvae however, it is possible to image multiple brain volumes per second allowing unbiased discovery of brain regions involved in behaviour (Chen et al., 2018; Cong et al., 2017; Kim et al., 2017). Additionally, their small size, high fecundity, amenability to genetic manipulation and permeability to water soluble compounds has led them to be

a reliable organism for use in high throughput behavioural assays for gene and drug-discovery screens which to this day remains a mainstay of their use (Baraban et al., 2013; Ghannad-Rezaie et al., 2019; Wolman and Granato, 2012). Consisting of approximately 100,000 neurons, the larval zebrafish nervous system represents a reductionist system in comparison to mammalian models. Despite this, many behaviours are conserved across mammals and zebrafish (including those which will be assessed in this chapter) (Baraban et al., 2005; Burgess and Granato, 2007; Curzon et al., 2009; Lovett-Barron et al., 2017; Shi et al., 2018) with aspects of neuroanatomy and neurophysiology bearing degrees of similarity (Kalueff et al., 2014; Panula et al., 2006). Thus, if we can begin to understand circuit mechanisms in a simple system it will arm us with the information we need to interrogate larger, more complex systems.

Despite extensive use of larval zebrafish in behavioural neuroscience to date, our knowledge of larval zebrafish behaviours that are affected by changes in myelination remains primitive. Consequently, there are no established behavioural assays that quantify the behavioural sequelae of disrupted myelination in the CNS. However, a single study exists describing the consequence of PNS hypomyelination on the performance of the escape response. In this study, Erbb3$^{-/-}$ larval zebrafish mutants displayed reduced response rates to a water jet stimulus in addition to a prolonged latency to escape response. Consistent with myelin's function in the nervous system, these findings could correspond with a delay in conduction velocity along the peripheral components of the circuitry underlying this behaviour i.e. sensory and/or motor neurons, although confirming this mechanism was not within the remit of the study. Identifying a behavioural assay able to detect alterations in CNS myelination in larval zebrafish is within the main aims of this project and would be of huge benefit to the wider field of researchers.

Reticulospinal mediated behaviour and CNS myelination

The majority of locomotor behaviours performed by larval zebrafish are mediated by the reticulospinal (RS) system which is extensively myelinated at by 6dpf (Almeida et al., 2011; Kimmel et al., 1974; Mensch et al., 2015). The structure of the RS system will be described in detail in the next section. Fortunately for the purposes of my project, the RS system has received extensive characterisation providing us with a comprehensive understanding of the individual neurons that are necessary for and

modulate specific behaviours. In Chapter 3, I presented the Myrf$^{-/-}$ mutant zebrafish line as a novel model of CNS specific hypomyelination. The Myrf$^{-/-}$ mutant displays a 66% reduction in the number of myelinated axons in the spinal cord, with a 73% reduction observed in the ventral tract alone (Chapter 3, Figure 3.13). Given that the ventral tract harbours the majority of axons belonging to RS neurons, we predicted that RS mediated behaviours would prove an appropriate starting point to assess the role of myelin in maintaining circuit function and behaviour. As discussed in the previous chapter, the timing of myelination in the spinal cord coincides extremely closely with the emergence and development of specific RS mediated behaviours (Chapter 3, Figure 3.1). The similarity in the timing of these two processes builds the hypothesis of this chapter that **myelination of RS axons refines circuit function and locomotor behaviour during development.**

In Chapter 3, I completed the first aim of this thesis which was to establish a larval zebrafish model of CNS specific hypomyelination. The next aim of the project is to investigate how disruption to the normal program of myelination affects RS mediated behaviours during development. To begin to address this, I recruited the Myrf$^{-/-}$ larval zebrafish model to existing behavioural assays for in-depth phenotyping of locomotor behaviour.

The aims of this chapter are as follows:

- Identify RS mediated behaviours which are affected by hypomyelination
- Isolate a behavioural phenotype which will allow interrogation of the effects of myelin structure at a circuit level

It is important to note that hypomyelination in our model is not restricted to RS neurons of the spinal cord. Furthermore, although we have not assessed the myelination status of the brain, given the widespread expression of Myrf throughout the CNS it is anticipated that this region is hypomyelinated to a similar extent as the spinal cord. Theoretically, this could influence the recruitment of RS neurons and influence behavioural output. Therefore, in the event of a phenotype being identified in a RS mediated behaviour it will be essential to investigate which aspect of the circuitry hypomyelination is exerting its effect.

Reticulospinal mediated behaviours

The reticulospinal system

By 6dpf, larval zebrafish perform a diverse range of behaviours which are largely mediated by neurons of the RS system (Budick and O'Malley, 2000; Burgess and Granato, 2007; Kalueff et al., 2013; Saint-Amant and Drapeau, 1998). The RS system consists of approximately 150 neurons whose cell bodies reside in the midbrain and hindbrain and axons extend along the medial and lateral fasciculus of the ventral spinal cord. Many RS neurons are individually identifiable based on their location and morphological features, as seen in Figure 4.1, which are consistent across larvae (Gahtan et al., 2002; Metcalfe et al., 1986). Together with the expression of GECIs and optogenetic proteins, these features have made larval zebrafish a tractable system to investigate the contribution of individual neurons to specific behaviours. Here, I will introduce the neuronal circuitry underlying the behaviours tested in this chapter, with a specific emphasis on the RS neurons involved.

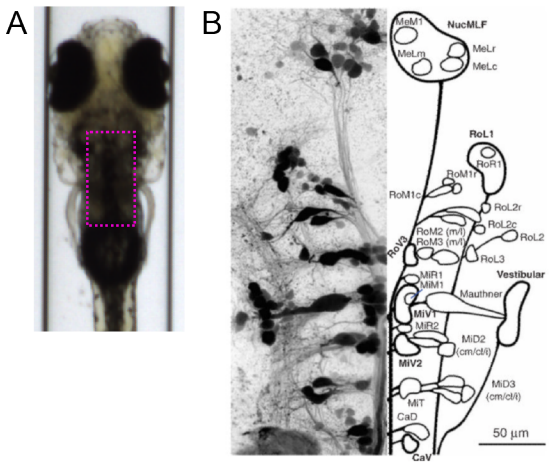

Figure 4.1: The reticulospinal system
(A.) Dorsal view of the anterior region of a larval zebrafish. The magenta dashed box marks the approximate region of the hindbrain containing the neuronal soma of the RS system depicted in (B.). **(B.)** A schematic (right) of RS cells identified using retrograde labelling using Texas Red dextran (left). Image taken from Orger et al. (2008)

The Mauthner system and the escape response

The escape response, also known as the startle response, is perhaps the most robust RS-mediated behaviour for experimental examination. Essential for survival, the escape response is an innate, reflexive behaviour elicited by threatening visual, auditory or mechanosensory stimuli and characterised by a rapid high angular turn (known as a

'c-bend'), a counterbend turn and a rapid burst swim away from the stimulus (Kimmel et al., 1974; Zottoli et al., 1995). The ability to perform this behaviour is integral to the survival of zebrafish larvae, developing soon after hatching when risk of predation is high. The functional unit that drives this behaviour has been identified as a bilateral array of RS neurons known as the 'Mauthner system', comprising a pair of giant Mauthner cells and its smaller homologs Mid2CM and Mid3CM (Figure 4.1 and Figure 4.2A). The somata of these cells reside in the hindbrain region spanning rhombomere 4 to 6 where they are easily identifiable by their morphology - including distinctive lateral and ventral dendrites (Kimmel et al., 1982; Metcalfe et al., 1986). From here, their axons immediately cross the midline and extend along the ventral tract of the contralateral spinal cord, forming synapses with motor neurons and interneurons along its length. The Mauthner axon is easily recognisable here, even using the brightfield microscopy, due to its huge caliber. This trajectory is essential to allow movement in a direction away from the perceived threat: activation of the Mauthner cell on the side closest to the stimulus leads to recruitment of motor neurons and subsequent muscle contracture on the opposing side of the body leading to a high magnitude bend *away* from stimulus (Figure 4.2C). The startle response is an example of a reflex that is robustly conserved across species; in mammals the startle response is mediated by giant neurons of the caudal pontine reticular nucleus in the lower brainstem, likely homologous to the Mauthner system in fish (Koch, 1999).

The cells of the Mauthner array can be differentially activated according to the location and threat level of the stimulus. For example, calcium imaging of the Mauthner system during stimulus application showed that all three cell types of the array are activated by stimuli applied to the head but only the Mauthner is activated by a water jet stimulus applied to the tail (O'Malley et al., 1996). This was supported by a subsequent study that demonstrated that unilateral ablation of all three neurons increased the latency of response to both head and tail stimuli, yet ablation of Mauthner alone only affected responses to tail stimuli (Liu and Fetcho, 1999). However, these findings may be specific to the context of this experimental paradigm and the type of stimulus involved. In more recent studies, it was discovered that larval zebrafish can perform two different types of escape response to mechanosensory stimuli which can be defined by their latency, resulting in their nomenclature as 'short latency c-starts' (SLCs) or 'long

latency c-starts' (LLCs) (Burgess and Granato, 2007) (Figure 4.2B). The kinematics of the resulting c-bends of these two types of response also display subtle differences. For example, LLCs display a longer duration, slower angular velocity and smaller angled c-bend, but ultimately achieve the same physical displacement as SLCs. In the same study, laser ablation of the Mauthner cell completely abolished SLC responses, leaving LLCs in tact. For this reason, it has been suggested that the LLCs are primarily driven by the Mauthner homologues and likely represent a back-up mechanism for when Mauthner recruitment fails. Alternatively, they may act as a more energy efficient means to move away from less threatening stimuli given the degree of depolarisation required to induce an action potential in the larger caliber Mauthner axon.

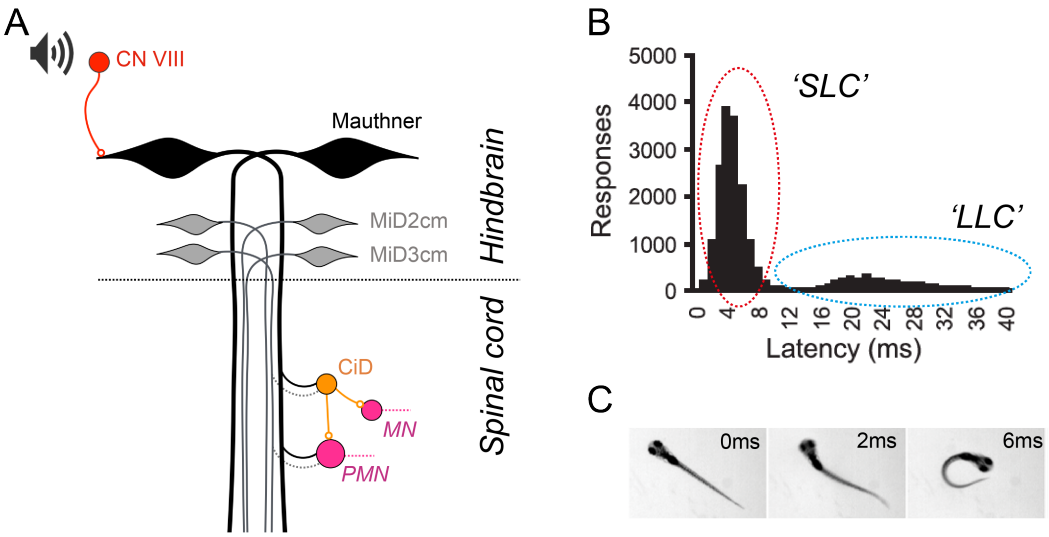

Figure 4.2: The Mauthner system and the escape response
(A.) The circuitry of the Mauthner system. Sensory input, for example from the ear via the vestibulocochlear nerve (CN VIII), is received at the lateral dendrite of the Mauthner cell body. The axon of the Mauthner cell crosses the midline and extends down the ventral spinal cord where it synapses directly with primary motor neurons (PMNs) and Circumferential Descending (CiD) cells. The CiD cells can subsequently recruit other motor neurons. Recruitment of motor neurons on the contralateral side of the body to the stimulus results in a 'c-bend' away from the stimulus. **(B.)** The latency of an escape response is defined as the time taken from the stimulus onset to the maximum change in heading angle (c-bend) (Figure 4.10). Here, a histogram of the latency to response is adapted from Burgess and Granato (2007). Short latency escape responses form the first peak of the distribution (red dashed ellipse) whereas long latency escape responses are found in the second, flatter peak of the distribution (blue dashed ellipse). **(C.)** Still images of a typical escape response. In the last frame (6ms) a c-bend is observed. Taken from McClenahan et al. (2012).

Alongside sensory input, the Mauthner receives information from a number of inhibitory and excitatory interneurons (reviewed in Hale et al. (2016)). To summarise these, feed-

back interneurons such as cranial relay neurons (CRNs) and passive hyperpolarising potential (PHP) collateral cells act to provide inhibition to the ipsilateral M-cell to prevent repetitive firing (Koyama et al., 2011; Zottoli and Faber, 2000). Whereas feed-forward neurons such as PHP commissural interneurons serve to inhibit the contralateral Mauthner cell to ensure a unilateral response. Another group of commissural neurons are the spiral fibre neurons which spiral around the axon hillock of the Mauthner cell, modulating its activity via glutamatergic synapses (Koyama et al., 2011; Zottoli and Faber, 2000). Together, these excitatory and inhibitory systems afford the Mauthner circuitry with flexible decision making behaviour - that is, the ability to integrate sensory stimuli, compute threat level and select an appropriate motor response. In humans and rodents, the startle response demonstrates short term plasticity such as habituation to repetitive stimuli. Additionally, the startle response can be modulated by a mechanism known as pre-pulse inhibition (PPI) whereby providing a subthreshold stimulus almost immediately prior to the standard stimulus results in inhibition of the startle response. This mechanism has been harnessed as a diagnostic test for sensory gating deficits which are often experienced by patients with psychiatric disorders such as schizophrenia (Braff et al., 1978). In their pivotal study, Burgess and Granato (2007) demonstrated that both habituation and PPI of the acoustic startle response are conserved in larval zebrafish, providing a means to investigate mechanisms of short-term plasticity in this reduced circuit. Indeed, subsequent studies have revealed aspects of circuitry involved in mediating this response, including a population of neurons which provide presynaptic inhibition to the Mauthner cell at the level of the lateral dendrite (Bergeron et al., 2015; Tabor et al., 2018). These behaviours also represent a useful high-throughput assay to identify chemical and genetic modulators of these responses (Wolman et al., 2011).

In summary, the principal function of the Mauthner neuron is to provide fast latency escape responses to alarming stimuli, which can be modulated according to the stimulus properties. In the absence of Mauthner, longer latency escape responses can be recruited via alternative RS pathways including the Mauthner homologs MiD2CM and MiD2CM. It has recently been suggested that long latency escapes can be also recruited by non-RS mediated pathways, via a novel population of prepontine neurons (Marquart et al., 2019). Overall, despite multiple descriptions of the neurons involved in initiating

an escape response, recruitment of the wider RS system is ultimately required for its completion. In support of this, calcium imaging of the entire RS system following head tap stimuli has revealed that up to 82% of RS neurons are activated during an escape response (Gahtan et al., 2002). It is also important to note that larval zebrafish can employ a number of movements to escape from a stimulus, and that SLC and LLC responses are specific to escape responses induced by mechanosensory and light-flash stimuli (Marques et al., 2018).

Looming-evoked escape responses

The Mauthner system receives multimodal sensory inputs, predominantly from the visual system, posterior lateral line and auditory system via the vestibulocochlear nerve. Researchers have discovered that across multiple organisms, escape responses can be reliably induced by presenting a looming visual stimulus (Ewert, 1974; Sun and Frost, 1998; von Reyn et al., 2017). This behaviour has recently been established in larval zebrafish and represents another means to interrogate the recruitment of the RS circuitry (Dunn et al., 2016; Temizer et al., 2015). The presentation of a looming stimulus comprises of a dark (although other colours, contrasts and patterns can be used with varying effects) expanding spot which is designed to simulate an impending collision or predator. When the disk reaches a critical size, larvae perform an escape response. In contrast to the escape responses induced by mechanosensory stimuli, for which SLCs or LLCs are specific, the escape behaviours performed in response to looming-stimuli are more diverse (Dunn et al., 2016; Marques et al., 2018).

Performance of loom-evoked escapes requires processing of sensory information and recruitment of an appropriate motor response, also known as sensorimotor transformation. Briefly this involves detection of the visual stimulus by loom-specific retinal ganglion cells (RGCs) which project to the optic tectum where spatial information regarding the stimulus is retinotopically organised (Dunn et al., 2016; Temizer et al., 2015). Additional tectal input from the thalamus has been proposed to boost response rate by integrating information on stimulus 'dimming' when available (Heap et al., 2018). Specialised cells within the ipsilateral tectobulbar tract have been suggested to relay looming-information from the tectum to the caudal hindbrain where RS neurons are recruited (Helmbrecht et al., 2018). The motor component of the response is driven

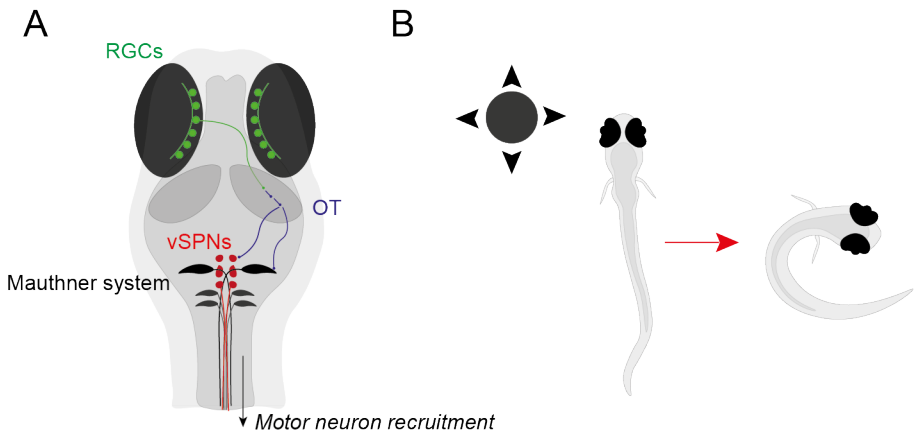

Figure 4.3: The circuitry underlying looming-evoked escape responses
(A.) Visual information concerning a stimulus is relayed to the optic tectum via retinal ganglion cells (green). Stimulus features are encoded by populations of neurons in the optic tectum (OT) which determine whether an escape response is required. Ipsilateral pathways from the OT to the hindbrain allow subsequent recruitment of RS neurons such as the Mauthner system (black - Mauthner, grey - Mauthner homologs) and ventral spinal projection neurons (vSPNs) (red). In turn this will lead to motor neuron activation and escape behaviour. **(B.)** Illustration of a looming stimulus driving an escape response.

by the RS system, namely the Mauthner system and ventral spinal projection neurons (vSPNS) which are involved in turning (Orger et al., 2008) (Figure 4.3). In contrast to auditory stimuli, during looming-evoked escape responses the soma of the Mauthner receives input onto its *ventral* dendrite (Zottoli et al., 1987). Interestingly, the presence of a Mauthner system does not appear to be as integral to loom-evoked escape responses compared to those elicited by mechanosensory stimuli, with M-cell ablation only influencing the turn angle and swim trajectory of loom-evoked escape responses (Dunn et al., 2016). In fact, Bhattacharyya et al. (2017) demonstrated that in response to high velocity looms, approximately 80% loom-evoked escapes involved Mauthner cell or homolog activity, with 20% occurring under the silence of Mauthner with activity in the vSPNs. Contrastingly, slow velocity looming stimuli trigger a larger proportion of non-Mauthner RS-mediated escapes which exhibit larger variability in their kinematic parameters.

In summary of the looming-evoked escape response: visual information is relayed to the RS system via the tectum. High-threat stimuli encode for the recruitment of the Mauthner system and fast escape responses similar to SLCs performed in response to mechanosensory stimuli. While slower, less threatening stimuli evoke escape responses via alternative pathways likely mediated by the vSPNs.

Spontaneous swimming and the optomotor response

The optomotor response (OMR) is an innate, conserved position-stabilising reflex performed by larval zebrafish in response to optic flow. It allows larvae to maintain their position according to the direction of water flow in naturalistic environments and can be artificially induced from 5dpf by displaying whole field visual gratings to freely moving or head fixed larvae (Naumann et al., 2016; Neuhauss et al., 1999; Orger et al., 2000). The OMR recruits two behaviours: forward swims and turning, both of which are fundamental components of spontaneous swimming behaviour. Consequently, researchers have harnessed this reflex for investigation into the circuitry underlying the control of swimming behaviour (Huang et al., 2013; Orger et al., 2008; Severi et al., 2014; Thiele et al., 2014) and sensorimotor processing (Naumann et al., 2016). Combining OMR assays with whole brain calcium imaging, Orger et al. (2008) were the first to identify RS neurons whose activity was highly correlated to forward swims (cells of the nucleus of the medial longitudinal fasciculus (nMLF) in the midbrain) and turning (vSPNs). Using optogenetic stimulation and laser ablation, RS neurons belonging to the nMLF have been demonstrated to control swim speed by modulating tail beat frequency and provide directional control over swimming by altering tail orientation (Severi et al., 2014; Thiele et al., 2014). Additionally, ablation of the vSPNs cells completely eliminated turning behaviour during OMRs (Orger et al., 2008). An intricate study by Huang et al. (2013) further investigated the contribution of vSPNs to tail kinematics during turns and forward swims across multiple behaviours, including the OMR response. A defining signature of turning bouts, relative to forward swims, was the presence of a larger amplitude angle (theta) and longer cycle period of the first tail undulation in a turning bout, otherwise the subsequent tail undulations were kinematically indistinct from each other. Ablation of vSPNs abolished turns and increased the frequency of forward swims, suggesting that vSPNs convert forward swims into turns by modulating local spinal circuit activity. In support of this, subsets of RS neurons form part of a population of v2a neurons in the hindbrain - a molecular subtype of glutamatergic cells which provide excitation to local spinal circuits during swimming in the form of tonic and phasic synaptic input (Kimura et al., 2013). Indeed, optogenetic stimulation and inhibition of v2a neurons is sufficient to drive and abolish spontaneous swimming behaviour respectively. Interestingly, the majority of v2a neurons are CiDs which are known to be myelinated in the larval stages (Koudelka et al., 2016).

Similar to the looming-evoked escape response, the OMR involves the processing of visual information prior to the release of motor commands that drive turning and forward swimming. Visual stimulus information is transmitted to the optic tectum via RGCs, here binocular information is integrated and behavioural output determined via recruitment of the nMLF for forward swims by and vSPNs for turning (Naumann et al., 2016).

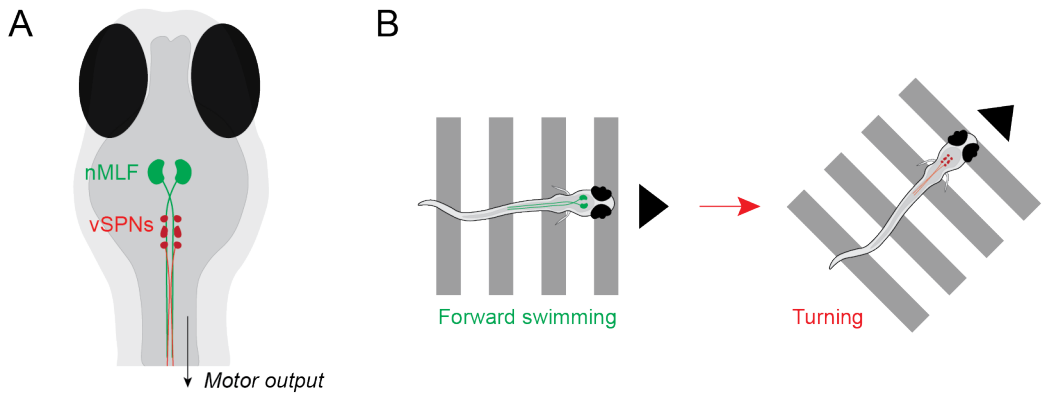

Figure 4.4: Reticulospinal neurons involved in driving forward swims and turns during the optomotor response and swimming behaviour
(A.) Forward swims are driven by neurons belonging to the nucleus of the medial longitudinal fasiculus (nMLF) while turns are mediated by ventral spinal projection neurons (vSPNs). **(B.)** Illustration of an optomotor stimulus driving forward swimming and turning behaviour.

Reticulospinal neurons and hunting behaviour

Hunting behaviour manifests from 5dpf and represents one of the most sophisticated behaviours displayed at this stage of development. Individual hunting epochs (events) consist of complex sequences of kinematically distinct modules of behaviour consisting of saccadic convergence of the eyes, 'J turns' and capture swims (Bianco et al., 2011; Borla et al., 2002; McElligott and O'Malley, 2005; Trivedi and Bollmann, 2013). Underlying the complexity of hunting behaviour is the ability of larvae to adapt axial control over multiple bouts within an epoch. Initially, multiple J turns – characterised by unilateral, far caudal tail bends (Figure 4.5B, first frame) - orient the larvae into an optimal position to strike its prey (Bianco et al., 2011; McElligott and O'Malley, 2005). Contrastingly, the capture swims which finalise the hunting sequence are high velocity events produced by a shift from caudal to rostral tail bending, high tail beat

frequency and large tail bend amplitude (Borla et al., 2002) (Figure 4.5B, final frame). Thus, hunting represents an adaptive locomotor response which requires fine rostral to caudal control of locomotion.

Hunting behaviour is entirely visually guided in larval zebrafish (Gahtan, 2005; McElligott and O'Malley, 2005). Visual information is transmitted from the retina to the retinal ganglion arborisation fields and tectum, where neurons analyse specific features of the visual stimulus, such as size, contrast and speed of movement, to allow recognition of prey. Motor outputs are mediated via downstream circuits that control the RS system, to allow approach behaviour, and oculomotor neurons, to permit ocular saccadic convergence (Bianco and Engert, 2015). The pathways that mediate information transfer between the tectum and reticulospinal system are less well characterised, however it is suggested that the RS system may be recruited via subsets of neurons in the recently defined ipsilateral tectobulbar tracts (Helmbrecht et al., 2018). RS neurons that are known to be involved in hunting behaviour include the MeLr and MeLc neurons of the nMLF. Ablation of these neurons significantly impairs prey capture whereas Mauthner and other RS neurons have been shown to be dispensible for prey capture behaviour (Borla et al., 2002; Gahtan, 2005). The complexity of hunting behaviour suggests that local control mechanisms such as central pattern generation (CPG) activity, rostral to caudal excitation of motor neurons and spinal interneuron activity are required to modulate unilateral J-turns and their transition into capture swims, although these mechanisms are less well understood (Borla et al., 2002; McElligott and O'Malley, 2005).

Conclusion

This is by no means an exhaustive list of RS-mediated behaviours. However, even this small number of examples is enough to provide an appreciation of the complexities of the RS system. For some behaviours functionally distinct groups of neurons exist, for example: turning behaviour is completely abolished by the ablation of vSPNs (Huang et al., 2013), whereas other behaviours such as the escape response involve distributed activity across many RS neurons (Gahtan et al., 2002). In the context of the escape response, ablation of the Mauthner cell does not abolish the behaviour completely but simply prolongs its latency (Burgess and Granato, 2007). Additionally, individual RS

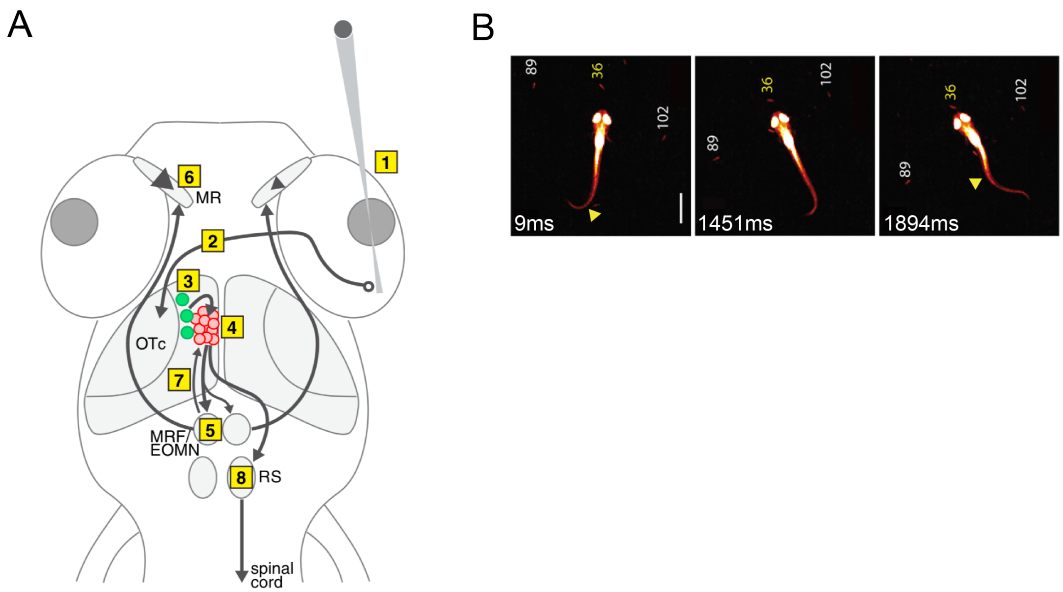

Figure 4.5: The circuitry underlying hunting behaviour
(A.) Proposed circuitry for prey detection and initiation of hunting behaviour. Overview of the pathway involved (not all-inclusive): (1) RGCs in the retina detect a prey-like stimulus. (2) Visual information is transmitted to RGC arborisation fields in the contralateral hemisphere. (3) Non-linear mixed selectivity neurons (NLMS, green cells), selective for stimulus features that are prey-like, are activated at corresponding locations in the tectum. (4) NMLM neurons recruit tectal assemblies (red cells). (5) Tectal assemblies also recruit circuits in the mesencephalic reticular formation (MRF) which drive a saccadic motor program involving activation of extra-ocular medial rectus motoneurons (EOMNs) in the oculomotor nucleus. (6) EOMNs control eye movement to drive ocular convergent saccades. (8) Tectal assemblies activate reticulospinal (RS) neurons which recruit spinal circuits required to produce an orienting turn towards the visual target. Taken from Bianco and Engert (2015). **(B.)** Video frames of a hunting routine in which a j-turn is depicted in the first two images, followed by a burst/capture swim in the last. Adapted from Henriques et al. (2019)

neurons can be recruited over multiple different behaviours e.g. nMLF for hunting and forward swimming. With such a diverse locomotor repertoire, it has been suggested that different modules of the RS system may combine to produce individual behaviours (Huang et al., 2013; Thiele et al., 2014). With this in mind, the marked hypomyelination observed throughout the ventral tracts of the spinal cord in our Myrf$^{-/-}$ mutants could be predicted to disrupt the function of multiple RS mediated behaviours. However, it is also possible that the flexibility in behaviour provided by such a diverse array of neurons could protect against the effects of hypomyelination in which case we may only expect to see phenotypes involving functionally distinct groups of neurons. Given the functional importance of the Mauthner axon in sustaining SLCs to mechanosensory stimuli, and the traditional role of myelin in maintaining action potential conduction speed, we would predict to detect a phenotype in escape behaviour in Myrf$^{-/-}$ mutants

which possess severely hypomyelinated Mauthner axons. Such phenotypes in the startle response have been noted in both zebrafish PNS and mice CNS hypomyelination models before (Poggi et al., 2016; Pogoda et al., 2006) supporting this as an initial behaviour for interrogation. Indeed, the Mauthner system itself would represent a relatively simplistic and accessible circuitry for ongoing functional assessment. However, the extensive circuitry underlying other RS mediated behaviours provides us with the opportunity to investigate the effects of myelination on the control of action potential timing across more *complex* circuitry, allowing interrogation of the function of myelin away from simple conduction speed propagation along individual axons. As this is the first time that behavioural characterisation has been performed on a zebrafish CNS model of hypomyelination, we cast the net wide and performed in-depth behavioural phenotyping across an extensive range of locomotor behaviours.

4.2 Materials and Methods

Behaviour set up for free-swimming larvae

The free swimming behaviour rig, software and original analysis scripts were designed and written by Dr. Isaac Bianco (Department of Neuroscience, Physiology and Pharmacology, UCL). All experiments were performed by myself at UCL with guidance from Dr. Isaac Bianco and his group members. All behavioural experiments on this rig were conducted at 6dpf using larvae from Myrf tg(mbp:eGFP-caax) heterozygous adult in crosses. Larvae were produced and maintained within the UCL zebrafish facility and were not transported from the University of Edinburgh to avoid confounding effects on behaviour. **All larvae used for behavioural experiments were produced from third generation lines or younger**. Larvae were raised on a 14/10 hour light/dark cycle at a temperature of 28.5°C and a maximum stocking density of n = 50. At 5dpf, larvae received a live feed of paramecia and a water exchange. On the same day, larvae were anaesthetised with tricaine and screened using an epifluorescence microscope (Nikon Intensilight C-HGFI Precentered Fiber Illuminator and Nikon SMZ1270 stereomicroscope) for reduced expression of green fluorescent protein. This allowed pre-selection of mutants prior to behavioural experiments, allowing adequate numbers to be tested. Wild type and heterozygous siblings are indistinguishable from each other using this technique and thus throughput of larvae belonging to these geno-

types was dependent on mendelian ratios. Larvae were recovered from anaesthesia and placed individually into a 35mm petri dishes (the behavioural arena) containing 3.5ml fresh fish facility water and given a fresh feed of live paramecia before being returned to the incubator overnight. The outer rims of the behavioural arenas were lined with black tape in an attempt to minimise thigmotactic behaviour during the assay. On the morning of experimentation, the arenas were removed from the incubator and placed into an acclimation zone in the behaviour suite at 26°C. Embryo media was exchanged and 200 paramecia added to each dish prior to the assay.

The behavioural arena was placed onto a transparent plastic platform lined with light diffusing paper (#3026, Rosco Cinegel). The arena was illuminated from below with an infrared LED panel. Images were recorded using an infrared sensitive high speed camera (eOsENS CLCmc1362, Mikrotron GmbH) mounted with a fixed aperture lens (35mm) with a bandpass filter attached to block visible light. Images from a projector (P2 JR pico projector, AAXA technologies) were reflected off a cold mirror and back projected onto the diffusive paper. Imaging and tracking were performed using a camera frame rate of 700Hz. Online tracking and stimulus presentation were controlled with custom built software using LabVIEW (National Instruments, Newbury, UK) and MATLAB (Mathworks, Cambridge, UK).

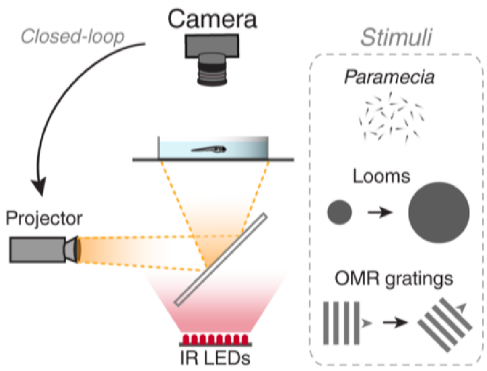

Figure 4.6: Behavioural rig for free swimming larva
The larva is placed in a 35mm petri dish on top of a platform which is illuminated from below by a panel of LED lights. Tracking of the larvae is performed by a camera positioned above the behavioural arena, at a rate of 700Hz. Information concerning the location and movement of the larvae is used to drive the presentation of visual stimuli via a closed-loop system. Visual stimuli are projected onto the platform via a 45°cold-mirror. Figure taken from Antinucci et al. (2019).

Live tracking

Larval zebrafish were tracked by their centroid position, determined by background subtraction on live images and calculation of an absolute value for each pixel. Thresholds were manually adjusted for the accurate detection and tracking of the body and eyes at the start of each experiment. Eye angles were determined by fitting an ellipse to each eye and recording the angle between the long axis of the ellipse and a line parallel to the midline of the larvae. Eye movements to the right are indicated by increases in values (movement clockwise from the midline) and eye movements to the left are indicated by decreases (movement anticlockwise from the midline). Tail tracking records the x,y coordinates of 9 equidistant points from the caudal swim bladder to the tip of the tail, these can subsequently be used to calculate angles of the resulting 8 segments of the tail. Raw data is saved in real time in .xls format and consists of: timestamp, fish centroid x position, fish centroid y position, orientation (radians), left eye angle, right eye angle and x-y coordinates of 9 points along the tail. The timings of visual stimulus presentations are also recorded. Background subtracted footage was recorded for a subset of larvae to ensure appropriate tracking and confirmation of computed parameters.

Visual stimuli

Visual stimuli were designed using Psychophysics Toolbox Version 3 (Brainard, 1997) and driven using LabVIEW software (National Instruments, Texas, USA). The parameters of looming stimuli are represented by the ratio between their length and velocity (L/V ratio). Looming spots were presented with a fixed L/V ratio of 255ms and expanded from 10 degrees to 100 degrees in size (Dunn et al., 2016). Optomotor gratings were delivered at 8mm/sec for 6 seconds. Optomotor gratings and looming spots were presented in relative direction to the fish such that directional gratings always moved 90 degrees to the left or right side of the fish and looming spots were centred 5mm from the fish centroid and at 90 degrees to the left or right side. Visual stimuli were presented in random order with an inter-stimulus interval of minimum 30 seconds. Stimuli were only presented to fish if their centroid was positioned in the 'in middle' defined region of the dish (set at 280-300pixels) to ensure that behavioural responses are not interrupted due to the close proximity of the edge of the arena and to prevent tracking faults. If fish were not occupying this area then the stimulus trigger would wait until they return

to the 'inmiddle' zone. To encourage fish to move back into the inner area concentric circular directional gratings directed into the centre of the dish were projected to the entire arena.

Calculation of general parameters

All data analysis was performed using custom-written code in MATLAB. Raw data was processed using the Bianco Lab AFAP repository (Bitbucket, Atlassian, Australia). Brief descriptions of how main parameters used for analysis were calculated from raw data are as follows:

-**Orientation:** The raw orientation value is converted from radians to degrees and used to calculate cumulative orientation and change in orientation over time

-**Ocular vergence angles:** Ocular vergence at each timepoint is computed as the left ocular angle minus right ocular angle.

-**Centroid velocity:** Pythagorean theorem $x^n + y^n = z^n$ is used to calculate the distance between the x and y coordinates at each time point. This distance is converted into speed by taking the change in distance between frames and multiplying by frame rate and camera scale to obtain values for speed in units of mm/s. Centroid velocity represents the speed of movement of the *body* of the larvae. The start and end of swim bouts are detected using a threshold of 1.5mm/s and a minimum bout duration of 280 frames (400ms) applied to a 100ms filtered centroid velocity trace (see Figure 4.7)

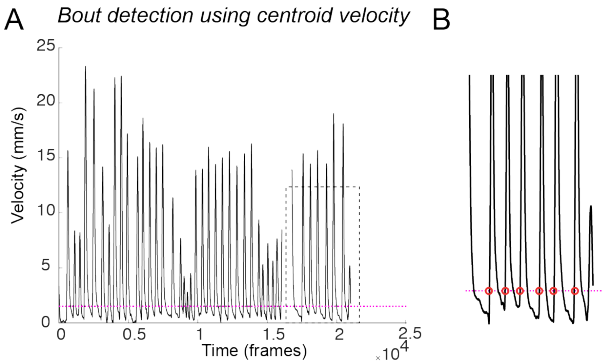

Figure 4.7: Bout detection using centroid velocity
(A.) Smoothed centroid velocity trace for a 30 second period (black trace). Magenta line marks the threshold for bout detection (1.5mm/s). **(B.)** Enlarged view of the region outlined with a dashed box in (A.). Red circles mark the computed onset of swim bouts.

Definitions of tail kinematics parameters

During online tracking, the x-y coordinates of 9 equidistant points along the tail (starting from behind the swim bladder) were recorded. These values were used to compute the inter-segment angle between the 8 resulting segments. This data was then interpolated to construct values for 11 tail segments (i.e. existing data was 'stretched' across 11 points and values estimated for the additional segment angles using existing data for the 8 segments. This step is required to allow the dataset to be compatible with analysis from two-photon imaging pipelines which are also used in the Bianco Lab). For the computation of tail parameters, a swim bout was detected using the vigour and angle of the tail (Figure 4.8). This is a more sensitive indicator for the start of a swim bout given that the tail must start moving before body acceleration (centroid velocity) is achieved. Additionally, multiple 'tail bouts' can be found within one 'centroid bout' given that tail movements may stop and start while a fish is still gliding through the water. Tail vigour represents the smoothed, absolute angular velocity trace of the 11th tail segment (Figure 4.8). To screen the data for bouts, a threshold of 1100°/sec for bout onset and 700°/sec for bout offset is applied to the tail vigour data (green line, Figure 4.8A). The start and end of bouts are then fine tuned using the tail angle threshold for the same tail segment, with a threshold of 20°for bout onset and offset (black line, Figure 4.8A). Threshold values were checked against raw data to ensure they were appropriate for the detection of true swim bouts prior to application across the entire dataset. Once a swim bout was detected in this way, specific parameters of tail movement were extracted from the cumulative angle trace for all tail segments (Figure 4.8B). Swim bouts consist of alternating left or right tail deflections, termed 'half cycles' or 'half beats' (pink dashed line, Figure 4.8B). Half cycles were detected by finding the local maxima in velocity of the 9th tail segment (trace not shown, but location represented by pink dots). After segmenting the tail bouts into half cycles, tail kinematic parameters for each bout were computed in the following way:

-**Tail angle:** the cumulative sum of all tail segment angles. Positive values indicate rightward bending whereas negative angles indicated leftward bending.

-**Mean and maximum tail beat frequency:** reciprocal of the mean and maximum full-cycle period during a swim bout (hertz).

-**Tail vigour:** sum of the absolute tail angular velocity (40ms smoothed and box car

filtered) values over the first 120ms of the bout (arbitrary units (a.u.))

-**Tail velocity:** the maximum angular velocity (°/sec) detected across the bout using the 11th tail segment.

-**Theta1:** The maximum tail angle during the first half beat.

-**Theta2:** The maximum tail angle during the first half beat of the second tail cycle.

-**Vel1:** The maximum tail velocity during the first half beat.

-**Duration:** Duration of time (ms) between the onset and offset of the bout - as defined using threshold parameters applied to the 11th tail segment.

-**Forward and lateral displacement:** Forward and lateral distance moved.

Tail kinematics were only analysed for 'inmiddle' data where tail tracking was most accurate. When larvae enter the outer zone of the arena, the wall of the arena can interfere with movement and tail tracking making values unreliable. For analysis of tail parameters during spontaneous swimming, swim bouts which occurred during hunting routines (defined by high ocular convergence) or during visual stimulus presentation were excluded.

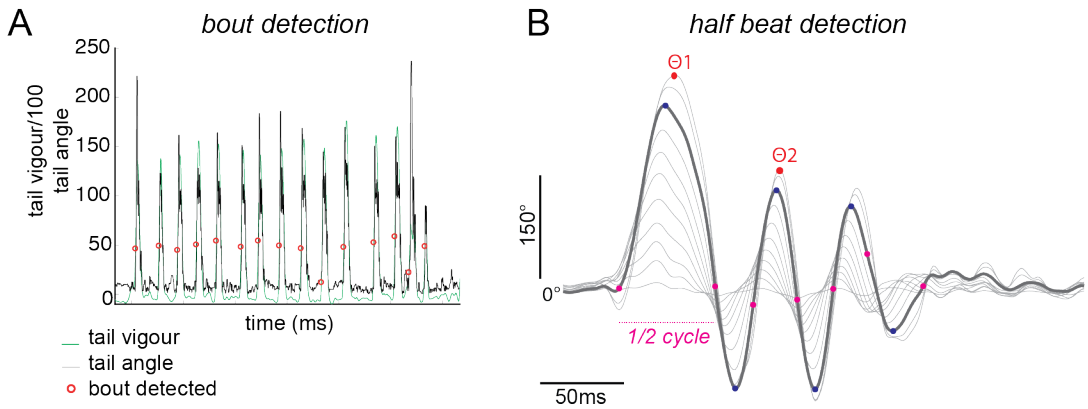

Figure 4.8: Bout detection and half beat analysis using tail tracking data **(A.)** Example trace of tail vigour (green) and tail angle (black) with the start of detected bouts marked with red circles. Tail vigour values have been divided by 100 to allow representation of both traces on a similar scale. Traces were checked across a subset of fish and bout detection parameters deemed accurate at the current settings (threshold = 1100 a.u. for tail vigour, and 20°for tail angle). **(B.)** Cumulative angle trace for all 11 tail segments (grey lines). Pink dots mark the local maxima in tail velocity, these represent the turning points or 'half cycles' of the swim bout. One 'half beat' or 'half cycle' represents the period in between two pink markers (marked on this graph with a pink dashed line). Blue solid markers label the peak amplitude of the 9th tail segment during one half cycle. Red solid markers label theta1 and theta2 angles, the maximum angle found across all segments. In this bout, theta1 angle = 205°and theta2 angle = 114°.

4.3 Results

To assess locomotor behaviours in Myrf$^{-/-}$ larval zebrafish mutants we collaborated with the groups of Dr. Isaac Bianco (University College London, London) and Professor Michael Granato (University of Pennsylvania, Philadelphia, USA). It was important to test our mutants on established behavioural rigs to identify dependable behavioural phenotypes for ongoing pursuits. The behavioural rig in the Bianco lab is specifically designed to allow in-depth phenotyping across multiple RS-mediated behaviours in *individual* free swimming larvae - providing a goldmine of data for each fish, at the cost of a lower throughput (Antinucci et al., 2019; Henriques et al., 2019). In the Granato lab, behavioural assays have long been established for testing the escape response and its modulation in a high-throughput format (Burgess and Granato, 2007; Wolman et al., 2011).

4.3.1 Myrf$^{-/-}$ mutants display a delayed latency to escape response and a bias towards long latency responses

Given the severity of hypomyelination affecting the Mauthner axons of the RS system in Myrf$^{-/-}$ mutants, we predicted that conduction velocity along this axon would be delayed resulting in an increase in the latency to an escape response. Indeed, the escape response and its modulation during pre-pulse inhibition have been identified as behavioural phenotypes in rodent and zebrafish models of disrupted myelination in the past (Poggi et al., 2016; Pogoda et al., 2006; Tanaka et al., 2009). With this knowledge, we wanted to establish whether similar phenotypes existed by testing the escape response and its modulation in Myrf$^{-/-}$ mutants. This work was kindly performed by Elelbin Ortiz (Granato Lab) in parallel to my own work in the lab of Dr. Isaac Bianco. Details on the methodology for these experiments can be found in Appendix 2.

Larvae were arrayed in a custom built 36 well plate (Figure 4.9A) and provided with mechanosensory stimuli at 20 second intervals via an amplifier. Across multiple trials, Myrf$^{-/-}$ mutants were found to exhibit, on average, a 28% increase in latency to escape response compared to wild type ($p = 0.0009$, Kruskal-Wallis test followed by Dunn's multiple comparisons) and heterozygous siblings ($p = 0.0007$, Kruskal-Wallis test followed by Dunn's multiple comparisons) (Figure 4.9B). This phenotype persisted with a subsequent repeat of the experiment (Appendix 2, Figure 5.9). Plotting all

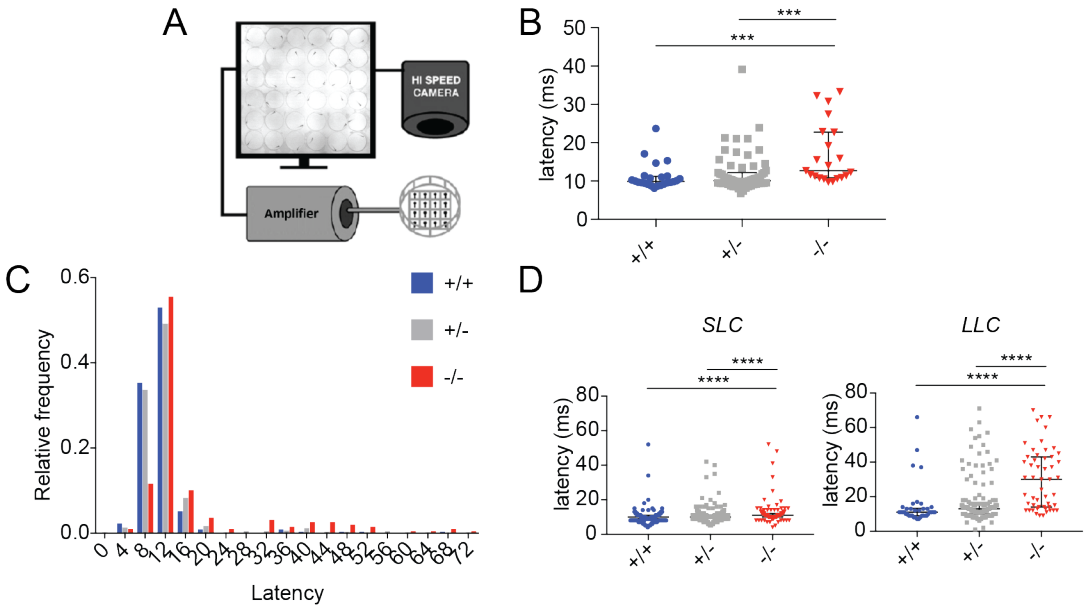

Figure 4.9: High throughput assessment of the escape response
(A.) Schematic of the behavioural rig used to test mechanosensory startle responses (figure provided by Elelbin Ortiz, Granato Lab, UPenn). **(B.)** Mean latency value per fish across multiple trials. Median (IQR): 9.9 (9.26 to 11.25ms) in wild types, 10.10 (9.38 to 12.20ms) in heterozygotes and 12.67 (10.84 to 22.78ms) in homozygous mutants (p = 0.0003, Kruskal-Wallis test. Dunn's multiple comparisons: WT-Het ns, WT-Hom p = 0.0009, Het-Hom p = 0.0007). N = 24 WT, N = 63 Het, N = 21 Hom. **(C.)** Relative frequency histogram displaying the distribution of all escape events per genotype. **(D.)** Escape events are split into SLCs or LLCs according to their angular velocity (>19°/sec). **SLC:** Average latency to SLC is 10 (9 to 11)ms in wild types, 10 (9 to 11)ms in heterozygotes and 11 (10 to 12)ms in homozygotes (p = <0.0001, Kruskal-Wallis test, Dunn's multiple comparisons: WT-Het p = >0.99, WT-Hom p = <0.0001, Het-Hom p = <0.0001) n = 171 WT events, n = 422 Het events, n = 135 Hom events. **LLC:** Average latency to LLC is 11 (9 to 13.25)ms in wild types, 13 (10 to 16)ms in heterozygotes, 30 (14 to 42)ms in homozygous mutants (p = <0.0001, Kruskal-Wallis test. Dunn's multiple comparisons test: WT-Het p = 0.22, WT-Hom p = <0.0001, Het-Hom p = <0.0001) n = 38 events WT, n = 138 events Het, n = 52 events Hom. Values and error bars represent median and IQR

escape events as a frequency distribution histogram (Figure 4.9C) demonstrates a shift towards longer latency responses in Myrf$^{-/-}$ mutants. To establish whether this phenotype was due to delays in SLC (mauthner mediated) or LLC (non-Mauthner mediated) responses, data points were segmented into SLCs or LLCs for comparison. SLCs and LLCs are usually classified according to their latency, but in this situation that would not be an appropriate means to split the data given that latency is not an independent variable. Therefore an alternative parameter, angular velocity, was used to segment the data. SLCs usually display an angular velocity >19°/sec whereas LLCs display slower angular velocity responses (Burgess and Granato, 2007). Segmenting the data using this parameter revealed a significant delay in both SLCs and LLCs in Myrf$^{-/-}$ mutants

compared to wild type and heterozygous siblings (Figure 4.9D), although the effect size was much greater for LLCs with over a two fold delay in latency. This finding implies that action potential conduction delays are occurring across all neurons of the Mauthner system. To question whether a bias existed in the type of escape response recruited by larvae, a ratio of SLC:LLC response was calculated from all events per genotype. Interestingly, wild types displayed a 4.5:1 ratio of SLC:LLC, heterozygotes 3:1 and homozygous mutants a 2.6:1 ratio. This suggests a shift towards non-Mauthner mediated responses, given that SLCs rely on Mauthner activity. Additional tests of pre-pulse inhibition and short term habituation of the escape response were unremarkable in Myrf$^{-/-}$ mutants compared to wild type and heterozygous siblings (data not shown).

The identification of a latency phenotype in the Myrf$^{-/-}$ mutant was predictable yet played an integral part in the establishment of this model for investigation into other RS-mediated behaviours. Knowing that we can detect behavioural indicators of action potential conduction delays across a simple circuit i.e. the Mauthner system, we set out to show that myelination is required for the control of timing across more complex, integrated behaviours by performing in depth locomotor phenotyping of individual larvae during the performance of spontaneous and stimulus driven behaviours.

In-depth phenotyping of RS-mediated behaviours in individual free-swimming larval zebrafish

For detailed analysis of RS mediated behaviours we collaborated with Dr. Isaac Bianco and his group (Department of Neuroscience, Physiology and Pharmacology, University College London, London). The locomotor behaviour of freely swimming individual 6dpf larvae was recorded on a custom made behaviour rig (see Figure 4.6) over a duration of approximately 50 minutes. During this time larvae were presented with optomotor gratings and looming visual stimuli at regular intervals in a pseudorandom order, amongst a background of spontaneous swimming and hunting behaviour. Online tracking of body, eye and tail movements was performed during the assay allowing post-hoc extraction and in-depth analysis of multiple kinematic parameters across the suite of spontaneous and stimulus driven behaviours. In this results section, I will present the results from each behaviour individually and return to summarise the key findings in the discussion.

4.3.2 Myrf$^{-/-}$ mutants perform normal loom-evoked escape responses

Having established a phenotype in the escape response to mechanosensory/auditory stimuli (Section 4.3.1), I set out to establish whether this phenotype was persistent when escapes were induced using another sensory modality - visual looming stimuli. Looming-evoked escape behaviour involves the transformation of complex visual information into motor commands required to execute an escape. Thus, this assay provides us with the opportunity to interrogate the effects of hypomyelination on both the reticulospinal and central sensory processing components of this circuitry. It is important to note that escape responses induced by looming stimuli are different to those observed in response to mechanosensory and light flash stimuli, for which the SLC and LLC behaviours are very specific (Marques et al., 2018).

Detection of looming-evoked escape events

Escape responses induced by looming stimuli were identified as centroid velocity values exceeding 75mm/s between the stimulus onset and stimulus offset times. Exact escape onset was defined as the point at which angular velocity exceeded 5300°/s (as per Burgess and Granato (2007) criteria of a change in 16°over 3ms). If angular velocity did not exceed this threshold during the stimulus presentation then the time point at which centroid velocity exceeded 75mm/s was taken as the escape onset. Once escape events had been detected programatically using these thresholds, cumulative orientation traces were plotted for each escape event (Figure 4.10B) and checked manually to ensure adequate tracking and detection of escape onset prior to inclusion in the analysis. Events were excluded from analysis if tracking was suboptimal. The critical angle (size of loom stimulus that triggers an escape) was calculated as the radius of the looming stimulus at the time of escape onset. The initial bend angle was defined as the amplitude of the first peak in cumulative orientation trace following escape onset as shown in Figure 4.10B (Burgess and Granato, 2007). Duration of the initial c-bend, angular velocity and maximum tail angle were calculated between escape onset and initial bend angle.

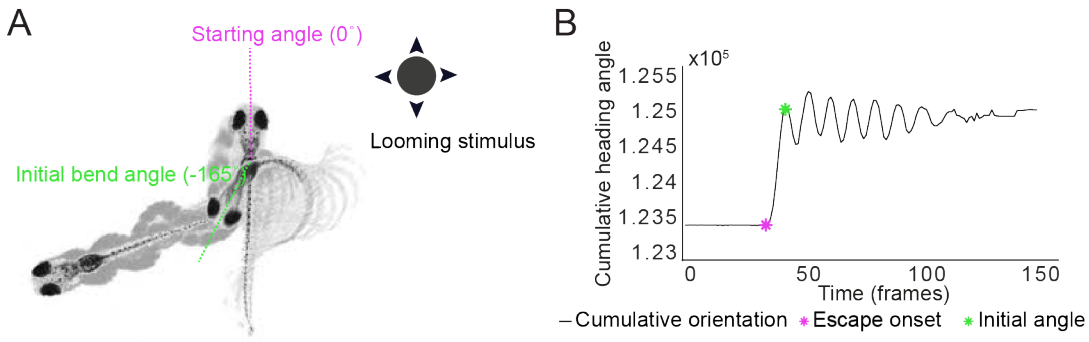

Figure 4.10: Detection and calculation of loom escape kinematics
(A.) An image of the escape response of a zebrafish demonstrating how the angle of an escape response (c-bend) is calculated. The initial bend angle is calculated as the difference between the starting angle (pink) and the maximum initial bend angle (green). Adapted from Bhattacharyya et al. (2017). **(B.)** An example of a cumulative heading angle trace from an escape response such as that in (A.). The pink asterisk defines starting angle at escape onset (change in angular velocity exceeding 5300°/sec) and the green asterisk marks the maximum initial bend angle. The initial bend angle is the difference between these two points (150°in this example)

Kinematics of loom-evoked escape responses are preserved in Myrf$^{-/-}$ mutants

Response rates were calculated as the absolute proportion of looming stimuli that each larvae responded to, the average of these is presented for each genotype (Figure 4.11A). Response rates were found to be similar across all groups ($p = 0.62$, one-way ANOVA) (Figure 4.11C), demonstrating that Myrf$^{-/-}$ mutants perceive and respond to visual threat in a similar manner to their siblings. In support of this, the critical angle (the size of the loom) at the time of escape response initiation was also similar between groups ($p = 0.36$, one-way ANOVA) (all Figure 4.11 C). This critical angle is close to published values which present stimuli at the same L/V ratio, confirming that larvae are responding at an appropriate threshold (Antinucci et al., 2019; Bhattacharyya et al., 2017; Dunn et al., 2016). As looming stimuli are only released when the larva is in the middle of the behavioural arena, interstimulus interval time was computed for each fish to ensure that stimuli were presented at a similar frequency. For example, if one group spent more time in the centre of the arena and subsequently received more stimuli, they may habituate faster causing a falsely low response rate compared to other groups. The interstimulus interval for looming stimuli was close to 60 seconds across all groups ($p = 0.44$, Kruskal-Wallis test), consistent with the program settings which provide either an OMR or looming stimulus every 30 seconds if larvae meet the 'inmiddle' condition.

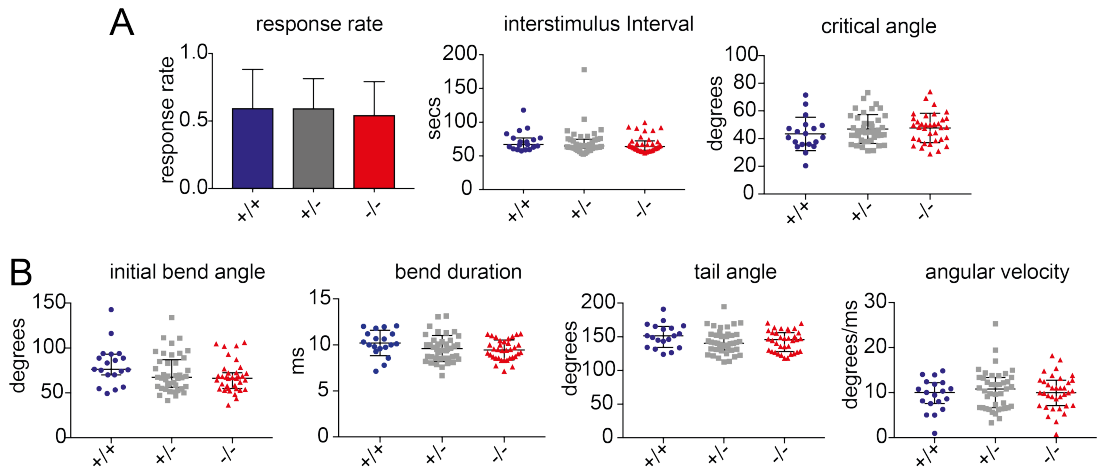

Figure 4.11: Kinematic analysis of looming-evoked escape responses
(A.) Response rate: The proportion of the presented looming stimuli that induced an escape response was: 0.59 ± 0.29 in wild type, 0.59 ± 0.22 in heterozygotes and 0.55 ± 0.25 in homozygous mutants (F (2,95) = 0.48, p = 0.62, one-way ANOVA). **Interstimulus interval:** Average intervals between loom presentations were 66.86s (60.36 to 76.54)s for wild types, 64.71s (61.66 to 74.74)s for heterozygotes and 63.89s (58.01 to 72.32)s for homozygous mutants (p = 0.44, Kruskal-Wallis test). **Critical angle:** The critical angle at escape onset was 43.36 ± 12.1°in wild types, 46.89 ± 10.44°in heterozygotes and 47.7 ± 10.65°in homozygous mutants (F (2,92) = 1.033, p = 0.36), one-way ANOVA). **(B.)** C-bend kinematics: **Initial angle:** The maximal initial bend angle achieved was 76.34°(70.01 to 93.25°) in wild types, 67.45°(56.07 to 86.92°]) in heterozygotes and 66.36°(54.76 to 72.49°) in homozygous mutants (p = 0.08, Kruskal-Wallis test). **Bend duration:** The initial bend lasted for 10.21 ± 1.38ms in wild types, 9.61 ± 1.43ms in heterozygotes and 9.45 ± 1.09ms in homozygous mutants (F (2,92) = 2.164, p = 0.12, one-way ANOVA). **Angular velocity:** On average, wild type larvae achieved an angular velocity 10.05 (7.57 to 12.21)°/ms. Heterozygotes reached 10.82 (6.64 to 13.37)°/ms and homozygous mutants achieved 9.99 (7.11 to 12.77)°/ms (p = 0.81, Kruskal-Wallis test). **Tail angle:** Maximum tail angle was 151.5 (134.3 to 165.4)°in wild types, 140.4 (130.6 to 153.6)°in heterozygotes and 145.8 (128.1 to 156.1)°homozygous mutants (p = 0.17, Kruskal-Wallis test). Values and error bars represent median and IQR for interstimulus interval, initial angle, angular velocity and tail angle. Error bars represent mean ± standard deviation for response rate, latency to response, critical angle and bend duration. N = 19 WT, N = 41 Het, N = 35 Hom.

The kinematics of the escape response were calculated in a similar manner to Burgess and Granato (2007) and compared across groups. No significant differences were found between groups across all four kinematic parameters assessed (Figure 4.11B), however, mutants displayed a modest trend towards a smaller initial bend angle (median (IQR): 66.36°(54.76 to 72.49°)) than their wild type siblings (76.34°(70.01 to 93.25°)), with heterozygotes occupying an intermediate trend (67.45°(56.07 to 86.92°)) (p = 0.08, Kruskal-Wallis test).

Conclusion on looming-evoked responses

In summary, there were minimal differences in the kinematics of loom-evoked escape responses between Myrf$^{-/-}$ mutants and their siblings. However, the kinematic data across Myrf larvae of *all* genotypes deviates from what is published in the literature. As I described in my introduction, larval zebrafish are able to demonstrate flexibility in their response to certain stimuli. As such, behaviours that are recruited to allow escape from a looming stimuli are variable and can consist of (in order of most likely) spot-avoidance turns, O-bends, routine turns, high angle turns and slow swims (Marques et al., 2018). In my data, the wild type values values obtained for each kinematic parameter of the loom-evoked escape behaviour (Figure 4.11B, initial bend angle: 76.34 (70.01 to 93.25)°, bend duration: 10.21 ± 1.38ms, angular velocity: 10.05 (7.57 to 12.21)°/ms) are lower than those described in published studies using similar behavioural assays. Dunn et al. (2016) find an initial bend angles of 133.4 ± 2.1°, with a bend duration of 9.4± 0.1ms and angular velocity of 19.5 ± 0.2°/ms, similar to the kinematics for SLC responses to mechanosensory stimuli (c-bend angle: 105 ± 18°, c-bend duration: 7.5 ± 1.4ms, angular velocity: 22.5 ± 4.1°/ms) (Burgess and Granato, 2007). Thus, it seems likely that all larvae (regardless of genotype) from the Myrf line are performing escape behaviours which are perhaps more consistent with routine or high angle turns. Routine turns typically exceed 30° in heading angle, exhibit low angular velocities and do not demonstrate the classical counter bend angles and burst swim seen in escapes (Budick and O'Malley, 2000). The reason for these 'suboptimal' responses to looming stimuli is unclear but may be due to genetic background differences between larvae of the Myrf line and those recruited in the published literature. In conclusion, no overt differences were detected in the performance of loom-evoked escape responses between genotypes. However, because loom-evoked escape behaviour appears to be unreliable in this line, we cannot confidently state whether or not this behaviour is truly affected by hypomyelination in Myrf$^{-/-}$ mutants.

4.3.3 Optomotor responses are maintained in Myrf$^{-/-}$ mutants

The optomotor response (OMR) is composed of turns and forward swims to match the direction and speed of whole field visual gratings over the duration of stimulus presentation. RS neurons involved in this behaviour include the nMLF (Severi et al., 2014; Thiele et al., 2014) and vSPNs (Huang et al., 2013; Orger et al., 2008). Therefore,

driving this behaviour provides a means to test the function of another subset of RS neurons outside of the Mauthner system. In contrast to loom avoidance behaviour, the OMR response requires *continuous* integration of visual information and performance of a matching behavioural output. Thus, we could predict that larvae may struggle to modulate their swim speed and direction to the optomotor gratings over time.

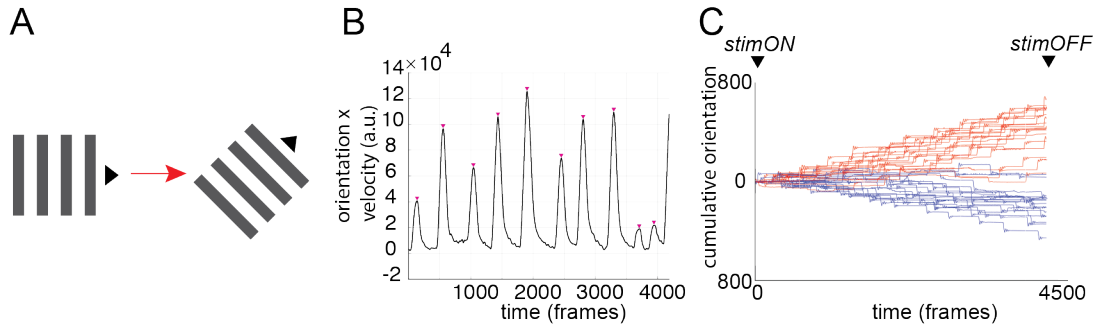

Figure 4.12: Detection of optomotor responses
(A.) Illustration of an optomotor stimulus. Optomotor gratings had a period of 10mm and moved at 1 cycle/sec for 6 seconds (4200 frames). Stimuli were presented on a closed loop locked to the orientation of the larva. **(B.)** Example of the trace obtained by multiplying the orientation of the larva by velocity. Bouts were detected using peak detection with a threshold of 5000a.u. **(C.)** Example of cumulative orientation traces over stimulus duration for all stimulus presentations over one experiment (red = right OMR stimuli, blue = left OMR stimuli.

Detection of optomotor responses

The timings of optomotor stimulus presentation were extracted from the raw data. Cumulative orientation plots (Figure 4.12C) during stimulus presentation were screened manually and fish were excluded if tracking quality was poor or few responses were observed. Optomotor responses for each fish were analysed if tracking data was available for the entire stimulus presentation and the fish was not already moving at the time of stimulus onset. OMR induced swim bouts were identified by detecting peaks (threshold = 5000 a.u. for peak detection) in the trace obtained by multiplying orientation data by filtered swim velocity values (100 frames box-car filter) as per the methods of Naumann et al. (2016) (Figure 4.12B) . This step is performed to ensure that the bouts analysed are induced responses to the OMR stimuli rather than spontaneously occuring forward swims. Latency was defined as the time from stimulus onset to the first swim bout during an OMR presentation. General swimming and tail kinematic parameters were averaged across bouts for each OMR. A positive OMR response was defined as the

occurrence of more than 3 swim bouts over the duration of an OMR response. Response rate was then calculated as the proportion of the presented OMR stimuli that each larva responded to. The angular velocity of the response was defined as the total change in orientation divided by the length of stimulus presentation.

Main features of the OMR response are unchanged in Myrf$^{-/-}$ larvae

The main performance indicator of an OMR is the overall gain (angular velocity) achieved over the stimulus presentation period. The overall gain of response was invariable across genotypes suggesting that in general, Myrf$^{-/-}$ mutants perform this behaviour adequately (Figure 4.13A and 4.13C, angular velocity). General parameters such as response rate ($p = 0.39$, Kruskal-Wallis test), latency ($p = 0.46$, Kruskal-Wallis test) and bout number per OMR ($p = 0.45$, Kruskal-Wallis test) were also indistinct between groups (Figure 4.13B). Swim bout parameters including bout length ($p = 0.35$, Kruskal-Wallis test), velocity ($p = 0.80$, one-way ANOVA) and change in heading angle ($p = 0.16$, Kruskal-Wallis test) were also unchanged. Importantly, all computed swim bout values were within or close to published reference ranges suggesting that appropriate extraction and analysis of OMR behaviour had been performed (Naumann et al., 2016; Severi et al., 2014).

Tail kinematics during OMR swim bouts are preserved in Myrf$^{-/-}$ larvae

Ablation of vSPNs or nMLF neurons has been shown to have subtle effects on the kinematics of tail movement during turning and forward swimming respectively (Huang et al., 2013; Thiele et al., 2014). Additionally, Severi et al. (2014) demonstrated that modulation of tail beat frequency was required to achieve swim velocities to match different speeds of optomotor gratings. Although the OMR grating speed was fixed at 8mm/s in our experiments, we predicted that hypomyelination in the RS neurons mediating this behaviour may disrupt tail beat frequency and symmetry during the OMR. Using the repository of tail tracking data, I extracted data for relevant tail parameters during OMRs and compared them across genotypes. Computed values for a range of tail parameters were remarkably similar between genotypes (Figure 4.14) suggesting that this prediction was not true. In summary, optomotor behaviour was remarkably preserved in Myrf$^{-/-}$ mutants despite widespread defects in CNS myelination.

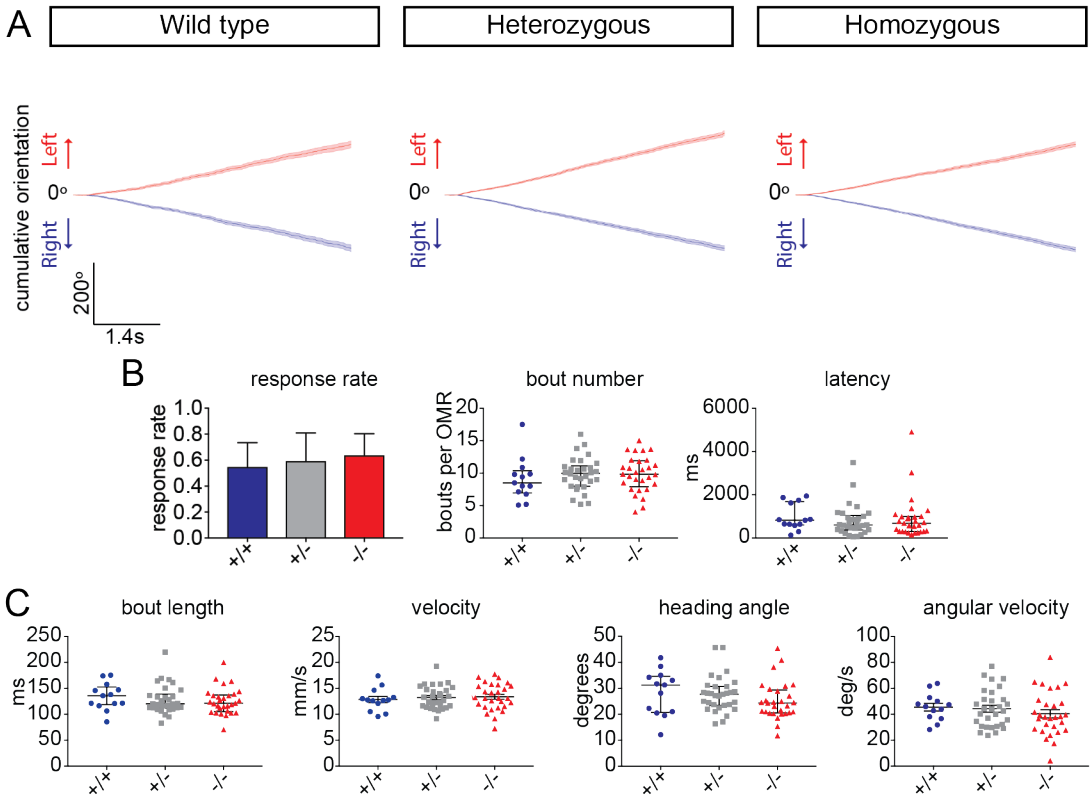

Figure 4.13: Quantification of optomotor responses.
(A.) Cumulative delta orientation of fish in response to leftwards (red) or rightwards (blue) OMR gratings in wild type, heterozygous and homozygous siblings. Lines represents the mean across all responses with shaded error bars representing SEM across responses. (WT: N = 15 fish, n = 691 responses (left) and 665 responses (right); Het: N = 40 fish, n = 848 respones (left) and 842 responses (right); Hom:N=34 fish, n = 750 responses (left) and 716 responses (right). **(B.)** General parameters: **Response rate:** On average, OMR response rate probability was 0.59 (0.39 to 0.68) for wild types, 0.62 (0.42 to 0.77) for heterozygotes and 0.66 (0.51 to 0.76) for homozygous mutant (p = 0.39, Kruskal-Wallis test). **Bout number per OMR:** The frequency of bouts within an OMR presentation reached 8.5 (6.93 to 10.38) bouts per OMR in wild types, 9.99 (7.97 to 11.13) bouts per OMR in heterozygotes and 9.85 (7.92 to 11.90) bouts per OMR in mutants (p = 0.45, Kruskal-Wallis test). **Latency:** Latency to first swim bout from onset of OMR stimulus was 823.4ms (609.6 to 1684ms) in wild types, 601.7ms (271.5 to 1046ms) in heterozygotes and 685.7ms (305.4 to 995.2ms) in homozygous mutants (p=0.46, Kruskal-Wallis test). Values and error bars represent median and IQR. **(C.)** Swim bout parameters: **Bout length:** On average bout duration was 135.7ms (118.6 to 152.3ms) in wild types, 120ms (111.9 to 138.9ms) in heterozygotes and 121.3ms (105ms to 137.3ms) in homozygous mutants (p = 0.35, Kruskal-Wallis test). **Velocity:** Mean velocity across bouts in an OMR was 12.85 ± 2.18mm/s wild type, 13.21mm/s ± 2.18mm/s heterozygotes and 13.37± 2.57 in homozygous mutants (F (2,69) = 0.2273, p =0.80, one-way ANOVA). **Heading angle:** Orientation changes during individual bouts reached 31.25 (20.75 to 24.63)° in wild types, 27.71 (23.44 to 30.73)° in heterozygotes and 24.34 (20.5 to 29.29)° in homozygous mutants (p = 0.16, Kruskal-Wallis test). **Angular velocity:** The angular velocity across the whole stimulus presentation was 45.45 ± 10.45°/sec in wild type, 44.3 ± 14.57°/sec in heterozygotes and 40.35 ± 17.01°/sec homozygous mutants (F (2,69) = 0.7357, p = 0.48, one-way ANOVA). Values and error bars represent median (IQR) for response rate, bouts per OMR, latency, gradient, bout length and orientation change. Values and error bars represent mean ± SEM for mean velocity and angular velocity. N = 13 WT, N = 30 Het, N = 29 Hom

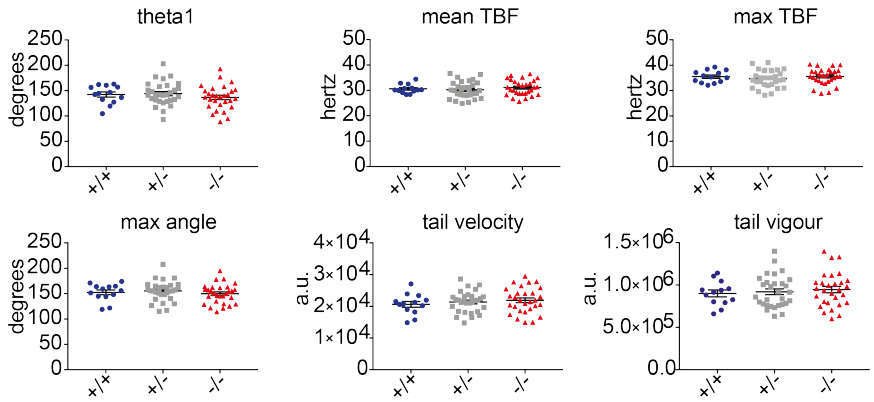

Figure 4.14: Tail kinematics during OMR
Top panel: Theta1 angle during OMR bouts: 142.5° ± 4.99° in wild types, 144.1° ± 4.10° in heterozygotes and 136.6° ± 4.38° in homozygous mutants (F (2,69) = 0.8933, p = 0.41, one-way ANOVA). **mean TBF**: 30.59 ± 0.49Hz in wild types, 30.24 ± 0.59hHz in heterozygotes and 31.3 ± 0.55Hz in homozygous mutants (F (2,69) = 0.6551, p = 0.52, one-way ANOVA). **Max TBF:** 35.52 ± 0.65Hz in wild type, 34.69 ± 0.62Hz in heterozygotes and 35.56 ± 0.59hz in homozygous mutants (F (2,69) = 0.6528, p = 0.52, one-way ANOVA). **Bottom panel: Maximum tail angle:** 152.5° ± 4.73° in wild types, 155.2° ± 3.59° in heterozygotes and 149.9° ± 3.55° in homozygous mutants (F (2,69) = 0.5927, p = 0.56, one-way ANOVA). **Tail velocity:** 2.1 x 10^4 ± 0.9 x 10^3°/s in wild types, 2.1 x 10^4 ± 0.6x 10^3°/s in heterozygotes and 2.2 x 10^4 ± 0.7x 10^3°/s in homozygous mutants (F (2,69) = 0.56, p = 0.57, one-way ANOVA). **Tail vigour:** 9.0 x 10^5 ± 0.4 x 10^5 a.u. in wild types, 9.2 x 10^5 ± 0.3 x 10^5 a.u. in heterozygotes and 9.5 x 10^5 ± 0.4 x 10^5 a.u. in homozygous mutants (F (2,69) = 0.30, p = 0.75, one-way ANOVA). N = 13 WT, N= 30 Het, N = 29 homozygous mutants. Values and error bars represent mean ± SEM

4.3.4 Hunting behaviour is unaffected in Myrf$^{-/-}$ mutants

Detection of hunting epochs

High ocular vergence angles are a robust detector of hunting behaviour in larval zebrafish (Bianco et al., 2011). To detect hunting bouts, the ocular vergence angles for each fish were plotted as a frequency distribution histogram (Figure 4.15B). Ocular vergence angles display a bimodal distribution where the second peak (high vergence angles) represent hunting behaviour. To compute a vergence threshold for each fish, two Gaussian curves were fitted to the distribution of the data and the threshold for high convergence (i.e. hunting) taken as the angle one standard deviation below the centre of the higher angle Gaussian curve. Angles above this threshold represent hunting epochs and were used to classify corresponding swim bouts as hunting bouts. The percentage of time spent hunting represents the proportion of the experiment length where the vergence angle exceeds the threshold. Fish were accepted for hunting behaviour analysis if this value was equal to or greater than 10%, to ensure that robust behaviour was available for hunting bout analysis. Using ocular vergence angles to de-

fine the start and end of hunting epochs, multiple parameters could then be extracted from the hunting bouts within each epoch (Figure 4.15A).

Main features of hunting behaviour are unchanged in Myrf$^{-/-}$ mutants

As one of the most intricate RS mediated behaviours, examination of hunting bout parameters could offer insight into the role of myelination in the coordination of complex spinal circuitry. To begin with, general hunting epoch parameters were assessed across genotypes (Figure 4.15C). On average, fish used for analysis of hunting behaviour spent 16.44 ± 4.23% of their time hunting with no statistical difference between groups (p = 0.65, one-way ANOVA). Ocular vergence angles increased to 61.01 ± 4.60° in wild types, 63.01 ± 4.56° in heterozygotes and 63.71 ± 3.34° in homozygous mutants (p = 0.29, one-way ANOVA), in line with published values for freely swimming larvae of the same age (66.9 ± 1.81°(mean ± std) (Bianco et al., 2011)). The duration of hunting epochs was comparable between groups (p = 0.28, one-way ANOVA) with a similar number of swim bouts forming each epoch (p=0.45, one-way ANOVA). These results are in keeping with published values for freely swimming larvae (2 to 4 J-turns per hunting routine) (McElligott and O'Malley, 2005). No differences were observed in the interbout interval, peak centroid velocity or change in orientation during hunting bouts (all Figure 4.15C).

Myrf$^{-/-}$ mutants maintain normal tail kinematics during hunting routines

Given the absence of an overt hunting phenotype at the level of the entire hunting *epoch*, I turned to the tail tracking data to investigate whether any disruption of axial control existed in the Myrf$^{-/-}$ mutants within hunting *bouts*. Remarkably, across all parameters tested no significant differences were identified in tail kinematics between groups during hunting behaviour (Figure 4.16). It has been shown that during J-turns the majority of cumulative tail angle is localised to the final 20% of the tail length (Bianco et al., 2011). Having observed an increase in swim speed during spontaneous swimming behaviour (Section 4.3.5), which I postulated may be due to disruption of rostrocaudal motor neuron recruitment, I returned to this dataset to assess whether rostral-caudal recruitment of the J-turn may be affected. Using cumulative tail angle data available for the 11 tail segments, I computed the location of the maximum tail bend during J-turns for each animal. Similar values were obtained for all animals, with the maximum tail bend location being restricted to the last two tail segments (p =

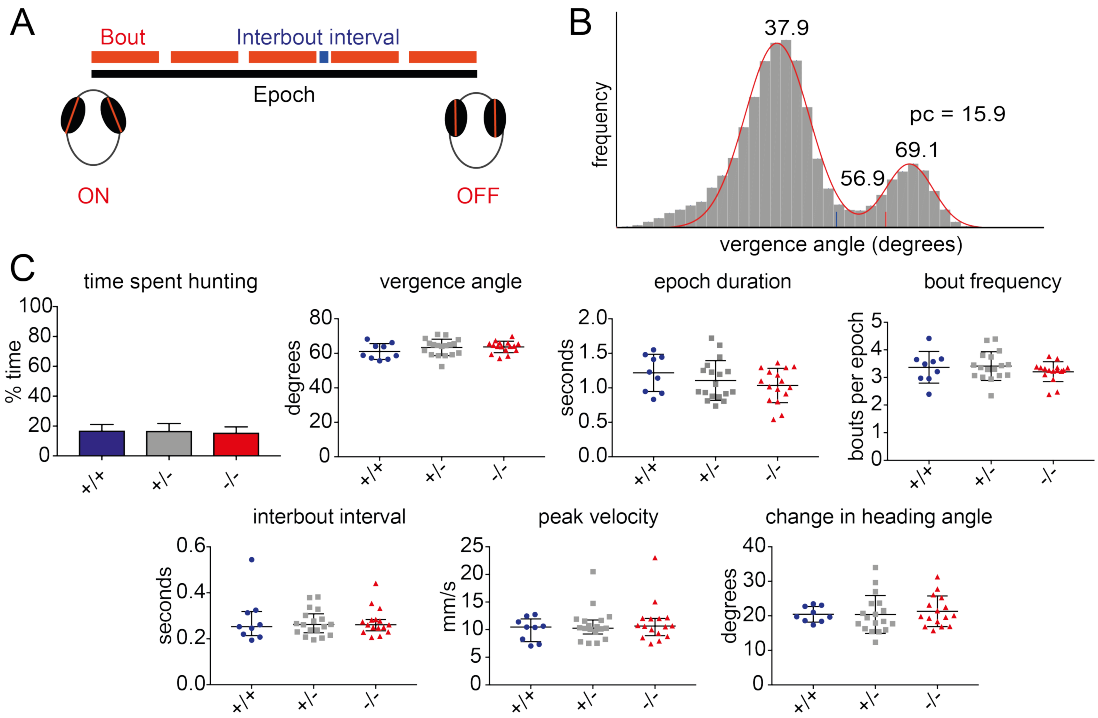

Figure 4.15: Detection and quantification of hunting epoch parameters **(A.)** Schematic illustrating the structure of a hunting epoch. Hunting epochs consist of multiple bouts (red) separated by interbout intervals (blue). The start of hunting epochs is defined by high ocular vergence angles (ON) and the end by loss of high vergence angle (OFF). **(B.)** Frequency distribution histogram of all ocular vergence angles. A two term Gaussian model is fitted to the data (red line). Peaks in ocular vergence angle occur at 37.9° and 69.1° in this example. The second peak contains ocular vergence angles associated with hunting. A threshold of 56.9° is calculated one standard deviation below the value of the second peak (56.9°). Percentage of time spent hunting (pc) is calculated as the proportion of vergence angles above this threshold (15.9%). **(C.) Time spent hunting:** 17.06 ± 3.97% in wild types, 16.85 ± 4.88% in heterozygotes and 15.67 ± 3.74% in homozygous mutants (F (2,39) = 0.43, p = 0.65, one-way ANOVA). **Vergence angles:** Average vergence angles were 61.01 ± 4.60° in wild types, 63.01 ± 4.56° in heterozygotes and 63.71 ± 3.34° in homozygous mutants (F (2,39) = 1.24, p - 0.30, one-way ANOVA). **Epoch duration:** Hunting epochs lasted for 1.22 ± 0.27 seconds in wild types, 1.12 ± 0.29 seconds in heterozygotes and 1.04 ± 0.25 seconds in homozygous mutants on average (F 2(39) = 1.36, p = 0.27, one-way ANOVA). **Hunting bout frequency:** Number of hunting bouts performed per epoch equates to 3.37 ± 0.57 bouts per minute in wild types, 3.41 ± 0.52 in heterozygotes and 3.21 ± 0.36 bouts per minutes in homozygous mutants (F (2,39) = 0.81, p = 0.45, one-way ANOVA). **Interbout interval:** Interbout intervals lasted for 0.25 (0.21 to 0.32) seconds in wild types, 0.26 (0.22 to 0.30) seconds in heterozygotes and 0.26 (0.23 to 0.28) seconds in homozygous mutants (p = 0.89, Kruskal-Wallis test). **Peak velocity:** Velocities reach a maximum of 10.47 (8.82 to 11.94) mm/s in wild types, 10.33 (9.79 to 11.80) mm/s in heterozygotes and 10.66 (8.90 to 12.04) mm/s in homozygous mutants (p = 0.82, Kruskal-Wallis test) **Orientation change:** The change in heading angle during a hunting routine was 20.46 ± 2.24° in wild types, 20.66 ± 5.55° in heterozygotes and 21.32 ± 4.44° in homozygous mutants. N = 9 WT, N = 17 Het, N = 16 Hom. Values and error bars represent mean ± standard deviation for time spent hunting, ocular vergence angle, epoch duration, bout frequency, heading angle change. Values and error bars represent median (IQR) for IBI and peak velocity

0.76, Kruskal-Wallis test). In conclusion, no discrepancies were found between genotype groups in the performance of hunting behaviour analysed either at the level of the epoch or individual hunting bouts. This suggests that the kinematics of this complex behaviour were spared from the effects of hypomyelination in the CNS.

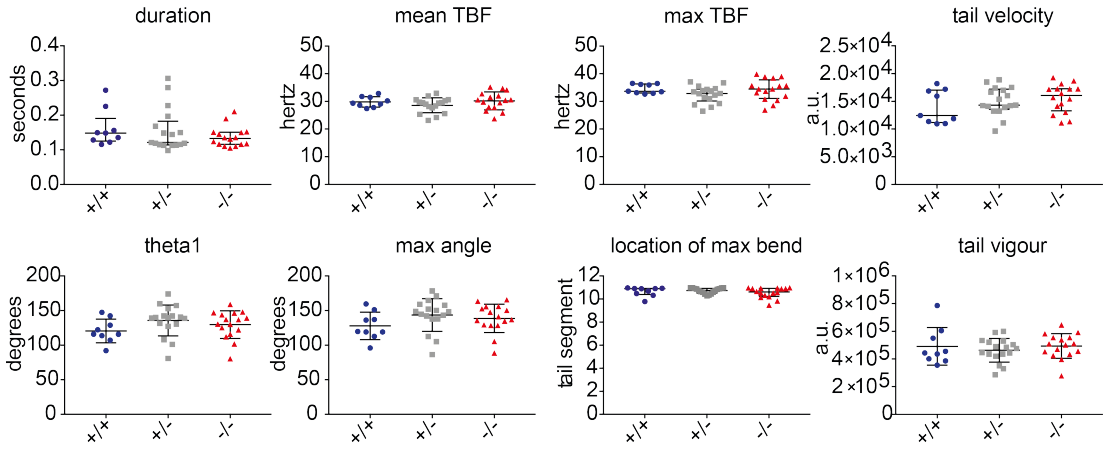

Figure 4.16: Tail parameters during individual hunting bouts
Top panel: Bout duration: 0.15s (0.13 to 0.19s) in wild types, 0.12s (0.11 to 0.18s) in heterozygotes and 0.13s (0.12 to 0.15s) in homozygous mutants (p = 0.43, Kruskal-Wallis test). **Mean tail beat frequency:** 29.83Hz ± 1.88Hz in wild types, 28.58Hz ± 2.68Hz in heterozygotes and 30.19Hz ± 3.24Hz in homozygous mutants (F (2,39) = 1.48, p = 0.24, one way ANOVA). **Maximum tail beat frequency:** 33.67Hz (33.03 to 36.31Hz) in wild types, 32.86Hz (30.16 to 34.5Hz) in heterozygotes and 34.47Hz (31.09 to 37.79Hz) in homozygous mutants (F (2,39) = 1.055, p = 0.36, one way ANOVA). **Tail velocity:** 14.0 ± 3.0 x 10^3 a.u. in wild types, 15.0 ± 2.5 x 10^3 a.u. in heterozygotes and 15.6 ± 2.6 x 10^3 a.u. in homozygous mutants (F (2,39) = 1.055, p = 0.36, one-way ANOVA). **Bottom panel: Theta1 angle:** 120.6°±17.16° in wild types, 135.7°± 22.48° in heterozygotes and 129.7°± 19.9° in homozygous mutants (F (2,39) = 1.592, p = 0.22, one-way ANOVA). **Maximum tail angle:** 127.9 ± 19.93° in wild Type, 143.6 ± 23.47° in heterozygous mutants and 138.7 ± 20.53° in homozygous mutants (F (2,39) = 0.075, p = 0.93, one-way ANOVA). **Location of maximum tail bend** The maximum cumulative tail angle was found at segment 10.89 (10.4 to 10.93) in wild types, 10.74 (10.52 to 10.94) in heterozygotes and segment 10.62 (10.24 to 10.94) homozygous mutants (p = 0.76, Kruskal-Wallis test). **Tail vigour:** 4.90 x 10^5 ±1.3 x 10^5 a.u. in wild types, 4.64 x 10^5 ± 0.86 x 10^5 a.u. in heterozygotes and 4.94 x 10 5 ± 0.89 x 10^5 a.u. in homozygous mutants (F (2,39) = 0.445, p = 0.64, one way ANOVA). Values and error bars represent median (IQR) for bout duration, max TBF, location of max tail bend. Values and error bars represent mean ± standard deviation for mean TBF, tail velocity, theta1, maximum tail angle and tail vigour. N = 9 WT, 17 Het, 16 Hom for each parameter.

4.3.5 Myrf$^{-/-}$ mutants exhibit an increased frequency of fast swims

It was surprising to us that Myrf$^{-/-}$ mutants did not display any overt phenotypes during OMR, hunting and looming-evoked escape behaviour despite a significant degree of hypomyelination in the spinal cord and an established latency phenotype in the auditory-evoked escape response. I decided to turn my attention to the data available for spontaneous swimming behaviour, which includes all swimming behaviour performed by the larvae in the absence of any stimulus (including hunting routines). Armed with the knowledge that a behavioural phenotype would likely be subtle (given the absence of obvious differences on analysis thus far) I decided to delve deeper into the structure of the behavioural data to see if I could uncover a phenotype in Myrf$^{-/-}$ mutants during natural exploration of their environment. At 6dpf, larvae naturally swim in discrete 'bouts' separated by periods of inactivity, called 'interbout intervals' (Budick and O'Malley, 2000). For this analysis, swim bouts were detected using two different methods: centroid velocity values and tail parameters - these will be discussed in detail in their relevant sections.

Myrf$^{-/-}$ mutants display a bimodal distribution in the velocity of their swim bouts

The initial approach to detecting swim bouts used centroid velocity - the speed at which the body of the fish moves through the water. Thresholds of 1.5mm/s and 1.24mm/s were applied to centroid velocity data to detect the beginning and end of swim bouts respectively (see Materials and Methods section of this chapter, Figure 4.7). Using this method, no significant differences in the basic parameters of swim behaviour, such as duration or velocity of bouts, were detected when data was computed as a mean value per fish. However, a modest trend towards higher velocity swim bouts was observed in Myrf$^{-/-}$ mutants (Figure 4.17B). It was clear by this point that a large proportion of the behavioural data obtained was non-parametric in its distribution. In this case, calculating a mean value per fish for comparison would not represent differences that reside in the distribution of data for each fish. To assess whether the mean values per fish were sampled from normal distributions, I plotted a normalised relative frequency histogram of swim bout velocities for each individual fish and then averaged across fish to produce an average histogram for each genotype (Figure 4.17A). When I displayed

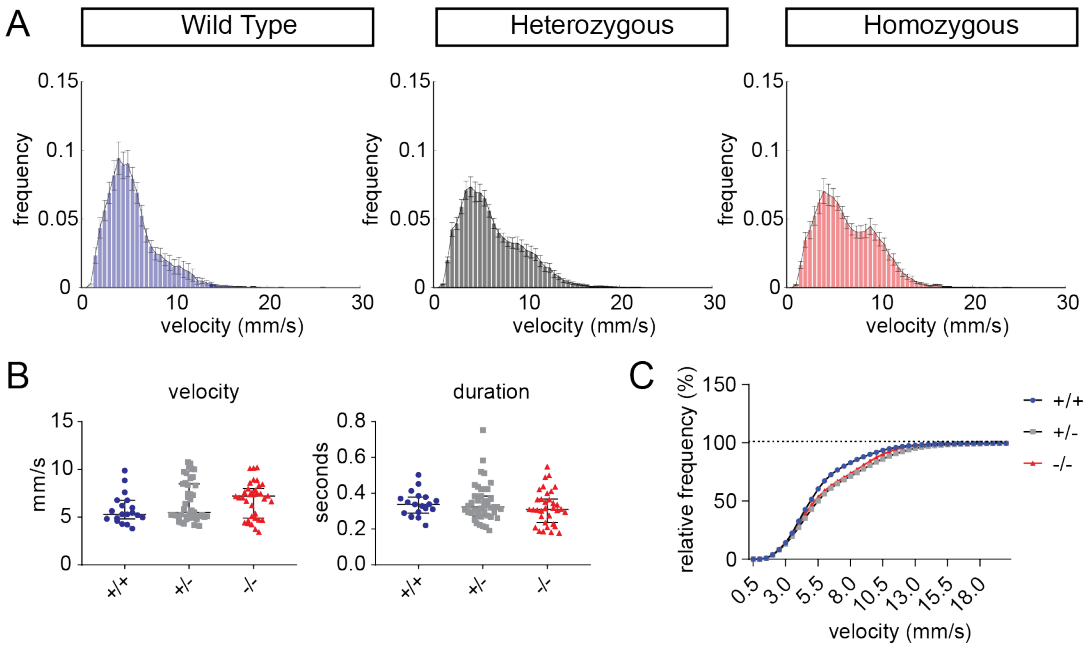

Figure 4.17: Spontaneous swim bouts detected using centroid velocity
(A.) Relative frequency histograms representing the average distribution of velocity data across fish within each genotype group. **(B.)** Velocity and duration of swim bouts detected using centroid velocity. **Mean velocity:** 5.30mm/s (4.82 to 6.76mm/s) wild type, 5.5mm/s (5.03 to 8.49mm/s) heterozygous, 7.19mm/s (4.91 to 7.99mm/s) in homozygous mutants (p = 0.22, Kruskal-Wallis test). **Mean duration**: 0.34 (0.29 to 0.38)s wild type, 0.32 (0.27 to 0.38)s heterozygotes, 0.31 (0.24 to 0.37)s homozygous mutants (p = 0.55, Kruskal-Wallis test). Values and error bars represent median and IQR. **(C.)** Cumulative frequency histogram for velocity data for every swim bout from wild type, heterozygous and homozygous mutants groups. N = 19 fish, n = 28822 swim bouts, wild types. N = 43, n = 77879 swim bouts, heterozygous mutants. N = 35, n = 74800 swim bouts, homozygous mutants.

data in this way it became evident that the distribution of data was different across the groups. Although each dataset displayed a non-parametric distribution (p = <0.0001 wild type, p = 0.0015 heterozygous, p = 0.0068 homozygous mutants, D'agostino & Pearson test for normal distribution) there was a shift towards a bimodal distribution in the heterozygous and homozyogus mutant dataset. To demonstrate this shift in distribution using all available data, values for every swim bout per fish per genotype were plotted as a cumulative frequency distribution. Plotting data in this way shows a clear shift towards faster swims in the heterozygous and homozygous group (Figure 4.17C). We next questioned whether the larger proportion of high velocity swims observed in the homozygous mutant group was a feature of all subjects in the group or whether it caused by a subset of outlier fish. Relative frequency distribution histograms were plotted for each individual to assess the distribution of swim bout velocity values (Appendix 2: Figure 5.11, 5.12, and 5.13). Distributions were variable and largely

non-parametric across fish. In an attempt to quantify the distribution of velocity values within each fish, I calculated the standard deviation of the data and performed Pearson's coefficient of skewness, whereby a negative value would indicate a skew of data towards higher velocities (Appendix 2, Figure 5.10). Although the difference between groups was not statistically significant, there was a trend towards a more negative skew (faster swims), and a larger standard deviation in the mutant group consistent with the bimodal distribution observed in the average frequency histogram.

Myrf$^{-/-}$ mutants perform a higher frequency of 'fast' swims than 'slow' swims

The bimodal distribution observed in the homozygous data could be explained by two scenarios. In the first, the swim bout frequency remains the same but a larger proportion of the swims have a faster velocity. In the second, the swim bout frequency increases due to more fast swims being performed. To test which scenario was true, a threshold was set to classify data into slow or fast swims, allowing calculation of the frequency of fast or slow swims. To set the threshold, the velocity data for the entire *population* (N = 97 fish) was fitted with a two term Gaussian model and the intersect of the two curves computed to provide a threshold value of 7.3mm/s (Figure 4.18A). Data was subsequently segmented into 'fast' (> 7.3mm/s) or 'slow' (<7.3mm/s) swims, and the frequency of their performance calculated. Prior to splitting the data, homozygous mutants show a modest trend towards an increased bout frequency, displaying on average 1.2 fold more swim bouts than wild type siblings. Intriguingly, heterozygous mutants occupied an intermediate phenotype between the two (p = 0.28, one-way ANOVA) (Figure 4.18B, all swim bouts). In general, larvae across all genotypes tended to perform more slow swims than fast swims. Although the frequency of swim bouts in either category was not significantly different, a trend towards a higher frequency of fast swims was observed in Myrf$^{-/-}$ mutants (p = 0.12, Kruskal-Wallis test). When more stringent thresholds of <5mm/s for slow bouts, and >8mm/s for fast bouts are applied to the data a near significant difference in the frequency of fast swims is achieved (data not shown, p = 0.05, Kruskal-Wallis test. Dunn's multiple comparison test: WT-Hom p = 0.05, WT-Het ns, Het-Hom ns). From this data, it appears that the bimodal distribution in homozygous and heterozygous mutants is caused by a subtle increase in

the frequency of fast swim bout recruitment. However, given the lack of statistically significant result in the current analysis this cannot be stated for certain. Further analysis will aim to provide supporting evidence to strengthen this claim.

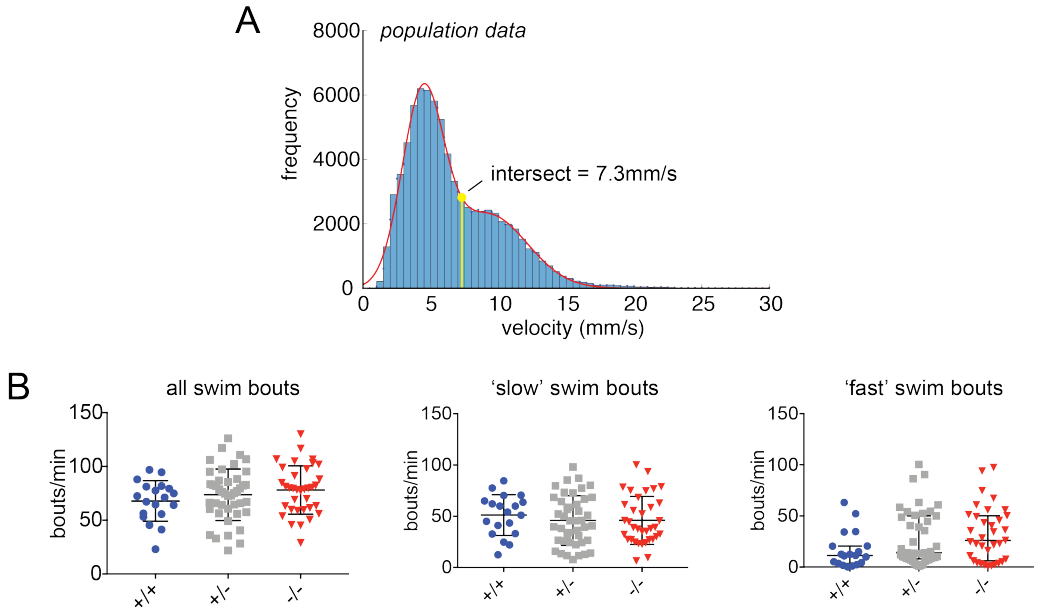

Figure 4.18: Quantification of fast and slow swim bout frequency. **(A.)** Average relative frequency histogram representing population (all genotypes) velocity data. The intersection (yellow solid marker and line) of two overlapping Gaussian curves fitted to the population of the data was used as a threshold to define swim bouts as 'fast' or 'slow. Here the intersection = 7.3mm/s. **(B.)** Frequency of all swim bouts, 'slow' swim bouts and 'fast' swim bouts per minute. **All bouts:** On average, the total bout frequency is 67.82 ± 18.81 bouts per minute in wild types, 73.64 ± 23.92 bouts per minute in heterozygotes and 78.05 ± 22.49 bouts per minute in homozygous mutants (F (2,94) = 1.28, p = 0.28, one-way ANOVA). **'Slow' swims:** The number of slow swims per minutes reached 51.22 ± 19.86 per minute in wild types, 45.89 ± 24.19 per minute in heterozygotes and 46.01 ± 23.39 bouts per minute in homozygous mutants (F (2,94) = 0.41, p = 0.66, one-way ANOVA). **'Fast' bouts**: On average, wild types performed 11.28 (3.58 to 20.62) fast bouts per minute, heterozygotes performed 14.07 (7.94 to 50.07) fast bouts per minute and homozygous mutants performed 26.04 (6.04 to 50.21) fast bouts per minutes (p = 0.12, Kruskal-Wallis test).Values and error bars represent mean ± std for all bouts and slow bouts, and median (IQR) for fast bouts. Data was only analyzed for 'inmiddle' bouts and bout frequency was normalized to time spent 'inmiddle'. N = 19 WT, N = 43 Het, N = 35 Hom.

Fitting individual data to a defined Gaussian model

Given the variability in the distribution of data across individual fish, using a 'one size fits all' threshold (as performed in the prior analysis) may obscure the detection of subtle differences in the recruitment of swim speeds across fish. By fitting data from individual fish to a two-term Gaussian model generated from the population data, I could compute an individual threshold for each fish to determine the probability of their performance of fast or slow bouts. Additionally, this would allow me to quantify the distribution of data for each fish by calculating the area under each curve and comparing this across genotypes. To achieve this I fitted two Gaussian curves with overlapping distribution to the population data, as in Figure 4.18A. The centres of each Guassian were then used to create a model with which to fit the datasets of individual fish (i.e. data is assessed for its fit into a model where the peak of the first Gaussian must be between 2 and 7.3mm/s, and the peak of the second curve between 7.3 and 20mm/s).

Computing the intersects in this way produced predictably variable thresholds, however the average intersect per genotype was similar to that for the population data (population intersect: 7.3mm/s, average WT intersect: 8.86 ± 2.47mm/s, Het intersect: 7.78 ± 2.60mm/s, Hom intersect: 7.56 ± 1.88mm/s) (Figure 4.19B) suggesting that the distributions of each dataset fit this model well, and there is not an entire shift of the data towards faster speeds in mutants. This would imply that the increase in swim velocity seen is due to a difference in the weighting of the bimodal distribution, i.e. more 'fast' bouts are selected in mutants than their siblings. To test this, I used the individual thresholds to calculate the percentage of slow or fast bouts recruited by each fish and compared these across genotypes. In support of my prediction, Myrf$^{-/-}$ mutants performed, on average, 52% (24 to 91%) slow bouts and 48% (8 to 66%) fast bouts. This is in contrast to wild type siblings who performed 93% (57% to 99%) slow bouts and 0.07% (0.01 to 0.43%) fast bouts. Values from heterozygous larvae were intermediate between the two, but closer to wild type values (80% (22% to 95%) slow bouts and 20% (2 to 80% fast bouts). However, due to a significant degree of variability across fish, these differences were not significant across groups (Figure 4.19C). Despite this, these values support the notion that Myrf$^{-/-}$ mutants are more likely to recruit faster bouts than their siblings. In order to assess the distribution of data across fish, the area under each curve was computed and represented as a ratio of the area of the slow

curve : area of the fast curve (Figure 4.19D). In general, Myrf$^{-/-}$ mutants possessed a *lower* ratio, consistent with a smaller proportion of the data fitting the 'slow' Gaussian curve than the 'fast' (median (IQR): 1.5 (0.67 to 5) in wild types, 1.4 (0.29 to 5) in heterozygotes and 0.8 (0.43 to 7.94) in homozygous mutants) (Figure 4.19D).

In summary, using individual thresholds to calculate the probability of fish performing fast or slow swims did not reveal any significant differences, however the findings were supportive of a preference towards an increased performance of fast swim bouts relative to slow swim bouts in homozygous mutants, with heterozygotes remaining in an intermediate position.

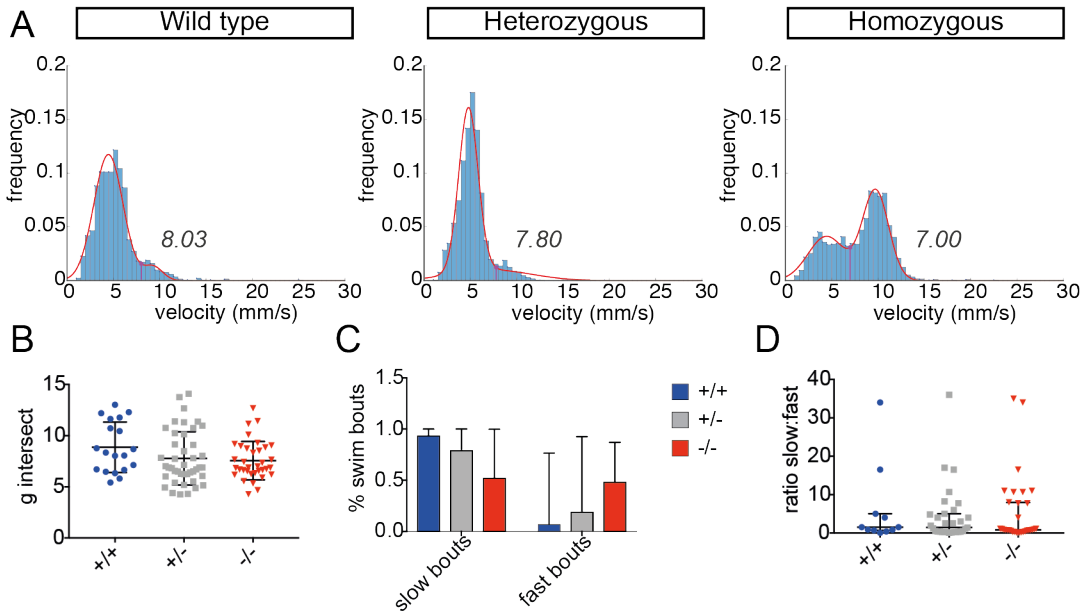

Figure 4.19: Fitting data for individual fish to a two-term Gaussian model **(A.)** Representative relative frequency histograms for an *individual* wild type, heterozygous and homozygous mutant. Red line depicts the model fitted to the data. The numbers represent the intersect between the two overlapping Gaussian curves. **(B.)** Individual intersect values for each fish per genotype. The threshold varies across fish but on average is no different between genotypes (8.87 ± 2.47mm/s in wild types, 7.78 ± 2.60mm/s in heterozygotes and 7.56 ± 1.88mm/s in homozygous mutants, F(2,94) = 2.04, p = 0.14, one-way ANOVA). **(C.)** The probability of swim bouts for each fish that are classified as slow or fast according to individually computed threshold. Slow bouts: 0.93 (0.57 to 0.99) in wild types, 0.80 (0.22 to 0.98) in heterozygotes and 0.52 (0.24 to 0.91) in homozygous mutants (p = 0.10, Kruskal-Wallis test). Fast bouts: 0.07 (0.01 to 0.43) in wild types, 0.20 (0.02 to 0.80) in heterozygotes and 0.48 (0.08 to 0.66) in homozygous mutants (p = 0.10, Kruskal-Wallis test, Dunn's multiple comparisons). N = 19 WT, N = 43 Het, N = 35 Hom. **(D.)** Ratio of slow:fast curve areas. 1.5 (0.67 to 5) in wild types, 1.4 (0.29 to 5) in heterozygotes and 0.8 (0.43 to 7.94) in homozygous mutants (p =0.84, Kruskal-Wallis test). N = 11 WT, N = 32 Het, N = 32 Hom. N numbers are reduced due to the fact that some fish possess an area of zero for the second curve, thus a ratio cannot be computed.

4.3.6 Fast swims in Myrf$^{-/-}$ mutants are driven by subtle adjustments in tail kinematics

An alternative method of detecting swim bouts uses tail tracking data (Section 4.2). This method is adapted from its original application where it is used to detect swim bouts in tracking data obtained from head-fixed larvae, which are restrained to allow *in vivo* imaging while simultaneously recording behaviour. In this situation centroid velocity cannot be used to detect swim bouts as the fish is unable to move forwards. This method is more sensitive to the detection of swim bouts, given that tail oscillations are typically generated prior to the acceleration of centroid velocity. Furthermore, this form of detection represents *active movement* whereas bouts detected by centroid velocity include passive gliding through the water. For this reason, bouts detected by tail movement are often much shorter than those detected by centroid velocity. This dataset provides us with the opportunity to corroborate the observed swim bout frequency phenotype using another technique and also perform in depth assessment of tail kinematic parameters that may underpin an increase in velocity.

Swim bout frequency is increased in Myrf$^{-/-}$

Using this detection method, Myrf$^{-/-}$ mutants were found to perform 25% more swim bouts per minute than their wild type siblings ($p = 0.05$, one-way ANOVA followed by Tukey's multiple comparisons) (Figure 4.20C right). When the analysis was extended to swim bouts across the entire arena, i.e. not just those that were performed in the middle zone, this difference became significant ($p = 0.01$, one-way ANOVA) (Figure 4.20C left). Interestingly, including this data caused the values for Myrf homozygous **and** heterozygous mutants to deviate further from wild type values with both groups now showing a significant increase (51% and 40% respectively) in swim bout frequency compared to their wild type siblings. This data supports the trend towards significance seen in previous datasets (Figure 4.18).

Subtle differences in tail kinematics drive the increase in swim speed observed in Myrf$^{-/-}$ mutants

In larval zebrafish, swim speed can be dynamically modulated by altering tail beat frequency or the strength with which they beat their tail, i.e. tail vigour. Tail vigour is determined by the amplitude of the tail angle (theta) and velocity at which it moves

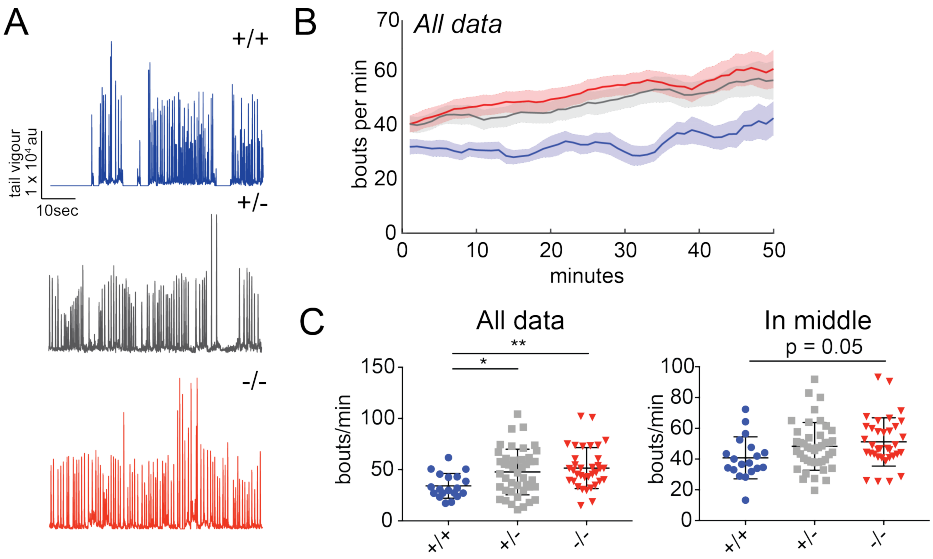

Figure 4.20: Swim bout frequency detected using tail movement
(A.) Example traces of tail vigour over one minute for a wild type, heterozygous and homozygous mutant fish. **(B.)** Rolling average swim bout frequency over time for each genotype from 0 to 50 minutes (average length of experiment) regardless of location in the arena. Solid line represents mean, shaded error bars represent SEM. **(C.)** Left: Mean swim bout frequency per fish calculated as total number of swim bouts divided by length of experiment (34.24 ± 12.02 bouts per minute wild type, 47.76 ± 22.31 bouts per minute heterozygotes, 51.56 ± 20.02 bouts per minute homozygous mutants (F (2,94) = 4.835, p = 0.01, one-way ANOVA. Tukey's multiple comparisons: wild type vs het p = 0.04, wild type vs homozygous mutants p = 0.0008, heterozygous siblings vs homozygous mutants p = 0.68). Right: Mean swim bout frequency per fish calculated as the total number of swim bouts *inmiddle* divided by total time spent in middle in minutes (40.80 ± 13.64 bouts per minute in wild types, 48.29 ± 13.64 bouts per minute in heterozygotes, 51.15 ± 15.73 bouts per minute in homozygous mutants (F (2,93) = 2.88, p = 0.06, one-way ANOVA. Tukey's multiple comparisons: WT-Het p = 0.18, WT-Hom p = 0.05, Het-Hom p = 0.69). Error bars represent mean ± standard deviation. N = 19 Wild Type, N = 43 Heterozygous siblings, N = 35 Homozygous siblings.

over the half cycles of a swim bout (see Figure 4.8B). These parameters can be modulated by RS neurons such as the nMLF and vSPNs (Huang et al., 2013; Severi et al., 2014). To investigate whether these mechanisms may be associated with the increase in frequency of fast swim bouts observed in Myrf$^{-/-}$ mutants, I performed analysis of the tail tracking data to extract relevant parameters of tail movement and compare them across genotypes. In a similar manner to the centroid velocity analysis, I plotted the average distribution of individual tail parameters for each genotype using relative frequency histograms (Appendix 2, Figure 5.15). Many of the tail parameters were

remarkably similar across all genotypes and values were within published reference ranges, indicating that the detection of swim bouts using this method was adequate across fish. However, subtle differences in the distribution of core tail parameters (tail beat frequency and tail vigour values) were revealed when data was displayed as average histograms or cumulative frequency distribution graphs (Figure 4.21A and B). To assess which features might be contributing to the increase in tail strength, theta (theta1) angle and the velocity (vel1) of the first half beat were also assessed across swim bouts. These parameters displayed similar shifts in their distribution towards higher values. Theta1 angles usually occupy a bimodal distribution, consistent with the natural occurrence of forward swims (low amplitude theta1) and routine turns (high amplitude theta1). In the average histograms for heterozygous and homozygous mutants, the frequency of lower amplitude theta1 angles appears to be reduced with a subtle shift towards higher amplitude theta1 angles (theta1, Figure 4.21C). A similar effect was observed for the velocity of the first half beat (velocity1, Figure 4.21D). Due to the subtleties in the distribution changes and the non-parametric nature of the data, I was not surprised that no statistical differences were observed when parameters were plotted as an average per fish (Appendix 2, Figure 5.14). However, it is interesting that Myrf$^{-/-}$ mutant values are consistently higher than those of wild types, with close similarity to heterozygous siblings across the majority of parameters assessed. In conclusion, the tail kinematics identified in this analysis corroborate the distribution changes in centroid velocity observed in Figure 4.17.

Differences in tail kinematics represent a modulation of swim bouts

Recent work by Marques et al. (2018) demonstrated that zebrafish larvae can display a behavioural repertoire of at least thirteen kinematically distinct swim bouts, which can be defined by their tail parameters. To assess whether the increased frequency of fast swims in homozygous and heterozygous mutants represents the recruitment of an alternative bout type versus modulation of an existing bout type, we attempted an analysis similar to that performed by Severi et al. (2014). An example of this analysis is shown in Figure 4.22. In this study, the author had identified that larvae swim faster when presented with high speed OMR gratings. To address whether this was due to modulation of a single bout type, or recruitment of a distinct gait (which allows faster swims), they plotted paired tail parameters from discrete bouts and compared their

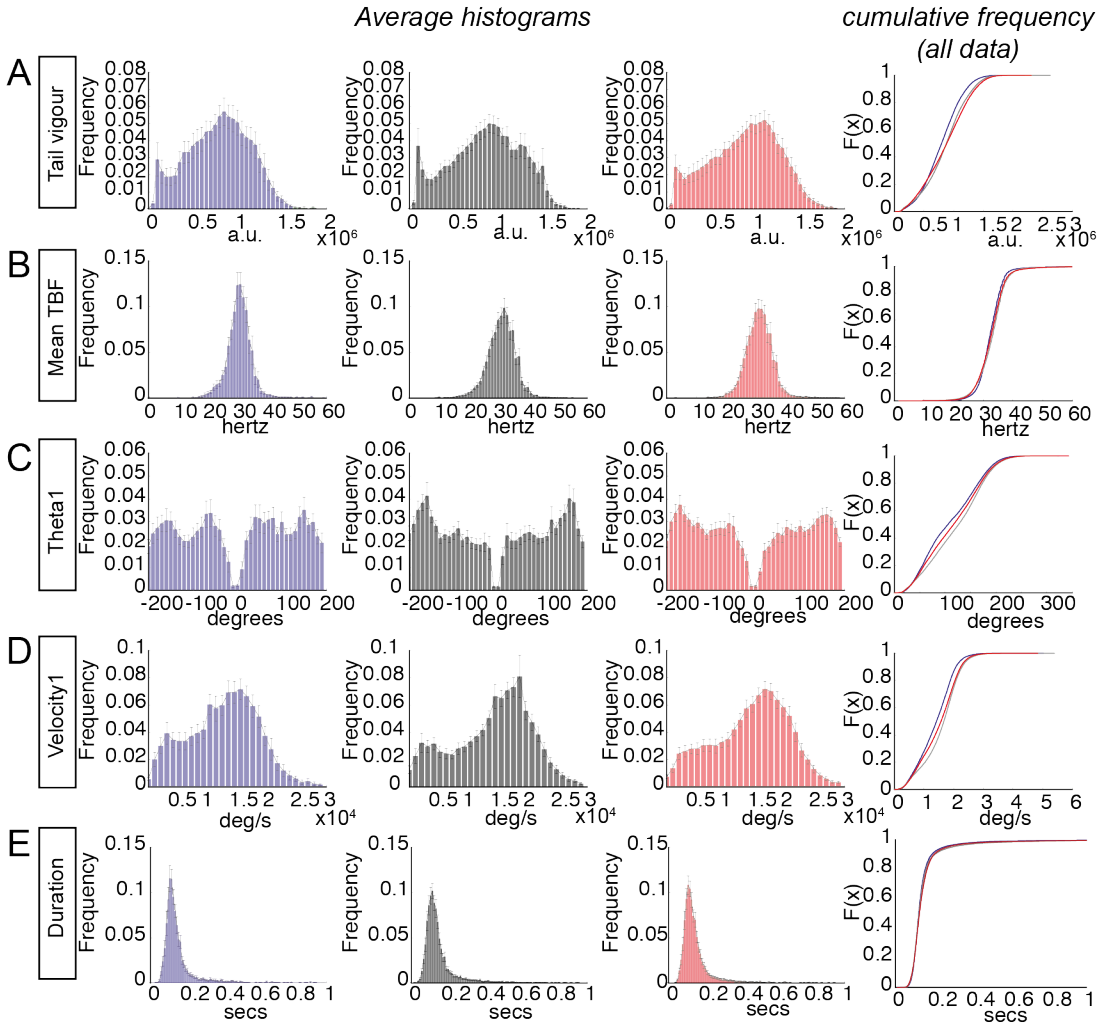

Figure 4.21: Quantification of core tail metrics which contribute to centroid velocity.
(A.) Tail vigour. **(B.)** Mean TBF. **(C.)** Theta1. **(D.)** Velocity1. **(E.** Duration. L to R: Average histograms per genotype are displayed, followed by cumulative frequency distributions of *all* events from every fish per genotype. Histograms represent the average distribution across N = 19 WT, N = 43 Hets, N = 35 homozygous mutants. Error bars represent standard error. Cumulative frequency distributions: n = 18656 events from wild type fish, n = 51142 events from heterozygous fish, n = 50223 events from homozygous fish.

distribution during 'slow' and 'fast' OMR gratings. As you can see, at slow speeds a single cluster is observed for each pair of tail parameters measured. With an increase in grating speed, a second cluster emerges forming two distinct distributions which represent the different bout types recruited at each speed. If the observed fast swims were due to modulation of the bout type performed during slow OMR gratings, we would expect to see the kinematic parameters distributed continuously throughout the 2D space. Thus, if fast swims in homozygous mutants are caused by recruitment of

different bout *types* then I expected to see the formation of more than one cluster when the distribution of tail parameters is compared, whereas if different speeds are achieved by *modulation* of swimming behaviour then the data will be distributed more widely across the 2D space environment.

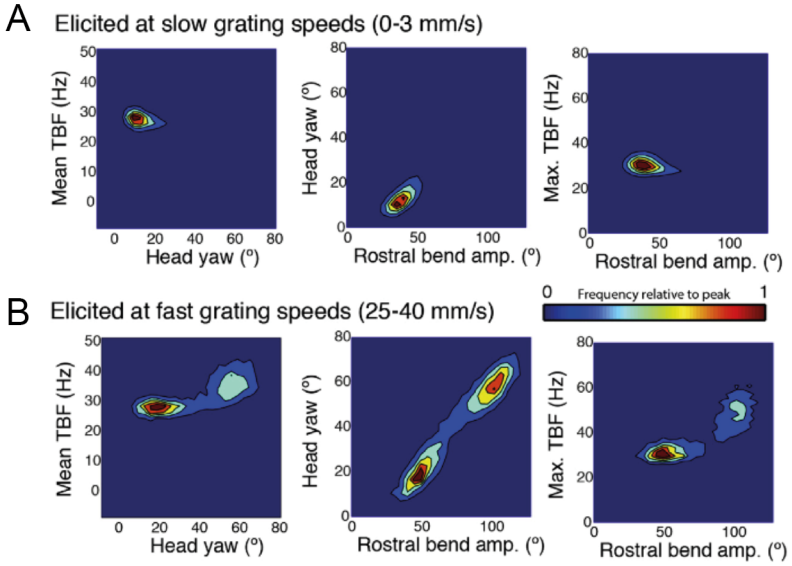

Figure 4.22: Figures from Severi et al. (2014) demonstrating the use of this analysis.

Core tail parameters were computed for each swim bout for each fish and binned into a 2D space. An average distribution across this 2D space was subsequently computed for each genotype (Figure 4.23). Interestingly, both heterozygous and homozygous mutants demonstrate a wider distribution in tail beat frequency (mean and maximum) data plotted against the amplitude and velocity of the first tail undulation (theta1 and vel1) (Figure 4.23A to C). When tail vigour data was plotted against mean tail beat frequency, a subtle shift in the distribution of tail vigour towards higher values occurs in heterozygous and homozygous mutants while they maintain a similar range of tail beat frequency values (Figure 4.23D). These data support the findings in the previous analysis which showed an altered distribution in these parameters across frequency distribution histograms and cumulative frequency distributions (Figure 4.21 A and B). In summary of the analysis of tail kinematics during spontaneous swimming, although no overt statistical differences are observed across groups (Figure 4.21 and Appendix 2 Figure 5.14) subtle differences were discovered in the distribution of the

swim bouts defined by the parameters: mean and maximum tail beat frequency, theta1 and tail vigour. This is an encouraging finding as modifications in these parameters could explain the increase in centroid velocity observed in Myrf$^{-/-}$ mutants. There was no evidence of segregation of bout clusters in space, suggesting that these changes represent modulations of existing swim bouts rather than recruitment of different types of swim bouts.

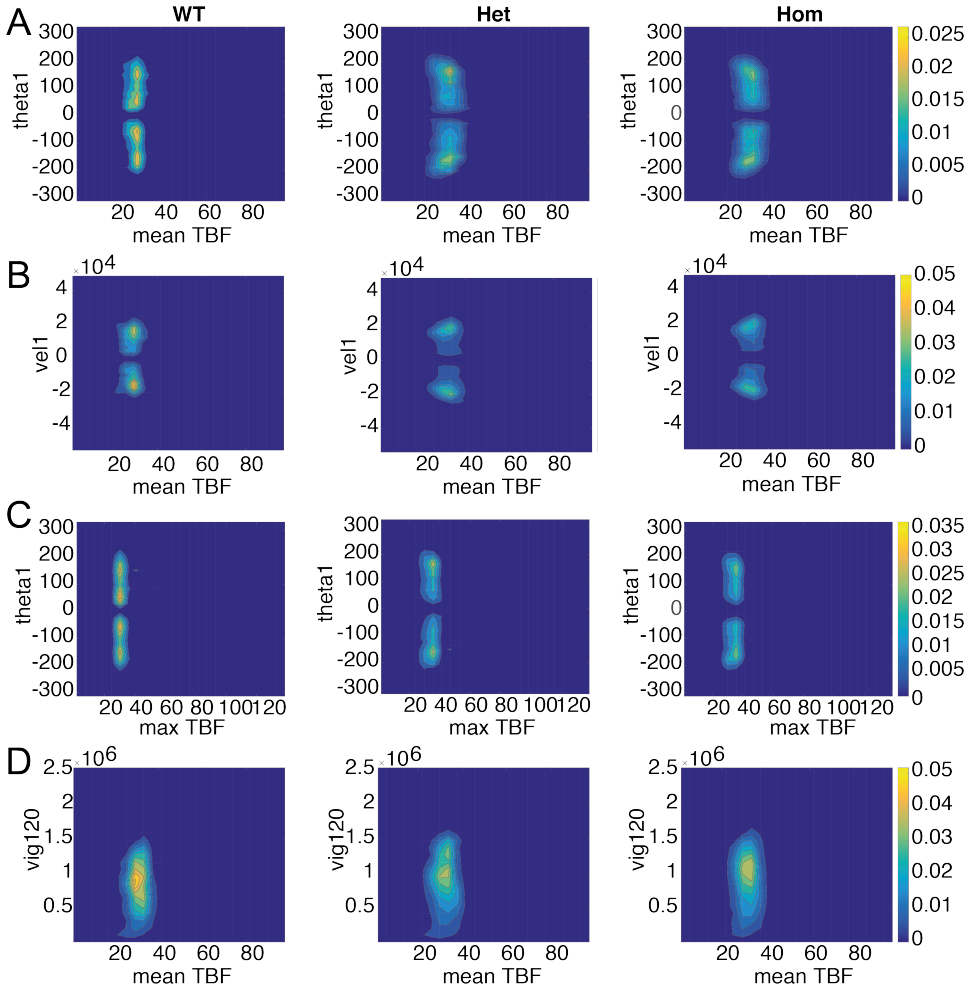

Figure 4.23: Contour maps of tail parameters plotted in 2D space.
Average 3D histograms for each genotype are formed for each pair of kinematic parameters and plotted back onto a 2D space presented as a colour map. Colour bars for each row are provided adjacent to the homozygous samples and are representative for each image in a figure panel. **(A.)** Theta1 angle versus mean tail beat frequency. **(B.)** Velocity1 vs mean tail beat frequency. **(C.)** Theta1 angle versus maximum tail beat frequency. **(D.)** Tail vigour versus mean tail beat frequency.

4.3.7 Assessing rostrocaudal propagation of tail curvature

It is well established in the literature that different patterns of motor neuron activity underly the recruitment of fast or slow swims: anterior and dorsal motor neurons are predominantly recruited for fast swims and posterior, ventral motor neurons for slow swims (Budick and O'Malley, 2000). This is illustrated nicely by larval zebrafish hunting routines, where slow, measured movements driven by caudal tail bends (J-turns) are followed by a fast capture swim (Borla et al., 2002). This behavioural switch requires a transition from caudal to rostral bend location and amplitude as illustrated in Figure 4.5. At this point, I hypothesised that the increased swim speeds observed in Myrf$^{-/-}$ mutants would be detectable as altered patterns of motor neuron recruitment in the spinal cord of Myrf$^{-/-}$ mutants. This hypothesis could be tested with electrophysiological techniques and functional imaging which will form the basis of future work (see Discussion and Appendix 4). However, the repository of behavioural data that I had collected also provided a means to address this hypothesis. Using tail tracking data, the propagation of tail curvature could be calculated programatically to produce a parameter termed *wavespeed*. From this I could not only infer the speed of motor neuron recruitment in an anterior-posterior direction, but also assess whether spatial differences in wavespeed are detectable i.e. in the anterior versus posterior regions of the tail. In addition to the existing finding of altered tail kinematics, I made a prediction that wavespeed would be faster for homozygous mutants than their wild type siblings, which would further support a fast swim phenotype.

Calculating wavespeed

I used two approaches to calculate wavespeed from the trail tracking data. In the first analysis, the wavespeed for each swim bout is calculated as the average, or absolute, difference in time between the peak angle of each tail segment across half beats (see Figure 4.24A) using the following equation (speed = distance/time):

wavespeed = 1/mean difference in time between tail segments across half cycles x 0.001

which provides wavespeed in raw units of tail segments per second. This was converted into mm/second by measuring the distance covered by tail tracking using bright field, dorsal view images of 6dpf larvae from the same line. This distance equates to

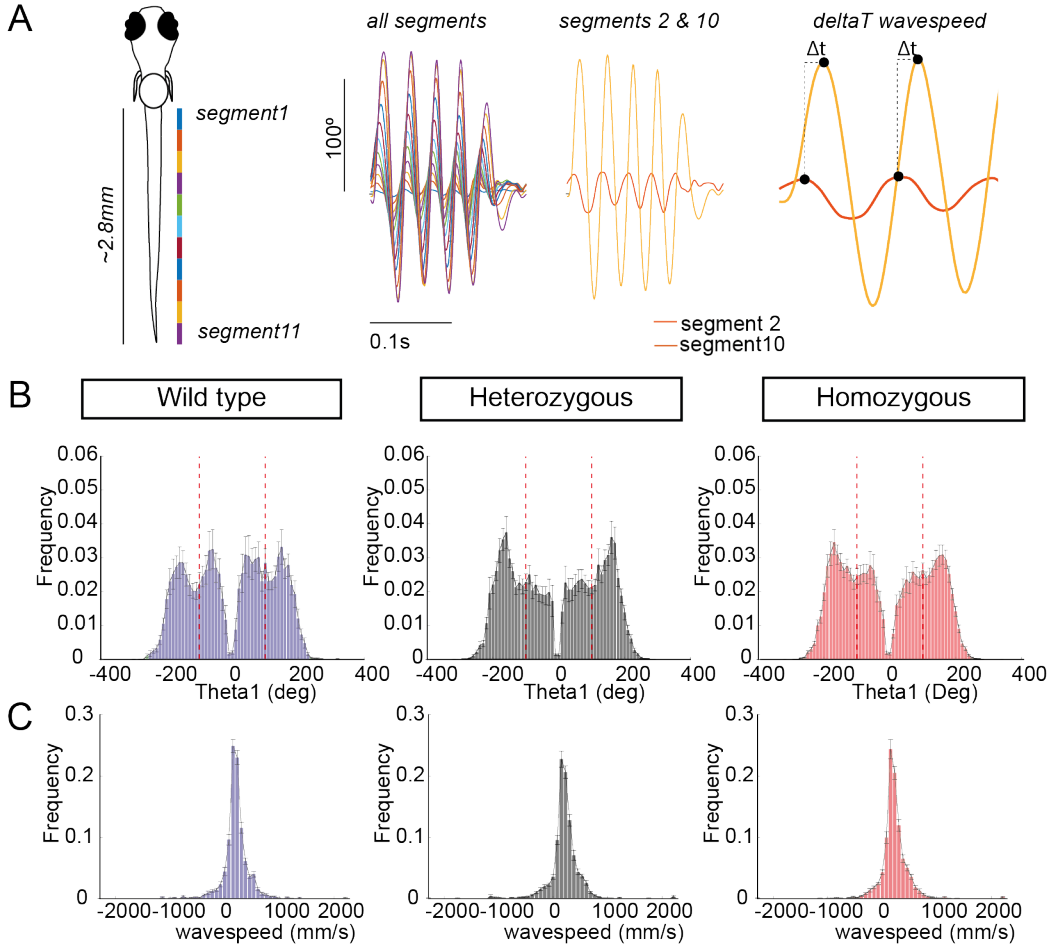

Figure 4.24: Calculation and analysis of wavespeed across genotypes
(A.) Schematics demonstrating the region and distance covered by tail tracking and examples of tail angle traces used for analysis. Data for 11 segments in total is available, subsets of these segments were used for analysis. The deltaT method for calculating wavespeed used the average difference in time between peak angles in segments 2 and 10 across every half cycle. **(B.)** Frequency distribution histograms displaying average distribution of theta1 angles across all swims per genotype. Vertical red lines mark the threshold bounded by -100°and 100°. Data within these regions was utilised for wavespeed analysis. **(C.)** 2D histograms displaying the average distribution of wavespeed across genotypes. Average distributions are displayed for N = 19 WT, N = 43 Het, N = 35 Hom. Error

approximately 2.8mm (the entire length of a larva is equal to 3-3.5mm), thus 0.254mm per segment (10 segments (Figure 4.24A)). There were many variables to define when calculating wavespeed (i.e. the number of tail segments and half beats per bout to include). Therefore, the initial analysis focussed on investigating which variables provided a reliable output. This data is supplied in Appendix 2, Figure 5.18 and 5.19. The results appeared to be consistent across analyses, therefore I opted to use the 'deltaT' method to calculate wavespeed ongoing. This method computes the average time difference between the 10th segment and the 2nd tail segment across the first 3 half

cycles (which generally display the largest amplitude) (see Figure 4.24A). In general, wavespeed values correlated positively with centroid velocity, suggesting that computed values would be appropriate to test my prediction that mutants, which exhibit faster swims, would possess faster wavespeed values (Figure 5.16).

In the second approach, wavespeed was computed by performing cross correlation of tail angle traces belonging to the 3rd tail segment and 10th tail segment. Cross correlation is a technique to measure the similarity between two signals and subsequently identify the displacement of one signal relative to the other. Using the cross correlation function (xCorr function, Matlab, 2016b) on these data sets provided me with a time value (ms) of the delay between the two signals. This was converted into speed using the known distance between the two segments. In this way, wavespeed determined by cross correlation provided me with very similar values to the previously computed wavespeed values using the deltaT method (Appendix 2, Figure 5.17).

Distribution of wavespeed values correlates with changes in tail vigour and tail beat frequency

Wavespeed analysis was restricted to forward swims by selecting swim bouts whose theta1 value were between -100° and 100° (Figure 4.24). No clear differences were observed in the average distributions of wavespeed values for each genotype using the deltaT or cross correlation calculation (Figure 4.24C and Appendix 2 Figure 5.17). However, when deltaT wavespeed values were plotted against core tail parameters which had previously demonstrated differences in distribution across genotypes (e.g. tail beat frequency, velocity1, theta1 angle and tail vigour) subtle differences in distribution were observed (Figure 4.25). Interestingly, the distribution of wavespeed values encompassed higher values when plotted against tail vigour (Figure 4.25A) and maximum tail beat frequency (Figure 4.25B), consistent with the known contribution of these parameters to fast swims. Together, these data contribute to an emerging model whereby increases in centroid velocity in Myrf$^{-/-}$ mutants are permitted by modulation of tail beat frequency, tail vigour (due to increased velocity and amplitude of tail movement) and wavespeed. The output of both computational methods correlated with each other across genotypes (Appendix 2, Figure 5.17B).

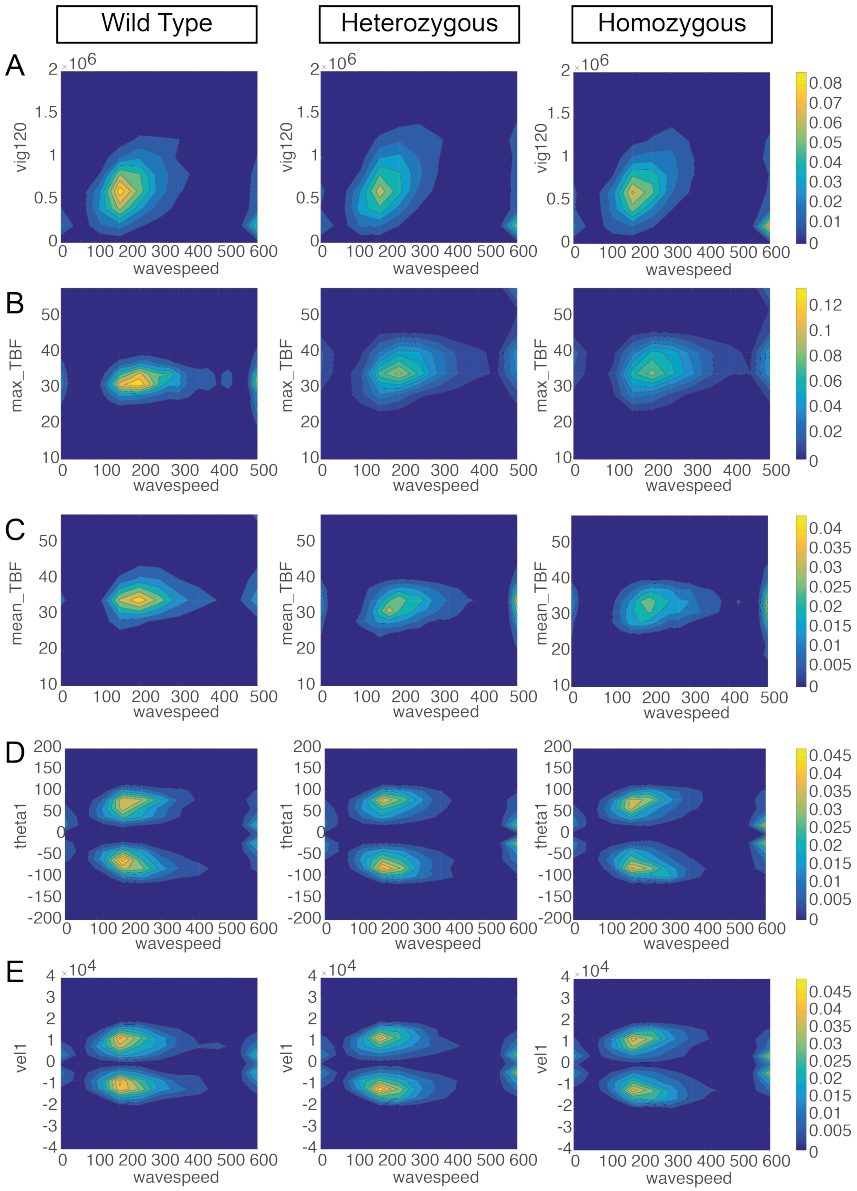

Figure 4.25: 2D histograms of wavespeed versus core tail parameters. **(A.)** Tail vigour (vig120) versus wavespeed. **(B.)** Theta2 angle versus wavespeed. **(C.)** Theta1 versus wavespeed. **(D.)** Mean TBF versus wavespeed. **(E.)** Maximum TBF versus wavespeed. Plots represent an average distribution across N = 19 WT, N = 43 Het, N = 35 Hom.

Conclusion of wavespeed analysis

In summary of this extended analysis, tail tracking data was used to compute the speed of the propagation of tail curvature during forward swims. No difference was observed in the distribution of wavespeed values between groups, however a positive association was observed between wavespeed and tail vigour, with higher wavespeed values observed in the heterozygous and homozygous mutant group when plotted against tail vigour and maximum tail beat frequency. This data supports an overall normal rostral to caudal propagation of tail curvature in Myrf homozygous mutants, but corroborates the finding that heterozygous and homozygous mutants perform a larger proportion of higher velocity swim.

4.3.8 Myrf$^{-/-}$ mutants do not exhibit thigmotactic behaviour

A final locomotor behaviour that I could assess from this dataset was thigmotaxis. Thigmotaxis, or 'wall hugging', is a valid indicator of anxiety in rodent species and has more recently has been used to classify anxiety behaviour in larval zebrafish (Schnörr et al., 2012). Given the emerging link between hypomyelination and social behaviour in other species, a thigmotactic phenotype would not be completely unexpected (Liu et al., 2012; Makinodan et al., 2012; Swire et al., 2019). A circle with a radius of 300 pixels centred in the middle of the behavioural arena was defined as the 'inmiddle' region or inner zone. The main function of this region was to act as a boundary to trigger the release of visual stimuli when the larvae have entered the inner zone. Using the centroid co-ordinates of fish location over the entire experiment, I was able to calculate the amount of time spent outside of the inner zone thus providing a read out of thigmotaxis. Average heat maps of time spent across the behavioural arena are presented in Figure 4.26A. It is evident from these maps that the majority of a larva's time was spent in the middle region of the behavioural arena, however a significant proportion of time is also spent in the outer region across all genotypes. This is unlikely to be related to hypomyelination given that there was no difference across genotypes when thigmotactic behaviour was quantified (Figure 4.26B) ($p = 0.29$, one-way ANOVA). This finding is in contrast to other wild type zebrafish lines which have been tested on this rig which display a much lower proportion of time spent in the outer region (Henriques, 2019). Similar to the findings in the analysis of loom-evoked escape behaviour, this is likely due to genetic background differences.

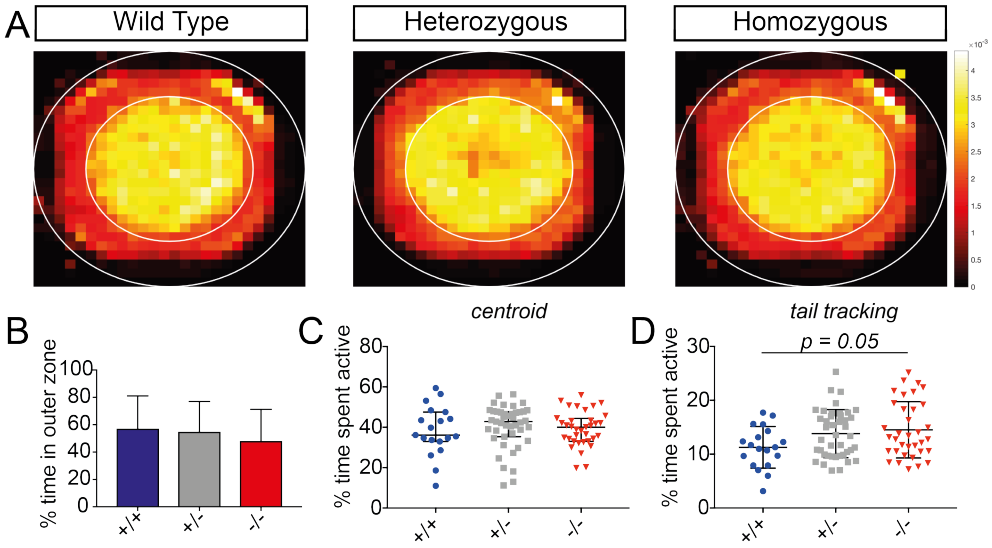

Figure 4.26: Assessment of thigmotactic behaviour
(A.) Average heat map for each genotype. The outer white ring delineates the edge of the behavioural arena while the inner white ring defines the 'inmiddle' region. **(B.)** Quantification of the amount of time spent in *outer zone*: 57.15% ± 23.91% wild types, 54.87% ± 22.05% heterozygotes, 48.16% ± 23.13% homozygous mutants (F (2,95) = 1.251, p = 0.29, one-way ANOVA. **(C.)** Activity levels are calculated as a percentage of time in the middle zone spent swimming using centroid velocity as an indicator of activity. On average, wild type siblings spent 36.17 (32.93 to 47.59)% of the experiment length active, heterozygous siblings spent 42.86 (35.36 to 47.8)% of the experiment length active and homozygous mutants spent 40.03 (33.02 to 44.42)% of the experiment length active (p = 0.46, Kruskal-Wallis test). Values and error bars represent median and IQR **(D.)** Activity levels calculated as the percentage of time spent swimming 'inmiddle' using tail data as the detector for swim bouts. On average, wild type siblings spent 11.27 ± 8.36% of the experiment length active, heterozygous siblings spent 13.81 ± 4.46% of the experiment length active and homozygous mutants spent 14.51 ± 5.22% of the time active (F (2,93) = 3.10, p = 0.05, one-way ANOVA.

Myrf$^{-/-}$ mutants spend more time active

To ensure that the quantification of thigmotaxis was not confounded by differing levels of activity between groups I computed the total amount of time spent swimming as a percentage of experiment length for each larva. No difference in total amount of time spent swimming (across entire arena) was detected when using centroid velocity for bout detection (p = 0.46, Kruskal-Wallis test) (Figure 4.26C). However, when tail features were used as a detector of swim bouts, although the total amount of time spent swimming was lower (because tail movements are shorter than whole body movements through the water), Myrf$^{-/-}$ and Myrf$^{+/-}$ mutants trended towards spending more time active. This finding was close to reaching significance (p = 0.05, one-way ANOVA. Tukey's multiple comparisons test: WT-Hom p = 0.05, WT-Het ns, Het-Hom ns). This is consistent with previous analyses which have demonstrated an increase in swim bout

frequency (Figure 4.18C). In summary, there was no evidence of thigmotactic behaviour caused by hypomyelination in Myrf$^{-/-}$ mutants. However, calculation of total time spent active using tail movement as the detector for swim bouts provided further evidence that homozygous mutants spend more time swimming, and their heterozygous siblings occupy an intermediate phenotype.

4.4 Discussion

The aim of this chapter was to identify candidate locomotor behaviours which are affected by CNS hypomyelination. These behaviours could then be taken forward for investigations into the functional effects of myelination at the circuit level. In summary of this chapter, I deployed a combination of behavioural assays to investigate the effects of CNS hypomyelination on the performance of multiple RS-mediated locomotor behaviours. In doing so, we confirmed a predicted phenotype in Myrf$^{-/-}$ mutants: a delay in the latency of escape responses to mechanosensory stimuli, and uncovered an unexpected role for myelination in the control of swim speed and frequency. Surprisingly, Myrf$^{+/-}$ larvae demonstrated an intermediate phenotype during spontaneous swimming behaviour while their escape responses remained intact, implying that precocious myelination (identified in Chapter 3) may be detrimental to the function of specific neuronal circuits. Perhaps the most intriguing discovery within this chapter is that across an array of behaviours tested, the phenotypes observed in Myrf$^{-/-}$ mutants were often subtle despite the loss of two thirds of their myelinated axons. In this discussion, I will cover each of these aspects in detail, reason to the mechanisms underlying these findings and discuss future experimental aims to interrogate newly formed hypotheses.

Myrf$^{-/-}$ mutants exhibit an increased latency to escape response

Myrf$^{-/-}$ mutants exhibit severe hypomyelination of the CNS characterised by a 66% reduction in the number of myelinated axons in the spinal cord, particularly in the ventral tract where the majority of large caliber axons belonging to RS neurons are located. I have shown in Chapter 3 that although the Mauthner axon, which is integral for the performance of short latency escape responses (SLCs) in response to mechanosensory stimuli, remains myelinated in these mutants, the thickness of the myelin sheath is severely compromised (Chapter 3, Figure 3.15). In knowledge of the relationship be-

tween myelin thickness and conduction speed, I predicted that the latency of escape responses would be delayed due to a slowed propagation of action potentials along the Mauthner axon. Indeed, we were encouraged to find that this prediction held true. Myrf$^{-/-}$ mutants displayed a robust (28%) increase in the latency to perform an escape in response to mechanosensory stimuli, compared to wild type and heterozygous siblings. In contrast to findings I will discuss later, there was no evidence of a heterozygous mutant phenotype in this assay.

Despite a delay to perform the behaviour, kinematic parameters of the eventual escape response were indistinguishable between genotypes. When escape responses were segmented into SLCs or LLCs based on the angular velocity of their response, it was revealed that the average increase in response latency was caused by delays across both behaviours. SLCs are driven by recruitment of the Mauthner axon, whereas LLCs can be performed in the absence of Mauthner activity through alternative pathways involving Mauthner homologs and prepontine neurons (Burgess and Granato, 2007; Marquart et al., 2019). The finding that both SLCs and LLCs are affected would fit with the generalised hypomyelination of the RS system that is present in Myrf$^{-/-}$ mutants. Although characterisation of the myelination status of the Mauthner homologs specifically has not yet been performed, they will fall into the category of the thirty largest axons in the spinal cord which I demonstrated are rarely myelinated in Myrf$^{-/-}$ mutants at this time point (Chapter 3, Figure 3.17). Interestingly, calculating the ratio of SLC:LLC performance within each genotype revealed a bias towards LLCs in Myrf$^{-/-}$ mutant, suggesting that Myrf$^{-/-}$ mutants preferentially recruit LLCs over SLCs. I suggest that this could be due to a number of factors. Firstly, Mauthner axons generally only produce one action potential for each escape response. Therefore, in the context of hypomyelination when sodium channels should be dispersed more irregularly throughout the axolemma and extracellular potassium levels may be raised due to a lack of OL buffering potential, the ability for such a large axon to depolarise will be constrained. Secondly, presynaptic activity may be disrupted such that the perceived threat of the stimulus is misinterpreted at the point of Mauthner versus Mauthner homolog recruitment. Indeed, the timing of action potential propagation from the otolith (hearing organ in the zebrafish) to the lateral dendrite of the Mauthner cell body, via the auditory nerve, may also be delayed if the central component of this afferent path-

way is hypomyelinated. This has not been directly assessed but given the involvement of myelination in the sound localization circuitry of the brainstem in rodents, it seems likely that this aspect of the circuitry would also be myelinated in zebrafish (Ford et al., 2015). Additionally, a lack of myelination could negatively affect the local field potential and subsequent inhibitory control over the Mauthner axon. The Mauthner axon receives inhibitory input via chemical (Bergeron et al., 2015; Korn and Faber, 2005; Tabor et al., 2018) as well as electrical (Faber and Pereda, 2018) synapses, which are important in setting the response threshold of the Mauthner cell. One proposed role of myelination is to prevent ephaptic signalling - electric field interactions between juxtaposed neurons. A lack of myelination in the hindbrain could theoretically result in increased ephaptic signalling, altered local field potentials and disruption of inhibitory and excitatory control over Mauthner firing. Finally, altered neuromodulation can influence Mauthner firing; treatment of larval zebrafish with dopamine agonists causes a switch of escape responses from SLCs to LLCs (Jain et al., 2018). Neuromodulatory control of behaviour is an important factor to consider in the context of hypomyelination and will be discussed in more detail in the next section.

The Mauthner cell is of ample size to allow direct electrophysiological recordings via whole cell recording. Collecting electrophysiological measurements concerning the resting membrane potential, conduction velocity along the axon and latency of action potential firing in response to mechanosensory stimuli would narrow down which of these mechanisms may be at play. In fact, experiments to collect this data in Myrf$^{-/-}$ mutants are already underway. Furthermore, to confirm whether a bias towards LLCs is due to preferential recruitment of non-Mauthner neurons, functional imaging could be performed to assess calcium activity in the cell bodies of RS neurons in the hindbrain in response to auditory stimuli, as per Jain et al. (2018), to identify the RS neuronal subtypes that respond. However, it seems most likely that the latency to escape response phenotype observed is the result of simple action potential conduction delays along the axons of Mauthner and its homologs and this can be confirmed by performing *in vivo* conduction velocity measurements.

The ability of larvae to modulate their escape response to subthreshold and repetitive stimuli via sensory gating (pre-pulse inhibition) and habituation mechanisms re-

spectively, was not affected by hypomyelination. The lack of a phenotype in pre-pulse inhibition in Myrf$^{-/-}$ mutants was disappointing given that deficits in this behaviour have previously been identified in mouse models with reduced CNS myelination (Poggi et al., 2016). In the study by Poggi et al. (2016), the heterozygous parents of the Mbp$^{-/-}$ shiverer mouse exhibit subtle hypomyelination characterised by reduced myelin sheath thickness around small caliber axons of the corpus callosum, and thinning of the corpus callosum on MRI. In these mice, general locomotor, sensory and cognitive behaviours were indistinguishable from wild type siblings across a battery of approximately 50 behavioural assays. Among these, significant behavioural phenotypes were detected as a reduced response probability to startle stimuli ($p = 0.01$), reduced pre-pulse inhibition ($p = 0.05$) and catatonia-like phenotypes in older age ($p = 0.01$). However, given the number of animals tested for pre-pulse inhibition ($N = 36$ wild type, $N = 48$ heterozygous siblings at 3 months of age; $N = 22$ wild types, $N = 33$ heterozygous siblings at 17 months of age) the reported p value is negligible and is not likely to survive multiple comparisons testing which should be employed to rule out the possibility that this phenotype is not a chance finding given the number of behaviours tested in this study. Furthermore, as social anxiety phenotypes are commonly reported in rodent models of CNS specific hypomyelination (Liu et al., 2016; Makinodan et al., 2012), we wanted to explore whether such a phenotype existed in the Myrf larval zebrafish mutants. We collaborated with colleagues in Herwig Baier's lab (Max Planck Institute for Neurobiology) who had recently published a virtual reality shoaling assay, which permits assessment of social affiliation (shoaling) of larval zebrafish as they interact with a virtual dot, representing a conspecific (Larsch and Baier, 2018). Unfortunately, no differences in shoaling behaviour were detected in the Myrf homozygous mutants compared to their wild type and heterozygous siblings in this assay. This is the first time that the effects of CNS specific hypomyelination on the social behaviour of larval zebrafish have been assessed and further work is warranted prior to fully excluding the presence of such a phenotype. However, this finding may hint towards species differences between the circuits or behaviours that are influenced by CNS hypomyelination. Alternatively, perhaps aspects of social behaviour requiring myelination are not present at these early developmental stages, in which case investigations using adult zebrafish may be indicated. This will be discussed further at the end of this chapter.

Myrf$^{-/-}$ maintain adequate visual sensory processing

Across the different behavioural paradigms I assessed, the detection of visual stimuli by Myrf$^{-/-}$ mutants appeared unaffected: the critical angle of looming evoked escapes, latency to respond to optomotor gratings and the percentage of time spent hunting were indifferent across groups. This is a good indicator that visual sensory processing does not appear to be affected by the reduction of CNS myelination in these mutants. I was not concerned by a lack of latency phenotypes in these behaviours in contrast to mechanosensory-induced escape responses, given that these responses are generally less urgent, involve additional central-processing pathways which may result in subtle effects on latency being lost, and are generally mediated by RS neurons outside of the Mauthner system. Across all three behaviours, there was minimal evidence of altered kinematic performance except for a trend towards a significant reduction in the initial bend angle and the duration of the initial bend during looming-evoked escape responses. Similar effects on c-bend kinematics were not detected on high-throughput analysis of the mechanosensory evoked startle responses (Section 4.3.1), data not shown), however, as previously mentioned these stimuli recruit different types of escape behaviour, thus they are not directly comparable. Tail kinematics were also remarkably preserved in Myrf$^{-/-}$ mutants during hunting routines. Given the fine axial control required for this behaviour, I predicted that a reduction in myelination along RS neurons would influence the timing requirements for successful execution of hunting routines. In agreement with the finding that wavespeed was unaffected during spontaneous swimming, the location of the maximum tail angle during hunting bouts was similar between fish suggesting that motor neuron recruitment was unaffected during hunting in Myrf$^{-/-}$ mutants. One parameter of hunting behaviour that was not assessed in this behavioural assay was the actual success of hunting routines. This would require video recordings of the entire behavioural arena and quantification of paramecia number at the start and end of the experiment. However, given the normal kinematic parameters it is unlikely that their ability to capture prey is diminished compared to their siblings.

Myrf$^{-/-}$ mutants perform an increased frequency of fast swim bouts

Extensive analysis into the structure of swim bouts during spontaneous exploratory behaviour revealed a set of complimentary results that together support the finding that Myrf$^{-/-}$ mutants perform an increased frequency of fast swim bouts. Although this phe-

notype is subtle, the data is robust and exemplifies the ability of the tracking program to measure kinematic parameters with millisecond precision and extraordinary detail. The degree of these behavioural phenotypes would not have been identified using a less sophisticated assay.

Two different methods were used to detect swim bouts in larval zebrafish in the analysis of this data. The first approach utilised the centroid velocity of the larva, the speed at which the *body* of the larva moves, to detect swim bouts. The distribution of centroid velocity values across genotypes provided the first evidence that homozygous mutants appeared to display an increased frequency of fast swim bouts, as demonstrated by the bimodal nature of the distribution and the cumulative frequency plot (Figure 4.17). Indeed, mutants displayed a modest trend towards an increased swim bout frequency overall, which was caused by a two-fold increase in the number of fast swims (Figure 4.18). When individual thresholds were computed for each fish, the probability of a larvae performing a slow or fast bout followed a similar pattern: Myrf$^{-/-}$ mutants were more likely to perform fast bouts (probability of 0.48) than their wild type siblings (probability of 0.07), with heterozygotes displaying an intermediate phenotype (probability of 0.20). However, given the degree of variability in the data these differences did not achieve statistical significance. Comparable findings were detected when using *tail movement* as the detector for swim bouts (Figure 4.20). As mentioned previously, this method of detecting swim bouts is reflective of *active* movement given that high centroid velocity values can be maintained without active movement of the tail, while the fish is gliding passively through water. Using this feature, the bout frequency (Figure 4.20) and total percentage of time spent active (Figure 4.26) were borderline significant (p=0.05).

In-depth analysis of tail metrics during swim bouts provided supporting evidence for these phenotypes. In Myrf$^{-/-}$ mutants, which performed an increased frequency of fast swims, modest yet matching adaptations in tail kinematics were observed including an increase in tail vigour, mean tail beat frequency, the amplitude (theta1) and the velocity of the first half cycle (velocity1). Adaptations which were mirrored, to a lesser extent, by their heterozygous siblings. Although these differences did not achieve significance, the values move in directions which are known to lead to increases in swim velocity

(Severi et al., 2014). Indeed, faster wavespeed values were associated with the high tail vigour and tail beat frequency values in heterozygous and homozygous mutants, consistent with the performance of an increased frequency of fast swim bouts in these groups. No overall differences in wavespeed values were identified between fish, from which I inferred that rostrocaudal patterns of motor neuron recruitment were similar across groups. However, as I will discuss in following sections, there were caveats with this calculation and a motor neuron recruitment phenotype should not be excluded on this analysis alone.

In conclusion, using two separate methods to detect swim bouts, tail movement and centroid velocity, I have demonstrated that Myrf$^{-/-}$ mutants, and to a lesser degree Myrf$^{+/-}$ mutants, display a subtle shift towards a higher frequency of fast swim bouts and the total time spent active, findings which were associated with appropriate modulations in tail kinematics.

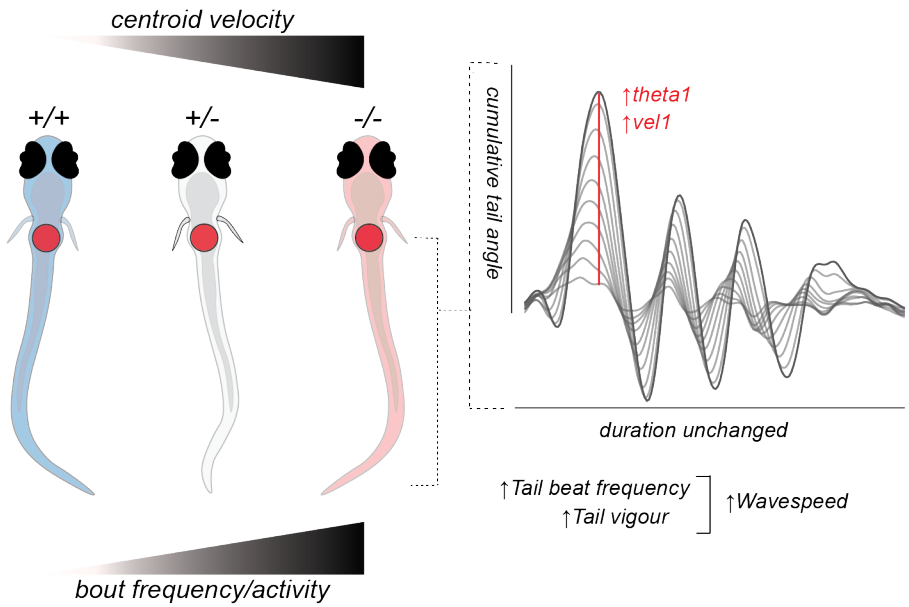

Figure 4.27: Summary of the kinematics underlying the spontaneous swimming phenotypes observed in heterozygous and homozygous mutants
Homozygous mutants perform an increased frequency of swim bouts, due to the performance of a larger number of fast swims. This was associated with anticipated modifications in the tail kinematics such as trend towards an increased tail beat frequency and increased tail vigour. The increase in tail vigour was contributed to by a larger tail angle (theta1) and faster velocity (velocity1) of the tail during the first half beat of a swim bout.

Myrf$^{+/-}$ mutants display an intermediate phenotype in spontaneous swimming

At the larval stages tested, heterozygous mutants demonstrated a phenotype consistent with precocious myelination: an increase in the number of myelinated axons in the presence of normal numbers of OLs. This effect was larger in the dorsal tract, where smaller caliber axons became myelinated, but was still significant in the ventral spinal tract where the axons of RS neurons reside (Chapter 3). This serendipitous discovery inadvertently allowed us to study the behavioural effects of precocious myelin in the CNS in heterozygotes at the same time as hypomyelination in homozygous mutants.

No difference was observed in the latency to perform an escape response between wild type and heterozygous mutant. This is not surprising given the normal thickness of myelin around the Mauthner axon in Myrf$^{+/-}$ mutants (Chapter 3, Figure 3.15). However, in my analysis of spontaneous swimming behaviour, the data from heterozygous larvae showed distributions and values closer to those of homozygous mutants than wild type siblings. This is most evident in the analysis of swim bout frequency, swim speed and the distribution of tail parameters. It is intriguing that opposing myelination phenotypes appear to disrupt swimming behaviour to a similar degree. Indeed, this phenotype may serve as an elegant example that a balance of myelination across more complex circuits is required for appropriate function and behavioural output.

In order to understand the potential mechanisms underlying these behavioural phenotypes, future experiments will be necessary to confirm the identity of the axons in the spinal cord that are precociously myelinated, particularly those in the dorsal spinal cord. Analysis of single cell morphology in Chapter 3 demonstrated that OLs in Myrf$^{+/-}$ mutants appear to have an increased capacity for myelination through the production of more myelin sheaths. Thus, it is possible that the behavioural phenotypes observed are due to the presence of more myelin sheaths along individual axons as well as myelination of axons that are usually unmyelinated at this stage. Indeed, many of the descending interneurons that are involved in controlling swim speed, such as circumferential descending (CiD) and commissural primary ascending (CoPa) interneurons, are located in the dorsal spinal cord. Characterisation of the patterns of

myelination along these specific neurons, using the transgenic techniques presented in the discussion of Chapter 3, should be made an immediate priority. Finally, it is imperative that future experiments interrogating the effects on neuronal circuit activity include heterozygous mutants, to strengthen our novel hypothesis that too much myelin may be equally detrimental to behaviour as too little.

Neuronal control of swim speed and frequency

The circuitry underlying the control of locomotion in larval zebrafish involves complex interactions between multiple aspects of the CNS including descending premotor neurons, local spinal circuits (central pattern generators) and sensory neurons (Berg et al., 2018). Upstream of these components, input from higher brain centres, influenced by neuromodulation and brain state, exerts final control over locomotor activity. Hypomyelination, and equally the precocious myelination observed in heterozygotes, is assumed to encompass the entire CNS, thus multiple elements of this circuitry could contribute to the current phenotype. Here I will propose candidate aspects of circuitry by which disruption to myelination could cause an increase in swim speed and frequency. These predictions will form the basis of future work which will be discussed in Section 4.5.

Central pattern generators:

The rhythmicity of locomotion in many animals is provided by activity in local spinal circuits, known as central pattern generators (CPGs). In larval zebrafish, CPGs are formed of early born primary motoneurons, later born secondary motoneurons and eight known classes of interneurons with their own neurotransmitter phenotypes (Higashijima et al., 2004). Many large motoneurons are robustly myelinated by 6dpf (Svara et al., 2018), with the central axonal component myelinated by OLs and the peripheral component by Schwann cells. Many of the spinal interneurons are also myelinated, including the glutamatergic Commissural Primary Ascending (CoPa) and Circumferential Descending (CiD) interneuron, whereas others remain unmyelinated at these stages of development, such as the glycinergic Commissural Bifurcating Longitudinal (CoBl) and Circumferential Ascending (CiA) interneurons (Koudelka et al., 2016). Thus, disruption to myelination has the potential to affect the function of CPGs in which a fine balance of inhibitory and excitatory tone is required to maintain undulatory tail

movements during swimming. Approximately three to four primary motoneurons are found in the dorsal region of each spinal hemisegment, with larger numbers of smaller secondary motoneurons occupying the ventral and dorsal spinal cord. Primary motoneurons are easily recognised by their large soma and large caliber motor axons. The recruitment of motoneurons during swimming behaviour has been shown to follow a 'size principle', whereby larger motoneurons are recruited with increasing speed. Specifically, ventral secondary motoneurons are typically engaged in slow swims, with sequential activation of more dorsal secondary and primary motoneurons with increasing swim speed (Liu and Westerfield, 1988; McLean et al., 2007). Thus, I would predict that there may be a shift towards more dorsal primary and/or secondary MN recruitment during spontaneous swimming in Myrf$^{-/-}$ mutants. This could be the consequence of increased excitability of motoneurons themselves, or a switch in premotor neuron recruitment which will be discussed in the next section. In addition to a dorsal-ventral pattern of motoneuron activity during swimming, differences in an anterior-posterior recruitment have also been associated with swim speed. For example, slow j-turns during hunting involve the preferential recruitment of caudal myotomes, whereas fast capture swims require a switch to anterior bending (Borla et al., 2002). However, the findings of invariable wavespeed values during forward swims in addition to a similar maximal tail bend angle location along the tail during hunting suggest that a difference in anterior-posterior recruitment may be less likely.

Pre-motor neurons:

The main source of excitatory drive to motor neurons in the spinal cord is provided by descending v2a interneurons (CiDs) (Kimura, 2006; McLean et al., 2007). Spinal interneurons can be classified by their transcriptional profile which is dependent on the ventral progenitor domain from which they originated (i.e. v0 to v3). For example, v2a neurons express transcription factor chx10. Under this classification system, many large RS neurons are also classified as v2a neurons (Kimura et al., 2013). V2a neurons show a similar modular organisation to motoneurons: during slow swims, ventral v2a neurons provide excitation to ventral motor neurons as shown in Figure 4.28. However, during fast swims these neurons become de-activated and dorsal v2a neurons drive excitation of primary motoneurons. Indeed, ablation of ventral v2a neurons completely abolishes locomotion, whereas ablation of dorsal v2a neurons alone prevents the generation of

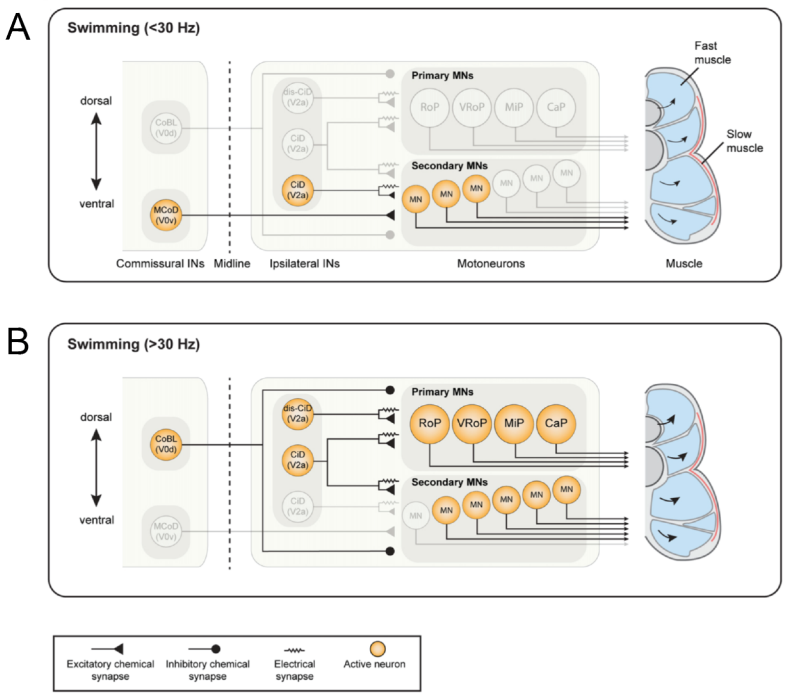

Figure 4.28: Neuron types and connectivity within the spinal CPG network of larval zebrafish.
Figure taken from Berg et al. (2018). **(A.)** During slow swimming, ventral motoneurons are active and receive excitatory input from ventral v2a neurons (CiDs). Commissural excitatory v0 neurons provide excitation from the contralateral side. Secondary Motoneurons recruit slow muscle. **(B.)** During fast swimming, ventral Motoneurons remain active but dorsal secondary Motoneurons and primary Motoneurons are added to the active pool. A switch to recruitment of dorsal v2a and v0 from their ventral equivalents occurs.

high speed swims (Eklof-Ljunggren et al., 2012; Sternberg et al., 2016). Interestingly, ablation of v2a neurons causes an increase in the phase lag of extracellular recordings from rostral and caudal myotomes, consistent with disrupted rostrocaudal propagation of activity, suggesting that, if present, increased v2a neuron activity would be detectable in the wavespeed analysis I performed (Eklof-Ljunggren et al., 2012). V1 interneurons, such as the glycinergic CiA interneurons, are required to provide the in phase inhibition of slow type v2a neurons during fast movement (Kimura and Higashijima, 2019). RS neurons of the nMLF also synapse directly onto motor neurons and have been shown to control swim speed by modulating tail beat frequency (Severi et al., 2014; Wang and McLean, 2014).

Together, RS neurons such as the v2a interneurons and those belonging to the nMLF appear well placed to underlie the increase in swim velocity observed in Myrf$^{-/-}$ mutants. These neurons are known to be myelinated in wild type conditions at the ages

tested in these experiments (Koudelka et al., 2016). Thus, it is possible that dysmyelination in these axons leads to altered excitability and/or action potential conduction velocity with a subsequent effect on motor neuron recruitment. To test this, it would be necessary to map the myelination profile of these particular neurons in Myrf$^{-/-}$ mutants and attempt to correlate this with functional circuit properties, this is discussed in more detail in Section 4.5. Paired electrophysiological recordings from the nMLF and spinal motor neuron population as per Wang and McLean (2014) would allow assessment of connectivity and measurement of latency to recruitment. Alternatively, functional imaging of the nMLF during head-fixed swimming behaviour would allow correlation between nMLF activity and tail movement in Myrf$^{-/-}$ mutants.

Brain input:

Swimming behaviour can be driven by activity in higher brain centres which recruit RS neurons to execute premotor commands. The mesencephalic locomotor region (MLR), which is conserved across vertebrate species, exists as one of these regions. The MLR consists of different neuronal subtypes which have been shown to have differential effect on locomotion in rodents (reviewed in Lau et al. (2019)). The MLR conveys signals to medial reticular formation (the equivalent of RS system) in mammals, allowing recruitment of appropriate spinal circuits (Noga et al., 2003). The MLR is yet to be identified in larval zebrafish, however it is thought to exist due to its presence in other fish species (i.e. lamprey) where it has been shown to form monosynaptic connections to RS cells (Le Ray et al., 2003). Therefore, the MLR could, in theory, pose a brain region whose activity is influenced by CNS hypomyelination.

Brain state and neuromodulators:

Locomotory drive can also be influenced by brain state, for example the level of arousal. Larval zebrafish are known to experience different brain states as exemplified by their circadian rhythm of sleep and wakefulness (Prober et al., 2006). Furthermore, larval zebrafish display conserved neuromodulatory systems for the control of brain state (Lovett-Barron et al., 2017). Interestingly, a relationship is emerging between disrupted myelination and neuromodulation (Takahashi et al., 2011). Cell type specific ablation of erbB3, a gene that has been linked to psychiatric diseases in humans, signalling in OLs has been shown to cause hypomyelination and increased levels of anxiety (Roy et al., 2007). Intriguingly, this was associated with significant increases in the levels

of dopamine receptors and transporters in the brain. In larval zebrafish, dopaminergic signalling is involved in permitting the developmental switch in locomotor behaviour at three to four days post fertilisation, from long burst swims to shorter 'beat and glide' swims which are consistent with exploratory locomotion (Lambert et al., 2012). Indeed, D1 receptor signalling has been shown to increase spontaneous locomotor activity in zebrafish and induce faster swim speed through recruitment of secondary motoneurons and enhanced excitability of PMNs (Irons et al., 2013; Jha and Thirumalai, 2019). Diencephalic dopaminergic projection neurons provide the only source of dopaminergic innervation to the spinal cord at the ages tested in these behavioural assays (McLean and Fetcho, 2004). At early stages of embryonic development, this dopaminergic innervation has been shown to regulate the generation of late born motor neurons and v2a neurons. In the absence of dopaminergic signalling, the number of motor neurons is reduced while v2a neurons show an increase in number at 33 hours post fertilisation. These effects are sustained into juvenile stages where they can be detected behaviourally as reduced activity and reduced response rate to tail touch stimuli (Reimer et al., 2013). Clearly, as myelin is not present in the CNS at these stages under normal circumstances, it is not feasible for myelination to exert an effect on dopaminergic regulation of motor neuron development. However, these studies demonstrate the potential for long-ranging dopaminergic inputs to influence CPG development and activity. Combining these findings together, one could speculate that a lack of myelination could influence dopaminergic signalling to the spinal cord at the developmental stages tested, contributing to the increase in fast swim bout frequency observed in Myrf$^{-/-}$ mutants. To pursue this line of investigation, measurement of dopamine receptor transcript levels by qRT-PCR, or tissue expression of dopamine receptors using in situ hybridization, in Myrf$^{-/-}$ mutants and wild type siblings could be a first port of call. If differences in dopaminergic signalling were revealed, then attempts to correlate dopamine levels with the swimming output would ensue. This could be accomplished by performing *in vivo* imaging of novel g-protein coupled receptor based fluorescent dopamine sensors in the brain and/or spinal cord during the performance of spontaneous swimming (Sun et al., 2018). Alternatively, rescue of the phenotype could be attempted by treating Myrf$^{-/-}$ mutants with dopamine receptor antagonists.

Sensory modulation:

Appropriate locomotion is dependent on sensory feedback. During active swimming in larval zebrafish, sensory Rohon-Beard (RB) neurons located in the dorsal spinal cord can induce fast swimming through activation of v2a neurons. Silencing RB neurons, using cell-type specific botulinum toxin expression, in freely swimming larvae has been shown to reduce tail beat frequency and swim bout velocity (Knafo et al., 2017). RB neurons also synapse onto CoPas which drive contralateral motoneuron recruitment and swimming away from the sensory stimuli (Downes and Granato, 2006; Gleason et al., 2003). Sensory RB neurons remain unmyelinated at these stages, however, subsets of v2a neurons and the majority of CoPa neurons are myelinated (Koudelka et al., 2016). Therefore, it is possible that the relay of sensory information could be disrupted in Myrf$^{-/-}$ mutants resulting in altered swimming kinematics. These interneurons are promising candidates for mediating the behavioural phenotypes observed in homozygous and heterozygous mutants, given their location in the dorsal spinal cord. Performance of swim bouts is also important to maintain, and correct, posture in larval and juvenile zebrafish whose centre of buoyancy is fairly anterior, rendering them 'top heavy'. When their centre of buoyancy is disrupted, by filling the swim bladder with paraffin oil, larvae perform more bouts per minute in a constant attempt to stabilise their posture while swimming through a water column (Ehrlich and Schoppik, 2017). A lack of postural control is possible in Myrf$^{-/-}$ mutants, and possibly more relevant in adults (see later section), however the experiments in this chapter were performed in a shallow volume of embryo media which would not require the same degree of postural stabilisation observed in the cited experiment. This study also highlights that swim bladder abnormalities are capable of causing an increase in swim bout frequency. To ensure this was not a confounding factor of my own finding I measured swim bladder size Myrf$^{-/-}$ mutants and found it to be unaffected (Chapter 3, Figure 3.8).

Pectoral fins:

One feature of the larval zebrafish that was overlooked by our analysis was pectoral fin movements, as they are not tracked with the current software. In contrast to adult zebrafish, larvae move their pectoral fins rhythmically with undulations of their body during slow spontaneous swims (Green et al., 2011; Thorsen, 2004). Thus, increased activity of pectoral fins could theoretically contribute to increased swim speeds. This

could occur if action potential conduction delays along the spinal cord resulted in anterior weighted motor neuron recruitment. However, evidence for the exact function of these pectoral fin movements is controversial. Assessment of the locomotion of a finless morphant during spontaneous swimming demonstrated no discernible difference compared to larvae with pectoral fins (Green et al., 2011). In a manner similar to my own experiments, multiple kinematics of fin, body and tail movement were assessed using high speed video tracking of larvae. No effects on bout duration, distance travelled, mean velocity, tail speed, axial stability or body curvature were detected in the absence of pectoral fins, providing strong evidence that, at least during spontaneous swimming in normal larvae, pectoral fins do not contribute greatly to locomotion. From this, it was suggested that pectoral fin movements are more likely to play a respiratory role, providing flow of oxygenated water to the gills, during spontaneous swimming. On the contrary, pectoral fin movements have been observed to occur specifically during LLCs of the escape response, however whether these movements contribute to the behavioural output of LLCs is yet to be tested (Jain et al., 2018; McClenahan et al., 2012). Seemingly, pectoral fins may play differential functions across different types of swimming behaviour; although they have not been shown to mediate swim speed under normal conditions (Green et al., 2011) they should still be considered as a potential locus of adaptation in mutants whose 'normal' swimming circuitry is disrupted.

4.5 Interpretation and predictions

To interrogate each of these levels individually would be an ambitious endeavour. Given the subtlety of phenotypes at the behavioural level, detection of circuit level changes may be challenging and will require high temporal resolution. I would argue that subsequent investigations should focus on corroborating the behavioural phenotypes of increased bout frequency and swim speed using functional assessment of motoneuron activity, as given our knowledge of the neuronal circuitry underlying swim speed, these phenotypes should be associated with adaptations in motoneuron recruitment. However, as motoneurons are the downstream target of all the aforementioned components of the relevant circuitry this will not enlighten us to the mechanism by which hypomyelination is influencing their activity. Thus, first we will seek to identify corresponding profiles of motoneuron activity, then we can prioritise targeting individual mechanisms.

Investigating altered patterns of motoneuron recruitment in the spinal cord:

I predict that the increased swim speeds observed in Myrf$^{-/-}$ mutants will be detectable as altered spatiotemporal recruitment of motoneurons in the spinal cord. This may be observed as:

• an increase in the recruitment of dorsal motoneurons to the active motor pool during locomotion,

• altered distribution of motoneuron recruitment in an anterior to posterior direction,

• or altered synchrony of motoneuron activity across the motoneuron population.

Theoretically, alterred motor neuron recruitment should be detectable with the wavespeed analysis I performed, which measures the speed of tail curvature propagation (thus speed of motor neuron recruitment) along the tail. In support of this, increases in tail vigour and tail beat frequency were associated with subtle increases in wavespeed in heterozygous and homozygous mutants. However, on analysis of the distribution of wavespeed values alone no overt differences were observed between groups. Although wavespeed values demonstrated a positive correlation with centroid velocity values, they were generally quite variable despite limiting the analysis to forward swims. It is possible that this reflects inconsistencies in the computation of wavespeed across data. Additionally, as a threshold for forward swims was computed using theta1 angles, and this variable shows an altered, albeit subtle, distribution in heterozygotes and homozygous mutants, it is possible that I have segmented out the relevant swim bouts that exhibit a faster wavespeed value. Thus, further optimisation of wavespeed analysis should be performed in conjunction with the circuit level investigations that I propose.

Direct measurements of motor neuron activity may provide more accurate detection and information on motor neuron subtype recruitment. The motor neurons of larvae are large enough to permit whole cell patch clamp recordings *in vivo* allowing assessment of connectivity via paired recordings from premotor and motor neurons, and excitability of primary and secondary motor neurons. In larval zebrafish, electrophysiological recordings from motor neurons required immobilisation with paralysing agents. Importantly, studies have shown that the patterns of motor neuron activity of immobilised larvae, known as 'fictive swims', correlate well with sequences of behaviour

observed in freely swimming fish allowing inference of swimming behaviour from electrophysiological recordings (Dunn et al., 2016). Thus, I would also predict that firing frequencies of motor neurons will be higher in Myrf$^{-/-}$ mutants compared to their wild type siblings, consistent with the increased swim bout frequency phenotype. This could also be measured indirectly using extracellular recordings from the musculature or peripheral nerves.

Additional information on *population level* motoneuron activity can be gleaned using functional imaging. By driving the expression of genetically encoded calcium indicators (GECIs) in the motor neuron population, motor neuron activity can be observed with high spatiotemporal resolution during fictive or spontaneous behaviour in immobilised or head-fixed larvae respectively. In this way, we can measure the frequency, synchrony, amplitude and subtype recruitment of motor neuron activity across large regions of the spinal cord simultaneously. In the final months of my PhD I began to explore suitable imaging systems, characterize potential driver lines for the expression of GECIs in motoneurons and assess optimal larval preparations which allowed for the performance of fictive, or spontaneous, swimming during live imaging. This information can be found in the Appendix 4.

In parallel with these experiments, it will be necessary to document the myelination status of candidate interneurons and RS neurons. This can be achieved by using existing driver lines chx10:gal4 (v2a neurons, (Kimura et al., 2013)) and rs:kalta4 (reticulospinal neurons, provided by Dr. Isaac Bianco, UCL) to drive mosaic neuronal expression of our transgenic construct tg(uas:gfp-cntn1a-2a-tdtomato). In this construct, the fluorescent protein tdtomato acts an axonal structural reporter, while gfp-cntn1a is extruded from the axolemma in myelinated regions. Thus, absence of gfp signal can be used to indicate the presence and length of myelin sheaths along the entire length of individual neurons (Koudelka et al., 2016). Data on myelin sheath parameters along these axons in heterozygous and homozygous mutants can then be correlated to the output of functional imaging studies and input into computer models to predict/confirm their circuit level effects.

Understanding the extent of behavioural phenotypes

The most robust behavioural phenotype identified in the Myrf$^{-/-}$ mutants was the delay in their latency to perform the escape response. Yet, despite a 66% reduction of myelinated axons in their spinal cord, the performance of Myrf$^{-/-}$ mutants across a wide range of other RS-mediated behaviours was generally indistinguishable from their wild type and heterozygous siblings. It was only upon analysis of the distribution of data that subtle increases in swim speed and associated adaptations in tail kinematics were identified. This raises the question as to why some behaviours would be largely preserved in the context of such marked hypomyelination, while others such as the escape response are obviously affected.

As discussed previously, the speed at which action potentials are conducted along the Mauthner axon (∼1.3mm/ms on antidromic measurements) compared to the size of a larval zebrafish (∼3.5mm at these ages) means that disruption to conduction speeds, even along what is known to be the fastest conducting axon of the entire CNS in zebrafish, can only ever result in millisecond delays. For example, the average time difference observed between the latency to escape response of a wild type sibling and a homozygous mutant was less than 3ms. The ability to detect these differences in freely swimming larvae pays homage to the sensitivity of behavioural assays that have been established by our collaborators. However, one could argue that if we can detect behavioural correlates of conduction delays along one of the fastest conducting axons, then uncovering delays in circuits made up of smaller caliber, slower conducting neurons should be feasible. On the contrary, perhaps the size of Mauthner renders its function more susceptible to the loss of myelin, while smaller caliber axons in organisms of this size can maintain a degree of function without substantial myelinating support.

Perhaps the answer lies in the organisation of the RS system. In the introduction to this chapter I explained that specific locomotor behaviours can be associated with distributed activity across multiple RS neurons. Furthermore, individual RS neurons can be involved in multiple behaviours suggesting that different modules of RS activity combine to produce specific behavioural outputs. Thus, it is possible that this system could offer a certain degree of functional redundancy. However, given the degree of hypomyelination across the ventral spinal cord I find this notion difficult to accept. Along

a similar vein, it is possible that mechanisms of developmental plasticity exist in the larval zebrafish that are able to compensate circuit function in the face of myelin loss. This would not be the first time that such mechanisms have been observed. When larval zebrafish are faced with supernumerary Mauthner axons, as a result of des/notch1a gene mutation, normal escape responses are maintained by regulating the distribution and number of collaterals that each axon forms (Liu et al., 2003). One way to maintain conduction velocities in the absence of myelin loss would be to increase axon caliber, however no such adaptation was noted on axon caliber measurements in Chapter 3. This does not mean to say that other, as of yet, unidentified adaptations are present.

The variability of behavioural data is likely a key contributor to the lack of more statistically significant findings in many of the behaviours tested. As this is a biological system, the Myrf mutation will not cause exactly the same pattern of hypomyelination in every fish. Having said this, the reduction in the number of myelinated axons is quite consistent across Myrf$^{-/-}$ larvae, but this does not mean to say that the axons that remain myelinated are the same across every fish. Combining this possibility with the presence of a modular system is likely to complicate behavioural outcomes even further. To circumvent this, now that a potential role of myelin in the function of circuits underlying spontaneous swimming has been identified, it would be interesting to ablate the myelin of the candidate neurons involved in this behaviour in wild type fish and assess the behavioural effect. Methods to achieve targeted myelin ablation have been established in larval zebrafish through the expression of genetically encoded photosensitiser KillerRed in oligodendrocytes (Auer et al., 2018). Upon light irradiation of individual cells, reactive oxygen species are generated resulting in apoptosis and destruction of associated myelin sheaths. Adapting imaging techniques to allow spatially targeted ablation of cells along a given axon, such as those belonging to the nMLF, v2a and CoPa interneurons, could allow for more standardised disruption of myelin. However, this technique is time consuming and one would have to take measures to deal with the subsequent migration of OPCs and differentiation into OLs that will likely take place in order to replace lost myelin.

Behaviour in adult Myrf$^{-/-}$ mutants

If the size of a larval zebrafish is protecting against the development of more prominent behavioural phenotypes, perhaps assessing behaviour in adult Myrf$^{-/-}$ mutants would yield more robust findings. In Chapter 3, I demonstrated that adult Myrf$^{-/-}$ have a near complete lack of myelin in their CNS, confirmed by a complete loss of Mbp transcript and the absence of myelinated axons on TEM (Chapter 3, Figure 3.22). In general, the swimming behaviour of adult mutants is indistinguishable from their siblings when observed in their normal housing conditions. However, over time I observed that Myrf$^{-/-}$ mutants spent more time shoaling at the bottom of their tank than their siblings. This is viewed as an indicator of anxiety in adult fish (Egan et al., 2009; Stewart et al., 2012). Indeed, disruption to myelin related genes and a loss of OLs are common pathologies in schizophrenic patients in which anxiety is a commonly symptom (Barley et al., 2009; Hakak et al., 2001; Mccullumsmith et al., 2007). Furthermore, anxiety behaviours have been observed in multiple animal models with mild disruption to CNS myelination (Makinodan et al., 2012; Poggi et al., 2016; Tanaka et al., 2009). However, it is also possible that this behaviour is a result of general motor deficits that render adult fish less capable of traversing the water column. In an attempt to document this behavioural phenotype, I subjected adults to the novel tank test - an established behavioural assay for anxiety that would allow me to record motor behaviour at the same time. In this assay, 'anxious' fish spend more time occupying the bottom half of the tank (Cachat et al., 2010), however this phenotype would also be observed if fish possessed a general locomotor phenotype. Thus, further analysis would be needed to distinguish between the two. As a preliminary experiment, individual fish were recorded for ten minutes following introduction into a novel environment. Post video acquisition, automated tracking was performed on the videos using the freely available software EzTrack (Pennington et al., 2019) and time spent in the bottom of the tank was quantified across genotypes (N = 5 per group). No differences were observed between groups over the time period tested, with all fish spending approximately 90% of their time in the bottom of the tank (data not shown). Future experiments would need optimisation to reliably rule out an anxiety phenotype, perhaps by extending the period of time tested or testing anxiety in a social context (Engeszer et al., 2004; Saverino and Gerlai, 2008). However, now that I have a repository of video data it would be interesting to analyse the motor behaviour of adult Myrf$^{-/-}$ mutants more closely.

Swimming behaviour appears generally normal in this environment, however there is a tendency towards a subtle loss of posture in adult Myrf$^{-/-}$ mutants observable as a more severe pitch axis (nose down) and axial rotation. Freely available machine learning algorithms such as DeepLabCut (Nath et al., 2019) allow users to define anatomical regions (e.g. the eye and swim bladder) over a collection of frames from a video. Following training of the algorithm, depiction and measurement of these regions can be collected over the entire video, permitting in depth analysis of movement and posture. Thus, employing DeepLabCut to the current video dataset may reveal interesting motor phenotypes in the adult mutants.

Summary

In summary, I have identified two candidate behavioural phenotypes whose circuitry is modulated by aberrant CNS myelination during development: the escape response and spontaneous swimming behaviour. Despite the subtleties of the phenotypes, they provide novel insight into the differential effects that myelination may afford to specific circuits of the CNS i.e. that both too much and too little myelin can be detrimental to circuit function. Importantly, these results have enlightened us to the temporal precision that will be required for future assessment of circuit level activity using electrophysiological or functional imaging techniques. These challenges will be discussed in Chapter 5. Indeed, the priority for subsequent experiments is to correlate functional circuit activity to the behavioural phenotypes identified in this chapter. Following this, to confirm that these are circuit specific effects, one will need to demonstrate that these findings can be recapitulated by inducing hypomyelination specific to the candidate neurons and circuitry that have been presented in this discussion. However, with currently available techniques this will not be a trivial undertaking and it must be considered whether behavioural / functional read outs of these more refined manipulations of myelination will be detectable. Finally, these results highlight the importance of considering heterozygous mutants as an independent group during experiments. Not infrequently, heterozygotes are combined with their wild type siblings to form a 'sibling' group for comparison to homozygous mutants. Given the finding of a gain of function phenotype in our Myrf$^{+/-}$ mutants, heterozygotes should be carefully assessed for their own phenotypes for this may reveal novel and unexpected consequences of your genetic manipulation.

Chapter 5

Discussion

With this thesis project, I explored the potential of larval zebrafish as a model to study the effects of CNS myelination on circuit function and behaviour. In my introduction, I outlined our current state of understanding surrounding the role that activity regulated myelination may play in the development of novel behaviours. I identified that the major barrier to establishing activity regulated myelination as a form of functional plasticity, to the level that mechanisms of synaptic plasticity are validated, is the current inability to perform longitudinal studies that allow correlation of myelin structure to functional assessment of circuit activity and behavioural output. In this discussion, I will present how the findings of my thesis attest to the suitability of larval zebrafish as a model to lift this barrier, identify potential difficulties that will need addressing and propose lines of investigation for this model in the future.

Before enrolling zebrafish into experiments to study activity regulated myelination, where myelin adaptations are predicted to be mild, it was integral to confirm that we could use this model to detect functional readouts of more robust changes to CNS myelination at a circuit and behavioural level. This was achievable for us by bringing together two well established fields of research: one which uses larval zebrafish as a model to study the mechanisms of myelination, and the other which employs larval zebrafish to interrogate neuronal circuits underlying behaviour.

The core aim of this project was to disrupt CNS myelination and assess the ensuing effects on behaviour. We successfully established the Myrf$^{-/-}$ larval zebrafish mutant as a CNS specific model of hypomyelination, characterised by a reduction in the number

of myelinating oligodendrocytes and a robust loss of two thirds of the myelinated axons in the spinal cord. It is unclear at present why this phenotype was not as extreme as anticipated, given our knowledge of equivalent rodent models in which Myrf gene function is lost. However, I believe that this worked to our advantage as more severe myelin phenotypes, at least in rodents, are often associated with premature death or disability which would have inhibited extensive behavioural phenotyping. The unforeseen discovery of precocious myelination in heterozygous mutants put this project in the unique position to simultaneously interrogate the role of precocious myelination on behaviour.

Using sophisticated behavioural assays, with the support of collaborators we were able to detect aberrations in the locomotor behaviour with millisecond precision. We confirmed that Myrf$^{-/-}$ mutants exhibited anticipated delays in their latency to perform escape responses to mechanosensory stimuli. This is in keeping with the traditional function of myelin in permitting enhanced action potential conduction speed along single axons. However, the discovery that swimming behaviour was modified in an unexpected direction – towards an increase in *fast* swims – in both homozygous *and* heterozygous mutants supports the notion that refined levels of myelination are required for the control of timing across more complex circuits. These behavioural phenotypes were certainly subtle but not outside the realms of expectation given the size of larval zebrafish. This emphasises the temporal sensitivity that future investigations into the circuit mechanisms underlying this phenotype will require.

To prepare this project for publication, we have started to address the circuit mechanisms underlying these phenotypes. Electrophysiological recordings from the Mauthner cell will inform us of the presence of an action potential conduction delay, confirming the predicted function of myelin along this axon. At present, the preparation of larvae for electrophysiological recordings is invasive and requires the removal of tissue which is not compatible with long term survival. For the purposes of demonstrating a conduction delay this is acceptable, but to place zebrafish as a model for the longitudinal assessment of circuit activity in relation to myelination, non-invasive techniques will need to be implemented. Additionally, to address the circuit mechanisms underlying the more subtle swimming phenotype in Myrf$^{-/-}$ mutants, electrophysiological techniques will not

allow the population level interrogation that is required. Needless to say, zebrafish are a sophisticated model for this pursuit. Existing technology allows *in vivo* non-invasive monitoring of neuronal activity in larval zebrafish with remarkable temporal precision. This is permitted by advanced imaging systems such as light sheet microscopy, which permit high-speed imaging (∼300Hz) through large populations of cells during the performance of behaviour (Abdelfattah et al., 2019; Migault et al., 2018). In combination with constantly evolving GECIs, this allows visualisation of neuronal activity in populations of neurons over extended periods of time. However, the kinematics of current GECIs limit their ability to indicate spike timings, and often individual action potentials depending on the frequency of firing. For focused interrogation of the role of myelination in controlling timing within specific circuits, particularly in the high frequency firing motor neurons involved in swimming, enhanced visualisation of spike timing and subthreshold voltage changes could be achieved with newly developed genetically encoded voltage indictors (GEVIs). Conveniently, these have been validated for the exact purpose that we would require: monitoring neuronal dynamics during visually driven fictive swims (Abdelfattah et al., 2019). Thus, the technology exists to permit non-invasive circuit level analysis in larval zebrafish at the temporal resolution required to detect mechanisms underlying our current phenotypes, and for the interrogation of circuit function in response to activity-regulated myelination if deemed a fruitful endeavour. However, to establish these techniques is a specialist undertaking and not achievable in the short term. Thus, defining the circuit mechanisms underlying the swim bout frequency and velocity phenotypes observed in Myrf$^{-/-}$ mutants should be incorporated into the long-term goals of the laboratory.

Importantly, the findings of this PhD thesis have enlightened us to the scale of behavioural adaptation that can be expected from CNS specific manipulations to myelination in larval zebrafish. Despite a robust reduction in the level of myelination in the CNS of Myrf$^{-/-}$ mutants, the phenotypes found at a behavioural level were modest by comparison. In my introduction, I raised the concern that existing rodent studies demonstrating activity-mediated changes in myelination document subtle changes in myelin morphology and behavioural output (Gibson et al., 2014). This makes me question whether equivalent adaptations in myelination across *individual* circuits will lead to detectable behavioural and/or functional changes in the larval zebrafish, even with

the aforementioned imaging techniques and existing sophisticated behavioural assays.

Interesting work from our own laboratory has shown that reticulospinal neurons in larval zebrafish myelinate via activity-mediated mechanisms and exhibit a critical period whereby individual myelin sheaths along an axon demonstrate fluctuations in growth and are susceptible to increases in neuronal activity (Koudelka et al., 2016; Williamson, 2020). It has been proposed that the presence of this critical period may allow for the shaping of myelin across reticulospinal circuits and early refinement of circuit function and subsequently behaviour. I would argue that detecting any behavioural adaptations that occur as a result of these plastic changes would be problematic given the extent of analysis required to identify a phenotype in the Myrf$^{-/-}$ mutant which possesses a substantial reduction in myelination. Perhaps the Mauthner circuitry holds the most promise for further investigations into activity-mediated myelination and circuit function, given that this system demonstrated the most susceptibility to changes in myelination. However, the Mauthner neuron is unusual in the fact that it does not possess traditional patterns of myelination: nodal regions are more punctate in appearance and are only present at collateral branching points. Thus, measurement of standard parameters such as myelin sheath length and number, to correlate to circuit output, are not straightforward.

In summary, given the modest effect that hypomyelination in the Myrf$^{-/-}$ mutant model had on behaviour my current opinion is that pursuing larval zebrafish as a model to detect the functional sequelae of activity-mediated myelination *specifically* will be challenging. However, the current Myrf model presents an unrivalled opportunity to further investigate the notion that a balance in myelination is required for complex circuit function. In the following section, I will discuss how I would approach each of these lines of investigation using the insight gained from this project.

Future perspectives

Using the Myrf model to investigate population level dynamics of neuronal activity

The finding that both increases and decreases in CNS myelination can contribute to aberrations in swimming behaviour is extremely interesting and supports a role for myelination in controlling timing across more complex circuits. Although the behavioural findings were subtle, I believe that more information will be gleaned by using the Myrf model at the current larval stages to investigate the effects hypomyelination or precocious myelination on CNS *population level* activity. This should first be performed in the context of motor neurons in the spinal cord, to corroborate the current behavioural phenotypes, as discussed in Chapter 4. In the longer term, I believe that the Myrf model could lend itself well to a similar assessment of hypomyelination on *brain-wide* neuronal population and network activity. Given the indication that spatiotemporal recruitment of neurons is affected in the complex spinal circuits underlying swim behaviour, it seems reasonable to assume that such an effect could also exist in the complex networks of the brain. As presented in my general introduction, many clinical disorders of connectivity are associated with a loss of white matter and dysregulation of myelin genes (Chapter 1, Section 1.10.1). Indeed, ensembles of neurons exist in the larval zebrafish brain which display synchronous recruitment during spontaneous and stimulus evoked activity (Diana et al., 2019; Romano et al., 2015). These ensembles are often located in spatially compact regions of the brain and display similar temporal activity profiles across fish, where they have been shown to be involved in sensory processing (Diana et al., 2019; Romano et al., 2015; Sumbre et al., 2008; Wolf et al., 2017). Thus, patterns of ensemble activity could be used as a readout for the effects of hypomyelination or precocious myelination across complex brain networks. This may be detectable as altered ensemble activity, connectivity, distribution and coherence (within ensemble activity) (Diana et al., 2019). Given emerging theories on the role of myelination in oscillatory brain activity (Pajevic et al., 2014), this makes for an exciting area of research for which the Myrf larval zebrafish would be a fitting model.

Zebrafish as a model to pursue investigations of activity-mediated myelination

Despite the many advantageous qualities presented by the larval zebrafish for the integrated assessment of myelin, circuit function and behaviour, my findings suggest that the functional implications of subtle adjustments to myelination that occur during activity-mediated myelination would be undetectable at these developmental stages. As I discussed in Chapter 4, this is likely due to the small size of the larval zebrafish which confers some protection from robust changes in conduction velocity. For example, loss of two-thirds of the myelinated axons in Myrf$^{-/-}$ mutants caused only millisecond delays in the latency to perform an escape response. Thus, the effects of potentially modest adaptations of myelin that would occur during activity-mediated myelination may only alter timing on a submillisecond timescale which would be undetectable with even the most sophisticated behavioural and functional imaging techniques.

Larvae may still be a suitable model for studying activity-mediated myelination from a different perspective. One could take advantage of their innate and inducible behaviours to drive increased activity across circuits, e.g. by displaying optomotor gratings to drive continuous motor behaviour, and subsequently assess the effects on myelination across the underlying circuitry. Although this would not inform us of a functional effect of myelination, it would provide evidence that physiological levels of neuronal activity can induce changes to patterns of myelination across multiple neurons in a circuit – a feat that has not yet been achieved in any system.

If one were to pursue the functional implications of activity-mediated myelination, I would advise them to move into a larger model, which could include juvenile/adult zebrafish. The caveat with moving into larger models is that you lose optical penetration, surrendering the main advantage that larval zebrafish provide. Thus, using juvenile (∼1-3 months of age) stages of zebrafish which may provide the size required to detect behavioural effects of subtle adaptations in myelination, yet are small enough to permit imaging of their circuits may represent a suitable middle ground. Another advantage of using juvenile zebrafish is that at this age, they perform an even wider spectrum of behaviours for interrogation including social behaviour and conditional learning. Optical clarity could be achieved at these stages by using existing pigmenta-

tion mutants such as Casper (White et al., 2008) and Crystal (Antinucci and Hindges, 2016) mutants. Indeed, some researchers have even successfully performed functional imaging of more superficial regions of the brain, such as the dorsal pallium (topographical equivalent of the cortex in mammals) in adult nacre mutant (Okamoto, 2018), although at this size imaging entire circuits would not be feasible.

In summary, although the size of a larval zebrafish is advantageous for cellular resolution imaging of myelination and activity across circuits of the nervous system, it represents a disadvantage for the detection of subtle alterations in neuronal activity which would impede its use as a model for studying the functional effects of activity-mediated myelination. On the contrary, the size of rodent models may make them more suitable for the latter pursuit, yet techniques to allow equivalent optical access to entire circuits *in vivo* is limited. Thus, until imaging techniques have advanced there is a trade off to be made in the choice of model to use for cellular, circuit or behavioural assessment of activity-mediated myelination. However, the juvenile stages of zebrafish may represent a perfect compromise and should be explored as a model for future investigations.

Conclusion

This project represents the first attempt to perform an integrated analysis of CNS myelination on circuit function and behaviour *in vivo*. We have identified that complex circuits in the CNS may depend on a balance of myelination to maintain appropriate behavioural output, supporting a role for myelin in the control of action potential timing across distributed circuits. Additionally, this study has alerted us to the robustness of the larval zebrafish to deficits in myelination and highlighted the difficulties that may be faced in detecting behavioural and functional adaptation to more refined changes in myelination, i.e. in response to activity regulated myelination. Long term we should take advantage of this unique model, which conveniently provides us with the opportunity to study gain and loss of myelin function in Myrf heterozygous and homozygous models respectively, to investigate the role of myelination on population level dynamics of neuronal activity in the CNS. Although an ambitious endeavour, it could yield rewarding and novel insights into the role of myelination in the function of complex circuits across the CNS.

Appendix 1: Supplementary data to Chapter 3

Expression pattern of Myrf in the larval zebrafish

Little is published on the spatiotemporal expression pattern of Myrf in zebrafish. In situ hybridisation data kindly provided by Dr. Kelly Monk's laboratory group (The Vollum Institute, OHSU) demonstrates a CNS specific expression of Myrf with staining mainly confined to cell bodies within the CNS, consistent with its expression in myelinating OLs and not Schwann cells (Figure 5.1C). A recently published transgenic line tg(myrf-GFP) displays a similar distribution pattern with cellular GFP expression restricted to the CNS (Treichel and Hines, 2018). Within our own lab, RT-PCR on FACS sorted neurons and oligodendrocytes has demonstrated the presence of Myrf cDNA in myelinating glia (MG) but not in neurons (Klingseisen et al., 2019, *in review*), consistent with the mouse RNAseq databases which shows Myrf expression unique to oligodendrocyte lineage cells (Zhang et al., 2014). There is little information regarding the expression of Myrf elsewhere in the zebrafish. However, given the gross morphological phenotype seen in adult mutants (Figure 5.6) it is likely that Myrf function exists outside of the CNS in zebrafish as is observed in mammals. Semi-quantitative RT-PCR performed on cDNA from whole wild type embryos aged from 0 to 4dpf demonstrated onset of Myrf expression of Myrf as early as 1dpf, prior to the onset of myelination at 60hpf (Figure 5.1B) (Almeida et al., 2011). Together, this data supports our prediction that Myrf expression is specific to the myelinating cells of the CNS (i.e. is not present in PNS), similar to what has been shown in mice (Emery et al., 2009).

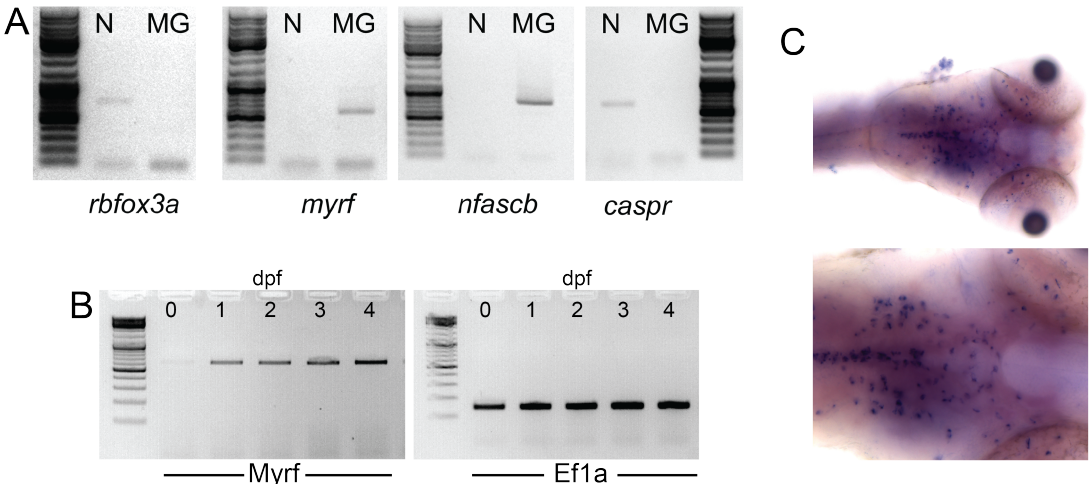

Figure 5.1: Myrf expression in larval zebrafish (A.) semi-quantiative RT-PCR using cDNA of FACS sorted neurons and myelinating glia from whole larval zebrafish (data courtesy of Dr. Anna Klingseisen). The absence of Myrf expression in neurons is consistent with rodent databases. **(B.)** Semi-quantitative RT-PCR demonstrates an onset of Myrf mRNA expression at 1dpf. **(C.)** In situ hybridization with probes targeted against Myrf RNA (Data courtesy of the lab of Dr Kelly Monk)

Investigating mechanisms of genetic compensation in Myrf$^{-/-}$ mutants

Mechanisms of genetic compensation are an important consideration when using genetic knockdown techniques in any organism, particularly in zebrafish where upregulation of paralogous genes has been shown to underlie phenotypic differences observed in knockdown mutants compared to translational or transcriptional block using morpholinos (Rossi et al., 2015). Given a deviation in the myelination phenotype between the larval Myrf$^{-/-}$ mutant and rodent Myrf CKO mutant, I wanted to investigate whether compensatory mechanisms could be providing a partial rescue in our model. From discussions and the literature, I predicted two mechanisms that may be at play: maternal transmission of RNA and/or upregulation of paralogous genes.

Maternal transmission of mRNA does not ameliorate Myrf$^{-/-}$ myelination phenotype

Myrf$^{+/-}$ in-crosses were performed to provide embryos for all experiments. This strategy was intentional to provide wild type siblings as internal controls, but was also enforced due to the infertility of Myrf$^{-/-}$ adults. Using heterozygous females runs the risk of wild type maternal RNA being transmitted to the fertilised embryo and compensating for

loss of zygotic gene function (Jimenez and Campos-Ortega, 1982; Perrimon et al., 1984). In zebrafish, maternal products have been documented to persist until approximately 8 hours post fertilisation (Tadros and Lipshitz, 2009), however it has been speculated by some that they may persist further into the larval stages. To test this theory I set out to perform morpholino (MO) knockdown of Myrf on top of a Myrf$^{-/-}$ background and assess whether it worsened the current hypomyelination phenotype. First, it was necessary to ensure that the Myrf MO phenocopied the germline mutation.

Myrf morpholino injected embryos phenocopy germline Myrf$^{-/-}$ mutants

Two commercially available MOs (GeneTools, Oregon, USA) were used to target all transcripts of Myrf gene. To test that MO injected embryos phenocopied germline Myrf$^{-/-}$ mutants, non-toxic doses of each MO were co-injected into the transgenic line Tg(mbp:eGFP-caax). In this line, the expression of green fluorescent protein (GFP) is expressed in the membrane of all myelinating glia, thus allowing visualisation of the gross myelination status of larvae. In Myrf$^{-/-}$ mutants expressing this transgene a widespread dysmyelination phenotype is observed (see Figure 3.6). MO injected larvae were imaged at both 3 and 4dpf, in case the duration of MO effect was shorter than anticipated. Evidence of dysmyelination was present at both time points in the form of patchy myelination of the Mauthner axon, occasional myelinated profiles (aberrant myelination, likely of neuronal cell bodies) and reduction in GFP expression similar to that which is observed in Myrf$^{-/-}$ mutants (Figure 5.2). This phenotype was observed at both timepoints but appeared more severe during earlier stages of myelination at 3pdf.

Morpholino knockdown of Myrf in a Myrf$^{-/-}$ background does not exacerbate the hypomyelination phenotype

Fertilised embryos of Myrf$^{+/-}$ tg(mbp:eGFP-CAAX) in-crosses were injected with MO against Myrf transcripts or a standard MO control (Gene Tools). Larvae were imaged at 3dpf and confocal images obtained of the Mauthner axon to compare across treatments. I chose myelination of the Mauthner axon as a readout because it is consistently dysmyelinated in the stable Myrf$^{-/-}$ mutant line and I felt that a worsened phenotype would be readily detectable along this axon. In the embryos injected with standard MO, Myrf$^{+/+}$ larvae display full myelination along the length of the Mauthner axon, whereas Myrf$^{-/-}$ mutants display patchy dysmyelination along its length. In the group

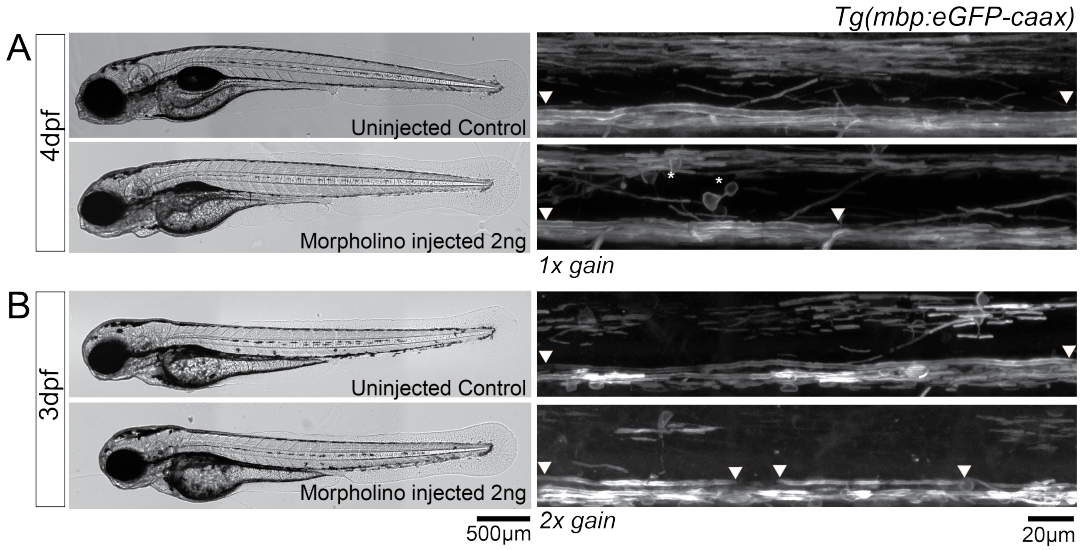

Figure 5.2: Morpholino knockdown of Myrf phenocopies myelin phenotype **(A.)** Bright field overview images of uninjected and MO injected larvae at 4dpf. Lateral images of myelinated tracts in the spinal cord labelled with tg(mbp:eGFP-CAAX). Arrowheads mark regions of patchy myelination along the Mauthner axon. **(B.)** As per (A.), images obtained at 3dpf.

treated with Myrf MO, Myrf$^{+/+}$ larvae now present a mild, patchy appearance to GFP expression along their Mauthner axon. Myrf$^{-/-}$ mutants display a similar phenotype to those injected with standard MO control, suggesting that Myrf MO injection into a homozygous background does not worsen the myelination phenotype. Interestingly, Myrf$^{-/-}$ larvae injected with standard MO and Myrf MO appeared to exhibit slightly shorter body lengths (Figure 5.3, bright field images, not quantified). Developmental effects can be observed due to off-target effects of MO, however if this was the case I would expect this to be observed in Myrf$^{+/+}$ larvae injected with MO. This made me consider whether a very mild developmental delay may exist (which is not detectable by measurement of morphological features in Figure 3.8) in homozygous mutants which is exacerbated by the addition of a MO.

Myrf mRNA is not detectable in the unfertilised eggs of Myrf$^{+/-}$ females

To check for maternal transmission of Myrf mRNA, unfertilised eggs were expressed from adult Myrf$^{+/-}$ females under general anaesthetic and total RNA was immediately extracted. Semi-quantitative RT-PCR was performed on cDNA using EF1a as a loading control and adult WT brain and larval cDNA as positive controls. Expression of Myrf was not detectable in unfertilised eggs suggesting that maternal transmission of Myrf does not occur or is present at extremely low levels. From these experiments I conclude

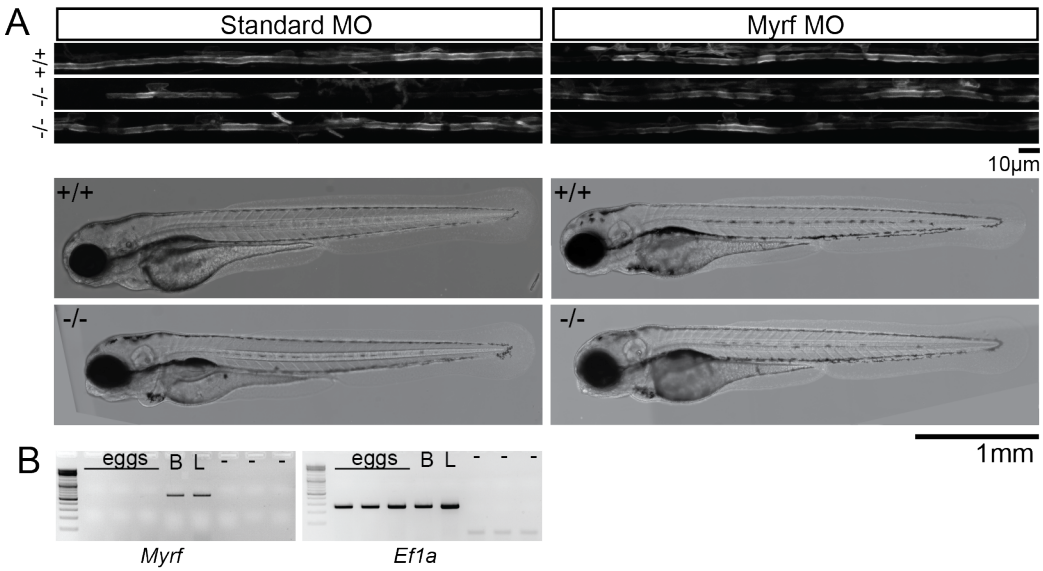

Figure 5.3: Morpholino knockdown of Myrf in a Myrf$^{-/-}$ background
(A.) Top panel: Confocal microscopy images of the Mauthner axon at 3dpf. Left: Standard MO injected into embryos Myrf heterozygous in-cross. Wild type embryos exhibit full myelination along the length of Mauthner axon whereas homozygous mutants display patchy myelination that is typical of this mutant. Right: Myrf MO injected into embryos of Myrf heterozygous in-crosses. Patchy myelination is observed along the Mauthner axon across genotypes, however the phenotype in Myrf$^{-/-}$ mutants is no worse than those injected with standard MO. **Bottom panel:** Bright field images of 3dpf larvae injected with standard (left) and Myrf (right) MO. **(B.)** Semi-quantitative RT-PCR for Myrf transcripts in unfertilised eggs of adult heterozygous females. EF1A was used as a loading control. cDNA from a wild type adult brain (B) and whole wild type larvae (L) were used as positive controls.

that maternal provision of Myrf mRNA is not rescuing Myrf gene function in developing Myrf$^{-/-}$ larvae.

Myrf-like knockdown does not exacerbate Myrf$^{-/-}$ hypomyelination phenotype

The gene homolog to Myrf is Myrf-like. The Myrf-like protein bears a 43% sequence homology to Myrf, predominantly in the functional domains which are similar between proteins (see Figures 3.3 and 5.4). However, unlike Myrf, Myrf-like is expressed at extremely low levels in the CNS (Zhang et al., 2014) and is predominantly found in the PNS of mammals. If mRNA transcripts of a mutated gene are not removed by mRNA surveillance mechanisms such as non-sense mediate decay, their persistence can cause upregulation of genes with sequence similarity (El-Brolosy 2019). In knowledge of this, I hypothesised that Myrf-Like may be up-regulated in our Myrf$^{-/-}$ mutants to compensate for loss of Myrf gene function. To test this I attempted to quantify the

levels of Myrf-Like alongside Myrf, and MBP transcript levels in the brains of adult Myrf$^{+/+}$ versus Myrf$^{-/-}$ mutants (Figure 3.7C). There was no statistically significant difference in transcript levels between groups ($p = 0.53$, unpaired t-test). Interpretation of this result is problematic as Myrf-like transcript levels were very low even in the control tissue and required a high number of PCR cycles to be detected. At these levels, a larger degree of variability in transcript levels is likely introduced with every PCR cycle which may not be biologically relevant. Therefore, from this experiment alone, I cannot reliably confirm whether upregulation of Myrf-like is occurring.

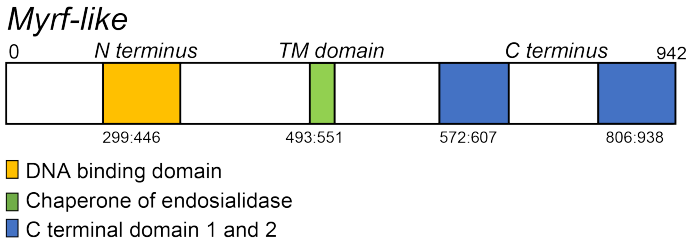

Figure 5.4: Protein structure of Myrf-like

As another means to tests this hypothesis, I designed guide RNAs against Myrf-like exons 6 and 8 and coinjected them into a Myrf$^{-/-}$ background at the single cell stage and imaged larvae at 4dpf. Levels of myelination in the CNS and PNS were compared between injected and uninjected mutants using the tg(mbp:eGFP-CAAX) reporter line. Successful injection technique was confirmed by PCR and digest of a fragment around the target sites on exon 6 and 8 in a subset of imaged larvae (as per Materials and Methods, Figure 2.2). No overt differences in myelination levels were observed between groups. In an attempt to quantify this, custom written scripts (provided by Dr. Jason Early) were used to delineate areas of fluorescent intensity and measure the total fluorescence of these regions (see Materials and Methods, Figure 2.5). Total fluorescent intensity was divided by area to provide average fluorescent intensity values, which were not different for the PNS ($p = 0.63$, unpaired t-test) or CNS ($p = 0.90$, Mann-Whitney test) between uninjected and injected Myrf$^{-/-}$ mutants.

Finally, as Myrf knockdown in rodent models is lethal early in development, I assessed whether Myrf-like knockdown would affect the survival of the Myrf$^{-/-}$ uninjected and Myrf$^{-/-}$/Myrf-like crispants. One hundred animals from each condition were raised and their survival rates checked at frequent intervals. Animals were followed up to

80 days post fertilisation at which point no difference in survival rates were observed (Figure 5.5D). Myrf$^{-/-}$ adults were present in both groups at the last measured time-point, as identified by their gross morphological phenotype (see Figure 5.6 for example).

In summary, I have used multiple experimental techniques to confirm that genetic compensation, in the form of upregulated paralogous gene expression or transfer of maternal mRNA, does not appear to be playing a role in Myrf$^{-/-}$ mutants. Having established this, I continued to pursue extensive characterisation of the myelination status of this mutant line.

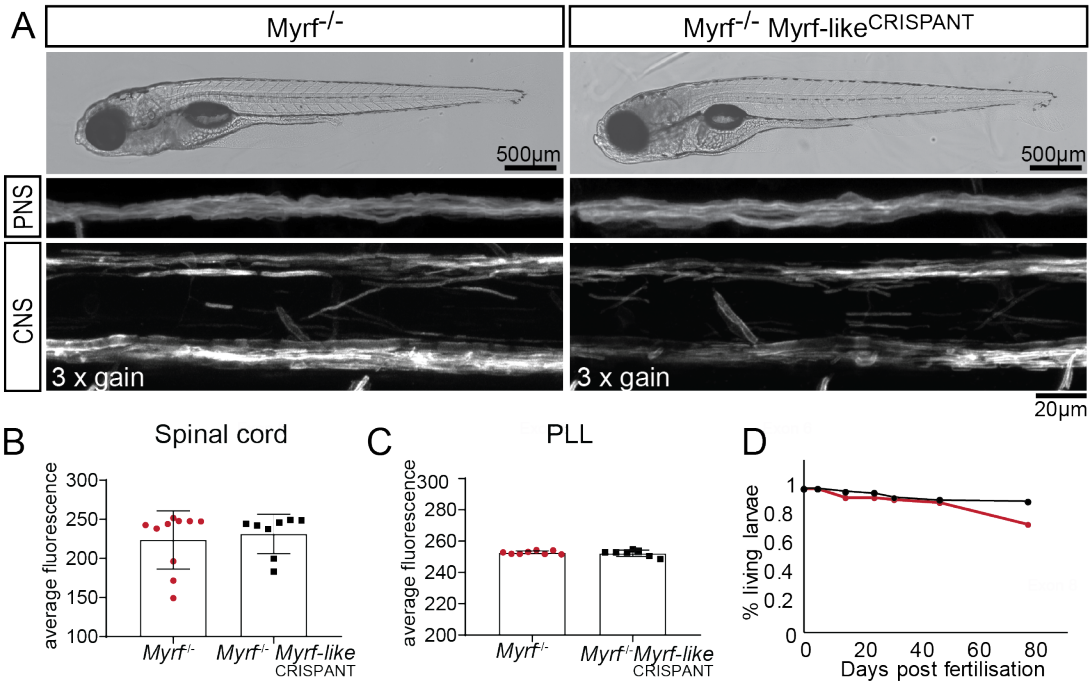

Figure 5.5: Myrf-like knockdown on a Myrf$^{-/-}$ background
(A.) Top: Brightfield images of Myrf$^{-/-}$ and Myrf$^{-/-}$/Myrf-like crispant larvae at 4dpf (10x). Middle: Example confocal microscopy images of the lateral line (PNS) and spinal cord (CNS). For the purpose of this figure alone, brightness levels have been enhanced to equal levels (3 x gain) across images to enable comparison. **(B.)** Quantification of the average fluorescent intensity across images of the spinal cord (243.2 (190.1 to 247.6) grey values in Myrf$^{-/-}$ uninjected animals, 243 (209.1 to 247.9) grey values in Myrf$^{-/-}$/Myrf-like crispants. p = 0.90, Mann Whitney test. Values represent median (IQR)) **(C.)** Quantification of the average fluorescent intensity across images of the PLL (252.7 ± 1.11 grey values in uninjected Myrf$^{-/-}$ controls, 252.2 ± 2.08 in Myrf$^{-/-}$/Myrf-like crispants, p = 0.63, unpaired t-test). CNS: N = 10 Myrf$^{-/-}$ uninjected controls, N = 8 Myrf$^{-/-}$/Myrf-like crispants, PNS: N = 8 Myrf$^{-/-}$ uninjected controls, N = 7 Myrf$^{-/-}$ Myrf-like crispants. **(D.)** Survival curve for uninjected Myrf$^{-/-}$ mutants versus Myrf$^{-/-}$/Myrf-like crispants over 80 days.

Adult Myrf$^{-/-}$ mutants display abnormal morphology

Myrf$^{-/-}$ mutants are viable into adulthood and exhibit surprisingly normal behaviour, however they display a number of morphological and physiological phenotypes consistent with global loss of Myrf gene function, for example:

1. Lack of pigmentation of the ventral abdomen rostral to the pelvic fin
2. Often smaller in size, particularly if not separated from siblings during development
3. Infertility in females due to a lack of functional ovarian tissue
4. Operculum is often missing

In contrast, heterozygous mutants are indistinguishable from wild type siblings at all ages. Many of these phenotypes are expected given that mouse and human gene expression databases confirm that Myrf is expressed in many tissues outside of the CNS, particularly in secretory tissues and organs such as the digestive tract and gonadal tissue. Interestingly, single nucleotide variant heterozygous mutations in the Myrf gene in humans have also been associated with sex development and urogenital disorders (Hamanaka et al., 2019; Rossetti et al., 2019).

Figure 5.6: Photos of adult Myrf fish. Adult homozygous mutants display a loss of pigmentation to their ventral abdomen (arrow head).

Checking for alternative start sites

Protection against deleterious mutations can be provided by the presence of alternative splice sites at the boundary of intronic/exonic regions. Although there are no annotated alternative splice sites which result in the skipping of exon 2 in either of the main genome reference databases (Ensembl and NCBI), it is possible that single nucleotide polymorphisms can result from targeted mutagenesis which may code for an alternative splice site and result in exon skipping. A simple means to check whether alternative splicing was occuring in Myrf$^{-/-}$ mutants was to extract RNA and reverse transcribe the entire mRNA coding sequence. When the Myrf coding sequence was aligned from wild type, heterozygous and homozygous mutant samples, exon 2 con-

taining the ΔCC+A mutation was coded for, suggesting that alternative splicing has not occurred (Figure 5.7).

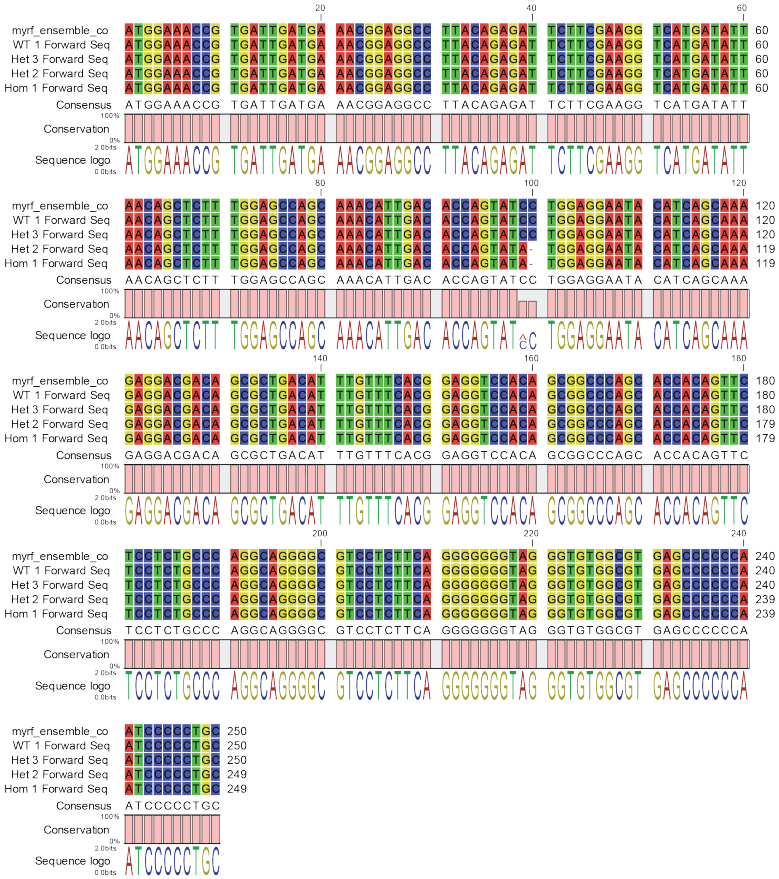

Figure 5.7: First 250bp of the coding sequence for the Myrf gene
Coding sequence provided for the first 250 base pairs upstream of the ATG start site. The δCC+A mutation site is observable at 100bp. Sequences are aligned to Myrf Ensemble appris P1 transcript (Ensembl).

Cell ID	Sheath Number	Length 4dpf (µm)	Length 6dpf (µm)
Ai	1	24.05	25.72
	2	62.24	67.65
Aii	1	21.92	21.77
	2	14.60	8.306
	4	48.234	60.44
	5	37.624	40.44
	6	14.79	7.54
	7	26.24	7.53
Aiii	1	18.39	15.34
	2	37.17	34.65
	3	18.42	29.50
	4	21.34	19.89

Figure 5.8: Sheath lengths to accompany the timecourse images of Myrf$^{-/-}$ cells in Figure 3.21

Appendix 2: Supplementary data to Chapter 4

Methodology for high throughput assays performed at UPenn

These experiments were kindly performed by Elelbin Ortiz (Granato Lab, University of Pennsylvania, Philadelphia, USA). High-throughput testing of the acoustic startle response was performed on 5-6dpf larvae. Larvae were placed into individual wells of a 6 x 6 custom made plate (Figure 4.9A). The plate was fixed to a metal arm attached to an amplifier which delivered mechanosensory stimuli to the plate (Burgess and Granato, 2007; Wolman et al., 2011).

Acoustic startle response

Analysis of the average startle latency was performed using FLOTE software, as previously described by Burgess and Granato (2007). Larvae were presented with a series of 10 mechanosensory stimuli with an interstimulus interval of 20 seconds. Larvae were then collected for genotyping. Any larvae that responded <70% of the time were omitted from further analysis. The average latency per larva was then calculated. The average latency per genotype was statistically analysed using the Kruskal-Wallis test with Dunn's test for multiple comparisons.

Pre-pulse inhibition and short term habituation of the escape response

A subthreshold stimulus was defined as a stimulus that elicited less than 20% SLC responses. The subthreshold stimulus was presented 300ms prior to a stimulus pulse as per Burgess and Granato (2007). The percentage of prepulse inhibition was calculated as:

$$Percent\ inhibition = \frac{\%SLC\ Pulse - \%SLC\ PPI}{\%SLC\ Pulse} \tag{5.1}$$

For habituation experiments, larvae were given 10 strong acoustic taps with a 20 second interstimulus interval to obtain a baseline response rate. This was followed by 30 strong acoustic taps with 1 second inter-stimulus interval. Habituation period was broken into 3 groups: habituation stimuli 1-10, 11-20 and 21-30. Habituation index was calculated as:

$$Habituation\ index = (1 - \frac{\%SLC\ in\ bin\ 21\ to\ 30}{\%SLC\ in\ baseline}) * 100 \tag{5.2}$$

The escape response phenotype persists on repeat experiments

The acoustic startle response assay was repeated in Myrf larvae to ensure that the previously identified phenotype (Chapter 4, Section 4.3.1) was persistent. Myrf$^{-/-}$ mutants maintained a delay in the average latency to the acoustic startle response relative to wild type and heterozygous siblings.

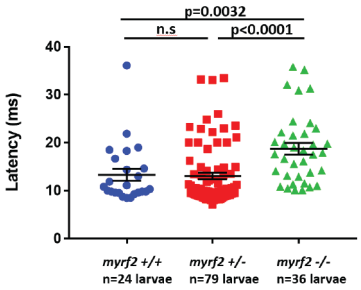

Figure 5.9: Latency to escape response is delayed in Myrf$^{-/-}$ mutants on repeat experiments. N = 24 wild type, N = 79 heterozygous mutants and N = 36 homozygous mutants. Data collected by Elelbin Ortiz.

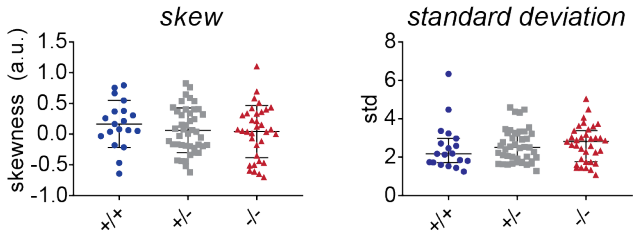

Figure 5.10: Skewness and standard deviation values of velocity data for individual animals
Additional analysis to Sections 4.3.5 and 4.3.6. The standard deviation and the skewness of centroid velocity values were calculated for each fish. Standard deviation values were 2.18 (1.73 to 2.98) in wild types, 2.51 (1.78 to 3.25) in heterozygotes and 2.82 (1.77 to 3.38) homozygous mutants (p = 0.42, Kruskal-Wallis test). Skewness values were calculated using Pearson's coefficient of skewness. Values were 0.16 ± 0.38 for wild types, 0.06 ± 0.36 for heterozygous mutants and 0.04 ± 0.42 in homozygous mutants (F (2,94) = 0.66, p = 0.52, one-way ANOVA). Error bars represent mean ± std for skew data and median (IQR) for standard deviation data. N = 19 WT, N = 43 Het, N = 35 Hom.

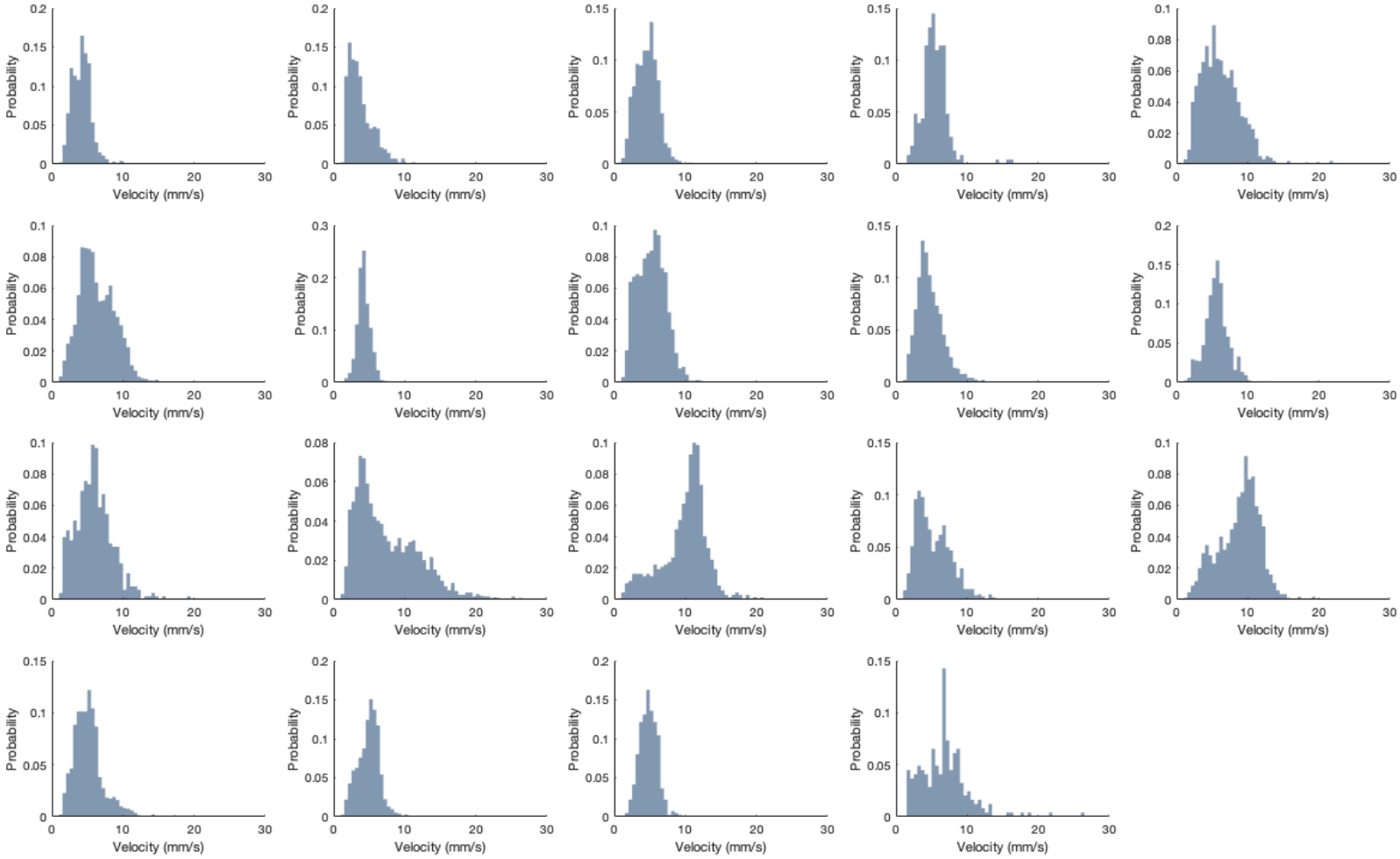

Figure 5.11: Relative frequency histograms of swim bout centroid velocity values for individual wild type fish N = 19

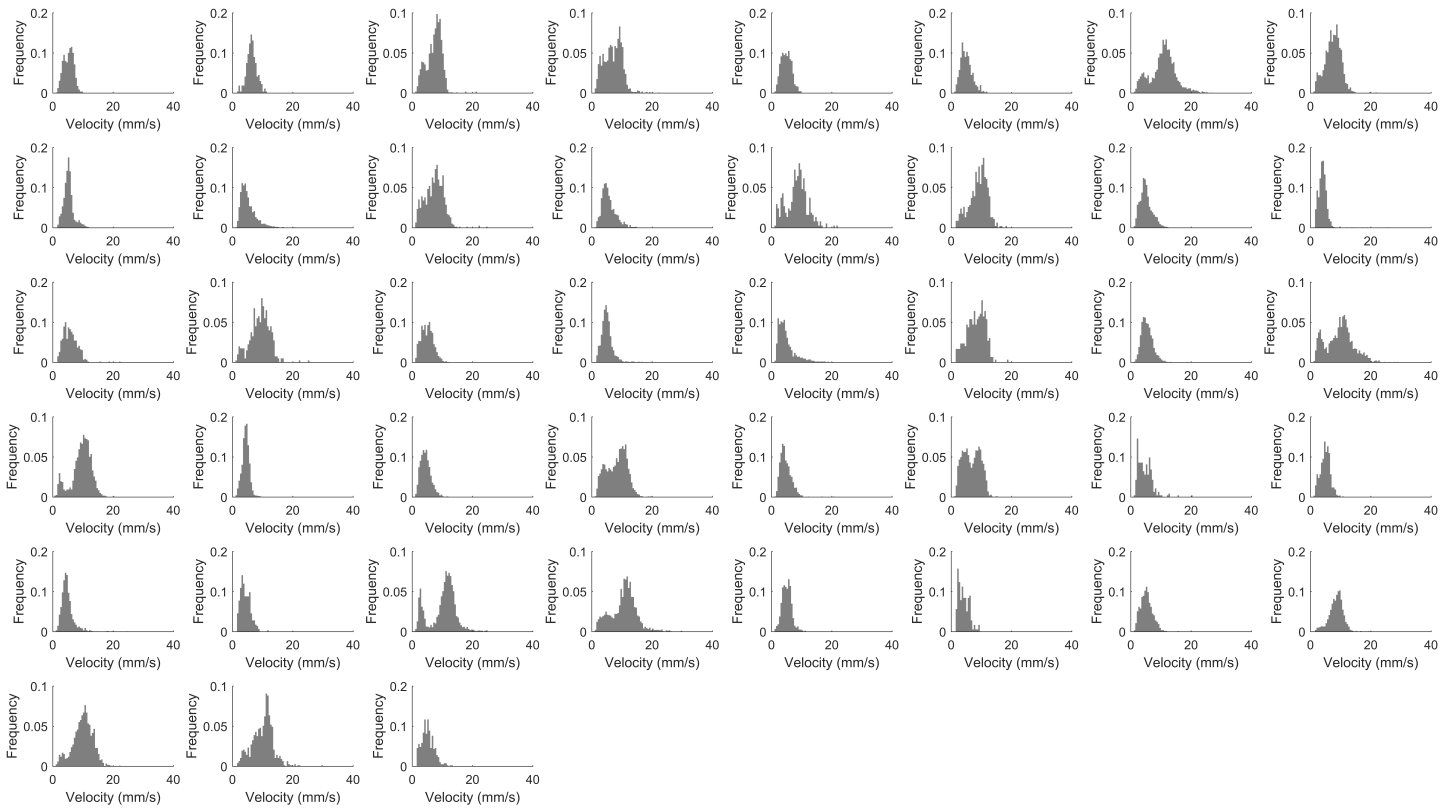

Figure 5.12: Relative frequency histograms of swim bout centroid velocity values for individual heterozygous fish N = 43

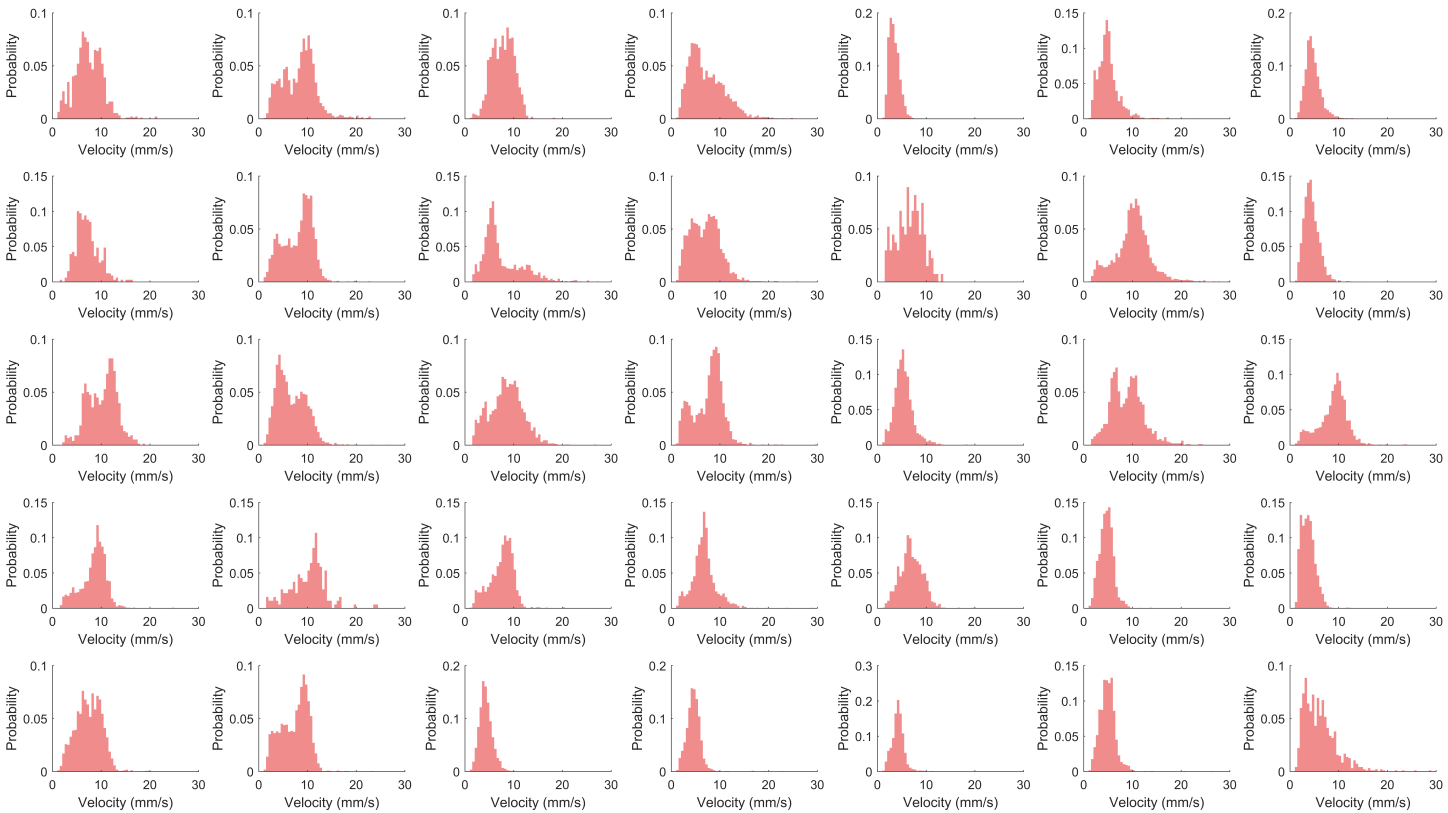

Figure 5.13: Relative frequency histograms of swim bout centroid velocity values for individual homozygous fish $\mathrm{N} = 35$

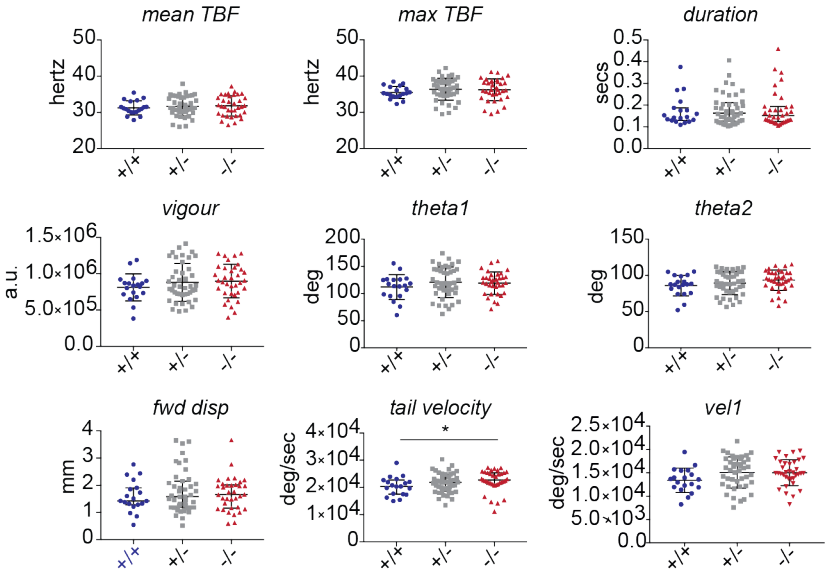

Figure 5.14: Quantification of tail kinematics during swim bouts for individual fish

Scatter plots represent the mean value per fish within each genotype. Values calculated from 'inmiddle' data only. **Mean TBF:** 31.24 ±1.95Hz wild type, 31.72 ± 2.74Hz heterozygotes, 31.80 ± 2.80Hz homozygous mutants (F (2,94) = 0.3, p = 0.74, one way ANOVA). **Max TBF:** 35.49 ± 1.70Hz wild type, 36.40 ± 3.04Hz heterozygotes, 36.23 ± 3.02 homozygous mutants ((F, 2,94) = 9.6986, P = 0.50, one way ANOVA). **Duration:** 0.15s (0.13 to 0.19s) wild type, 0.16s (0.13 to 0.21s) heterozygous, 0.15s (0.13 to 0.19s) homozygous mutants (p = 0.86, Kruskal-Wallis test). **Tail vigour:** 8.13 ± 1.8 x 10^5 au wild type, 8.8 ± 2.6 x 10^5 au heterozygotes, 9.0 ± 2.3 x 10^5 homozygous mutants (F (2,94) = 0.84, P = 0.44, one way ANOVA). **Theta1:** 111.9 ± 23.03 degrees wild type, 120.8 ± 28.18 degrees heterozygotes, 119.2 ± 20.55 degrees homozygous mutants (F (2,94) = 0.8846, p = 0.42, one way ANOVA). **Theta2:** 85.91 ± 14.2 degrees wild type, 89.29 ± 15.99 degrees heterozygotes, 93.53 ± 14.07 degrees homozygous mutants (F (2,94) = 1.722), p = 0.19, one way ANOVA). **Forward displacement:** 1.43mm (1.29 to 1.90mm) wild type, 1.58mm (1.18 to 2.15mm) heterozygotes, 1.66mm (1.16 to 2.01mm) homozygous mutants (p = 0.80, Kruskal-Wallis test). **Maximum tail velocity:** 2.03 (1.75 to 2.27) x 10^4 deg/s in wild types, 2.19 (1.87 to 2.48) x 10^4 deg/s in heterozygotes, 2.27 (2.12 to 2.54) x 10^4 deg/s in homozygotes (p = 0.05, Kruskal-Wallis test. Dunn's multiple comparisons: WT-Hom p = 0.05) **Vel1:** The average velocity of the tail during the first half beat: 1.3 ± 0.26 x 10^4 deg/s in wild types, 1.5 ± 0.34 x 10^4 deg/s in heterozygotes and 1.5 ± 0.27 x 10^4 deg/s in homozygous mutants (F (2,94) = 2.33, p = 0.10, one-way ANOVA). Error bars represent mean ± std for mean TBF, max TBF, vigour, theta1, theta2. Median (IQR) for vigour, forward displacement, duration, maximum velocity and vel1. N = 19 WT, N = 43 Het, N = 35 Hom.

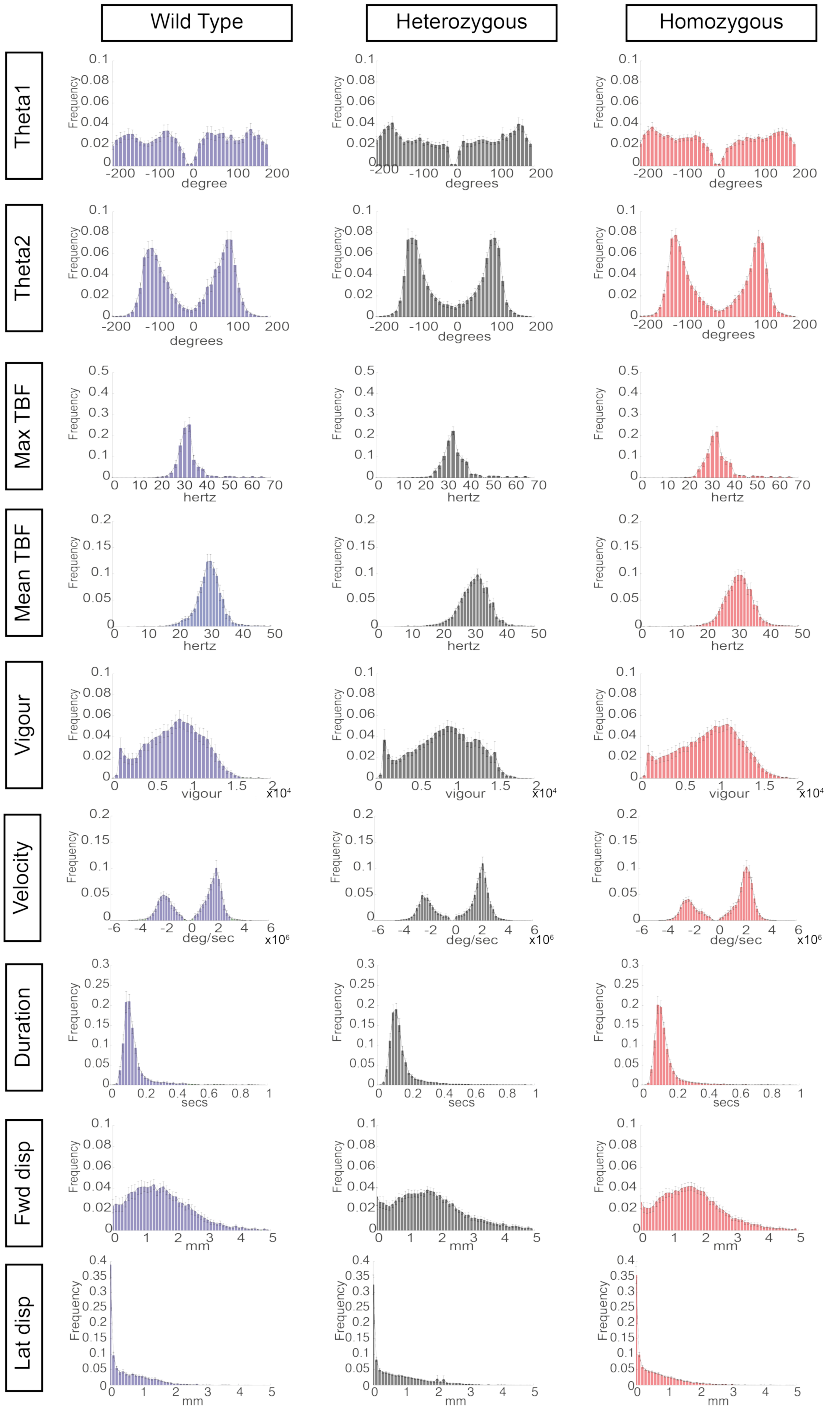

Figure 5.15: Average frequency distribution histograms for multiple tail parameters during spontaneous swimming. Error bars represent SEM. average histograms across N = 19 WT, N = 43 Hets, N = 35 homozygous mutants

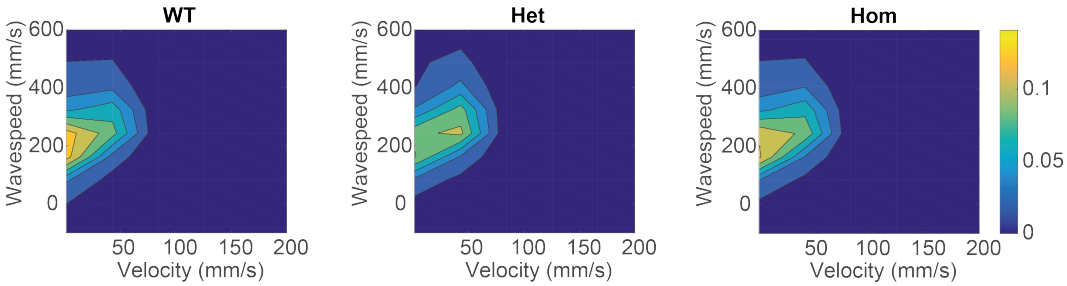

Figure 5.16: Wavespeed values correlate with centroid velocity
Average 2D histograms of wavespeed versus velocity for each genotype. A positive correlation between wavespeed and velocity is observed and data displays a similar distribution across genotypes. Data represents an average across N = 19 WT, N = 43 Het, N = 35 Hom.

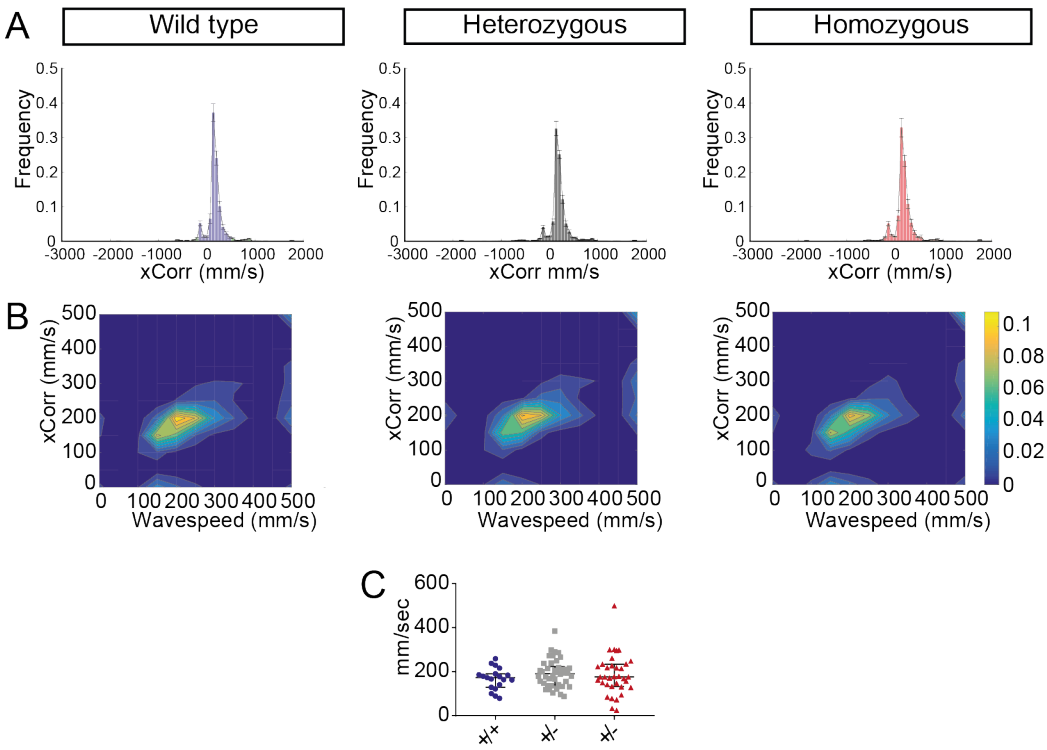

Figure 5.17: Wavespeed calculated using cross correlation of tail angle data from tail segment 3 and 10
(A.) Frequency distribution histograms displaying the average distribution of wavespeed (computed using xcorr) across genotypes. Error bars represent mean ± SEM. **(B.)** Contour maps displaying the distribution of wavespeed (xcorr) values plotted against wavespeed (deltaT) values. **(C.)** Average wavespeed value per fish: 172.8 (129.5 to 190.7) mm/s in wild types, 191.3 (139.6 to 224) mm/s in heterozygotes and 176.4 (133.2 to 234.4) mm/s in homozygous mutants (p = 0.48, Kruskal-Wallis test). Values and error bars represent median and IQR. N = 19 WT, N = 43 Het, N = 35 Hom.

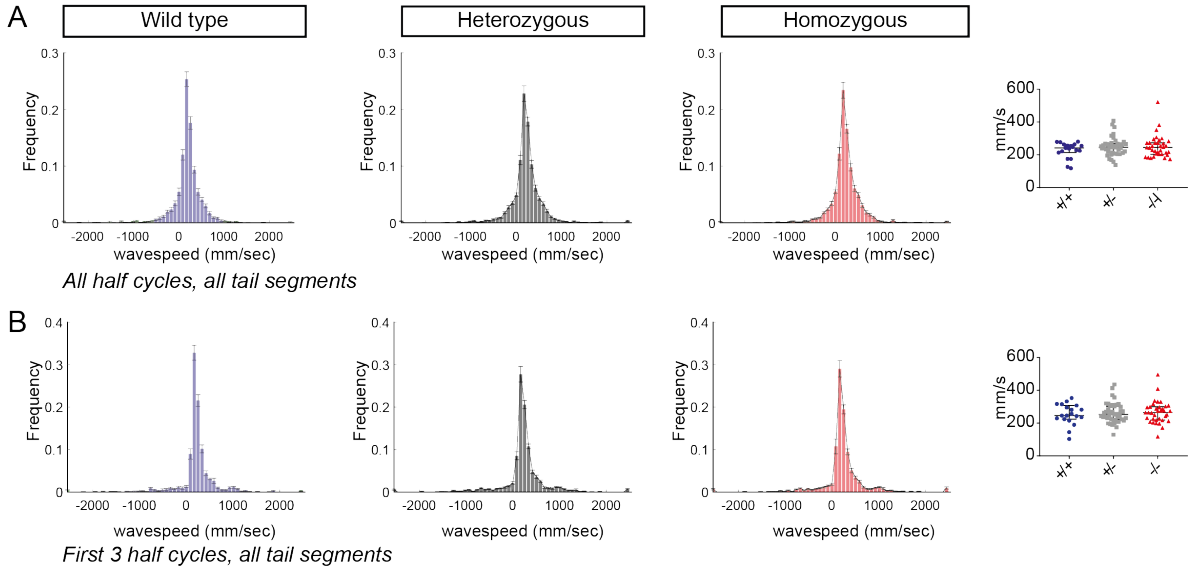

Figure 5.18: Wavespeed calculated using varying numbers of half cycles
Frequency distribution histograms display the average distribution of wavespeed across genotypes. Scatter plots (right) represent average values per individual fish. **(A.)** Average wavespeed value between all tail segments across all half beats. Wavespeed values: 241.7 (213.8 to 263.5) mm/s in wild types, 246.2 (211.2 to 268) mm/s in heterozygotes and 245.3 (203.6 to 273.2) mm/s in homozygous mutants (p = 0.75, Kruskal-Wallis test). **(B.)** Wavespeed calculated using all tail segments across the first three half beats. Wavespeed values: 245.8 (223.7 to 307.1) mm/s in wild types, 252.9 (222.4 to 302.5) mm/s in heterozygotes, 263.8 (219 to 299.8) in homozygous mutants (p = 0.90, Kruskal-Wallis test). Values and error bars for average values per fish (scatter plots) represent median and IQR. Error bars on histograms represent mean ± SEM. N = 19 WT, N = 43 Het, N = 35 Hom.

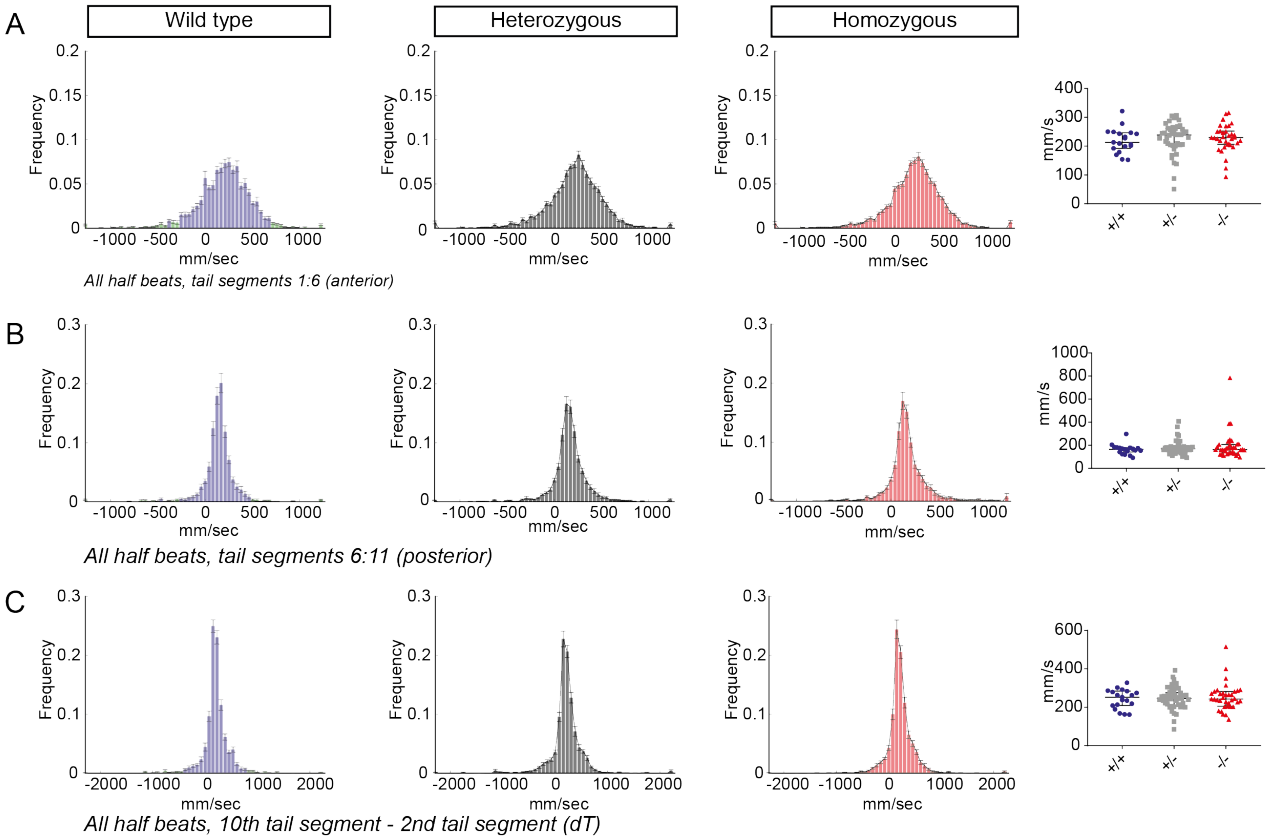

Figure 5.19: Wavespeed calculated using varying numbers of tail segments
Frequency distribution histograms display the average distribution of wavespeed across fish. Scatter plots (right) represent average values per individual fish. **(A.)** Wavespeed calculated using the average difference in time between peak angles of anterior tail segments (1:6) across all half beats per swim bout. Wavespeed values: 213.2 (192.2 to 236.6) mm/s in wild types, 238.8 (203.6 to 261.2) mm/s in heterozygotes, 229.9 (206.3 to 252.2) mm/s in homozygous mutants (p = 0.55, Kruskal-Wallis test). **(B.)** Wavespeed calculated using the average difference in time between peak angles of posterior tail segments (6 to 11) analysed across all half beats per swim bout. Wavespeed values: 164.9 (140.9 to 178.9) mm/s in wild types, 169.8 (142.6 to 188.8) mm/s in heterozygotes, 161.8 (132.7 to 206.7) mm/s in homozygous mutants (p = 0.58, Kruskal-Wallis test). **(C.)** Wavespeed calculated from the absolute difference in time between segment 10 and segment 2 (deltaT). Wavespeed values: 252.2 (208.6 to 283.6) mm/s in wild types, 245.9 (211.1 to 276.0) mm/s in heterozygotes, 242.8 (205.0 to 281.8) mm/s in homozygous mutants (p = 0.99). Values and error bars for average values per fish (scatter plots) represent median and IQR. Error bars on histograms represent mean ± SEM. N = 19 WT, N = 43 Het, N = 35 Hom.

Appendix 3: Investigating the effects of CNS hypomyelination on seizure susceptibility

Introduction

White matter abnormalities are a common MRI finding in patients suffering from epilepsy (Gross, 2011). Additionally, many rodent models with myelin disruption exhibit seizures (Delaney et al., 1995; Lang and Rosenbluth, 2003; Readhead and Hood, L, 1990; Schirmer et al., 2018), including the Myrf CKO mutants in Emery et al. (2009). Seizure activity is characterised by highly synchronous firing of neuronal networks with a reorganisation of functional connectivity between brain regions (Kramer and Cash, 2012). More recently, is has been established that glial cells also play a role in epileptogenesis and display a similar pattern of synchronous activity prior to the onset of a seizure (Diaz Verdugo et al., 2019). As presented in my introduction, the structure of the myelin sheath is reasoned to contribute to neuronal excitability by regulating the distribution of ion channels throughout the axolemma and isolating the axon from electric field effects of other neurons (Kim et al., 2013; Weiss, 2010). Furthermore, oligodendrocytes play an important role in potassium buffering following periods of neuronal activity (Larson et al., 2018; Schirmer et al., 2018). Given the presence of seizure phenotypes in the rodent models of Myrf mutation, I set out to investigate whether the larval zebrafish Myrf$^{-/-}$ mutant, which exhibits robust myelination (Chapter 3), exhibits a similar behavioural phenotype.

Combining their genetic tractability with their suitability for *in vivo* functional brain

imaging and drug screening, larval zebrafish have become an established model for epilepsy research (reviewed in (Copmans et al., 2017; Stewart et al., 2012)). Baraban et al. (2005) were the first to characterise larval zebrafish seizure behaviour in response to pentylenetetrazol (PTZ), a GABA receptor antagonist commonly used to induce seizures in mammalian models. Baraban et al. (2005) observed three stages of response to PTZ treatment: 1) increase in swimming activity, 2) whirlpool like swimming behaviour and 3) loss of posture and a period of immobility. The authors established that these behaviours could be quantified by measuring the total distance travelled and percentage of time spent moving, using a commercially available high-speed video tracking system (Noldus et al., 2001).

Although spontaneous seizure behaviour has not been observed in larval or adult Myrf$^{-/-}$ mutants, I hypothesised that larval Myrf$^{-/-}$ mutant zebrafish, which exhibit marked hypomyelination and a reduction in OL number, may be more susceptible to seizures than their wild type siblings. To test this, I used the commercially available DanioVision System (Noldus, Ethovision) to record activity of 4 and 6dpf larval zebrafish in response to subthreshold doses of PTZ. Here, I will present the results of this side project.

Materials and Methods

General set up for behavioural assay of seizure behaviour

These experiments were designed following the methodology of Baraban et al. (2005), who established the high-throughput analysis of seizure behaviour in larval zebrafish, and Hoffman et al. (2016) for guidance on experimental design, statistical analysis and presentation of data when testing mutant lines. Larvae were arrayed individually into single wells of a 96 well plate (greiner bio-one, Germany) containing embryo medium the evening prior to experimentation. Seizure activity in response to treatment with PTZ was recorded using a Daniovision Box and Ethovision XT software (both Noldus Information Technology, Wageningen, The Netherlands) (Figure 5.20). The DanioVision Box records behaviour at a frame rate of 25Hz. Center-point tracking was used to record velocity and distance moved, parameters which can be used as a readout of seizure activity as per (Baraban et al., 2005). Initially, a dose response experiment was performed using wild type (TL) larvae at the following concentrations of PTZ: 2.5mM,

5mM, 7.5mM, 10mM, 15mM, 20mM. The addition of distilled water was used as a positive control (to account for movement stimulated by the addition of a liquid) and 0.04% tricaine as a positive control. Each treatment was applied to one row (i.e. 12 wells) of the plate. The dose response curve demonstrated a toxic effect at 20mM and a sub-threshold effect at 2.5mM. Future dose response experiments utilised a narrower range of 2.5 to 15mM. The slight reduction in activity following the addition of distilled water may be a result of the amount of time spent in the chamber (which is not temperature controlled) or a behavioural 'freezing' effect following addition of substance to the well. Regardless, as an *increase* in activity is not observed, as is seen with the addition of PTZ, this control was deemed adequate. For ongoing seizure susceptibility experiments I used a 2.5mM concentration of PTZ as a sub-threshold treatment and continued to use the addition of distilled water as a control. The same experimental protocol was followed as per Figure 5.20, with half the plate (four rows) being treated with distilled water and the other half (four rows) treated with 2.5mM PTZ. Where experiments were duplicated or triplicated, larvae from different clutches were spread across each plate to avoid a batch effect. Analysis was blinded.

Quantification of seizure activity

For initial quantification of seizures, distance moved was automatically calculated for each fish in Ethovision software. Tracking efficiency was assessed for each well and fish were excluded from analysis if tracking was erroneous. Length and number of seizures, inter-seizure interval and latency to first seizure were calculated using custom written MATLAB scripts to analyse the raw velocity data provided by the Ethovision software (see next section).

Identification of individual seizure events

To allow the detection of seizure events, a velocity threshold was established for each individual larva based on their baseline activity levels (Figure 5.21 A-C). Any events higher than this threshold following treatment would subsequently be classified as a seizure. By using an individual value for each larva, I postulated that I would account for any individual variation in baseline activity which may make a generalised threshold value less sensitive for individual larvae which moved more or less often. Baseline activity typically consists of lower velocity swims (<10mm/s) with the rare occurrence

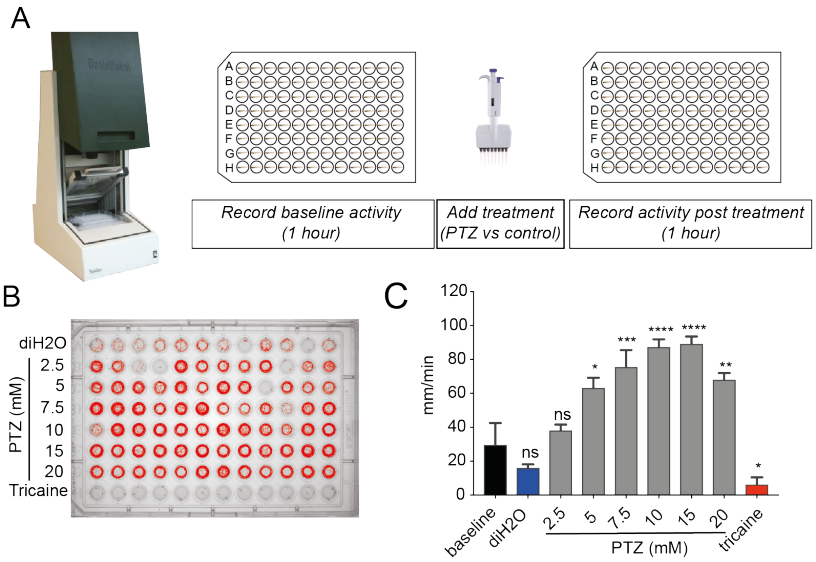

Figure 5.20: Experimental set up for seizure susceptibility experiments. **(A.)** Daniovision box used to record activity of individual larvae in a 96 well plate. Schematic of the experimental design: baseline activity is recorded for one hour, then treatment is added using a multichannel pipette and activity is recorded for a further hour post treatment. **(B.)** Example of the treatment array for dose response experiments. Red lines represent the movement of the larva over the previous 30 seconds. **(C.)** Activity (distance moved) in response to treatment compared to a baseline level of activity. Baseline: 29.59mm/min (21.46 to 42.47mm/min), distilled H2O: 16.07 ± 6.91mm/min, p = 0.04, 2.5mM PTZ: 38.11 ± 11.69mm/min, p = >0.99, 5mM PTZ: 63.22 ± 21.03mm/min, p = 0.0045, 7.5mM PTZ: 75.56 ± 34.32mm/min, p = 0.0011, 10mM PTZ: 87.36 ±15.54mm/min, p = <0.0001, 15mM PTZ: 89.26± 14.9mm/min, p = <0.0001, 20mM PTZ: 68.13 ± 13.52mm/min, p = 0.0004, tricaine: 6.21mm/min (0.9 to 10.46mm/min), p = 0.0019 (Kruskal-Wallis test with Dunn's multiple comparisons. Each treatment group compared to baseline). N = 96 at baseline, N = 12 per treatment group. Bars and error bars represent median (IQR) for baseline and tricaine group and mean ± standard deviation for remaining groups.

of high velocity swims, likely caused by random escape events. Data values which fell above the 75th percentile of all velocities recorded during the baseline condition were defined as high speed events. A threshold for each fish was calculated as the 95th percentile value of high speed events. Threshold values were similar across fish and genotypes (Figure 5.21C).

Having established a seizure detection threshold, velocity data was smoothed using a moving average boxcar filter (span of 30 values) (Figure 5.21 D). Smoothing the data in this was necessary to remove the possibility that short duration, high velocity events such as escape responses would be falsely detected as seizures. Smoothing the data retained the longer lasting, high velocity seizure events and provided them with a single peak allowing efficient detection of individual events. Seizures were identified

where the smoothed velocity trace exceeded the individual's threshold.The start and end of the seizure were calculated as the closest zero value before or after the seizure event. This allows calculation of the length of seizures (end of seizure-start of seizure), inter-seizure interval (time between onsets of seizures) and latency to first seizure.

To validate this method of seizure detection, I manually compared the output of this analysis to the timing of seizure events seen on raw video footage collected during the experiment. I did this for a subset of fish and found that this threshold was sensitive and specific to seizure events. In addition, when comparing the number of seizure events detected using this analysis between groups, a significant increase in the number of events was seen in the PTZ group (34 (15.25 to 58.50) events) compared to baseline and control groups (2 (1 to 3.75) events and 0 events) respectively (Figure 5.21 E left). The number of 'events' is significantly reduced in the control group compared to baseline. This may be due to the amount of time spent in the chamber, as mentioned previously. The data presented in this figure originates from the seizure susceptibility tests using a 2.5mM concentration of PTZ. This was intended as a subthreshold seizure dose but as you can see from this graph, and ongoing results, it seemed that for this cohort 2.5mM was not subthreshold. The length of events detected in the PTZ group (169.3 (150.4 to 189) frames) was significantly higher than in the control group (15 (12.5 to 19.5) frames), consistent with seizure behaviour (Figure 5.21 E right)). Given that no seizures were detected in the control group, this group was excluded from analysis for this parameter.

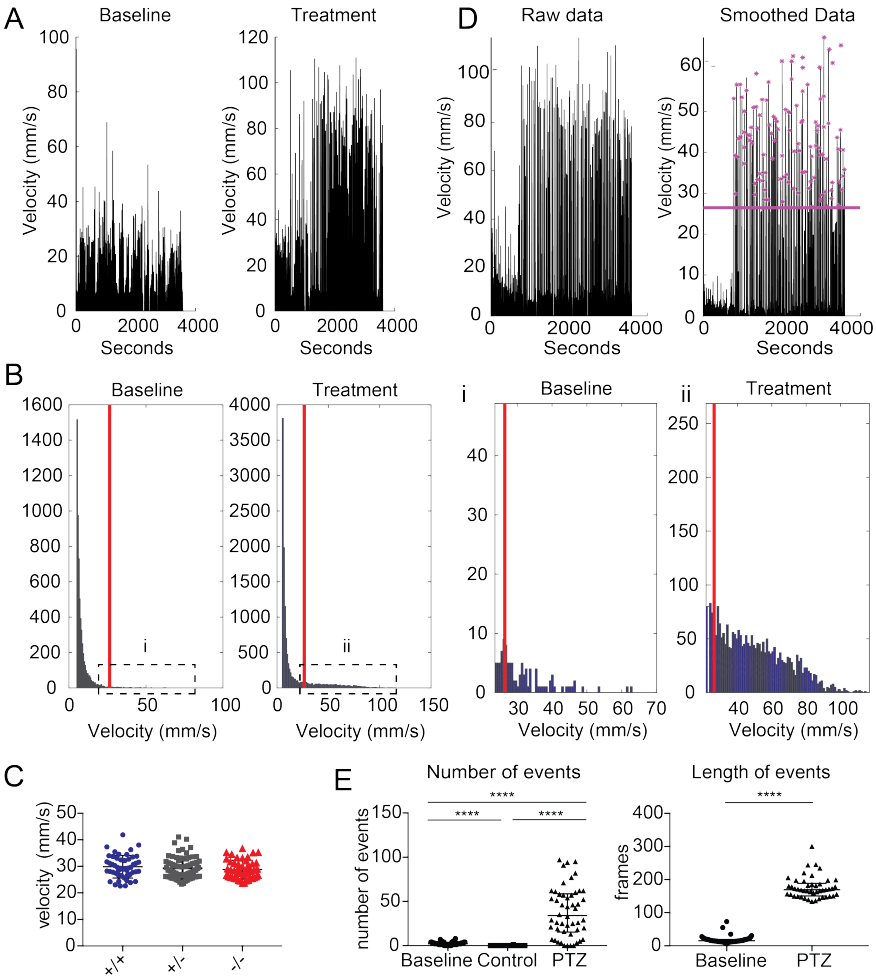

Figure 5.21: Analysis of velocity data to allow identification of individual seizures

(A.) Example traces of velocity over time during baseline recording and following treatment. Numerous high velocity events are seen in the treatment condition compared to baseline.**(B.)** Data from A displayed as frequency histograms. Red line indicates the threshold set for this fish. Dashed boxes indicate region containing data shown in panel i and ii. **(i and ii)** Frequency of high velocity swims over threshold during baseline condition and following treatment. **(C.)** Comparison of individual threshold values for each fish: 29.82 ± 4.25mm/s wild type, 29.24 ± 3.86 heterozygotes, 28.75 ± 3.56 homozygous mutants (F (2, 173) = 0.8964, p = 0.41, one-way ANOVA). N = 50 wild type, N= 80 heterozygotes, N = 46 homozygous mutants. Error bars represent mean and standard deviation. Five outliers were removed using a ROUT test (Q = 0.1%). **(D.)** Velocity data for an example fish: raw data (left) and smoothed data (right). Magenta line indicates the threshold for seizure detection. Magenta asterisks indicate isolated seizure events. **(E.)** Left: Number of seizure events was significantly increased in the PTZ group compared to baseline (p = <0.0001) and control groups (p = <0.0001). High velocity events were also detected less often in control group compared to baseline (p = <0.0001) (Kruskal-Wallis test, Dunn's multiple comparisons). Bottom: Length of seizure events was significantly increased in PTZ group (169.3 frames (150.4 to 189 frames) compared to baseline (15 (12.5 to 19.5 frames)) (p = <0.0001, Mann-Whitney test). Values represent median (IQR).

Results

Development of locomotor activity is normal across genotypes

Using data from the baseline recordings, I assessed activity levels across genotypes at four and six days post fertilisation (Figure 5.22). Given the finding of increased bout frequency observed in Chapter 4, I questioned whether an activity phenotype may also be detectable using this behavioural assay. Distance moved (mm/min) was not significantly different between genotypes at four or six days post fertilisation (p = 0.6365, two-way ANOVA). However, a significant effect of age was found on locomotor activity (p = <0.0001, two-way ANOVA) with no interaction of genotype observed (p = 0.86, two-way ANOVA). This data corresponds with a known developmental switch that occurs in which swimming behaviour between 4 and 6dpf, moving from short, infrequent bursts to a more refined 'beat and glide' motion (Budick and O'Malley, 2000; Buss and Drapeau, 2001). I was not concerned by the lack of an activity phenotype here as the low frame rate (25Hz) of this system likely renders it insensitive to the subtle swim bout frequency phenotypes observed in Chapter 4. Additionally, the level of exploratory behaviour of a larva is much lower in the well of a 96-well plate compared to a 3.5mm petri dish.

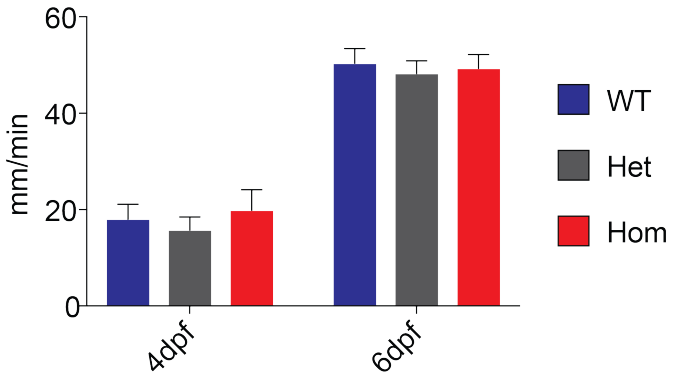

Figure 5.22: Baseline activity levels at four and six days post fertilisation
Bar chart showing distance moved (mm/min) by each genotype during baseline recording at four and six days old. Mean distanced moved was similar across groups at 4dpf (18.04 ± 21.47mm/min wild types, 15.78 ± 22.57mm/min heterozygotes, 19.89 ± 30.26mm/min homozygous mutants) and 6dpf (50.4 ± 21.43mm/min wild type, 48.29 ± 23.5mm/min heterozygotes, 49.32 ± 19.45mm/min homozygous mutants). two-way ANOVA: no significant effect of genotype (F (2,345) = 0.4524, p = 0.6365, two-way ANOVA), locomotor activity was significantly increased between 4 and 6dpf (F (1,345) = 150.8, p = ¡0.0001, two-way ANOVA) but no interaction was observed between the genotype and activity (F (2,345) = 0.1478, p = 0.8627, 2-way ANOVA). N = 48 WT, N = 71 Het, N = 51 Hom at 4dpf. N = 50 WT, N = 84 Het, N = 47 Hom at 6dpf. Different larvae were used at each timepoint.

Seizures are induced in a dose responsive manner in Myrf larvae

Larvae from Myrf$^{+/-}$ in crosses were subjected to a PTZ response curve, using concentrations ranging from 2.5 to 15mM, at 4 and 6dpf. Experiments were repeated in triplicate (i.e. three 96-well plates) to ensure that enough fish per genotype were present within each treatment group. I wanted to establish that the Myrf line exhibited a similar dose response curve to wild type larvae of the same genetic background. Indeed, a similar dose response to wild types was observed at both ages (Figure 5.23). Heterozygous and wild type siblings were grouped together initially to determine if there was a difference in response between siblings and homozygous mutants at any of the treatment concentrations. Response patterns were similar between groups at 4dpf with a significant increase in activity at all PTZ concentrations compared to baseline levels ($p = <0.0001$ treatment, $p = 0.77$ genotype, $p = 0.62$ interaction, two-way ANOVA). No difference between genotypes was observed within any treatment group. A similar pattern was observed at 6dpf, with a significant interaction observed between genotype and treatment ($p = <0.0001$ treatment, $p = 0.45$ genotype, $p = 0.04$ interaction, two-way ANOVA). Following multiple comparison testing, no significant difference was found between genotypes at each treatment level, however a near significant increase in locomotor activity was seen at 2.5mM ($p = 0.07$, Bonferonni's multiple comparisons).

In contrast to the dose response graph in wild type larvae (Figure 5.20), a significant increase in activity levels was now observed across all groups at 2.5mM PTZ (Figure 5.23), a dose previously assumed to be subthreshold. This increase in activity may be due to a genetic background effect in this line (although initial experiments were performed using the same wild type background that Myrf mutants are crossed into for line maintenance), batch effect of the drug, or a real effect of the mutation. Furthermore, at the time of analysing this experiment, I was unaware of the precocious myelination phenotype in heterozygous mutants. If heterozygous mutants exhibited a partial phenotype they could drive activity levels up in the sibling group and compromise a significant finding when analysed in this way. Thus, it was integral from this point forward to assess heterozygotes as an isolated group from wild type siblings.

I was intrigued by the *slight* divergence in response between mutants and siblings at 2.5mM at 6dpf (Figure 5.23B). When this was analysed using matched data from base-

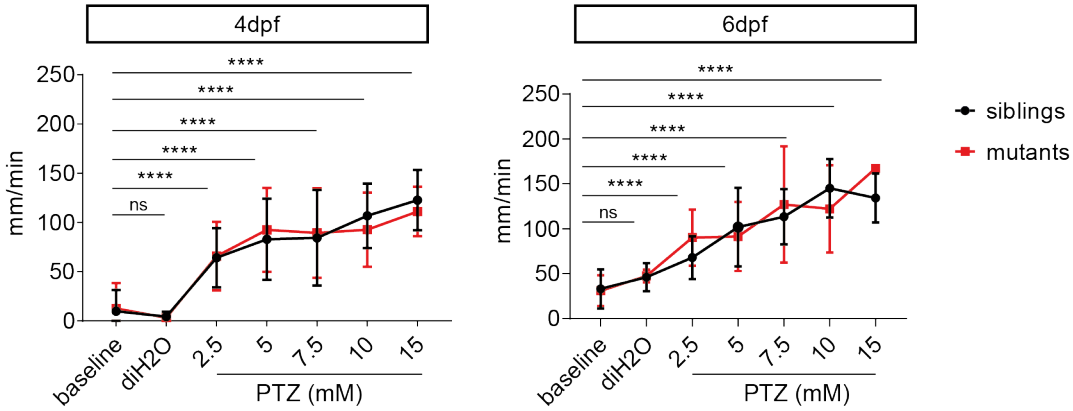

Figure 5.23: Dose response curves in Myrf mutant line at four and six days post fertilisation: Myrf mutants respond to increasing doses of PTZ in a similar manner to siblings at four (p = <0.0001 treatment, p = 0.77 genotype, p = 0.62 interaction, two-way ANOVA) and six days post fertilisation (p = <0.0001 Treatment, p = 0.45 genotype, p = 0.04 interaction, two-way ANOVA). Asterisks represent p-values following Sidak's multiple comparisons test comparing the effect of treatment on distance moved independent of genotype (row effect). No differences were observed between genotypes (between column effect) in any treatment groups. 4dpf: baseline: N = 192 siblings, mutants N = 74 mutants; distilled H2O: N = 21 siblings, N = 7 mutants; 2.5mM PTZ: N = 31 siblings, N = 19 mutants; 5mM PTZ: N = 49 siblings, N = 14 mutants; 7.5mM PTZ: N = 23 siblings, N = 9 mutants; 10mM PTZ: N = 23 siblings, N = 10 mutants; 15mM PTZ: N = 20 siblings, N = 10 mutants. 6dpf: baseline: N = 128 siblings, N = 47 mutants; distilled H2O: N = 5 siblings, N = 2 mutants; 2.5mM PTZ: N = 40 siblings, N = 16 mutants; 5mM PTZ: N = 41 siblings, N = 13 mutants; 7.5mM PTZ: N = 21 siblings, N = 8 mutants; 10mM PTZ: N = 19 siblings, N = 8 mutants; 15mM PTZ: N = 5 siblings, N = 1 mutant.

line and 2.5mM treatment groups, a significant interaction was found between genotype and treatment (p = <0.0001 treatment, p = 0.04 genotype, p = 0.02 interaction; N = 37 siblings, N = 13 mutants, matched data for each group, two-way ANOVA) and a significant difference between genotypes was found at 2.5mM (p = 0.006, Bonferroni's multiple comparisons test) (Figure 5.24A). Given this finding, I decided to repeat experiments with a larger sample size using 2.5mM PTZ even though it was not truly 'subthreshold' in this line - activity levels in response to this dose have not reached a plateau leaving scope for a significant deviation in response as already demonstrated by the matched analysis. I performed an a priori sample size calculation using the calculated effect size between siblings and mutants at 2.5mM (Figure 5.24B) and an alpha error probability of 0.05 in order to achieve a power of 0.8 (G*Power 3.1, Heinrich-Heine University, Dusseldorf, Germany). I computed that I would need 26 larvae per group (siblings versus mutants).

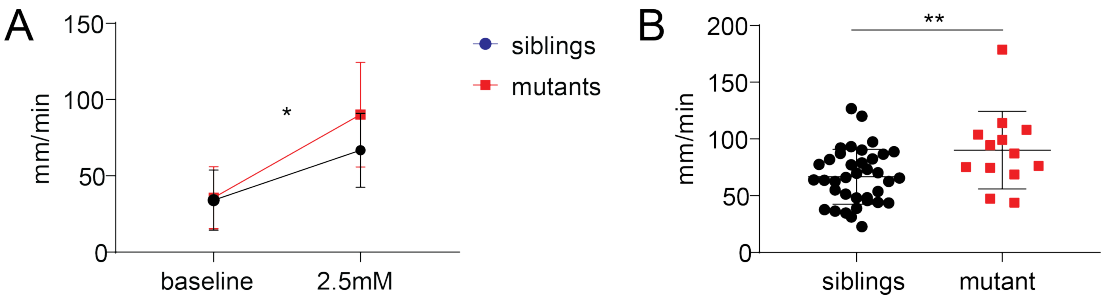

Figure 5.24: Data for 2.5mM PTZ treatment extracted from the dose response experiment and presented as a two-way analysis of variance and t-test.
(A.) Activity in response to 2.5mM PTZ compared to baseline. Values are matched between treatments. Two-way ANOVA: effect of treatment p = <0.0001, genotype p = 0.04 and interaction p = 0.02. Bonferroni's multiple comparisons: siblings-mutants baseline p = ns, 2.5mM p = 0.006. **(B.)** The effect size in the increase in activity levels of homozygous mutants compared to siblings at 2.5mM was used to perform a sample size calculation. Average activity levels were 69.15 ± 25.09mm/min in siblings, 92.35 ± 40.97mm/min in homozygous mutants (p = 0.001, unpaired t-test). N = 26 siblings, N = 9 Homozygous mutants. Values and error bars represent mean ± standard deviation.

Seizure susceptibility to 2.5mM PTZ is similar across genotypes

To assess whether a deviation in response to 2.5mM PTZ was repeatable with larger numbers of larvae, experiments were performed at each timepoint. Following the baseline recording each half of the plate was treated with distilled H2O (control) or 2.5mM PTZ (treatment) (Figure 5.25A). Assuming mendelian frequencies and random assignment of larvae into individual wells, I calculated that I would need to repeat the experiment twice at each age in order to achieve adequate sample sizes for statistical interrogation. Values were matched between baseline and treatment groups and differences in activity in response to control and 2.5mM PTZ treatment were plotted per genotype. Responses were broadly similar between genotypes at both 4 and 6dpf (Figure 5.25B), in contrast to the observation in the previous experiment. Furthermore, plotting activity levels between siblings and homozygous mutants (as per Figure 5.24C) did not reveal any differences in behavioural response to 2.5mM PTZ at 4 or 6dpf (p = 0.59 and p = 0.94, unpaired t-test, respectively).

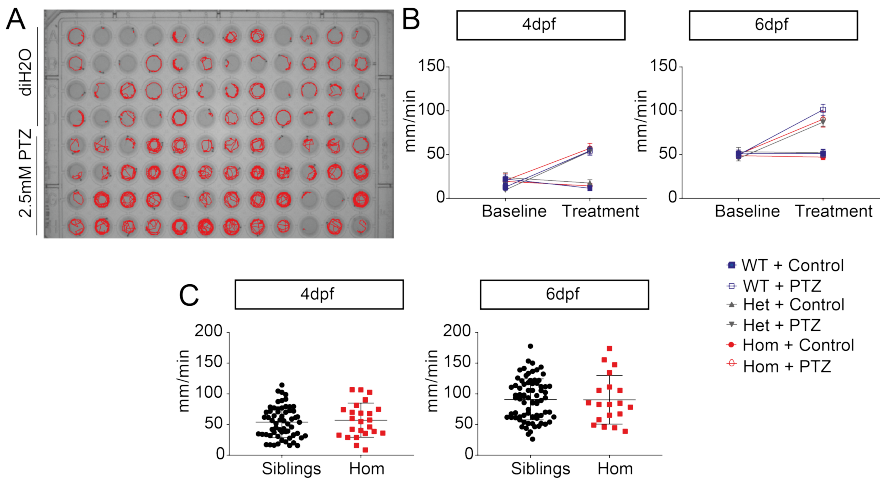

Figure 5.25: Assessment of seizure susceptibility to 2.5mm concentration of PTZ at 4 and 6dpf: **(A.)** Treatment array of 96 well plate. Following baseline recording half the plate was assigned as a control (addition of distilled water) while the other plate is treated with 2.5mM PTZ. **(B.)** No difference was observed in response to control or 2.5mM PTZ treatment at 4 or 6dpf. Data is matched between baseline and treatment groups. 4dpf: Control group: N = 27 wild type, N = 31 heterozygotes, N = 27 homozygous mutants. 2.5mM PTZ group: N = 21 wild type, N = 40 heterozygotes, N = 24 homozygous mutants. No effect of genotype on response to treatment was observed (p = <0.0001 treatment, p = 0.71 interaction, p = 0.31 genotype, two-way ANOVA). 6dpf: Control group: N = 29 wild type, N = 30 heterozygotes, N = 28 homozygous mutants. 2.5mM PTZ group: N = 21 wild type, N = 54 heterozygotes, N = 19 homozygous mutants. No effect of genotype on response to treatment was found (p = <0.0001 treatment, p = 0.46 interaction, p = 0.29 genotype, two-way ANOVA). **(C.)** Mutants exhibit similar activity levels to siblings following treatment with 2.5mM PTZ (4dpf: 33.78 ± 25.29mm/min siblings (N = 61), 57.08 ± 27.79mm/min homozygous mutants (N=24), p = 0.59, unpaired t-test; 6dpf: 90.95 ± 33.38mm/min siblings (N = 75), 90.32 ± 39.61mm/min mutants (N =19), p = 0.94, unpaired t-test.

Additional parameters of seizure activity are not different between groups

Although distance moved (mm/min) has traditionally been used as the principal read-out of seizure activity in zebrafish (Baraban et al., 2005), given the a lack of phenotype using this parameter I wanted to ensure that I had exploited the available dataset completely before ruling out a seizure susceptibility phenotype. Extended analysis using custom written code allowed the detection of isolated seizure events and calculation of parameters such as seizure number, latency to first seizure, inter-seizure interval and seizure length. Surprisingly values were indistinct between groups with no significant differences detectable following statistical testing (Figure 5.26). Having performed this additional analysis, I am confident that I can accept the null hypothesis of this experiment, that Myrf$^{-/-}$ mutants do not exhibit an increase in seizure susceptibility relative to their wild type siblings.

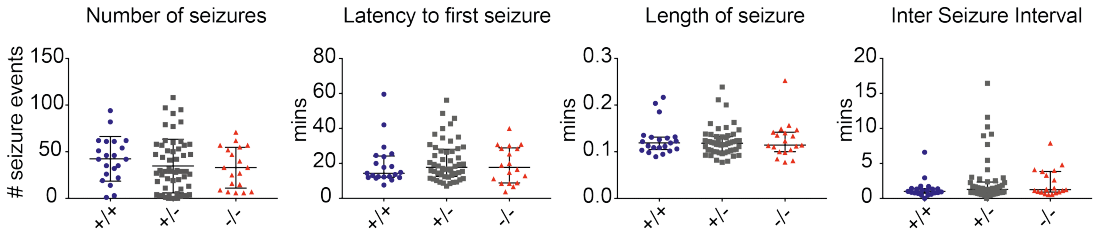

Figure 5.26: Identification of individual seizure events allows quantification of additional seizure parameters: Number of seizures was similar between groups: 42.38 ± 23.93 wild types, 34.7 ± 28.79 heterozygotes, 32.89 ± 21.89 in homozygous mutants over entire treatment period (F (2,93) = 0.80, p = 0.45, one-way ANOVA). No difference was observed in latency to first seizure: 14.37 mins (12.05 to 24.2 mins) wild type, 17.76 mins (12.56 to 28.08 mins) heterozygotes, 17.74 mins (8.80 to 28.91 mins) in homozygous mutants (p = 0.60, Kruskal-Wallis test). Seizure lengths were similar between groups: 0.12s (0.10 to 0.13s) wild type, 0.12s (0.10 to 0.13s) heterozygotes, 0.11s (0.10 to 0.14s) homozygous mutants (p = 0.93, Kruskal-Wallis test). Inter-stimulus intervals were also indistinct between groups: 1.00 min (0.75 to 1.4 min) wild type, 1.29 min (0.80 to 2.34 min) heterozygotes, 1.25 min (0.91 to 3.84 min) homozygous mutants (p = 0.32, Kruskal-Wallis test). N = 21 wild types, N = 52 heterozygotes, N = 18 homozygous mutants for latency, interstimulus interval and length of seizure. Error bars represent median (IQR). N = 21 wild type, N = 56 heterozygotes, N = 18 homozygous mutants for number of seizures. Error bars represent mean ± std. All data collected at 6dpf.

Discussion

In summary, there is no evidence from these experiments to support an increase in seizure susceptibility in Myrf$^{-/-}$ larvae. An initial increase in activity (distance moved) was observed in mutants relative to siblings on treatment with 2.5mM PTZ, however this difference was not maintained when experimental numbers were increased on subsequent experiments. The loss of a significant difference between experiments appears to be due to a larger increase in activity in the sibling group in response to PTZ in the repeat experiment (Figure 5.24B) which is not observed in the initial dose response experiment (Figure 5.25C). There is no obvious explanation for this difference. Despite attempts to maintain consistent experimental conditions, it is possible that an uncontrolled environmental effect was in action during the initial experiment which unveiled a significant phenotype. Alternatively, it is possible that I was close to a subthreshold dose of PTZ and at lower concentrations a consistent phenotype would be identified.

Given the subtleties of behavioural phenotypes found in Chapter 4, I dug deeper into the structure of the data from these experiments to assess parameters of individual seizure events, such as the latency to first seizure, the number of seizures, seizure length and inter-seizure interval. Surprisingly, there was very little difference between groups (Figure 5.26) which gave me confidence in rejecting my hypothesis that CNS hypomyelination in the Myrf$^{-/-}$ larvae would render them more susceptible to seizure activity. It is possible that a seizure phenotype would be uncovered in later stages of development, perhaps in adult stages when hypomyelination is more severe. However, due to limitations of Home Office licensing, testing in adults was not pursued during this project.

The absence of a seizure phenotype in larval Myrf$^{-/-}$ mutant represents another discrepancy between larval and rodent Myrf mutant models. As a constitutive deletion of Myrf causes death in rodents, analysis of behaviour is restricted to mice with cell-type specific CKO of Myrf. Despite Myrf expression only being lost from OL lineage cells, Myrf CKO mice display spontaneous seizure phenotypes and early death (Emery et al., 2009). The reason for a difference in phenotype may be due to the severity of OL loss in the mice model, which completely lack OLs, compared to the larval zebrafish that show only a 36% reduction in the number of OLs. Although the myelination phenotype

is severe in Myrf$^{-/-}$ mutants (66% reduction in myelinated axons), it is possible that the persisting OLs are able to contribute to the maintenance of circuit function in a myelin-independent manner e.g. potassium buffering (Larson et al., 2018; Schirmer et al., 2018). Alternatively, it is possible that the residual third of myelinated axons in the CNS is enough to maintain excitability across neurons of the brain. Importantly, our TEM analysis of myelinated axons was restricted to the spinal cord. It is currently unknown whether this phenotype extends to the brain. Given the presence of a dorsal/ventral difference in the number of myelinated axons in the spinal cord, it is possible that myelination in the brain is less severely affected. Live imaging of the brain using the transgenic reporter tg(mbp:eGFP-CAAX), to assess gross levels of myelination, and further TEM analysis using larval brains would inform us if this is indeed the case.

In conclusion, in contrast to studies of rodent Myrf mutants, larval zebrafish Myrf$^{-/-}$ do not demonstrate detectable seizure behaviour or an increase in seizure susceptibility. Further imaging to assess the myelination status of the brain could be performed to inform our understanding of this discrepancy. It is possible that a lower, truly sub-threshold dose of PTZ would reveal a phenotype. However, my prediction would be that this phenotype would be mild and likely not worth pursuing.

Appendix 4: Assessing motor neuron activity using functional imaging

The information provided here forms a continuum from the discussion of Chapter 4. To begin investigations into the circuit adaptations underlying the increased swim bout frequency and swim velocity observed in Myrf$^{-/-}$ mutants, I started exploring imaging techniques and protocols to perform functional imaging during spontaneous swimming in larval zebrafish. Here I will present data from troubleshooting experiments which were performed to inform the set-up of future experiments.

Materials and methods

For all experiments, GCamp6s was expressed in the motor neuron population using either a hb9 or nefma promotor (Figure 5.27). Wild type transgenic larvae were screened for gcamp6s (green fluorescent protein expression) expression the day prior to functional imaging experiments to prevent effects of the anaesthetic interfering with neuronal activity. Larvae were immobilised using the paralysing agent mivacurium chloride (25μL/ml, 1:50 dilution in embryo media) (abcam, Cambridge, UK) prior to mounting in a lateral or dorsal position in 1.5-2.0% agarose on a cover slip (see Figure 5.30). For head-fixed preparations larvae were lightly anaesthetised and mounted in a dorsal position in 2% agarose on a 50mm glass bottom dish (No. 1.5, MatTek Corporation, Massachusetts, USA). Agarose was cut away from the tail and the dish filled with fresh embryo media. Larvae were allowed to recover for a minimum of a few hours prior to imaging. Larvae were imaged using a 10x (NA = 0.45) or 20x (NA = 1.0) water

dipping objective (both Zeiss Plan-Apochromat, Carl Zeiss Microscopy, Oberkochen, Germany). Z-stack images were taken through the region of interest prior to time series imaging using the 488nm laser. When possible, red fluorescent protein (RFP) was used as a structural reporter and the z-stack was also imaged with 561nm laser to allow subsequent registration of calcium images during image processing. Initial time series were obtained for 5-10 minutes at 10-50 fps depending on position of the fish and field of view, during which time spontaneous activity could be observed. In scenarios where activity was induced, larvae were stimulated at the head region with a bipolar electrode. Images were assessed and registered/motion corrected if required using FIJI plugins: Imgstabiliser and Registration descriptor based series reg (Preibisch et al., 2010). Semi-automated analysis of motoneuron calcium activity was performed using GECIquant plugin (Srinivasan et al., 2015). Initial experiments focused on troubleshooting the optimal set up for allowing adequate rates of spontaneous activity therefore I was not selective in the subtype of motoneuron that was selected for analysis at this stage. Fluorescent traces were smoothed with a boxcar filter (span of 30 frames) and plotted over time (Figure 5.30A-C). The frequency of events was quantified manually.

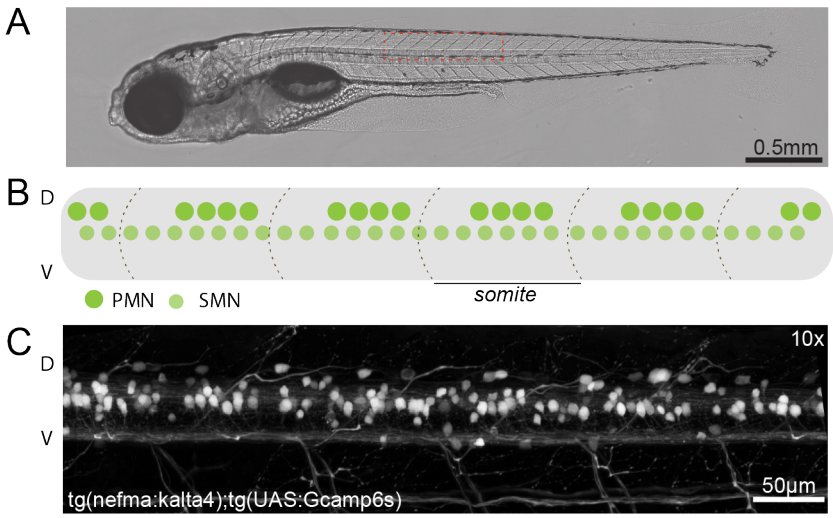

Figure 5.27: Imaging motor neuron populations
(A) Brightfield view of a 5dpf larva mounted in agarose in a lateral position. Red dashed box indicates the field of view using a 10x objective (approximately) in super resolution mode, as shown in panel (C). **(B)** Schematic of the position of primary and secondary motor neurons in the spinal cord. **(C)** Super resolution image of the spinal cord of a transgenic fish driving expression of GCamp6s under the promotor nefma, which labels motor neurons as well as reticulospinal and Rohon-Beard neurons.

Results

Exploring suitable imaging systems to monitor motor neuron activity

To detect differences in spatial recruitment across populations of motoneurons, the ideal imaging system should be able to image at high speeds across a wide field of view. In favour of achieving fast temporal resolution, it was not deemed necessary to image through volumes of tissue initially, given that many motor neurons are visible within a single plane of imaging. I tested two imaging systems which would provide these qualities. Firstly, our Zeiss LSM Airyscan 880 confocal microscope (Carl Zeiss, Microscopy GmbH, Jena, Gemany) fitted with a 5x or 10x objective (Zeiss Plan Apochromat 20x dry, NA = 0.8, Carl Zeiss Microscopy) provided a field of view which encompassed roughly fourteen or eight somites (spinal segments) of the larvae respectively. Time-series imaging along these lengths (x), with a narrow window (y), achieved respectable frame rates of up to 50Hz with adequate resolution for detecting calcium transients in the soma of motoneurons. Single plane light sheet microscopy (Leica SP8 confocal with a light sheet add on, Leica Microsystems GmbH, Wetzlar, Germany) allowed imaging at similar speeds across a similar distance (x), with improved resolution and a larger image width (y) allowing incorporation of both ventral and dorsal motor neurons into the image at high speeds. Both systems provide optimal temporal and image resolution to monitor population level dynamics. Additionally, they both allow flexibility in the positioning of the larval zebrafish relative to the laser or light sheet, such that left-right (dorsal position) and dorsal-ventral (lateral position) motoneuron activity can be imaged if required. For the convenience of data storage and system availability, I opted to move forward using the Zeiss LSM 880 confocal microscope which is already implemented in our laboratory.

The Zeiss LSM 880 confocal microscope is also equipped with a line-scan system, whereby imaging can be performed bidirectionally along a single-pixel wide line set through a defined region of interest (Figure 5.28). I surmised that this would be an excellent tool to measure the anterior to posterior recruitment of motor neurons during spontaneous or induced fictive swims. Using a line scan directed through the soma of motoneurons, I was able to achieve much higher frame rates of 500 to 1000Hz. To calculate how fast we would need to image across these distances to detect a delay

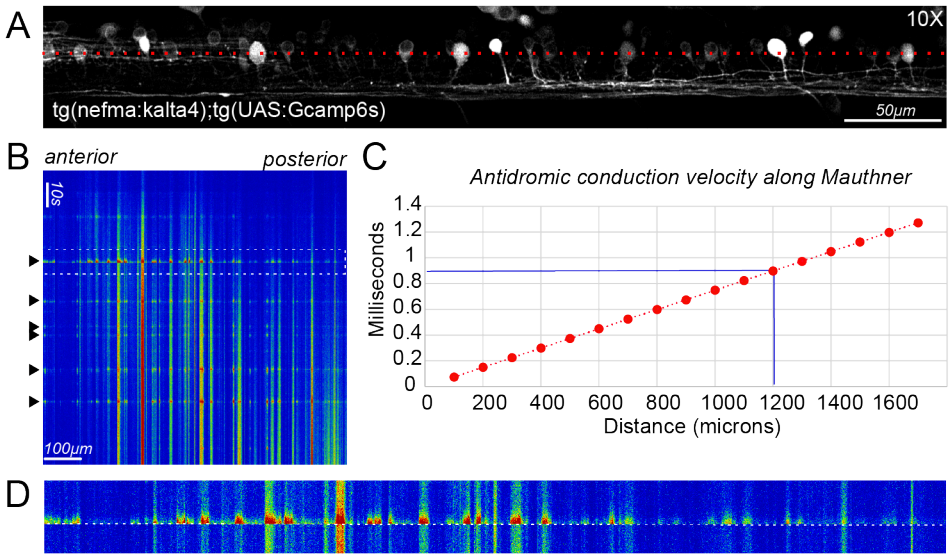

Figure 5.28: Line scans to detect anterior to posterior motor neuron activity **(A.)** Example image of a single plane in the spinal cord with motor neurons expressing GCamp6s in the spinal cord. The red dashed line through the soma of motoneurons is an example of the region that can be defined for line scanning on this system. **(B.)** Example of the output of a line scan imaging obtained across a distance of 850μm (left to right) over two minutes (top to bottom) scanning at 500Hz. Black arrowheads indicate stimulated events. white dashed line delineates the 10 second region provided in panel (D). **(C.)** Estimation of the conduction speed along Mauthner axon across different imaging distances to allow determination of imaging speeds that would be required to detect delays in motor neuron recruitment. Mauthner conduction velocity is approximately 1.3mm/ms in wild type 5dpf larvae. For the maximum distance we can image (1200μm with a 5x objective), the conduction delay would be approximately 0.92ms. **(D.)** 10 second region from panel (A) spanning an event. Fluorescent traces of multiple motor neurons in an anterior to posterior direction (L to R) show simultaneous activation at 500Hz imaging speed (dashed white line)

in conduction velocity and subsequent motor neuron recruitment, I extrapolated data from *in vivo* antidromic recordings of conduction velocity from the Mauthner axon in wild type larvae (provided courtesy of Dr. Dau Suminaite). With a 5x objective it is possible to perform a line scan across a distance of 14 somites, which is roughly equivalent to 1.2mm. The action potential conduction speed along the Mauthner axon is 1.3mm/ms in wild type embryos at 5dpf. Thus, motor neuron recruitment across this field of view could occur within a single millisecond. This recruitment delay is approximated, as excitatory drive to motoneurons does not usually originate from the Mauthner neuron during spontaneous swimming and we do not have conduction velocity measurements available for more appropriate premotor neurons such as the nMLF. Using a conduction speed of 1.3mm/ms, even if conduction velocity is halved along premotor neurons in Myrf$^{-/-}$ mutants, the delay will be on the order of milliseconds.

Therefore, our current maximum imaging speed on this line scan system may impede us from detecting such miniscule delays. To overcome this, we have recently installed a high-performance camera (ORCA-Flash4.0 V3 Digital CMOS camera, Hamamatsu) to allow improved acquisition speeds. This will be tested for its compatibility with the line scanning system and implemented in future experiments.

Characterisation of available driver lines

To image motor neuron activity, we can take advantage of a plethora of GECIs that are available and validated for similar imaging applications in larval zebrafish. New generations of GECIs are available with excellent sensitivity and fluorescent kinematics allowing detection of individual single action potentials in some instances (Chen et al., 2013; Dana et al., 2019). The choice of GECI is based on the experimental situation and features of neuronal activity that the user is aiming to detect, for example slow sensors are better suited for detecting all active cells, whereas fast sensors are more suitable for monitoring the dynamics of activity in individual neurons over time. To measure recruitment of motor neurons during fictive swims, which occur at a frequency of approximately 1Hz, most of the new generation of GECIs are suitable, of which the slowest decay time is currently around 550ms in vivo (Chen et al., 2013). Spike rates of motor neurons are much higher, reaching up to 600Hz (McLean and Fetcho, 2009; Menelaou and McLean, 2012). At this spike frequency, most GECIs would be saturated making detection of individual action potentials impossible with current sensors.

I took advantage of the UAS:Gal4 system to drive expression of GCamp6s specifically in the motor neuron population. In this system, the transcriptional activator Gal4 is expressed downstream of a tissue specific promotor. Gal4 binds to UAS enhancer sequences in DNA when they are present in the same cell, inducing expression of any gene fused to the UAS sequence. We had two driver lines available to us: Tg(hb9:gal4) (Wyart et al., 2009) and Tg(nefma:KalTA4) (unpublished), to which I crossed UAS:GCamp6s reporter lines and characterised expression levels of Gcamp6s in spinal motor neurons at 3 and 5dpf using confocal microscopy. Although the hb9 (also known as mnx1) promotor is fairly specific to spinal motor neurons, the neurofilament medium polypeptide a (nefma) promotor additionally labels reticulospinal neurons such as the Mauthner cells (Baraban et al., 2013). I imaged the combinations

of driver and reporter lines at 3 and 5dpf to establish whether expression levels of GCamp6s persisted at the ages that we would want to test (as close to 6dpf as possible) and assess whether adequate numbers of primary motor neurons were labelled to allow detection of primary versus secondary motor neuron recruitment (Figure 5.29 A). Basal expression levels of GCamp6s was adequate in both driver lines at 3dpf, however by 5dpf the level of expression in the tg(hb9:gal4) driver line had significantly reduced making it difficult to observe neuronal morphology as well as adequate detectable calcium transients on timeseries imaging. A low basal expression level of a GECI is not a problem assuming that calcium transients are sensitive and detectable, as other fluorescent proteins can be co-expressed to allow assessment of structural morphology. However, in this situation it was deemed that tg(hb9:gal4) line would not be a suitable reporter at these ages. Furthermore, the number of identifiable primary motor neurons in the tg(nefma:kalta4) line was significantly higher than in the tg(hb9:gal4), likely as a result of the poor transgene expression (Figure 5.29C). From these results, I determined that either tg(nefma:KalTA4) line would be suitable for our experimental purposes. This driver line was subsequently crossed into the Myrf mutant background.

Effect of larval zebrafish preparation on swim bout frequency

Larvae must be restrained to allow imaging of motor neuron activity with minimal movement artefacts. Typically, if it is not necessary to record behaviour (i.e. tail movement) simultaneously with imaging, this is achieved using paralyzing agents. I began testing this set up using the neuromuscular blocker mivacurium chloride and mounting the larvae in agarose in a lateral position (Figure 5.30A). Motor neuron activity was imaged in the spinal cord for a period of five minutes, shortly after immobilisation was achieved. Following image acquisition, the frequency of calcium transients was measured using the GECIquant plugin (ImageJ, NEH) selecting the somas of a well delineated motoneurons as the regions of interest. At this point, as I was interested in general activity levels, I was not selective over the type of motoneuron that I was picking as a ROI. The frequency of spontaneous activity, detected as peaks in the deltaF/F trace, was unexpectedly low (∼one event per minute) across replicates with this preparation (Figure 5.30D). Therefore, I began to troubleshoot the larval preparation using different types of neuromuscular blockers and changing the position of the larvae for imaging. No difference was found in the frequency of sponta-

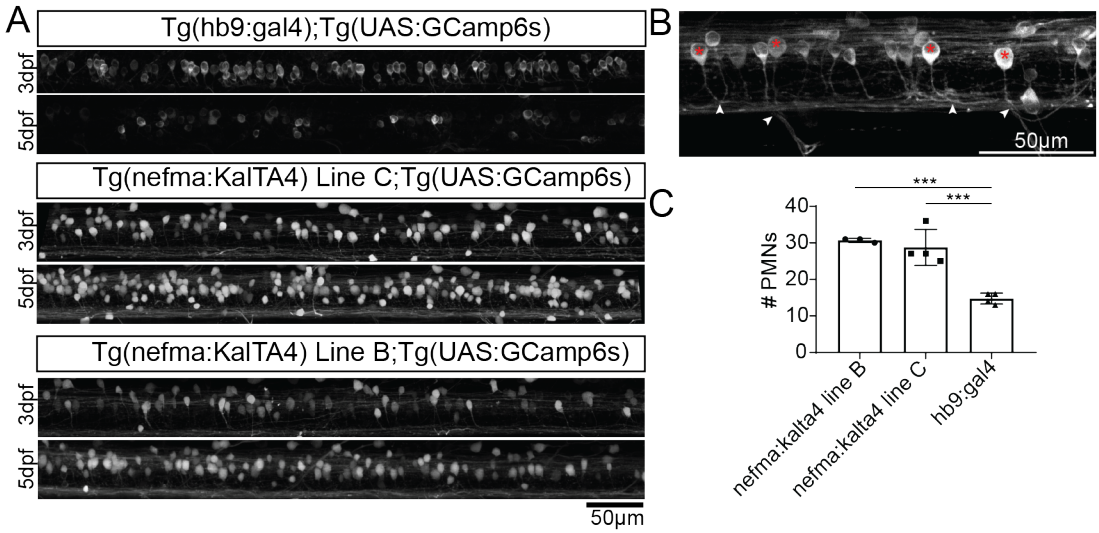

Figure 5.29: Driver lines for motor neuron expression of genetically encoded calcium indicators
(A.) Lateral images of the spinal cord provided for three available driver lines: Tg(hb9:Gal4), Tg(nefma:KalTA4) line b and Tg(nefma:KalTA4) line, driving expression of Gcamp6s at 3 and 5dpf. Different larvae were imaged at each timepoint. **(B.)** Super resolution image of one somite. Red arrows mark soma of motor neurons that are easily identifiable as primary motor neurons by their large soma and large caliber axons that are traceable to the ventral motor root. **(C.)** Quantification of the number of primary motor neurons identifiable in 5 dpf larvae across a full z-stack image of the spinal cord across spanning 5 somites. 30.67 ± 0.58 primary motor neurons are visible in the tg(nefma:kalta4) line B driver line, 28.75 ± 4.92 primary motor neurons in tg(nefma:kalta4) line C driver line and 14.75 ± 1.5 primary motor neurons in tg(hb9:gal4) line expressing GCamp6s. The number of identifiable primary motor neurons is significantly reduced in the tg(hb9:gal4) line ($F(2,8) = 28.21$, $p = 0.0002$, one-way ANOVA. Tukey's multiple comparisons: tg(nefma:kalta4) line B - hb9:gal4 $p = 0.0005$, nefma line C - hb9:Gal4 $p = 0.0005$, nefma line B - nefma line C $p = 0.45$.)

neous events when alternative neuromuscular blockers alpha-bungarotoxin (125μmol) or tubocurarine (1mg/ml) were used (data not shown). We posited that mounting the larvae in a ventral, more physiologically relevant, position may promote fictive swim bout frequency (Figure 5.30B). In general, the frequency of activity was variable across fish and although a subtle increase in events was observed in fish in a ventral position this was not significant between groups ($p = 0.87$, Kruskal-Wallis test followed by Dunn's multiple comparisons) (Figure 5.30D). Finally, I tried head-fixing larvae in agarose, reasoning that having their tails free to move would provide sensory feedback and encourage spontaneous movement. On the morning of experiments, larvae were anaesthetised lightly and mounted in a ventral position in agarose. The agarose was cut away from the tail and larvae were subsequently recovered from anaesthesia and left to acclimatise to this new scenario. In this preparation, larvae are awake and free to move

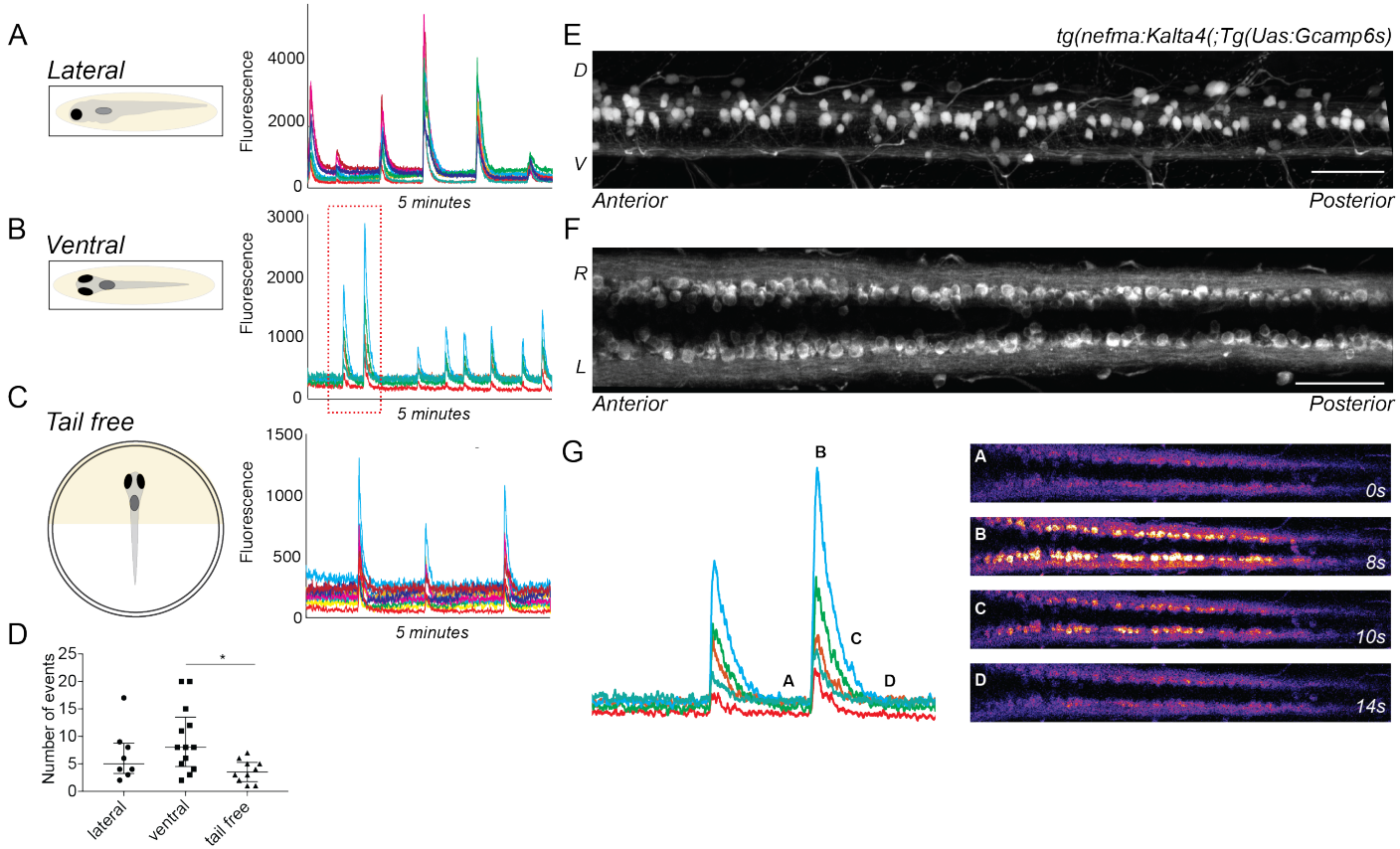

Figure 5.30: Troubleshooting positioning of larvae to obtain optimal levels of spontaneous activity
(A) to (C) Left: Schematics illustrating the different positions that larvae were placed in for imaging. Right: Fluorescent traces for a selection of ROIs across the spinal cord over a period of 5 minutes acquisition time. Frames rates vary between experiments as the width of the image varies according to the position the fish is in. **(D)** Manual quantification of the number of events observed over five minutes. **E)** Maximal intensity projection of the lateral view of motor neurons expressing GCamp6s in the spinal cord at 5dpf. D = dorsal, V = ventral. Scale bar = 50μm **(F)** Maximal intensity projection of the dorsal view of motor neurons in the spinal cord at 5dpf. R = right, L = left. Scale bar = 50μm. **(G)** Example of two calcium transients from panel (B). Image inserts are single frames extracted from the timeseries at the time points labelled A-D on the trace. Activation of a large number of motor neurons occurs during a spontaneous event. Images obtained at a frame rate of 43fps.

their tail, but their anterior body and head are fixed permitting anterior imaging of the spinal cord. Spontaneous activity frequency was surprisingly lower in this preparation than in a fixed ventral position ($p = 0.02$, Kruskal-Wallis test followed by Dunn's multiple comparisons) (Figure 5.30D). This may be due to anaesthetic being delivered on the same day of imaging, and perhaps head fixing larvae the day before would allow better recovery and spontaneous neuronal activity during imaging. In summary, levels of spontaneous activity were low across the different types of preparation tested. It is important to note that temperature was not controlled across experiments as this is not currently a stable feature on our microscope system - this will need to be implemented for further experiments.

Potential experimental methods to induce swimming

The frequency of spontaneous activity is too low in the current set up to obtain enough activity events per fish to allow analysis of motoneuron population dynamics. In order to drive spontaneous swimming in a physiologically relevant way, I propose two ideas. In the first, we drive forward swims in head fixed or paralysed larvae by providing visual gratings during in vivo imaging, as per the methods of Ahrens et al. (2012) and Naumann et al. (2016). The robust nature of the OMR response should allow swims to be induced at a physiologically relevant level. Indeed, both studies achieve fictive swim frequencies of 1Hz using this technique. The second option involves using optogenetic stimulation to drive premotor activity and drive swimming behaviour at regular intervals. By using existing reticulospinal specific driver lines to promote the expression of optogenetic proteins such as Channel Rhodopsin 2, selective activation of the nMLF in the midbrain can be used to drive swimming behaviour while monitoring neuronal activity (dal Maschio et al., 2017). However, given that I have hypothesised that premotor neuron activity may be disrupted in $Myrf^{-/-}$ larvae, this may not be the most suitable approach. We have previously established that electrode stimulation was an effective means of inducing fictive events in transgenic larvae, however this is more likely to be inducing struggles than spontaneous swims which will confound interpretation of dorsal motor neuron recruitment.

Conclusion

These experiments will inform the design of future experiments which will aim to monitor population level motoneuron activity during fictive swims in larval zebrafish. This will allow correlation of circuit level activity with the behavioural phenotypes observed in Chapter 4, namely the increase in spontaneous activity and increased frequency of fast swim bouts. I have demonstrated that current imaging systems are adequate for the assessment of population level activity, however, future work is required to establish the image analysis pipeline to allow data to be extracted regarding spatial and temporal recruitment of motoneurons. Additionally, we require a method to drive fictive swims efficiently as under current conditions they occur at a suboptimal frequency. The next priority should be to integrate the provision of visual stimuli to larvae during functional imaging experiments in order to boost the frequency of fictive swim events available for analysis within each fish.

Bibliography

Abbracchio, M. P., Burnstock, G., Verkhratsky, A. and Zimmermann, H. (2009), 'Purinergic signalling in the nervous system: An overview', *Trends in Neurosciences* **32**(1), 19–29.

Abdelfattah, A. S., Kawashima, T., Singh, A., Novak, O., Liu, H., Shuai, Y., Huang, Y.-C., Campagnola, L., Seeman, S. C., Yu, J., Zheng, J., Grimm, J. B., Patel, R., Friedrich, J., Mensh, B. D., Paninski, L., Macklin, J. J., Murphy, G. J., Podgorski, K., Lin, B.-J., Chen, T.-W., Turner, G. C., Liu, Z., Koyama, M., Svoboda, K., Ahrens, M. B., Lavis, L. D. and Schreiter, E. R. (2019), 'Bright and photostable chemigenetic indicators for extended in vivo voltage imaging', *Science* p. eaav6416.

Aggarwal, S., Snaidero, N., Pähler, G., Frey, S., Sánchez, P., Zweckstetter, M., Janshoff, A., Schneider, A., Weil, M.-T., Schaap, I. A. T., Görlich, D. and Simons, M. (2013), 'Myelin Membrane Assembly Is Driven by a Phase Transition of Myelin Basic Proteins Into a Cohesive Protein Meshwork', *PLoS Biology* **11**(6), e1001577.

Ahrens, M. B., Huang, K. H., Narayan, S., Mensh, B. D. and Engert, F. (2013), 'Two-photon calcium imaging during fictive navigation in virtual environments', *Frontiers in Neural Circuits* **7**.

Ahrens, M. B., Li, J. M., Orger, M. B., Robson, D. N., Schier, A. F., Engert, F. and Portugues, R. (2012), 'Brain-wide neuronal dynamics during motor adaptation in zebrafish', *Nature* **485**(7399), 471–477.

Allen, N. J. (2014), 'Astrocyte Regulation of Synaptic Behavior', *Annual Review of Cell and Developmental Biology* **30**(1), 439–463.

Allen, N. J. and Eroglu, C. (2017), 'Cell Biology of Astrocyte-Synapse Interactions', *Neuron* **96**(3), 697–708.

Allen, N. J. and Lyons, D. A. (2018), 'Glia as architects of central nervous system formation and function', *Science* **362**(6411), 181–185.

Almeida, R. G. (2018), 'The Rules of Attraction in Central Nervous System Myelination', *Frontiers in Cellular Neuroscience* **12**, 367.

Almeida, R. G., Czopka, T., ffrench-Constant, C. and Lyons, D. A. (2011), 'Individual axons regulate the myelinating potential of single oligodendrocytes in vivo', *Development* **138**(20), 4443–4450.

Antinucci, P., Folgueira, M. and Bianco, I. H. (2019), 'A pretectal command system controls hunting behaviour', *Biorxiv* .

Antinucci, P. and Hindges, R. (2016), 'A crystal-clear zebrafish for in vivo imaging', *Scientific Reports* **6**(1), 29490.

Arancibia-Cárcamo, I. L., Ford, M. C., Cossell, L., Ishida, K., Tohyama, K. and Attwell, D. (2017), 'Node of Ranvier length as a potential regulator of myelinated axon conduction speed', *eLife* **6**, e23329.

Auer, F., Vagionitis, S. and Czopka, T. (2018), 'Evidence for Myelin Sheath Remodeling in the CNS Revealed by In Vivo Imaging', *Current Biology* **28**(4), 549–559.e3.

Bai, Q., Sun, M., Stolz, D. B. and Burton, E. A. (2011), 'Major isoform of zebrafish P0 is a 23.5 kDa myelin glycoprotein expressed in selected white matter tracts of the central nervous system', *The Journal of Comparative Neurology* **519**(8), 1580–1596.

Baraban, M., Anselme, I., Schneider-Maunoury, S. and Giudicelli, F. (2013), 'Zebrafish Embryonic Neurons Transport Messenger RNA to Axons and Growth Cones In Vivo', *Journal of Neuroscience* **33**(40), 15726–15734.

Baraban, M., Koudelka, S. and Lyons, D. A. (2018), 'Ca2+ activity signatures of myelin sheath formation and growth in vivo', *Nature Neuroscience* **21**(1), 19–23.

Baraban, S., Taylor, M., Castro, P. and Baier, H. (2005), 'Pentylenetetrazole induced changes in zebrafish behavior, neural activity and c-fos expression', *Neuroscience* **131**(3), 759–768.

Barley, K., Dracheva, S. and Byne, W. (2009), 'Subcortical oligodendrocyte- and astrocyte-associated gene expression in subjects with schizophrenia, major depression and bipolar disorder', *Schizophrenia Research* **112**(1-3), 54–64.

Barres, B. A. and Raff, M. C. (1993), 'Proliferation of oligodendrocyte precursor cells depends on electrical activity in axons', *Nature* **361**(6409), 258–260.

Barres, B., Hart, I., Coles, H., Burne, J., Voyvodic, J., Richardson, W. and Raff, M. (1992), 'Cell death and control of cell survival in the oligodendrocyte lineage', *Cell* **70**(1), 31–46.

Barres, B., Jacobson, M., Schmid, R., Sendtner, M. and Raff, M. (1993), 'Does oligodendrocyte survival depend on axons?', *Current Biology* **3**(8), 489–497.

Barros, L. F. and Weber, B. (2018), 'CrossTalk proposal: An important astrocyte-to-neuron lactate shuttle couples neuronal activity to glucose utilisation in the brain: CrossTalk', *The Journal of Physiology* **596**(3), 347–350.

Basser, P., Mattiello, J. and LeBihan, D. (1994), 'MR diffusion tensor spectroscopy and imaging', *Biophysical Journal* **66**(1), 259–267.

Beaulieu, C. (2002), 'The basis of anisotropic water diffusion in the nervous system - a technical review', *NMR in Biomedicine* **15**(7-8), 435–455.

Bechler, M. E., Byrne, L. and ffrench-Constant, C. (2015), 'CNS Myelin Sheath Lengths Are an Intrinsic Property of Oligodendrocytes', *Current Biology* **25**(18), 2411–2416.

Bélanger, M., Allaman, I. and Magistretti, P. J. (2011), 'Brain Energy Metabolism: Focus on Astrocyte-Neuron Metabolic Cooperation', *Cell Metabolism* **14**(6), 724–738.

Bellinger, S. C., Miyazawa, G. and Steinmetz, P. N. (2008), 'Submyelin potassium accumulation may functionally block subsets of local axons during deep brain stimulation: A modeling study', *Journal of Neural Engineering* **5**(3), 263–274.

Bengtsson, S. L., Nagy, Z., Skare, S., Forsman, L., Forssberg, H. and Ullén, F. (2005), 'Extensive piano practicing has regionally specific effects on white matter development', *Nature Neuroscience* **8**(9), 1148–1150.

Berg, E. M., Björnfors, E. R., Pallucchi, I., Picton, L. D. and El Manira, A. (2018), 'Principles Governing Locomotion in Vertebrates: Lessons From Zebrafish', *Frontiers in Neural Circuits* **12**, 73.

Bergeron, S. A., Carrier, N., Li, G. H., Ahn, S. and Burgess, H. A. (2015), 'Gsx1 expression defines neurons required for prepulse inhibition', *Molecular Psychiatry* **20**(8), 974–985.

Bergles, D. E., Roberts, J. D. B., Somogyi, P. and Jahr, C. E. (2000), 'Glutamatergic synapses on oligodendrocyte precursor cells in the hippocampus', *Nature* **405**(6783), 187–191.

Bhattacharyya, K., McLean, D. L. and MacIver, M. A. (2017), 'Visual Threat Assessment and Reticulospinal Encoding of Calibrated Responses in Larval Zebrafish', *Current Biology* **27**(18), 2751–2762.e6.

Bi, G.-q. and Poo, M.-m. (1998), 'Synaptic Modifications in Cultured Hippocampal Neurons: Dependence on Spike Timing, Synaptic Strength, and Postsynaptic Cell Type', *The Journal of Neuroscience* **18**(24), 10464–10472.

Bianco, I. H. and Engert, F. (2015), 'Visuomotor Transformations Underlying Hunting Behavior in Zebrafish', *Current Biology* **25**(7), 831–846.

Bianco, I. H., Kampff, A. R. and Engert, F. (2011), 'Prey Capture Behavior Evoked by Simple Visual Stimuli in Larval Zebrafish', *Frontiers in Systems Neuroscience* **5**.

Bilbool, N., Kaitz, M., Feinsod, M., Soffer, D. and Abramsky, O. (1983), 'Visual evoked potentials in experimental allergic encephalomyelitis', *Journal of the Neurological Sciences* **60**(1), 105–115.

Birchmeier, C. and Nave, K.-A. (2008), 'Neuregulin-1, a key axonal signal that drives Schwann cell growth and differentiation', *Glia* **56**(14), 1491–1497.

Bird, T. D., Farrell, D. F. and Sumi, S. M. (1978), 'Brain lipid composition of the shiverer mouse: (genetic defect in myelin development)', *Journal of Neurochemistry* **31**(1), 387–391.

Blakemore, W. (1973), 'Remyelination of the superior cerebellar peduncle in the mouse following demyelination induced by feeding cuprizone', *Journal of the Neurological Sciences* **20**(1), 73–83.

Blumenfeld-Katzir, T., Pasternak, O., Dagan, M. and Assaf, Y. (2011), 'Diffusion MRI of Structural Brain Plasticity Induced by a Learning and Memory Task', *PLoS ONE* **6**(6), e20678.

Borla, M. A., Palecek, B., Budick, S. and O'Malley, D. M. (2002), 'Prey Capture by Larval Zebrafish: Evidence for Fine Axial Motor Control', *Brain, Behavior and Evolution* **60**(4), 207–229.

Bostock, H., Baker, M. and Reid, G. (1991), 'Changes in excitability of human motor axons underlying post-ischaemic fasciculations: Evidence for two stable states.', *The Journal of Physiology* **441**(1), 537–557.

Boyle, M. E., Berglund, E. O., Murai, K. K., Weber, L., Peles, E. and Ranscht, B. (2001), 'Contactin Orchestrates Assembly of the Septate-like Junctions at the Paranode in Myelinated Peripheral Nerve', *Neuron* **30**(2), 385–397.

Braff, D., Stone, C., Callaway, E., Geyer, M., Glick, I. and Bali, L. (1978), 'Prestimulus Effects on Human Startle Reflex in Normals and Schizophrenics', *Psychophysiology* **15**(4), 339–343.

Brainard, D. H. (1997), 'The Psychophysics Toolbox', *Spatial Vision* **10**(4), 433–436.

Brasko, C., Hawkins, V., De La Rocha, I. C. and Butt, A. M. (2017), 'Expression of Kir4.1 and Kir5.1 inwardly rectifying potassium channels in oligodendrocytes, the myelinating cells of the CNS', *Brain Structure and Function* **222**(1), 41–59.

Brazhe, A. R., Maksimov, G. V., Mosekilde, E. and Sosnovtseva, O. V. (2011), 'Excitation block in a nerve fibre model owing to potassium-dependent changes in myelin resistance', *Interface Focus* **1**(1), 86–100.

Brill, M. H., Waxman, S. G., Moore, J. W. and Joyner, R. W. (1977), 'Conduction velocity and spike configuration in myelinated fibres: Computed dependence on internode distance.', *Journal of Neurology, Neurosurgery & Psychiatry* **40**(8), 769–774.

Brinkmann, B. G., Agarwal, A., Sereda, M. W., Garratt, A. N., Müller, T., Wende, H., Stassart, R. M., Nawaz, S., Humml, C., Velanac, V., Radyushkin, K., Goebbels, S., Fischer, T. M., Franklin, R. J., Lai, C., Ehrenreich, H., Birchmeier, C., Schwab, M. H. and Nave, K. A. (2008), 'Neuregulin-1/ErbB Signaling Serves Distinct Functions in Myelination of the Peripheral and Central Nervous System', *Neuron* **59**(4), 581–595.

Brivio, V., Faivre-Sarrailh, C., Peles, E., Sherman, D. L. and Brophy, P. J. (2017), 'Assembly of CNS Nodes of Ranvier in Myelinated Nerves Is Promoted by the Axon Cytoskeleton', *Current Biology* **27**(7), 1068–1073.

Brösamle, C. and Halpern, M. E. (2002), 'Characterization of myelination in the developing zebrafish: Myelination in Zebrafish', *Glia* **39**(1), 47–57.

Budick, S. A. and O'Malley, D. M. (2000), 'Locomotor repertoire of the larval zebrafish: Swimming, turning and prey capture', *The Journal of Experimental Biology* **203**, 2565–2579.

Bujalka, H., Koenning, M., Jackson, S., Perreau, V. M., Pope, B., Hay, C. M., Mitew, S., Hill, A. F., Lu, Q. R., Wegner, M., Srinivasan, R., Svaren, J., Willingham, M., Barres, B. A. and Emery, B. (2013), 'MYRF Is a Membrane-Associated Transcription Factor That Autoproteolytically Cleaves to Directly Activate Myelin Genes', *PLoS Biology* **11**(8), e1001625.

Burgess, H. A. and Granato, M. (2007), 'Sensorimotor Gating in Larval Zebrafish', *Journal of Neuroscience* **27**(18), 4984–4994.

Buss, R. R. and Drapeau, P. (2001), 'Synaptic Drive to Motoneurons During Fictive Swimming in the Developing Zebrafish', *Journal of Neurophysiology* **86**(1), 197–210.

Buzsaki, G. (2006), *Rhythms of the Brain*, Oxford University Press, New York.

Cachat, J., Stewart, A., Grossman, L., Gaikwad, S., Kadri, F., Chung, K. M., Wu, N., Wong, K., Roy, S., Suciu, C., Goodspeed, J., Elegante, M., Bartels, B., Elkhayat, S., Tien, D., Tan, J., Denmark, A., Gilder, T., Kyzar, E., DiLeo, J., Frank, K., Chang, K., Utterback, E., Hart, P. and Kalueff, A. V. (2010), 'Measuring behavioral and endocrine responses to novelty stress in adult zebrafish', *Nature Protocols* **5**(11), 1786–1799.

Cahoy, J. D., Emery, B., Kaushal, A., Foo, L. C., Zamanian, J. L., Christopherson, K. S., Xing, Y., Lubischer, J. L., Krieg, P. A., Krupenko, S. A., Thompson, W. J. and Barres, B. A. (2008), 'A Transcriptome Database for Astrocytes, Neurons, and Oligodendrocytes: A New Resource for Understanding Brain Development and Function', *Journal of Neuroscience* **28**(1), 264–278.

Caporale, N. and Dan, Y. (2008), 'Spike Timing–Dependent Plasticity: A Hebbian Learning Rule', *Annual Review of Neuroscience* **31**(1), 25–46.

Chang, A., Nishiyama, A., Peterson, J., Prineas, J. and Trapp, B. D. (2000), 'NG2-Positive Oligodendrocyte Progenitor Cells in Adult Human Brain and Multiple Sclerosis Lesions', *The Journal of Neuroscience* **20**(17), 6404–6412.

Chang, N., Sun, C., Gao, L., Zhu, D., Xu, X., Zhu, X., Xiong, J.-W. and Xi, J. J. (2013), 'Genome editing with RNA-guided Cas9 nuclease in Zebrafish embryos', *Cell Research* **23**(4), 465–472.

Chen, T.-W., Wardill, T. J., Sun, Y., Pulver, S. R., Renninger, S. L., Baohan, A., Schreiter, E. R., Kerr, R. A., Orger, M. B., Jayaraman, V., Looger, L. L., Svoboda, K. and Kim, D. S. (2013), 'Ultrasensitive fluorescent proteins for imaging neuronal activity', *Nature* **499**(7458), 295–300.

Chen, X., Mu, Y., Hu, Y., Kuan, A. T., Nikitchenko, M., Randlett, O., Chen, A. B., Gavornik, J. P., Sompolinsky, H., Engert, F. and Ahrens, M. B. (2018), 'Brain-wide Organization of Neuronal Activity and Convergent Sensorimotor Transformations in Larval Zebrafish', *Neuron* **100**(4), 876–890.e5.

Chen, X., Zhang, W., Li, T., Guo, Y., Tian, Y., Wang, F., Liu, S., Shen, H.-Y., Feng, Y. and Xiao, L. (2015), 'Impairment of Oligodendroglia Maturation Leads to Aberrantly Increased Cortical Glutamate and Anxiety-Like Behaviors in Juvenile Mice', *Frontiers in Cellular Neuroscience* **9**.

Chomiak, T. and Hu, B. (2009), 'What Is the Optimal Value of the g-Ratio for Myelinated Fibers in the Rat CNS? A Theoretical Approach', *PLoS ONE* **4**(11), e7754.

Chomiak, T., Peters, S. and Hu, B. (2008), 'Functional Architecture and Spike Timing Properties of Corticofugal Projections From Rat Ventral Temporal Cortex', *Journal of Neurophysiology* **100**(1), 327–335.

Chorghay, Z., Káradóttir, R. T. and Ruthazer, E. S. (2018), 'White Matter Plasticity Keeps the Brain in Tune: Axons Conduct While Glia Wrap', *Frontiers in Cellular Neuroscience* **12**, 428.

Cong, L., Wang, Z., Chai, Y., Hang, W., Shang, C., Yang, W., Bai, L., Du, J., Wang, K.

and Wen, Q. (2017), 'Rapid whole brain imaging of neural activity in freely behaving larval zebrafish', *eLife* **6**(e28158), 1–20.

Copmans, D., Siekierska, A. and de Witte, P. A. (2017), Chapter 26 - Zebrafish Models of Epilepsy and Epileptic Seizures, *in* 'Models of Seizures and Epilepsy', 2nd edn, Academic Press, pp. 369–384.

Corfas, G., Roy, K. and Buxbaum, J. D. (2004), 'Neuregulin 1-erbB signaling and the molecular/cellular basis of schizophrenia', *Nature Neuroscience* **7**(6), 575–580.

Corty, M. M. and Freeman, M. R. (2013), 'Architects in neural circuit design: Glia control neuron numbers and connectivity', *The Journal of Cell Biology* **203**(3), 395–405.

Court, F. A., Sherman, D. L., Pratt, T., Garry, E. M., Ribchester, R. R., Cottrell, D. F., Fleetwood-Walker, S. M. and Brophy, P. J. (2004), 'Restricted growth of Schwann cells lacking Cajal bands slows conduction in myelinated nerves', *Nature* **431**(7005), 191–195.

Cox, S. R., Ritchie, S. J., Tucker-Drob, E. M., Liewald, D. C., Hagenaars, S. P., Davies, G., Wardlaw, J. M., Gale, C. R., Bastin, M. E. and Deary, I. J. (2016), 'Ageing and brain white matter structure in 3,513 UK Biobank participants', *Nature Communications* **7**(1), 13629.

Cui, W. W. (2005), 'The Zebrafish shocked Gene Encodes a Glycine Transporter and Is Essential for the Function of Early Neural Circuits in the CNS', *Journal of Neuroscience* **25**(28), 6610–6620.

Curzon, P., Zhang, M. and Radek, R. (2009), The Behavioural Assessment of Sensorimotor Processes in the Mouse: Acoustic startle, Rotarod, and Beam Walking., *in* 'Methods of Behavioural Analysis in Neuroscience', 2nd edn, CRC Press/Taylor & Francis, Boca Raton (FL).

Czopka, T., ffrench-Constant, C. and Lyons, D. A. (2013), 'Individual Oligodendrocytes Have Only a Few Hours in which to Generate New Myelin Sheaths In Vivo', *Developmental Cell* **25**(6), 599–609.

Czopka, T. and Lyons, D. A. (2011), Dissecting Mechanisms of Myelinated Axon Formation Using Zebrafish, *in* 'Methods in Cell Biology', Vol. 105, Elsevier, pp. 25–62.

dal Maschio, M., Donovan, J. C., Helmbrecht, T. O. and Baier, H. (2017), 'Linking Neurons to Network Function and Behavior by Two-Photon Holographic Optogenetics and Volumetric Imaging', *Neuron* **94**(4), 774–789.e5.

Dana, H., Sun, Y., Mohar, B., Hulse, B. K., Kerlin, A. M., Hasseman, J. P., Tsegaye, G., Tsang, A., Wong, A., Patel, R., Macklin, J. J., Chen, Y., Konnerth, A., Jayaraman, V., Looger, L. L., Schreiter, E. R., Svoboda, K. and Kim, D. S. (2019), 'High-performance calcium sensors for imaging activity in neuronal populations and microcompartments', *Nature Methods* **16**(7), 649–657.

Davis, K. L., Stewart, D. G., Friedman, J. I., Buchsbaum, M., Harvey, P. D., Hof, P. R., Buxbaum, J. and Haroutunian, V. (2003), 'White Matter Changes in Schizophrenia: Evidence for Myelin-Related Dysfunction', *Archives of General Psychiatry* **60**(5), 443.

Dawson, M. (2003), 'NG2-expressing glial progenitor cells: An abundant and widespread population of cycling cells in the adult rat CNS', *Molecular and Cellular Neuroscience* **24**(2), 476–488.

De Biase, L. M., Kang, S. H., Baxi, E. G., Fukaya, M., Pucak, M. L., Mishina, M., Calabresi, P. A. and Bergles, D. E. (2011), 'NMDA Receptor Signaling in Oligodendrocyte Progenitors Is Not Required for Oligodendrogenesis and Myelination', *Journal of Neuroscience* **31**(35), 12650–12662.

De Biase, L. M., Nishiyama, A. and Bergles, D. E. (2010), 'Excitability and Synaptic Communication within the Oligodendrocyte Lineage', *Journal of Neuroscience* **30**(10), 3600–3611.

Delaney, K. H., Kwiecien, J. M., Wegiel, J., Wisniewski, H. M., Percy, D. H. and Fletch, A. (1995), 'Familial Dysmyelination in a Long Evans Shaker Rat Mutant', *Laboratory Animal Science* **45**(5), 547–553.

Demerens, C., Stankoff, B., Logak, M., Anglade, P., Allinquant, B., Couraud, F., Zalc, B. and Lubetzki, C. (1996), 'Induction of myelination in the central nervous system by electrical activity.', *Proceedings of the National Academy of Sciences* **93**(18), 9887–9892.

Deutsch, G. K., Dougherty, R. F., Bammer, R., Siok, W. T., Gabrieli, J. D. and Wandell, B. (2005), 'Children's Reading Performance is Correlated with White Matter Structure Measured by Diffusion Tensor Imaging', *Cortex* **41**(3), 354–363.

Devaux, J. and Gow, A. (2008), 'Tight junctions potentiate the insulative properties of small CNS myelinated axons', *The Journal of Cell Biology* **183**(5), 909–921.

Diana, G., Sainsbury, T. T. J. and Meyer, M. P. (2019), 'Bayesian inference of neuronal assemblies', *PLOS Computational Biology* **15**(10), e1007481.

Diaz Verdugo, C., Myren-Svelstad, S., Aydin, E., Van Hoeymissen, E., Deneubourg, C., Vanderhaeghe, S., Vancraeynest, J., Pelgrims, R., Cosacak, M. I., Muto, A., Kizil, C., Kawakami, K., Jurisch-Yaksi, N. and Yaksi, E. (2019), 'Glia-neuron interactions underlie state transitions to generalized seizures', *Nature Communications* **10**(1), 3830.

Distel, M., Wullimann, M. F. and Koster, R. W. (2009), 'Optimized Gal4 genetics for permanent gene expression mapping in zebrafish', *Proceedings of the National Academy of Sciences* **106**(32), 13365–13370.

Djukic, B., Casper, K. B., Philpot, B. D., Chin, L.-S. and McCarthy, K. D. (2007), 'Conditional Knock-Out of Kir4.1 Leads to Glial Membrane Depolarization, Inhibition of Potassium and Glutamate Uptake, and Enhanced Short-Term Synaptic Potentiation', *Journal of Neuroscience* **27**(42), 11354–11365.

Downes, G. B. and Granato, M. (2006), 'Supraspinal input is dispensable to generate glycine-mediated locomotive behaviors in the zebrafish embryo', *Journal of Neurobiology* **66**(5), 437–451.

Draganski, B., Gaser, C., Busch, V., Schuierer, G., Ultrich, B. and May, A. (2004), 'Changes in grey matter induced by training', *Nature* **427**(6972), 311–312.

D'Rozario, M., Monk, K. and Petersen, S. (2017), Analysis of myelinated axon formation in zebrafish, *in* 'Methods in Cell Biology', Vol. 138, Elsevier, pp. 383–414.

Dunn, T. W., Gebhardt, C., Naumann, E. A., Riegler, C., Ahrens, M. B., Engert, F. and Del Bene, F. (2016), 'Neural Circuits Underlying Visually Evoked Escapes in Larval Zebrafish', *Neuron* **89**(3), 613–628.

Dutta, D. J., Woo, D. H., Lee, P. R., Pajevic, S., Bukalo, O., Huffman, W. C., Wake, H., Basser, P. J., SheikhBahaei, S., Lazarevic, V., Smith, J. C. and Fields, R. D. (2018), 'Regulation of myelin structure and conduction velocity by perinodal astrocytes', *Proceedings of the National Academy of Sciences* **115**(46), 11832–11837.

Dutton, K. A. (2001), 'Zebrafish sox10 mutant', *Development* **128**, 4113–4125.

Early, J. J. (2016), Chemical Screening Using Zebrafish to Identify Modulators of Myelination, PhD thesis, University of Edinburgh.

Early, J. J., Cole, K. L., Williamson, J. M., Swire, M., Kamadurai, H., Muskavitch, M. and Lyons, D. A. (2018), 'An automated high-resolution in vivo screen in zebrafish to identify chemical regulators of myelination', *eLife* **7**, e35136.

Eaton, R. C., Farley, R. D., Kimmel, C. B. and Schabtach, E. (1977), 'Functional development in the mauthner cell system of embryos and larvae of the zebra fish', *Journal of Neurobiology* **8**(2), 151–172.

Egan, R. J., Bergner, C. L., Hart, P. C., Cachat, J. M., Canavello, P. R., Elegante, M. F., Elkhayat, S. I., Bartels, B. K., Tien, A. K., Tien, D. H., Mohnot, S., Beeson, E., Glasgow, E., Amri, H., Zukowska, Z. and Kalueff, A. V. (2009), 'Understanding behavioral and physiological phenotypes of stress and anxiety in zebrafish', *Behavioural Brain Research* **205**(1), 38–44.

Ehrlich, D. E. and Schoppik, D. (2017), 'Control of Movement Initiation Underlies the Development of Balance', *Current Biology* **27**(3), 334–344.

Eklof-Ljunggren, E., Haupt, S., Ausborn, J., Dehnisch, I., Uhlen, P., Higashijima, S.-i. and El Manira, A. (2012), 'Origin of excitation underlying locomotion in the spinal circuit of zebrafish', *Proceedings of the National Academy of Sciences* **109**(14), 5511–5516.

El-Brolosy, M. A., Kontarakis, Z., Rossi, A., Kuenne, C., Günther, S., Fukuda, N., Kikhi, K., Boezio, G. L. M., Takacs, C. M., Lai, S.-L., Fukuda, R., Gerri, C., Giraldez, A. J. and Stainier, D. Y. R. (2019), 'Genetic compensation triggered by mutant mRNA degradation', *Nature* **568**(7751), 193–197.

EMBL-EBI Expression Atlas (n.d.), https://www.ebi.ac.uk/gxa/home.

Emery, B., Agalliu, D., Cahoy, J. D., Watkins, T. A., Dugas, J. C., Mulinyawe, S. B., Ibrahim, A., Ligon, K. L., Rowitch, D. H. and Barres, B. A. (2009), 'Myelin Gene Regulatory Factor Is a Critical Transcriptional Regulator Required for CNS Myelination', *Cell* **138**(1), 172–185.

Engeszer, R. E., Ryan, M. J. and Parichy, D. M. (2004), 'Learned Social Preference in Zebrafish', *Current Biology* **14**(10), 881–884.

Etxeberria, A., Hokanson, K. C., Dao, D. Q., Mayoral, S. R., Mei, F., Redmond, S. A., Ullian, E. M. and Chan, J. R. (2016), 'Dynamic Modulation of Myelination in Response to Visual Stimuli Alters Optic Nerve Conduction Velocity', *Journal of Neuroscience* **36**(26), 6937–6948.

Ewert, J. (1974), 'The neural basis of visually guided behavior', *Scientific American* **230**, 34–42.

Faber, D. S. and Pereda, A. E. (2018), 'Two Forms of Electrical Transmission Between Neurons', *Frontiers in Molecular Neuroscience* **11**, 427.

Fields, R. D. (2008), 'White matter in learning, cognition and psychiatric disorders', *Trends in Neurosciences* **31**(7), 361–370.

Flores, A. I., Narayanan, S. P., Morse, E. N., Shick, H. E., Yin, X., Kidd, G., Avila, R. L., Kirschner, D. A. and Macklin, W. B. (2008), 'Constitutively Active Akt Induces Enhanced Myelination in the CNS', *Journal of Neuroscience* **28**(28), 7174–7183.

Flusberg, B. A., Nimmerjahn, A., Cocker, E. D., Mukamel, E. A., Barretto, R. P. J., Ko, T. H., Burns, L. D., Jung, J. C. and Schnitzer, M. J. (2008), 'High-speed, miniaturized fluorescence microscopy in freely moving mice', *Nature Methods* **5**(11), 935–938.

Ford, M. C., Alexandrova, O., Cossell, L., Stange-Marten, A., Sinclair, J., Kopp-Scheinpflug, C., Pecka, M., Attwell, D. and Grothe, B. (2015), 'Tuning of Ranvier node and internode properties in myelinated axons to adjust action potential timing', *Nature Communications* **6**(1), 8073.

Fournier, A. J., Hogan, J. D., Rajbhandari, L., Shrestha, S., Venkatesan, A. and Ramesh, K. T. (2015), 'Changes in Neurofilament and Microtubule Distribution following Focal Axon Compression', *PLOS ONE* **10**(6), e0131617.

Freeman, S. A., Desmazières, A., Simonnet, J., Gatta, M., Pfeiffer, F., Aigrot, M. S., Rappeneau, Q., Guerreiro, S., Michel, P. P., Yanagawa, Y., Barbin, G., Brophy, P. J., Fricker, D., Lubetzki, C. and Sol-Foulon, N. (2015), 'Acceleration of conduction velocity linked to clustering of nodal components precedes myelination', *Proceedings of the National Academy of Sciences* **112**(3), E321–E328.

Fünfschilling, U., Supplie, L. M., Mahad, D., Boretius, S., Saab, A. S., Edgar, J., Brinkmann, B. G., Kassmann, C. M., Tzvetanova, I. D., Möbius, W., Diaz, F., Meijer, D., Suter, U., Hamprecht, B., Sereda, M. W., Moraes, C. T., Frahm, J., Goebbels, S. and Nave, K.-A. (2012), 'Glycolytic oligodendrocytes maintain myelin and long-term axonal integrity', *Nature* **485**(7399), 517–521.

Gahtan, E. (2005), 'Visual Prey Capture in Larval Zebrafish Is Controlled by Identified Reticulospinal Neurons Downstream of the Tectum', *Journal of Neuroscience* **25**(40), 9294–9303.

Gahtan, E., Sankrithi, N., Campos, J. B. and O'Malley, D. M. (2002), 'Evidence for a Widespread Brain Stem Escape Network in Larval Zebrafish', *Journal of Neurophysiology* **87**(1), 608–614.

Gallo, V., Zhou, J. M., McBain, C. J., Wright, P., Knutson, P. and Armstrong, R. C. (1996), 'Oligodendrocyte Progenitor Cell Proliferation and Lineage Progression Are Regulated by Glutamate Receptor-Mediated K+ Channel Block', *Journal of Neuroscience* **16**(8), 2659–267012.

Gao, R., Asano, S. M., Upadhyayula, S., Pisarev, I., Milkie, D. E., Liu, T.-L., Singh, V., Graves, A., Huynh, G. H., Zhao, Y., Bogovic, J., Colonell, J., Ott, C. M., Zugates, C., Tappan, S., Rodriguez, A., Mosaliganti, K. R., Sheu, S.-H., Pasolli, H. A., Pang, S., Xu, C. S., Megason, S. G., Hess, H., Lippincott-Schwartz, J., Hantman, A., Rubin, G. M., Kirchhausen, T., Saalfeld, S., Aso, Y., Boyden, E. S. and Betzig, E. (2019), 'Cortical column and whole-brain imaging with molecular contrast and nanoscale resolution', *Science* **363**(6424), eaau8302.

Garnai, S. J., Brinkmeier, M. L., Emery, B., Aleman, T. S., Pyle, L. C., Veleva-Rotse, B., Sisk, R. A., Rozsa, F. W., Ozel, A. B., Li, J. Z., Moroi, S. E., Archer, S. M., Lin, C.-m., Sheskey, S., Wiinikka-Buesser, L., Eadie, J., Urquhart, J. E., Black, G. C., Othman, M. I., Boehnke, M., Sullivan, S. A., Skuta, G. L., Pawar, H. S., Katz,

A. E., Huryn, L. A., Hufnagel, R. B., The Genomic Ascertainment Cohort, Camper, S. A., Richards, J. E. and Prasov, L. (2019), 'Variants in myelin regulatory factor (MYRF) cause autosomal dominant and syndromic nanophthalmos in humans and retinal degeneration in mice', *PLOS Genetics* **15**(5), e1008130.

Geraghty, A. C., Gibson, E. M., Ghanem, R. A., Greene, J. J., Ocampo, A., Goldstein, A. K., Ni, L., Yang, T., Marton, R. M., Paşca, S. P., Greenberg, M. E., Longo, F. M. and Monje, M. (2019), 'Loss of Adaptive Myelination Contributes to Methotrexate Chemotherapy-Related Cognitive Impairment', *Neuron* **103**(2), 250–265.e8.

Ghannad-Rezaie, M., Eimon, P. M., Wu, Y. and Yanik, M. F. (2019), 'Engineering brain activity patterns by neuromodulator polytherapy for treatment of disorders', *Nature Communications* **10**(1), 2620.

Ghosh, A., Carnahan, J. and Greenberg, E., M. (1994), '1618.full.pdf', *Science* **263**, 1618–1623.

Ghosh, K. K., Burns, L. D., Cocker, E. D., Nimmerjahn, A., Ziv, Y., Gamal, A. E. and Schnitzer, M. J. (2011), 'Miniaturized integration of a fluorescence microscope', *Nature Methods* **8**(10), 871–878.

Gibson, E. M., Purger, D., Mount, C. W., Goldstein, A. K., Lin, G. L., Wood, L. S., Inema, I., Miller, S. E., Bieri, G., Zuchero, J. B., Barres, B. A., Woo, P. J., Vogel, H. and Monje, M. (2014), 'Neuronal Activity Promotes Oligodendrogenesis and Adaptive Myelination in the Mammalian Brain', *Science* **344**(6183), 1252304–1252304.

Gleason, M. R., Higashijima, S.-i., Dallman, J., Liu, K., Mandel, G. and Fetcho, J. R. (2003), 'Translocation of CaM kinase II to synaptic sites in vivo', *Nature Neuroscience* **6**(3), 217–218.

Gould, E., Reeves, A. J., Graziano, M. S. A. and Gross, C. G. (1999), 'Neurogenesis in the Neocortex of Adult Primates', *Science* **286**(5439), 548–552.

Gow, A., Southwood, C. M., Li, J. S., Pariali, M., Riordan, G. P., Brodie, S. E., Danias, J., Bronstein, J. M., Kachar, B. and Lazzarini, R. A. (1999), 'CNS Myelin and Sertoli Cell Tight Junction Strands Are Absent in Osp/Claudin-11 Null Mice', *Cell* **99**(6), 649–659.

Green, M. H., Ho, R. K. and Hale, M. E. (2011), 'Movement and function of the pectoral fins of the larval zebrafish (Danio rerio) during slow swimming', *Journal of Experimental Biology* **214**(18), 3111–3123.

Gross, D. W. (2011), 'Diffusion tensor imaging in temporal lobe epilepsy: DTI in Temporal Lobe Epilepsy', *Epilepsia* **52**, 32–34.

Gulani, V., Webb, A. G., Duncan, I. D. and Lauterbur, P. C. (2001), 'Apparent diffusion tensor measurements in myelin-deficient rat spinal cords', *Magnetic Resonance in Medicine* **45**(2), 191–195.

Haesemeyer, M., Robson, D. N., Li, J. M., Schier, A. F. and Engert, F. (2018), 'A Brain-wide Circuit Model of Heat-Evoked Swimming Behavior in Larval Zebrafish', *Neuron* **98**(4), 817–831.e6.

Hagemeyer, N., Goebbels, S., Papiol, S., Kästner, A., Hofer, S., Begemann, M., Gerwig, U. C., Boretius, S., Wieser, G. L., Ronnenberg, A., Gurvich, A., Heckers, S. H., Frahm, J., Nave, K.-A. and Ehrenreich, H. (2012), 'A myelin gene causative of a catatonia-depression syndrome upon aging', *EMBO Molecular Medicine* **4**(6), 528–539.

Hakak, Y., Walker, J. R., Li, C., Wong, W. H., Davis, K. L., Buxbaum, J. D., Haroutunian, V. and Fienberg, A. A. (2001), 'Genome-wide expression analysis reveals dysregulation of myelination-related genes in chronic schizophrenia', *Proceedings of the National Academy of Sciences* **98**(8), 4746–4751.

Hale, M. E., Katz, H. R., Peek, M. Y. and Fremont, R. T. (2016), 'Neural circuits that drive startle behavior, with a focus on the Mauthner cells and spiral fiber neurons of fishes', *Journal of Neurogenetics* **30**(2), 89–100.

Hamanaka, K., Takata, A., Uchiyama, Y., Miyatake, S., Miyake, N., Mitsuhashi, S., Iwama, K., Fujita, A., Imagawa, E., Alkanaq, A. N., Koshimizu, E., Azuma, Y., Nakashima, M., Mizuguchi, T., Saitsu, H., Wada, Y., Minami, S., Katoh-Fukui, Y., Masunaga, Y., Fukami, M., Hasegawa, T., Ogata, T. and Matsumoto, N. (2019), 'MYRF haploinsufficiency causes 46,XY and 46,XX disorders of sex development: Bioinformatics consideration', *Human Molecular Genetics* **28**(14), 2319–2329.

Hammerschmidt, M., Pelegri, F., Mullins, M. C., Kane, D. A. and Brand, M. (1996), 'Mutations affecting morphogenesis during gastrulation and tail formation in the zebrafish, Danio rerio', *Development* **123**, 143–151.

Harrington, E. P., Zhao, C., Fancy, S. P. J., Kaing, S., Franklin, R. J. M. and Rowitch, D. H. (2010), 'Oligodendrocyte PTEN is required for myelin and axonal integrity, not remyelination', *Annals of Neurology* **68**(5), 703–716.

Heap, L. A., Vanwalleghem, G., Thompson, A. W., Favre-Bulle, I. A. and Scott, E. K. (2018), 'Luminance Changes Drive Directional Startle through a Thalamic Pathway', *Neuron* **99**(2), 293–301.e4.

Hebb, D. O. (1949), *The Organization of Behaviour; A Neuropsychological Theory*, Vol. xix, Wiley, New York.

Helmbrecht, T. O., dal Maschio, M., Donovan, J. C., Koutsouli, S. and Baier, H. (2018), 'Topography of a Visuomotor Transformation', *Neuron* **100**(6), 1429–1445.e4.

Helmchen, F., Fee, M. S., Tank, D. W. and Denk, W. (2001), 'Two-Photon Microscope: High-Resolution Brain Imaging in Freely Moving Animals', *Neuron* **31**, 903–912.

Henriques, P. M. D. (2019), Neuronal Circuits Underlying Visual Attention during Naturalistic Behaviour in Zebrafish Larvae, PhD thesis, University College London.

Henriques, P. M., Rahman, N., Jackson, S. E. and Bianco, I. H. (2019), 'Nucleus Isthmi Is Required to Sustain Target Pursuit during Visually Guided Prey-Catching', *Current Biology* **29**(11), 1771–1786.e5.

Herbomel, P., Thisse, B. and Thisse, C. (2001), 'Zebrafish Early Macrophages Colonize Cephalic Mesenchyme and Developing Brain, Retina, and Epidermis through a M-CSF Receptor-Dependent Invasive Process', *Developmental Biology* **238**(2), 274–288.

Higashijima, S.-I., Schaefer, M. and Fetcho, J. R. (2004), 'Neurotransmitter properties of spinal interneurons in embryonic and larval zebrafish', *The Journal of Comparative Neurology* **480**(1), 19–37.

Hildebrand, C. and Hahn, R. (1978), 'Relation between myelin sheath thickness and axon size in spinal cord white matter of some vertebrate species', *Journal of the Neurological Sciences* **38**(3), 421–434.

Hildebrand, C., Remahl, S., Persson, H. and Bjartmar, C. (1993), 'Myelinated nerve fibres in the CNS', *Progress in Neurobiology* **40**(3), 319–384.

Hildebrand, D. G. C., Cicconet, M., Torres, R. M., Choi, W., Quan, T. M., Moon, J., Wetzel, A. W., Scott Champion, A., Graham, B. J., Randlett, O., Plummer, G. S., Portugues, R., Bianco, I. H., Saalfeld, S., Baden, A. D., Lillaney, K., Burns, R., Vogelstein, J. T., Schier, A. F., Lee, W.-C. A., Jeong, W.-K., Lichtman, J. W. and Engert, F. (2017), 'Whole-brain serial-section electron microscopy in larval zebrafish', *Nature* **545**(7654), 345–349.

Hill, A. (2003), 'Neurodevelopmental Defects in Zebrafish (Danio rerio) at Environmentally Relevant Dioxin (TCDD) Concentrations', *Toxicological Sciences* **76**(2), 392–399.

Hill, R. A., Li, A. M. and Grutzendler, J. (2018), 'Lifelong cortical myelin plasticity and age-related degeneration in the live mammalian brain', *Nature Neuroscience* **21**(5), 683–695.

Hill, R. A., Patel, K. D., Goncalves, C. M., Grutzendler, J. and Nishiyama, A. (2014), 'Modulation of oligodendrocyte generation during a critical temporal window after NG2 cell division', *Nature Neuroscience* **17**(11), 1518–1527.

Hines, J. H., Ravanelli, A. M., Schwindt, R., Scott, E. K. and Appel, B. (2015), 'Neuronal activity biases axon selection for myelination in vivo', *Nature Neuroscience* **18**(5), 683–689.

Hoffman, E. J., Turner, K. J., Fernandez, J. M., Cifuentes, D., Ghosh, M., Ijaz, S., Jain, R. A., Kubo, F., Bill, B. R., Baier, H., Granato, M., Barresi, M. J., Wilson, S. W., Rihel, J., State, M. W. and Giraldez, A. J. (2016), 'Estrogens Suppress a Behavioral Phenotype in Zebrafish Mutants of the Autism Risk Gene, CNTNAP2', *Neuron* **89**(4), 725–733.

Hofstetter, S., Tavor, I., Tzur Moryosef, S. and Assaf, Y. (2013), 'Short-Term Learning Induces White Matter Plasticity in the Fornix', *Journal of Neuroscience* **33**(31), 12844–12850.

Holtmaat, A. and Svoboda, K. (2009), 'Experience-dependent structural synaptic plasticity in the mammalian brain', *Nature Reviews Neuroscience* **10**(9), 647–658.

Hornig, J., Fröb, F., Vogl, M. R., Hermans-Borgmeyer, I., Tamm, E. R. and Wegner, M. (2013), 'The Transcription Factors Sox10 and Myrf Define an Essential Regulatory Network Module in Differentiating Oligodendrocytes', *PLoS Genetics* **9**(10), e1003907.

Howe, K., Clark, M. D., Torroja, C. F., Torrance, J., Berthelot, C., Muffato, M., Collins, J. E., Humphray, S., McLaren, K., Matthews, L., McLaren, S., Sealy, I., Caccamo, M., Churcher, C., Scott, C., Barrett, J. C., Koch, R., Rauch, G.-J., White, S., Chow, W., Kilian, B., Quintais, L. T., Guerra-Assunção, J. A., Zhou, Y., Gu, Y., Yen, J., Vogel, J.-H., Eyre, T., Redmond, S., Banerjee, R., Chi, J., Fu, B., Langley, E., Maguire, S. F., Laird, G. K., Lloyd, D., Kenyon, E., Donaldson, S., Sehra, H., Almeida-King, J., Loveland, J., Trevanion, S., Jones, M., Quail, M., Willey, D., Hunt, A., Burton, J., Sims, S., McLay, K., Plumb, B., Davis, J., Clee, C., Oliver, K., Clark, R., Riddle, C., Elliott, D., Threadgold, G., Harden, G., Ware, D., Begum, S., Mortimore, B., Kerry, G., Heath, P., Phillimore, B., Tracey, A., Corby, N., Dunn, M., Johnson, C., Wood, J., Clark, S., Pelan, S., Griffiths, G., Smith, M., Glithero, R., Howden, P., Barker, N., Lloyd, C., Stevens, C., Harley, J., Holt, K., Panagiotidis, G., Lovell, J., Beasley, H., Henderson, C., Gordon, D., Auger, K., Wright, D., Collins, J., Raisen, C., Dyer, L., Leung, K., Robertson, L., Ambridge, K., Leongamornlert, D., McGuire, S., Gilderthorp, R., Griffiths, C., Manthravadi, D., Nichol, S., Barker, G., Whitehead, S., Kay, M., Brown, J., Murnane, C., Gray, E., Humphries, M., Sycamore, N., Barker, D., Saunders, D., Wallis, J., Babbage, A., Hammond, S., Mashreghi-Mohammadi, M., Barr, L., Martin, S., Wray, P., Ellington, A., Matthews, N., Ellwood, M., Woodmansey, R., Clark, G., Cooper, J. D., Tromans, A., Grafham, D., Skuce, C., Pandian, R., Andrews, R., Harrison, E., Kimberley, A., Garnett, J., Fosker, N., Hall, R., Garner, P., Kelly, D., Bird, C., Palmer, S., Gehring, I., Berger, A., Dooley, C. M., Ersan-Ürün, Z., Eser, C., Geiger, H., Geisler, M., Karotki, L., Kirn, A., Konantz, J., Konantz, M., Oberländer, M., Rudolph-Geiger, S., Teucke, M., Lanz, C., Raddatz, G., Osoegawa, K., Zhu, B., Rapp, A., Widaa, S., Langford, C., Yang, F., Schuster, S. C., Carter, N. P., Harrow, J., Ning, Z., Herrero, J., Searle, S. M. J., Enright, A., Geisler, R., Plasterk, R. H. A., Lee, C., Westerfield, M., de Jong, P. J., Zon, L. I., Postlethwait, J. H., Nüsslein-Volhard, C., Hubbard, T. J. P., Crollius, H. R., Rogers, J. and Stemple, D. L. (2013), 'The zebrafish reference genome sequence and its relationship to the human genome', *Nature* **496**(7446), 498–503.

Huang, H., Teng, P., Du, J., Meng, J., Hu, X., Tang, T., Zhang, Z., Qi, Y. B. and Qiu, M. (2018), 'Interactive Repression of MYRF Self-Cleavage and Activity in Oligodendrocyte Differentiation by TMEM98 Protein', *The Journal of Neuroscience* **38**(46), 9829–9839.

Huang, K.-H., Ahrens, M. B., Dunn, T. W. and Engert, F. (2013), 'Spinal Projection Neurons Control Turning Behaviors in Zebrafish', *Current Biology* **23**(16), 1566–1573.

Huang, L.-K. and Wang, Mao-Jiun J (1995), 'Image thresholding by minimizing the measures of fuzziness', *Pattern Recognition* **28**(1), 41–51.

Hughes, E. G., Kang, S. H., Fukaya, M. and Bergles, D. E. (2013), 'Oligodendrocyte progenitors balance growth with self-repulsion to achieve homeostasis in the adult brain', *Nature Neuroscience* **16**(6), 668–676.

Hughes, E. G., Orthmann-Murphy, J. L., Langseth, A. J. and Bergles, D. E. (2018), 'Myelin remodeling through experience-dependent oligodendrogenesis in the adult somatosensory cortex', *Nature Neuroscience* **21**(5), 696–706.

Huxley, A. F. and Stämpeli, R. (1949), 'Evidence for saltatory conduction in peripheral myelinated nerve fibres', *The Journal of Physiology* **108**(3), 315–339.

Ibrahim, M., Butt, A. and Berry, M. (1995), 'Relationship between myelin sheath diameter and internodal length in axons of the anterior medullary velum of the adult rat', *Journal of the Neurological Sciences* **133**(1-2), 119–127.

Irons, T., Kelly, P., Hunter, D., MacPhail, R. and Padilla, S. (2013), 'Acute administration of dopaminergic drugs has differential effects on locomotion in larval zebrafish', *Pharmacology Biochemistry and Behavior* **103**(4), 792–813.

Ishibashi, T., Dakin, K. A., Stevens, B., Lee, P. R., Kozlov, S. V., Stewart, C. L. and Fields, R. D. (2006), 'Astrocytes Promote Myelination in Response to Electrical Impulses', *Neuron* **49**(6), 823–832.

Itoh, K., Stevens, B., Schachner, M. and Fields, R. D. (1995), 'Regulated Expression of the Neural Cell Adhesion Molecule Li by Specific Patterns of Neural Impulses', **270**, 5.

Jain, R. A., Wolman, M. A., Marsden, K. C., Nelson, J. C., Shoenhard, H., Echeverry, F. A., Szi, C., Bell, H., Skinner, J., Cobbs, E. N., Sawada, K., Zamora, A. D., Pereda, A. E. and Granato, M. (2018), 'A Forward Genetic Screen in Zebrafish Identifies the G-Protein-Coupled Receptor CaSR as a Modulator of Sensorimotor Decision Making', *Current Biology* **28**(9), 1357–1369.e5.

Jäkel, S., Agirre, E., Mendanha Falcão, A., van Bruggen, D., Lee, K. W., Knuesel, I., Malhotra, D., ffrench-Constant, C., Williams, A. and Castelo-Branco, G. (2019), 'Altered human oligodendrocyte heterogeneity in multiple sclerosis', *Nature* **566**(7745), 543–547.

Janova, H., Arinrad, S., Balmuth, E., Mitjans, M., Hertel, J., Habes, M., Bittner, R. A., Pan, H., Goebbels, S., Begemann, M., Gerwig, U. C., Langner, S., Werner, H. B., Kittel-Schneider, S., Homuth, G., Davatzikos, C., Völzke, H., West, B. L., Reif, A., Grabe, H. J., Boretius, S., Ehrenreich, H. and Nave, K.-A. (2017), 'Microglia ablation alleviates myelin-associated catatonic signs in mice', *Journal of Clinical Investigation* **128**(2), 734–745.

Jeffries, M. A., Urbanek, K., Torres, L., Wendell, S. G., Rubio, M. E. and Fyffe-Maricich, S. L. (2016), 'ERK1/2 Activation in Preexisting Oligodendrocytes of Adult Mice Drives New Myelin Synthesis and Enhanced CNS Function', *Journal of Neuroscience* **36**(35), 9186–9200.

Jha, U. and Thirumalai, V. (2019), Neuromodulatory selection of motor neuron recruitment patterns in a visuomotor behavior increases speed, Preprint, Neuroscience.

Jimenez, F. and Campos-Ortega, J. A. (1982), 'Maternal effects of zygotic mutants affecting early neurogenesis inDrosophila', *Wilhelm Roux's Archives of Developmental Biology* **191**(3), 191–201.

Johansen-Berg, H., Della-Maggiore, V., Behrens, T. E., Smith, S. M. and Paus, T. (2007), 'Integrity of white matter in the corpus callosum correlates with bimanual co-ordination skills', *NeuroImage* **36**, T16–T21.

Kaller, M. S., Lazari, A., Blanco-Duque, C., Sampaio-Baptista, C. and Johansen-Berg, H. (2017), 'Myelin plasticity and behaviour — connecting the dots', *Current Opinion in Neurobiology* **47**, 86–92.

Kalueff, A. V., Gebhardt, M., Stewart, A. M., Cachat, J. M., Brimmer, M., Chawla, J. S., Craddock, C., Kyzar, E. J., Roth, A., Landsman, S., Gaikwad, S., Robinson, K., Baatrup, E., Tierney, K., Shamchuk, A., Norton, W., Miller, N., Nicolson, T., Braubach, O., Gilman, C. P., Pittman, J., Rosemberg, D. B., Gerlai, R., Echevarria, D., Lamb, E., Neuhauss, S. C., Weng, W., Bally-Cuif, L. and Schneider, and the Zebrafish Neuros, H. (2013), 'Towards a Comprehensive Catalog of Zebrafish Behavior 1.0 and Beyond', *Zebrafish* **10**(1), 70–86.

Kalueff, A. V., Stewart, A. M. and Gerlai, R. (2014), 'Zebrafish as an emerging model for studying complex brain disorders', *Trends in Pharmacological Sciences* **35**(2), 63–75.

Káradóttir, R. and Attwell, D. (2007), 'Neurotransmitter receptors in the life and death of oligodendrocytes', *Neuroscience* **145**(4), 1426–1438.

Káradóttir, R., Cavelier, P., Bergersen, L. H. and Attwell, D. (2005), 'NMDA receptors are expressed in oligodendrocytes and activated in ischaemia', *Nature* **438**(7071), 1162–1166.

Karttunen, M. J. (2017), A Zebrafish Model of Demyelination and Remyelination, PhD thesis, University of Edinburgh.

Karttunen, M. J., Czopka, T., Goedhart, M., Early, J. J. and Lyons, D. A. (2017), 'Regeneration of myelin sheaths of normal length and thickness in the zebrafish CNS correlates with growth of axons in caliber', *PLOS ONE* **12**(5), e0178058.

Kim, D. H., Kim, J., Marques, J. C., Grama, A., Hildebrand, D. G. C., Gu, W., Li, J. M. and Robson, D. N. (2017), 'Pan-neuronal calcium imaging with cellular resolution in freely swimming zebrafish', *Nature Methods* **14**(11), 1107–1114.

Kim, J. H., Renden, R. and von Gersdorff, H. (2013), 'Dysmyelination of Auditory Afferent Axons Increases the Jitter of Action Potential Timing during High-Frequency Firing', *Journal of Neuroscience* **33**(22), 9402–9407.

Kimmel, C. B., Patterson, J. and Kimmel, R. O. (1974), 'The development and behavioral characteristics of the startle response in the zebra fish', *Developmental Psychobiology* **7**(1), 47–60.

Kimmel, C. B., Powell, S. L. and Metcalfe, W. K. (1982), 'Brain neurons which project to the spinal cord in young larvae of the zebrafish', *The Journal of Comparative Neurology* **205**(2), 112–127.

Kimura, Y. (2006), 'Alx, a Zebrafish Homolog of Chx10, Marks Ipsilateral Descending Excitatory Interneurons That Participate in the Regulation of Spinal Locomotor Circuits', *Journal of Neuroscience* **26**(21), 5684–5697.

Kimura, Y. and Higashijima, S.-i. (2019), 'Regulation of locomotor speed and selection of active sets of neurons by V1 neurons', *Nature Communications* **10**(1), 2268.

Kimura, Y., Satou, C., Fujioka, S., Shoji, W., Umeda, K., Ishizuka, T., Yawo, H. and Higashijima, S.-i. (2013), 'Hindbrain V2a Neurons in the Excitation of Spinal Locomotor Circuits during Zebrafish Swimming', *Current Biology* **23**(10), 843–849.

Klingberg, T., Hedehus, M., Temple, E., Salz, T., Gabrieli, J. D. E., Moseley, M. E. and Poldrack, R. A. (2000), 'Microstructure of Temporo-Parietal White Matter as a Basis for Reading Ability: Evidence from Diffusion Tensor Magnetic Resonance Imaging', *Neuron* **25**, 493–500.

Klingseisen, A., Ristoiu, A.-M., Kegel, L., Sherman, D. L., Rubio-Brotons, M., Almeida, R. G., Koudelka, S., Benito-Kwiecinski, S. K., Poole, R. J., Brophy, P. J. and Lyons, D. A. (2019), 'Oligodendrocyte Neurofascin Independently Regulates Both Myelin Targeting and Sheath Growth in the CNS', *Developmental Cell* **51**(6), 730–744.e6.

Knafo, S., Fidelin, K., Prendergast, A., Tseng, P.-E. B., Parrin, A., Dickey, C., Böhm, U. L., Figueiredo, S. N., Thouvenin, O., Pascal-Moussellard, H. and Wyart, C. (2017), 'Mechanosensory neurons control the timing of spinal microcircuit selection during locomotion', *eLife* **6**, e25260.

Koch, M. (1999), 'The neurobiology of startle', *Progress in Neurobiology* **59**(2), 107–128.

Koenning, M., Jackson, S., Hay, C. M., Faux, C., Kilpatrick, T. J., Willingham, M. and Emery, B. (2012), 'Myelin Gene Regulatory Factor Is Required for Maintenance of Myelin and Mature Oligodendrocyte Identity in the Adult CNS', *Journal of Neuroscience* **32**(36), 12528–12542.

Korn, H. and Faber, D. S. (2005), 'The Mauthner Cell Half a Century Later: A Neurobiological Model for Decision-Making?', *Neuron* **47**(1), 13–28.

Koudelka, S., Voas, M. G., Almeida, R. G., Baraban, M., Soetaert, J., Meyer, M. P., Talbot, W. S. and Lyons, D. A. (2016), 'Individual Neuronal Subtypes Exhibit Diversity in CNS Myelination Mediated by Synaptic Vesicle Release', *Current Biology* **26**(11), 1447–1455.

Kougioumtzidou, E., Shimizu, T., Hamilton, N. B., Tohyama, K., Sprengel, R., Monyer, H., Attwell, D. and Richardson, W. D. (2017), 'Signalling through AMPA receptors on oligodendrocyte precursors promotes myelination by enhancing oligodendrocyte survival', *eLife* **6**, e28080.

Koyama, M., Kinkhabwala, A., Satou, C., Higashijima, S.-i. and Fetcho, J. (2011), 'Mapping a sensory-motor network onto a structural and functional ground plan in the hindbrain', *Proceedings of the National Academy of Sciences* **108**(3), 1170–1175.

Kramer, M. A. and Cash, S. S. (2012), 'Epilepsy as a Disorder of Cortical Network Organization', *The Neuroscientist* **18**(4), 360–372.

Krasnow, A. M., Ford, M. C., Valdivia, L. E., Wilson, S. W. and Attwell, D. (2018), 'Regulation of developing myelin sheath elongation by oligodendrocyte calcium transients in vivo', *Nature Neuroscience* **21**(1), 24–28.

Kurahashi, H., Azuma, Y., Masuda, A., Okuno, T., Nakahara, E., Imamura, T., Saitoh, M., Mizuguchi, M., Shimizu, T., Ohno, K. and Okumura, A. (2018), '*MYRF* is associated with encephalopathy with reversible myelin vacuolization: *MYRF* and Myelin Vacuolization', *Annals of Neurology* **83**(1), 98–106.

Kwan, K. M., Fujimoto, E., Grabher, C., Mangum, B. D., Hardy, M. E., Campbell, D. S., Parant, J. M., Yost, H. J., Kanki, J. P. and Chien, C.-B. (2007), 'The Tol2kit: A multisite gateway-based construction kit forTol2 transposon transgenesis constructs', *Developmental Dynamics* **236**(11), 3088–3099.

Lambert, A. M., Bonkowsky, J. L. and Masino, M. A. (2012), 'The Conserved Dopaminergic Diencephalospinal Tract Mediates Vertebrate Locomotor Development in Zebrafish Larvae', *Journal of Neuroscience* **32**(39), 13488–13500.

Lang, E. J. and Rosenbluth, J. (2003), 'Role of Myelination in the Development of a Uniform Olivocerebellar Conduction Time', *Journal of Neurophysiology* **89**(4), 2259–2270.

Lapato, A. S., Szu, J. I., Hasselmann, J. P., Khalaj, A. J., Binder, D. K. and Tiwari-Woodruff, S. K. (2017), 'Chronic demyelination-induced seizures', *Neuroscience* **346**, 409–422.

Lappe-Siefke, C., Goebbels, S., Gravel, M., Nicksch, E., Lee, J., Braun, P. E., Griffiths, I. R. and Nave, K.-A. (2003), 'Disruption of Cnp1 uncouples oligodendroglial functions in axonal support and myelination', *Nature Genetics* **33**(3), 366–374.

Larsch, J. and Baier, H. (2018), 'Biological Motion as an Innate Perceptual Mechanism Driving Social Affiliation', *Current Biology* **28**(22), 3523–3532.e4.

Larson, V. A., Mironova, Y., Vanderpool, K. G., Waisman, A., Rash, J. E., Agarwal, A. and Bergles, D. E. (2018), 'Oligodendrocytes control potassium accumulation in white matter and seizure susceptibility', *eLife* **7**, e34829.

Lau, J. Y., Bianco, I. H. and Severi, K. E. (2019), 'Cellular-level understanding of supraspinal control: What can be learned from zebrafish?', *Current Opinion in Physiology* **8**, 141–145.

Laursen, L. S., Chan, C. W. and ffrench-Constant, C. (2009), 'An Integrin-Contactin Complex Regulates CNS Myelination by Differential Fyn Phosphorylation', *Journal of Neuroscience* **29**(29), 9174–9185.

Le Ray, D., Brocard, F., Bourcier-Lucas, C., Auclair, F., Lafaille, P. and Dubuc, R. (2003), 'Nicotinic activation of reticulospinal cells involved in the control of swimming in lampreys: Nicotinic inputs to reticulospinal cells', *European Journal of Neuroscience* **17**(1), 137–148.

Lee, B., Park, J.-Y., Jung, W. H., Kim, H. S., Oh, J. S., Choi, C.-H., Jang, J. H., Kang, D.-H. and Kwon, J. S. (2010), 'White matter neuroplastic changes in long-term trained players of the game of "Baduk" (GO): A voxel-based diffusion-tensor imaging study', *NeuroImage* **52**(1), 9–19.

Lee, Y., Morrison, B. M., Li, Y., Lengacher, S., Farah, M. H., Hoffman, P. N., Liu, Y., Tsingalia, A., Jin, L., Zhang, P.-W., Pellerin, L., Magistretti, P. J. and Roth-

stein, J. D. (2012), 'Oligodendroglia metabolically support axons and contribute to neurodegeneration', *Nature* **487**(7408), 443–448.

Lehman, D. M. and Harrison, J. M. (2002), 'Flash visual evoked potentials in the hypomyelinated mutant mouse shiverer', *Documenta Ophthalmologica* **104**, 83–95.

Li, M., Zhao, L., Page-McCaw, P. S. and Chen, W. (2016), 'Zebrafish Genome Engineering Using the CRISPR–Cas9 System', *Trends in Genetics* **32**(12), 815–827.

Li, Z., Park, Y. and Marcotte, E. M. (2013), 'A Bacteriophage Tailspike Domain Promotes Self-Cleavage of a Human Membrane-Bound Transcription Factor, the Myelin Regulatory Factor MYRF', *PLoS Biology* **11**(8), e1001624.

Lin, S.-c. and Bergles, D. E. (2004), 'Synaptic signaling between GABAergic interneurons and oligodendrocyte precursor cells in the hippocampus', *Nature Neuroscience* **7**(1), 24–32.

Liu, D. W. and Westerfield, M. (1988), 'Function of identified motoneurones and coordination of primary and secondary motor systems during zebra fish swimming.', *The Journal of Physiology* **403**(1), 73–89.

Liu, J., Dietz, K., DeLoyht, J. M., Pedre, X., Kelkar, D., Kaur, J., Vialou, V., Lobo, M. K., Dietz, D. M., Nestler, E. J., Dupree, J. and Casaccia, P. (2012), 'Impaired adult myelination in the prefrontal cortex of socially isolated mice', *Nature Neuroscience* **15**(12), 1621–1623.

Liu, J., Dupree, J. L., Gacias, M., Frawley, R., Sikder, T., Naik, P. and Casaccia, P. (2016), 'Clemastine Enhances Myelination in the Prefrontal Cortex and Rescues Behavioral Changes in Socially Isolated Mice', *The Journal of Neuroscience* **36**(3), 957–962.

Liu, K. S. and Fetcho, J. R. (1999), 'Laser Ablations Reveal Functional Relationships of Segmental Hindbrain Neurons in Zebrafish', *Neuron* **23**(2), 325–335.

Liu, K. S., Gray, M., Otto, S. J., Fetcho, J. R. and Beattie, C. E. (2003), 'Mutations in *deadly seven/notch1a* Reveal Developmental Plasticity in the Escape Response Circuit', *The Journal of Neuroscience* **23**(22), 8159–8166.

Love, S. (2006), 'Demyelinating diseases', *Journal of Clinical Pathology* **59**(11), 1151–1159.

Lovett-Barron, M., Andalman, A. S., Allen, W. E., Vesuna, S., Kauvar, I., Burns, V. M. and Deisseroth, K. (2017), 'Ancestral Circuits for the Coordinated Modulation of Brain State', *Cell* **171**(6), 1411–1423.e17.

Lund, C., Nakken, K. O., Edland, A. and Celius, E. G. (2014), 'Multiple sclerosis and seizures: Incidence and prevalence over 40 years', *Acta Neurologica Scandinavica* **130**(6), 368–373.

Lundgaard, I., Luzhynskaya, A., Stockley, J. H., Wang, Z., Evans, K. A., Swire, M., Volbracht, K., Gautier, H. O. B., Franklin, R. J. M., ffrench-Constant, C., Attwell, D. and Káradóttir, R. T. (2013), 'Neuregulin and BDNF Induce a Switch to NMDA Receptor-Dependent Myelination by Oligodendrocytes', *PLoS Biology* **11**(12), e1001743.

Lyons, D. A., Pogoda, H.-M., Voas, M. G., Woods, I. G., Diamond, B., Nix, R., Arana, N., Jacobs, J. and Talbot, W. S. (2005), 'Erbb3 and erbb2 Are Essential for Schwann Cell Migration and Myelination in Zebrafish', *Current Biology* **15**(6), 513–524.

Madden, D. J., Whiting, W. L., Huettel, S. A., White, L. E., MacFall, J. R. and Provenzale, J. M. (2004), 'Diffusion tensor imaging of adult age differences in cerebral white matter: Relation to response time', *NeuroImage* **21**(3), 1174–1181.

Maguire, E. A., Gadian, D. G., Johnsrude, I. S., Good, C. D., Ashburner, J., Frackowiak, R. S. J. and Frith, C. D. (2000), 'Navigation-related structural change in the hippocampi of taxi drivers', *Proceedings of the National Academy of Sciences* **97**(8), 4398–4403.

Mahad, D. J., Ziabreva, I., Campbell, G., Lax, N., White, K., Hanson, P. S., Lassmann, H. and Turnbull, D. M. (2009), 'Mitochondrial changes within axons in multiple sclerosis', *Brain* **132**(5), 1161–1174.

Maher, F. and Simpson, I. A. (1994), 'The GLUT3 glucose transporter is the predominant isoform in primary cultured neurons: Assessment by biosynthetic and photoaffinity labelling', *Biochemical Journal* **301**(2), 379–384.

Makinodan, M., Rosen, K. M., Ito, S. and Corfas, G. (2012), 'A Critical Period for Social Experience-Dependent Oligodendrocyte Maturation and Myelination', *Science* **337**(6100), 1357–1360.

Mangin, J.-M., Li, P., Scafidi, J. and Gallo, V. (2012), 'Experience-dependent regulation of NG2 progenitors in the developing barrel cortex', *Nature Neuroscience* **15**(9), 1192–1194.

Marisca, R., Hoche, T., Agirre, E., Hoodless, L. J., Barkey, W., Auer, F., Castelo-Branco, G. and Czopka, T. (2020), 'Functionally distinct subgroups of oligodendrocyte precursor cells integrate neural activity and execute myelin formation', *Nature Neuroscience* **23**(3), 363–374.

Markram, H., Lubke, J., Frotscher, M. and Sakmann, B. (1997), 'Regulation of Synaptic Efficacy by Coincidence of Postsynaptic APs and EPSPs', *Science* **275**, 213–215.

Marquart, G. D., Tabor, K. M., Bergeron, S. A., Briggman, K. L. and Burgess, H. A. (2019), Prepontine non-giant neurons drive flexible escape behavior in zebrafish, Preprint, Neuroscience.

Marques, J. C., Lackner, S., Félix, R. and Orger, M. B. (2018), 'Structure of the Zebrafish Locomotor Repertoire Revealed with Unsupervised Behavioral Clustering', *Current Biology* **28**(2), 181–195.e5.

Marques, S., Zeisel, A., Codeluppi, S., van Bruggen, D., Mendanha Falcao, A., Xiao, L., Li, H., Haring, M., Hochgerner, H., Romanov, R. A., Gyllborg, D., Munoz-Manchado, A. B., La Manno, G., Lonnerberg, P., Floriddia, E. M., Rezayee, F., Ernfors, P., Arenas, E., Hjerling-Leffler, J., Harkany, T., Richardson, W. D., Linnarsson, S. and Castelo-Branco, G. (2016), 'Oligodendrocyte heterogeneity in the mouse juvenile and adult central nervous system', *Science* **352**(6291), 1326–1329.

Marrie, R. A., Reider, N., Cohen, J., Trojano, M., Sorensen, P. S., Cutter, G., Reingold, S. and Stuve, O. (2015), 'A systematic review of the incidence and prevalence of sleep disorders and seizure disorders in multiple sclerosis', *Multiple Sclerosis Journal* **21**(3), 342–349.

Matthews, M. A. and Duncan, D. (1971), 'A quantitative study of morphological changes accompanying the initiation and progress of myelin production in the dorsal funiculus of the rat spinal cord', *The Journal of Comparative Neurology* **142**(1), 1–22.

McClenahan, P., Troup, M. and Scott, E. K. (2012), 'Fin-Tail Coordination during Escape and Predatory Behavior in Larval Zebrafish', *PLoS ONE* **7**(2), e32295.

Mccullumsmith, R., Gupta, D., Beneyto, M., Kreger, E., Haroutunian, V., Davis, K. and Meadorwoodruff, J. (2007), 'Expression of transcripts for myelination-related genes in the anterior cingulate cortex in schizophrenia', *Schizophrenia Research* **90**(1-3), 15–27.

McCurley, A. T. and Callard, G. V. (2008), 'Characterization of housekeeping genes in zebrafish: Male-female differences and effects of tissue type, developmental stage and chemical treatment', *BMC Molecular Biology* **9**(1), 102.

McElligott, M. B. and O'Malley, D. M. (2005), 'Prey Tracking by Larval Zebrafish: Axial Kinematics and Visual Control', *Brain, Behavior and Evolution* **66**(3), 177–196.

McGee, A. W. (2005), 'Experience-Driven Plasticity of Visual Cortex Limited by Myelin and Nogo Receptor', *Science* **309**(5744), 2222–2226.

McKenzie, I. A., Ohayon, D., Li, H., Paes de Faria, J., Emery, B., Tohyama, K. and Richardson, W. D. (2014), 'Motor skill learning requires active central myelination', *Science* **346**(6207), 318–322.

McLean, D. L., Fan, J., Higashijima, S.-i., Hale, M. E. and Fetcho, J. R. (2007), 'A topographic map of recruitment in spinal cord', *Nature* **446**(7131), 71–75.

McLean, D. L. and Fetcho, J. R. (2004), 'Ontogeny and innervation patterns of dopaminergic, noradrenergic, and serotonergic neurons in larval zebrafish', *The Journal of Comparative Neurology* **480**(1), 38–56.

McLean, D. L. and Fetcho, J. R. (2009), 'Spinal Interneurons Differentiate Sequentially from Those Driving the Fastest Swimming Movements in Larval Zebrafish to Those Driving the Slowest Ones', *Journal of Neuroscience* **29**(43), 13566–13577.

Menelaou, E. and McLean, D. L. (2012), 'A Gradient in Endogenous Rhythmicity and Oscillatory Drive Matches Recruitment Order in an Axial Motor Pool', *Journal of Neuroscience* **32**(32), 10925–10939.

Meng, J., Ma, X., Tao, H., Jin, X., Witvliet, D., Mitchell, J., Zhu, M., Dong, M.-Q., Zhen, M., Jin, Y. and Qi, Y. B. (2017), 'Myrf ER-Bound Transcription Factors Drive C. elegans Synaptic Plasticity via Cleavage-Dependent Nuclear Translocation', *Developmental Cell* **41**(2), 180–194.e7.

Mensch, S., Baraban, M., Almeida, R., Czopka, T., Ausborn, J., El Manira, A. and Lyons, D. A. (2015), 'Synaptic vesicle release regulates myelin sheath number of individual oligodendrocytes in vivo', *Nature Neuroscience* **18**(5), 628–630.

Metcalfe, W. K., Mendelson, B. and Kimmel, C. B. (1986), 'Segmental homologies among reticulospinal neurons in the hindbrain of the zebrafish larva', *The Journal of Comparative Neurology* **251**(2), 147–159.

Michailov, G. V. (2004), 'Axonal Neuregulin-1 Regulates Myelin Sheath Thickness', *Science* **304**(5671), 700–703.

Micheva, K. D., Wolman, D., Mensh, B. D., Pax, E., Buchanan, J., Smith, S. J. and Bock, D. D. (2016), 'A large fraction of neocortical myelin ensheathes axons of local inhibitory neurons', *eLife* **5**, e15784.

Micu, I., Jiang, Q., Coderre, E., Ridsdale, A., Zhang, L., Woulfe, J., Yin, X., Trapp, B. D., McRory, J. E., Rehak, R., Zamponi, G. W., Wang, W. and Stys, P. K. (2006), 'NMDA receptors mediate calcium accumulation in myelin during chemical ischaemia', *Nature* **439**(7079), 988–992.

Migault, G., van der Plas, T. L., Trentesaux, H., Panier, T., Candelier, R., Proville, R., Englitz, B., Debrégeas, G. and Bormuth, V. (2018), 'Whole-Brain Calcium Imaging during Physiological Vestibular Stimulation in Larval Zebrafish', *Current Biology* **28**(23), 3723–3735.e6.

Miller, D. J., Duka, T., Stimpson, C. D., Schapiro, S. J., Baze, W. B., McArthur, M. J., Fobbs, A. J., Sousa, A. M. M., Sestan, N., Wildman, D. E., Lipovich, L., Kuzawa, C. W., Hof, P. R. and Sherwood, C. C. (2012), 'Prolonged myelination in human neocortical evolution', *Proceedings of the National Academy of Sciences* **109**(41), 16480–16485.

Mitew, S., Gobius, I., Fenlon, L. R., McDougall, S. J., Hawkes, D., Xing, Y. L., Bujalka, H., Gundlach, A. L., Richards, L. J., Kilpatrick, T. J., Merson, T. D. and Emery, B. (2018), 'Pharmacogenetic stimulation of neuronal activity increases myelination in an axon-specific manner', *Nature Communications* **9**(1), 306.

Moore, J., Joyner, R., Brill, M., Waxman, S. and Najar-Joa, M. (1978), 'Simulations

of conduction in uniform myelinated fibers. Relative sensitivity to changes in nodal and internodal parameters', *Biophysical Journal* **21**(2), 147–160.

Morell, P. and Quarles, R. H. (1999), Characteristic Composition of Myelin, *in* 'Basic Neurochemistry: Molecular, Cellular and Medical Aspects', 6th edn, Lippincott-Raven, Philadelphia.

Murcia-Belmonte, V., Esteban, P. F., Martínez-Hernández, J., Gruart, A., Luján, R., Delgado-García, J. M. and de Castro, F. (2016), 'Anosmin-1 over-expression regulates oligodendrocyte precursor cell proliferation, migration and myelin sheath thickness', *Brain Structure and Function* **221**(3), 1365–1385.

Murray, J. and Blakemore, W. (1980), 'The relationship between internodal length and fibre diameter in the spinal cord of the cat', *Journal of the Neurological Sciences* **45**(1), 29–41.

Mutsaers, S. E. and Carroll, W. M. (1998), 'Focal accumulation of intra-axonal mitochondria in demyelination of the cat optic nerve', *Acta Neuropathologica* **96**(2), 139–143.

Nagy, B., Hovhannisyan, A., Barzan, R., Chen, T.-J. and Kukley, M. (2017), 'Different patterns of neuronal activity trigger distinct responses of oligodendrocyte precursor cells in the corpus callosum', *PLOS Biology* **15**(8), e2001993.

Nagy, J. I., Dudek, F. and Rash, J. E. (2004), 'Update on connexins and gap junctions in neurons and glia in the mammalian nervous system', *Brain Research Reviews* **47**(1-3), 191–215.

Nath, T., Mathis, A., Chen, A. C., Patel, A., Bethge, M. and Mathis, M. W. (2019), 'Using DeepLabCut for 3D markerless pose estimation across species and behaviors', *Nature Protocols* **14**(7), 2152–2176.

Naumann, E. A., Fitzgerald, J. E., Dunn, T. W., Rihel, J., Sompolinsky, H. and Engert, F. (2016), 'From Whole-Brain Data to Functional Circuit Models: The Zebrafish Optomotor Response', *Cell* **167**(4), 947–960.e20.

Nawaz, S., Sánchez, P., Schmitt, S., Snaidero, N., Mitkovski, M., Velte, C., Brückner, B. R., Alexopoulos, I., Czopka, T., Jung, S. Y., Rhee, J. S., Janshoff, A., Witke, W., Schaap, I. A., Lyons, D. A. and Simons, M. (2015), 'Actin Filament Turnover

Drives Leading Edge Growth during Myelin Sheath Formation in the Central Nervous System', *Developmental Cell* **34**(2), 139–151.

Neuhauss, S. C. F., Biehlmaier, O., Seeliger, M. W., Das, T., Kohler, K., Harris, W. A. and Baier, H. (1999), 'Genetic Disorders of Vision Revealed by a Behavioral Screen of 400 Essential Loci in Zebrafish', *The Journal of Neuroscience* **19**(19), 8603–8615.

Neusch, C., Rozengurt, N., Jacobs, R. E., Lester, H. A. and Kofuji, P. (2001), 'Kir4.1 Potassium Channel Subunit Is Crucial for Oligodendrocyte Development and *In Vivo* Myelination', *The Journal of Neuroscience* **21**(15), 5429–5438.

Nicholas, R., Magliozzi, R., Campbell, G., Mahad, D. and Reynolds, R. (2016), 'Temporal lobe cortical pathology and inhibitory GABA interneuron cell loss are associated with seizures in multiple sclerosis', *Multiple Sclerosis Journal* **22**(1), 25–35.

Noga, B. R., Kriellaars, D. J., Brownstone, R. M. and Jordan, L. M. (2003), 'Mechanism for Activation of Locomotor Centers in the Spinal Cord by Stimulation of the Mesencephalic Locomotor Region', *Journal of Neurophysiology* **90**(3), 1464–1478.

Noldus, L. P. J. J., Spink, A. J. and Tegelenbosch, R. A. J. (2001), 'EthoVision: A versatile video tracking system for automation of behavioral experiments', *Behavior Research Methods, Instruments, & Computers* **33**(3), 398–414.

Okamoto, H. (2018), 'The active inference in decision making by adult zebrafish revealed by in-vivo imaging of the telencephalic neural activities in the closed-loop virtual reality environment'.

O'Malley, D. M., Kao, Y.-H. and Fetcho, J. R. (1996), 'Imaging the Functional Organization of Zebrafish Hindbrain Segments during Escape Behaviors', *Neuron* **17**(6), 1145–1155.

Orger, M. B., Kampff, A. R., Severi, K. E., Bollmann, J. H. and Engert, F. (2008), 'Control of visually guided behavior by distinct populations of spinal projection neurons', *Nature Neuroscience* **11**(3), 327–333.

Orger, M. B., Smear, M. C., Anstis, S. M. and Baier, H. (2000), 'Perception of Fourier and non-Fourier motion by larval zebrafish', *Nature Neuroscience* **3**(11), 1128–1133.

Ozbay, B. N., Futia, G. L., Ma, M., Bright, V. M., Gopinath, J. T., Hughes, E. G., Restrepo, D. and Gibson, E. A. (2018), 'Three dimensional two-photon brain imaging in freely moving mice using a miniature fiber coupled microscope with active axial-scanning', *Scientific Reports* **8**(1), 8108.

Pajevic, S., Basser, P. and Fields, R. (2014), 'Role of myelin plasticity in oscillations and synchrony of neuronal activity', *Neuroscience* **276**, 135–147.

Panula, P., Sallinen, V., Sundvik, M., Kolehmainen, J., Torkko, V., Tiittula, A., Moshnyakov, M. and Podlasz, P. (2006), 'Modulatory Neurotransmitter Systems and Behavior: Towards Zebrafish Models of Neurodegenerative Diseases', *Zebrafish* **3**(2), 235–247.

Paolicelli, R. C., Bolasco, G., Pagani, F., Maggi, L., Scianni, M., Panzanelli, P., Giustetto, M., Ferreira, T. A., Guiducci, E., Dumas, L., Ragozzino, D. and Gross, C. T. (2011), 'Synaptic Pruning by Microglia is Necessary for Normal Brain Development', *Science* **333**(6048), 1456:1458.

Pennington, Z. T., Dong, Z., Bowler, R., Feng, Y., Vetere, L. M., Shuman, T. and Cai, D. J. (2019), ezTrack: An open-source video analysis pipeline for the investigation of animal behavior, Preprint, Neuroscience.

Perrimon, N., Engstrom, L. and Mahowald, A. P. (1984), 'The effects of zygotic lethal mutations on female germ-line functions in Drosophila', *Developmental Biology* **105**(2), 404–414.

Petanjek, Z., Judaš, M., Šimić, G., Rašin, M. R., Uylings, H. B. M., Rakic, P. and Kostović, I. (2011), 'Extraordinary neoteny of synaptic spines in the human prefrontal cortex', *Proceedings of the National Academy of Sciences* **108**(32), 13281–13286.

Pettus, E. H. and Povlishock, J. T. (1996), 'Characterization of a distinct set of intra-axonal ultrastructural changes associated with traumatically induced alteration in axolemmal permeability', *Brain Research* **722**(1-2), 1–11.

Pfeiffer, E., S., Warrington, E., A. and Bansal, R. (1993), 'The oligodendrocyte and its many cellular processes', *Trends in Cell Biology* **3**, 191–197.

Pinz, H., Pyle, L. C., Li, D., Izumi, K., Skraban, C., Tarpinian, J., Braddock, S. R., Telegrafi, A., Monaghan, K. G., Zackai, E. and Bhoj, E. J. (2018), 'De novo variants

in Myelin regulatory factor (MYRF) as candidates of a new syndrome of cardiac and urogenital anomalies', *American Journal of Medical Genetics Part A* **176**(4), 969–972.

Poggi, G., Boretius, S., Möbius, W., Moschny, N., Baudewig, J., Ruhwedel, T., Hassouna, I., Wieser, G. L., Werner, H. B., Goebbels, S., Nave, K.-A. and Ehrenreich, H. (2016), 'Cortical network dysfunction caused by a subtle defect of myelination: Network Function Upon Myelination Defect', *Glia* **64**(11), 2025–2040.

Pogoda, H.-M., Sternheim, N., Lyons, D. A., Diamond, B., Hawkins, T. A., Woods, I. G., Bhatt, D. H., Franzini-Armstrong, C., Dominguez, C., Arana, N., Jacobs, J., Nix, R., Fetcho, J. R. and Talbot, W. S. (2006), 'A genetic screen identifies genes essential for development of myelinated axons in zebrafish', *Developmental Biology* **298**(1), 118–131.

Politte, L. C. and Stern, T. A. (2008), 'Neuropsychiatric Manifestations of Multiple Sclerosis', *Prim Care Companion J Clin Psychiatry* **10**(4), 318–324.

Preibisch, S., Saalfeld, S., Schindelin, J. and Tomancak, P. (2010), 'Software for bead-based registration of selective plane illumination microscopy data', *Nature Methods* **7**(6), 418–419.

Prober, D. A., Rihel, J., Onah, A. A., Sung, R.-J. and Schier, A. F. (2006), 'Hypocretin/Orexin Overexpression Induces An Insomnia-Like Phenotype in Zebrafish', *Journal of Neuroscience* **26**(51), 13400–13410.

Readhead, C. and Hood, L (1990), 'The dysmyelinating mouse mutations shiverer (shi) and myelin deficient (shimld)', **20**(2), 213–234.

Regan, D. and Neima, D. (1984), 'Visual fatigue and visual evoked potentials in multiple sclerosis, glaucoma, ocular hypertension and Parkinson's disease.', *Journal of Neurology, Neurosurgery & Psychiatry* **47**(7), 673–678.

Reimer, M. M., Norris, A., Ohnmacht, J., Patani, R., Zhong, Z., Dias, T. B., Kuscha, V., Scott, A. L., Chen, Y.-C., Rozov, S., Frazer, S. L., Wyatt, C., Higashijima, S.-i., Patton, E. E., Panula, P., Chandran, S., Becker, T. and Becker, C. G. (2013), 'Dopamine from the Brain Promotes Spinal Motor Neuron Generation during Development and Adult Regeneration', *Developmental Cell* **25**(5), 478–491.

Remahl, S. and Hildebrand, C. (1982), 'Changing relation between onset of myelination and axon diameter range in developing feline white matter', *Journal of the Neurological Sciences* **54**(1), 33–45.

Remahl, S. and Hildebrand, C. (1990), 'Relations between axons and oligodendroglial cells during initial myelination. II. The individual axon', *Journal of Neurocytology* **19**(6), 883–898.

Richardson, W. D., Kessaris, N. and Pringle, N. (2006), 'Oligodendrocyte wars', *Nature Reviews Neuroscience* **7**(1), 11–18.

Rinholm, J. E., Hamilton, N. B., Kessaris, N., Richardson, W. D., Bergersen, L. H. and Attwell, D. (2011), 'Regulation of Oligodendrocyte Development and Myelination by Glucose and Lactate', *Journal of Neuroscience* **31**(2), 538–548.

Romano, S. A., Pietri, T., Pérez-Schuster, V., Jouary, A., Haudrechy, M. and Sumbre, G. (2015), 'Spontaneous Neuronal Network Dynamics Reveal Circuit's Functional Adaptations for Behavior', *Neuron* **85**(5), 1070–1085.

Rosen, J. N., Sweeney, M. F. and Mably, J. D. (2009), 'Microinjection of Zebrafish Embryos to Analyze Gene Function', *Journal of Visualized Experiments* (25), 1115.

Rosenbluth, J. (1980), 'Central myelin in the mouse mutant shiverer', *The Journal of Comparative Neurology* **194**(3), 639–648.

Rosenbluth, J. (2009), 'Multiple functions of the paranodal junction of myelinated nerve fibers', *Journal of Neuroscience Research* **87**(15), 3250–3258.

Rossetti, L. Z., Glinton, K., Yuan, B., Liu, P., Pillai, N., Mizerik, E., Magoulas, P., Rosenfeld, J. A., Karaviti, L., Sutton, V. R., Lalani, S. R. and Scott, D. A. (2019), 'Review of the phenotypic spectrum associated with haploinsufficiency of *MYRF*', *American Journal of Medical Genetics Part A* p. ajmg.a.61182.

Rossi, A., Kontarakis, Z., Gerri, C., Nolte, H., Hölper, S., Krüger, M. and Stainier, D. Y. R. (2015), 'Genetic compensation induced by deleterious mutations but not gene knockdowns', *Nature* **524**(7564), 230–233.

Roy, K., Murtie, J. C., El-Khodor, B. F., Edgar, N., Sardi, S. P., Hooks, B. M., Benoit-Marand, M., Chen, C., Moore, H., O'Donnell, P., Brunner, D. and Corfas, G. (2007),

'Loss of erbB signaling in oligodendrocytes alters myelin and dopaminergic function, a potential mechanism for neuropsychiatric disorders', *Proceedings of the National Academy of Sciences* **104**(19), 8131–8136.

Rushton, W. A. H. (1951), 'A theory of the effects of fibre size in medullated nerve', *The Journal of Physiology* **115**(1), 101–122.

Russel, S., Frand, A. R. and Ruvkun, G. (2011), 'Regulation of the C. elegans molt by pqn-47', *Developmental Biology* **360**(2), 297–309.

Saab, A. S. and Nave, K.-A. (2017), 'Myelin dynamics: Protecting and shaping neuronal functions', *Current Opinion in Neurobiology* **47**, 104–112.

Saab, A. S., Tzvetavona, I. D., Trevisiol, A., Baltan, S., Dibaj, P., Kusch, K., Möbius, W., Goetze, B., Jahn, H. M., Huang, W., Steffens, H., Schomburg, E. D., Pérez-Samartín, A., Pérez-Cerdá, F., Bakhtiari, D., Matute, C., Löwel, S., Griesinger, C., Hirrlinger, J., Kirchhoff, F. and Nave, K.-A. (2016), 'Oligodendroglial NMDA Receptors Regulate Glucose Import and Axonal Energy Metabolism', *Neuron* **91**(1), 119–132.

Saint-Amant, L. and Drapeau, P. (1998), 'Time course of the development of motor behaviors in the zebrafish embryo', *Journal of Neurobiology* **37**, 622–632.

Sakry, D., Neitz, A., Singh, J., Frischknecht, R., Marongiu, D., Binamé, F., Perera, S. S., Endres, K., Lutz, B., Radyushkin, K., Trotter, J. and Mittmann, T. (2014), 'Oligodendrocyte Precursor Cells Modulate the Neuronal Network by Activity-Dependent Ectodomain Cleavage of Glial NG2', *PLoS Biology* **12**(11), e1001993.

Salami, M., Itami, C., Tsumoto, T. and Kimura, F. (2003), 'Change of conduction velocity by regional myelination yields constant latency irrespective of distance between thalamus and cortex', *Proceedings of the National Academy of Sciences* **100**(10), 6174–6179.

Sampaio-Baptista, C., Khrapitchev, A. A., Foxley, S., Schlagheck, T., Scholz, J., Jbabdi, S., DeLuca, G. C., Miller, K. L., Taylor, A., Thomas, N., Kleim, J., Sibson, N. R., Bannerman, D. and Johansen-Berg, H. (2013), 'Motor Skill Learning Induces Changes in White Matter Microstructure and Myelination', *Journal of Neuroscience* **33**(50), 19499–19503.

Sampaio-Baptista, C., Vallès, A., Khrapitchev, A. A., Akkermans, G., Winkler, A. M., Foxley, S., Sibson, N. R., Roberts, M., Miller, K., Diamond, M. E., Martens, G. J., De Weerd, P. and Johansen-Berg, H. (2020), 'White matter structure and myelin-related gene expression alterations with experience in adult rats', *Progress in Neurobiology* **187**, 101770.

Saverino, C. and Gerlai, R. (2008), 'The social zebrafish: Behavioral responses to conspecific, heterospecific, and computer animated fish', *Behavioural Brain Research* **191**(1), 77–87.

Schalomon, P. and Wahlsten, D. (2002), 'Wheel running behavior is impaired by both surgical section and genetic absence of the mouse corpus callosum', *Brain Research Bulletin* **57**(1), 27–33.

Schebesta, M. and Serluca, F. C. (2009), 'Olig1 expression identifies developing oligodendrocytes in zebrafish and requires hedgehog and notch signaling', *Developmental Dynamics* **238**(4), 887–898.

Schirmer, L., Möbius, W., Zhao, C., Cruz-Herranz, A., Ben Haim, L., Cordano, C., Shiow, L. R., Kelley, K. W., Sadowski, B., Timmons, G., Pröbstel, A.-K., Wright, J. N., Sin, J. H., Devereux, M., Morrison, D. E., Chang, S. M., Sabeur, K., Green, A. J., Nave, K.-A., Franklin, R. J. and Rowitch, D. H. (2018), 'Oligodendrocyte-encoded Kir4.1 function is required for axonal integrity', *eLife* **7**, e36428.

Schlegel, A. A., Rudelson, J. J. and Tse, P. U. (2012), 'White Matter Structure Changes as Adults Learn a Second Language', *Journal of Cognitive Neuroscience* **24**(8), 1664–1670.

Schmithorst, V. J. and Yuan, W. (2010), 'White matter development during adolescence as shown by diffusion MRI', *Brain and Cognition* **72**(1), 16–25.

Schneider, S., Gruart, A., Grade, S., Zhang, Y., Kröger, S., Kirchhoff, F., Eichele, G., Delgado García, J. M. and Dimou, L. (2016), 'Decrease in newly generated oligodendrocytes leads to motor dysfunctions and changed myelin structures that can be rescued by transplanted cells: Reduced Oligodendrogenesis in the Adult Brain', *Glia* **64**(12), 2201–2218.

Schnörr, S., Steenbergen, P., Richardson, M. and Champagne, D. (2012), 'Measuring thigmotaxis in larval zebrafish', *Behavioural Brain Research* **228**(2), 367–374.

Scholz, J., Klein, M. C., Behrens, T. E. J. and Johansen-Berg, H. (2009), 'Training induces changes in white-matter architecture', *Nature Neuroscience* **12**(11), 1370–1371.

Schweitzer, J., Becker, T., Becker, C. G. and Schachner, M. (2003), 'Expression of protein zero is increased in lesioned axon pathways in the central nervous system of adult zebrafish', *Glia* **41**(3), 301–317.

Seidl, A. H., Rubel, E. W. and Harris, D. M. (2010), 'Mechanisms for Adjusting Interaural Time Differences to Achieve Binaural Coincidence Detection', *Journal of Neuroscience* **30**(1), 70–80.

Senoo, H., Araki, T., Fukuzawa, M. and Williams, J. G. (2013), 'A new kind of membrane-tethered eukaryotic transcription factor that shares an auto-proteolytic processing mechanism with bacteriophage tail-spike proteins', *Journal of Cell Science* **126**(22), 5247–5258.

Serrano-Regal, M. P., Luengas-Escuza, I., Bayón-Cordero, L., Ibarra-Aizpurua, N., Alberdi, E., Pérez-Samartín, A., Matute, C. and Sánchez-Gómez, M. V. (2019), 'Oligodendrocyte Differentiation and Myelination Is Potentiated via GABAB Receptor Activation', *Neuroscience* p. S0306452219304889.

Severi, K. E., Portugues, R., Marques, J. C., O'Malley, D. M., Orger, M. B. and Engert, F. (2014), 'Neural Control and Modulation of Swimming Speed in the Larval Zebrafish', *Neuron* **83**(3), 692–707.

Shi, C., Yuan, X., Chang, K., Cho, K.-S., Xie, X. S., Chen, D. F. and Luo, G. (2018), 'Optimization of Optomotor Response-based Visual Function Assessment in Mice', *Scientific Reports* **8**(1), 9708.

Simpson, A. H., Gillingwater, T. H., Anderson, H., Cottrell, D., Sherman, D. L., Ribchester, R. R. and Brophy, P. J. (2013), 'Effect of Limb Lengthening on Internodal Length and Conduction Velocity of Peripheral Nerve', *Journal of Neuroscience* **33**(10), 4536–4539.

Smith, K., Blakemore, W. and McDonald, W. (1979), 'Central remyelination restores secure conduction', *Nature* **280**(5721), 395–396.

Smith, K. and Hall, S. (1980), 'Nerve conduction during peripheral demyelination and remyelination', *Journal of the Neurological Sciences* **48**(2), 201–219.

Snaidero, N., Möbius, W., Czopka, T., Hekking, L. H., Mathisen, C., Verkleij, D., Goebbels, S., Edgar, J., Merkler, D., Lyons, D. A., Nave, K.-A. and Simons, M. (2014), 'Myelin Membrane Wrapping of CNS Axons by PI(3,4,5)P3-Dependent Polarized Growth at the Inner Tongue', *Cell* **156**(1-2), 277–290.

Snaidero, N., Velte, C., Myllykoski, M., Raasakka, A., Ignatev, A., Werner, H. B., Erwig, M. S., Möbius, W., Kursula, P., Nave, K.-A. and Simons, M. (2017), 'Antagonistic Functions of MBP and CNP Establish Cytosolic Channels in CNS Myelin', *Cell Reports* **18**(2), 314–323.

Spitzer, S. O., Sitnikov, S., Kamen, Y., Evans, K. A., Kronenberg-Versteeg, D., Dietmann, S., de Faria, O., Agathou, S. and Káradóttir, R. T. (2019), 'Oligodendrocyte Progenitor Cells Become Regionally Diverse and Heterogeneous with Age', *Neuron* **101**(3), 459–471.e5.

Srinivasan, R., Huang, B. S., Venugopal, S., Johnston, A. D., Chai, H., Zeng, H., Golshani, P. and Khakh, B. S. (2015), 'Ca2+ signaling in astrocytes from Ip3r2-/- mice in brain slices and during startle responses in vivo', *Nature Neuroscience* **18**(5), 708–717.

Stedehouder, J., Couey, J. J., Brizee, D., Hosseini, B., Slotman, J. A., Dirven, C. M. F., Shpak, G., Houtsmuller, A. B. and Kushner, S. A. (2017), 'Fast-spiking Parvalbumin Interneurons are Frequently Myelinated in the Cerebral Cortex of Mice and Humans', *Cerebral Cortex* **27**(10), 5001–5013.

Steele, C. J., Bailey, J. A., Zatorre, R. J. and Penhune, V. B. (2013), 'Early Musical Training and White-Matter Plasticity in the Corpus Callosum: Evidence for a Sensitive Period', *Journal of Neuroscience* **33**(3), 1282–1290.

Sternberg, J. R., Severi, K. E., Fidelin, K., Gomez, J., Ihara, H., Alcheikh, Y., Hubbard, J. M., Kawakami, K., Suster, M. and Wyart, C. (2016), 'Optimization of a Neurotoxin

to Investigate the Contribution of Excitatory Interneurons to Speed Modulation In Vivo', *Current Biology* **26**(17), 2319–2328.

Stevens, B., Porta, S., Haak, L. L., Gallo, V. and Fields, R. D. (2002), 'Adenosine: A Neuron-Glial Transmitter Promoting Myelination in the CNS in Response to Action Potentials', *Neuron* **36**(5), 855–868.

Stevens, B., Tanner, S. and Fields, R. D. (1998), 'Control of Myelination by Specific Patterns of Neural Impulses', *The Journal of Neuroscience* **18**(22), 9303–9311.

Stewart, A., Gaikwad, S., Kyzar, E., Green, J., Roth, A. and Kalueff, A. V. (2012), 'Modeling anxiety using adult zebrafish: A conceptual review', *Neuropharmacology* **62**(1), 135–143.

Stobart, J. L. and Anderson, C. M. (2013), 'Multifunctional role of astrocytes as gatekeepers of neuronal energy supply', *Frontiers in Cellular Neuroscience* **7**.

Stromnes, I. M. and Goverman, J. M. (2006), 'Active induction of experimental allergic encephalomyelitis', *Nature Protocols* **1**(4), 1810–1819.

Stummeyer, K., Schwarzer, D., Claus, H., Vogel, U., Gerardy-Schahn, R. and Muhlenhoff, M. (2006), 'Evolution of bacteriophages infecting encapsulated bacteria: Lessons from Escherichia coli K1-specific phages', *Molecular Microbiology* **60**(5), 1123–1135.

Sullivan, E. V., Adalsteinsson, E., Hedehus, M., Ju, C., Moseley, M., Lim, K. O. and Pfefferbaum, A. (2001), 'Equivalent disruption of regional white matter microstructure in ageing healthy men and women:', *Neuroreport* **12**(1), 99–104.

Sumbre, G., Muto, A., Baier, H. and Poo, M.-m. (2008), 'Entrained rhythmic activities of neuronal ensembles as perceptual memory of time interval', *Nature* **456**(7218), 102–106.

Suminaite, D., Lyons, D. A. and Livesey, M. R. (2019), 'Myelinated axon physiology and regulation of neural circuit function', *Glia* .

Sun, F., Zeng, J., Jing, M., Zhou, J., Feng, J., Owen, S. F., Luo, Y., Li, F., Wang, H., Yamaguchi, T., Yong, Z., Gao, Y., Peng, W., Wang, L., Zhang, S., Du, J., Lin, D., Xu, M., Kreitzer, A. C., Cui, G. and Li, Y. (2018), 'A Genetically Encoded Fluorescent Sensor Enables Rapid and Specific Detection of Dopamine in Flies, Fish, and Mice', *Cell* **174**(2), 481–496.e19.

Sun, H. and Frost, B. J. (1998), 'Computation of different optical variables of looming objects in pigeon nucleus rotundus neurons', *Nature Neuroscience* **1**(4), 296–303.

Sun, W., Matthews, E. A., Nicolas, V., Schoch, S. and Dietrich, D. (2016), 'NG2 glial cells integrate synaptic input in global and dendritic calcium signals', *eLife* **5**, e16262.

Svara, F. N., Kornfeld, J., Denk, W. and Bollmann, J. H. (2018), 'Volume EM Reconstruction of Spinal Cord Reveals Wiring Specificity in Speed-Related Motor Circuits', *Cell Reports* **23**(10), 2942–2954.

Swire, M., Kotelevtsev, Y., Webb, D. J., Lyons, D. A. and ffrench-Constant, C. (2019), 'Endothelin signalling mediates experience-dependent myelination in the CNS', *eLife* **8**, e49493.

Tabor, K. M., Smith, T. S., Brown, M., Bergeron, S. A., Briggman, K. L. and Burgess, H. A. (2018), 'Presynaptic Inhibition Selectively Gates Auditory Transmission to the Brainstem Startle Circuit', *Current Biology* **28**(16), 2527–2535.e8.

Tadros, W. and Lipshitz, H. D. (2009), 'The maternal-to-zygotic transition: A play in two acts', *Development* **136**(18), 3033–3042.

Takada, N. and Appel, B. (2010), 'Identification of genes expressed by zebrafish oligodendrocytes using a differential microarray screen', *Developmental Dynamics* **239**(7), 2041–2047.

Takahashi, M., Hackney, D. B., Zhang, G., Wehrli, S. L., Wright, A. C., O'Brien, W. T., Uematsu, H., Wehrli, F. W. and Selzer, M. E. (2002), 'Magnetic resonance microimaging of intraaxonal water diffusion in live excised lamprey spinal cord', *Proceedings of the National Academy of Sciences* **99**(25), 16192–16196.

Takahashi, N., Sakurai, T., Davis, K. L. and Buxbaum, J. D. (2011), 'Linking oligodendrocyte and myelin dysfunction to neurocircuitry abnormalities in schizophrenia', *Progress in Neurobiology* **93**(1), 13–24.

Tanaka, H., Ma, J., Tanaka, K. F., Takao, K., Komada, M., Tanda, K., Suzuki, A., Ishibashi, T., Baba, H., Isa, T., Shigemoto, R., Ono, K., Miyakawa, T. and Ikenaka, K. (2009), 'Mice with Altered Myelin Proteolipid Protein Gene Expression Display Cognitive Deficits Accompanied by Abnormal Neuron-Glia Interactions and Decreased Conduction Velocities', *Journal of Neuroscience* **29**(26), 8363–8371.

Tang, Y.-Y., Lu, Q., Geng, X., Stein, E. A., Yang, Y. and Posner, M. I. (2010), 'Short-term meditation induces white matter changes in the anterior cingulate', *Proceedings of the National Academy of Sciences* **107**(35), 15649–15652.

Tau, G. Z. and Peterson, B. S. (2010), 'Normal Development of Brain Circuits', *Neuropsychopharmacology* **35**(1), 147–168.

Temizer, I., Donovan, J. C., Baier, H. and Semmelhack, J. L. (2015), 'A Visual Pathway for Looming-Evoked Escape in Larval Zebrafish', *Current Biology* **25**(14), 1823–1834.

The Human Protein Atlas (n.d.), https://www.proteinatlas.org/.

Thiele, T. R., Donovan, J. C. and Baier, H. (2014), 'Descending Control of Swim Posture by a Midbrain Nucleus in Zebrafish', *Neuron* **83**(3), 679–691.

Thorsen, D. H. (2004), 'Swimming of larval zebrafish: Fin-axis coordination and implications for function and neural control', *Journal of Experimental Biology* **207**(24), 4175–4183.

Tkachev, D., Mimmack, M. L., Ryan, M. M., Wayland, M., Freeman, T., Jones, P. B., Starkey, M., Webster, M. J., Yolken, R. H. and Bahn, S. (2003), 'Oligodendrocyte dysfunction in schizophrenia and bipolar disorder', *The Lancet* **362**(9386), 798–805.

Tomassy, G. S., Berger, D. R., Chen, H.-H., Kasthuri, N., Hayworth, K. J., Vercelli, A., Seung, H. S., Lichtman, J. W. and Arlotta, P. (2014), 'Distinct Profiles of Myelin Distribution Along Single Axons of Pyramidal Neurons in the Neocortex', *Science* **344**(6181), 319–324.

Trapp, B. D. and Nave, K.-A. (2008), 'Multiple Sclerosis: An Immune or Neurodegenerative Disorder?', *Annual Review of Neuroscience* **31**(1), 247–269.

Treichel, A. J. and Hines, J. H. (2018), 'Development of an Embryonic Zebrafish Oligodendrocyte–Neuron Mixed Coculture System', *Zebrafish* **15**(6), 586–596.

Tripathi, R. B., Jackiewicz, M., McKenzie, I. A., Kougioumtzidou, E., Grist, M. and Richardson, W. D. (2017), 'Remarkable Stability of Myelinating Oligodendrocytes in Mice', *Cell Reports* **21**(2), 316–323.

Tripathi, R. B., Rivers, L. E., Young, K. M., Jamen, F. and Richardson, W. D. (2010), 'NG2 Glia Generate New Oligodendrocytes But Few Astrocytes in a Murine Experimental Autoimmune Encephalomyelitis Model of Demyelinating Disease', *Journal of Neuroscience* **30**(48), 16383–16390.

Trivedi, C. A. and Bollmann, J. H. (2013), 'Visually driven chaining of elementary swim patterns into a goal-directed motor sequence: A virtual reality study of zebrafish prey capture', *Frontiers in Neural Circuits* **7**.

Trotter, J., Karram, K. and Nishiyama, A. (2010), 'NG2 cells: Properties, progeny and origin', *Brain Research Reviews* **63**(1-2), 72–82.

Tuch, D. S., Salat, D. H., Wisco, J. J., Zaleta, A. K., Hevelone, N. D. and Rosas, H. D. (2005), 'Choice reaction time performance correlates with diffusion anisotropy in white matter pathways supporting visuospatial attention', *Proceedings of the National Academy of Sciences* **102**(34), 12212–12217.

Uhlhaas, P. (2009), 'Neural synchrony in cortical networks: History, concept and current status', *Frontiers in Integrative Neuroscience* **3**.

Verhoeven, K., De Jonghe, P., Van de Putte, T., Nelis, E., Zwijsen, A., Verpoorten, N., De Vriendt, E., Jacobs, A., Van Gerwen, V., Francis, A., Ceuterick, C., Huylebroeck, D. and Timmerman, V. (2003), 'Slowed Conduction and Thin Myelination of Peripheral Nerves Associated with Mutant Rho Guanine-Nucleotide Exchange Factor 10', *The American Journal of Human Genetics* **73**(4), 926–932.

von Bartheld, C. S., Bahney, J. and Herculano-Houzel, S. (2016), 'The search for true numbers of neurons and glial cells in the human brain: A review of 150 years of cell counting: Quantifying neurons and glia in human brain', *Journal of Comparative Neurology* **524**(18), 3865–3895.

von Reyn, C. R., Nern, A., Williamson, W. R., Breads, P., Wu, M., Namiki, S. and Card, G. M. (2017), 'Feature Integration Drives Probabilistic Behavior in the Drosophila Escape Response', *Neuron* **94**(6), 1190–1204.e6.

Vondran, M. W., Clinton-Luke, P., Honeywell, J. Z. and Dreyfus, C. F. (2010), 'BDNF+/- mice exhibit deficits in oligodendrocyte lineage cells of the basal forebrain', *Glia* pp. NA–NA.

Wake, H., Lee, P. R. and Fields, R. D. (2011), 'Control of Local Protein Synthesis and Initial Events in Myelination by Action Potentials', *Science* **333**(6049), 1647–1651.

Wake, H., Ortiz, F. C., Woo, D. H., Lee, P. R., Angulo, M. C. and Fields, R. D. (2015), 'Nonsynaptic junctions on myelinating glia promote preferential myelination of electrically active axons', *Nature Communications* **6**(1), 7844.

Walhovd, K., Johansen-Berg, H. and Káradóttir, R. (2014), 'Unraveling the secrets of white matter – Bridging the gap between cellular, animal and human imaging studies', *Neuroscience* **276**, 2–13.

Wang, F., Yang, Y.-J., Yang, N., Chen, X.-J., Huang, N.-X., Zhang, J., Wu, Y., Liu, Z., Gao, X., Li, T., Pan, G.-Q., Liu, S.-B., Li, H.-L., Fancy, S. P., Xiao, L., Chan, J. R. and Mei, F. (2018), 'Enhancing Oligodendrocyte Myelination Rescues Synaptic Loss and Improves Functional Recovery after Chronic Hypoxia', *Neuron* **99**(4), 689–701.e5.

Wang, H., Kunkel, D. D., Martin, T. M., Schwartzkroin, P. A. and Tempel, B. L. (1993), 'Heteromultimeric K+ channels in terminal and juxtaparanodal regions of neurons', *Nature* **365**(6441), 75–79.

Wang, W.-C. and McLean, D. L. (2014), 'Selective Responses to Tonic Descending Commands by Temporal Summation in a Spinal Motor Pool', *Neuron* **83**(3), 708–721.

Waxman, S. G. (1980), 'Determinants of conduction velocity in myelinated nerve fibers', *Muscle & Nerve* **3**(2), 141–150.

Waxman, S. G. and Bennett, M. L. (1972), 'Relative Conduction Velocities of Small Myelinated and Non-myelinated Fibres in the Central Nervous System', *Nature New Biology* **238**, 217–219.

Weiss (2010), 'Field effects in the CNS play functional roles', *Frontiers in Neural Circuits* .

Welsh, T. G. and Kucenas, S. (2018), 'Purinergic signaling in oligodendrocyte development and function', *Journal of Neurochemistry* **145**(1), 6–18.

White, R. M., Sessa, A., Burke, C., Bowman, T., LeBlanc, J., Ceol, C., Bourque, C., Dovey, M., Goessling, W., Burns, C. E. and Zon, L. I. (2008), 'Transparent Adult Zebrafish as a Tool for In Vivo Transplantation Analysis', *Cell Stem Cell* **2**(2), 183–189.

Wilkinson, R. N., Elworthy, S., Ingham, P. W. and van Eeden, F. J. (2013), 'A method for high-throughput PCR-based genotyping of larval zebrafish tail biopsies', *BioTechniques* **55**(6).

Williamson, J. M. (2020), Investigating the Formation and Remodelling of Myelinated Axons in Vivo, PhD thesis, University of Edinburgh.

Wolf, S., Dubreuil, A. M., Bertoni, T., Böhm, U. L., Bormuth, V., Candelier, R., Karpenko, S., Hildebrand, D. G. C., Bianco, I. H., Monasson, R. and Debrégeas, G. (2017), 'Sensorimotor computation underlying phototaxis in zebrafish', *Nature Communications* **8**(1), 651.

Wolman, M. A., Jain, R. A., Liss, L. and Granato, M. (2011), 'Chemical modulation of memory formation in larval zebrafish', *Proceedings of the National Academy of Sciences* **108**(37), 15468–15473.

Wolman, M. and Granato, M. (2012), 'Behavioral genetics in larval zebrafish: Learning from the young', *Developmental Neurobiology* **72**(3), 366–372.

Wong, A. W., Xiao, J., Kemper, D., Kilpatrick, T. J. and Murray, S. S. (2013), 'Oligodendroglial Expression of TrkB Independently Regulates Myelination and Progenitor Cell Proliferation', *Journal of Neuroscience* **33**(11), 4947–4957.

Wu, L. M. N., Williams, A., Delaney, A., Sherman, D. L. and Brophy, P. J. (2012), 'Increasing Internodal Distance in Myelinated Nerves Accelerates Nerve Conduction to a Flat Maximum', *Current Biology* **22**(20), 1957–1961.

Wyart, C., Bene, F. D., Warp, E., Scott, E. K., Trauner, D., Baier, H. and Isacoff, E. Y. (2009), 'Optogenetic dissection of a behavioural module in the vertebrate spinal cord', *Nature* **461**(7262), 407–410.

Xiao, L., Ohayon, D., McKenzie, I. A., Sinclair-Wilson, A., Wright, J. L., Fudge, A. D., Emery, B., Li, H. and Richardson, W. D. (2016), 'Rapid production of new

oligodendrocytes is required in the earliest stages of motor-skill learning', *Nature Neuroscience* **19**(9), 1210–1217.

Xin, W., Mironova, Y. A., Shen, H., Marino, R. A., Waisman, A., Lamers, W. H., Bergles, D. E. and Bonci, A. (2019), 'Oligodendrocytes Support Neuronal Glutamatergic Transmission via Expression of Glutamine Synthetase', *Cell Reports* **27**(8), 2262–2271.e5.

Xu, T., Yu, X., Perlik, A. J., Tobin, W. F., Zweig, J. A., Tennant, K., Jones, T. and Zuo, Y. (2009), 'Rapid formation and selective stabilization of synapses for enduring motor memories', *Nature* **462**(7275), 915–919.

Yeung, M. S., Zdunek, S., Bergmann, O., Bernard, S., Salehpour, M., Alkass, K., Perl, S., Tisdale, J., Possnert, G., Brundin, L., Druid, H. and Frisén, J. (2014), 'Dynamics of Oligodendrocyte Generation and Myelination in the Human Brain', *Cell* **159**(4), 766–774.

Young, K. M., Psachoulia, K., Tripathi, R. B., Dunn, S.-J., Cossell, L., Attwell, D., Tohyama, K. and Richardson, W. D. (2013), 'Oligodendrocyte Dynamics in the Healthy Adult CNS: Evidence for Myelin Remodeling', *Neuron* **77**(5), 873–885.

Zalc, B. and Douglas Fields, R. (2000), 'Do Action Potentials Regulate Myelination?', *The Neuroscientist* **6**(1), 5–13.

Zatorre, R. J., Fields, R. D. and Johansen-Berg, H. (2012), 'Plasticity in gray and white: Neuroimaging changes in brain structure during learning', *Nature Neuroscience* **15**(4), 528–536.

Zhang, Y., Chen, K., Sloan, S. A., Bennett, M. L., Scholze, A. R., O'Keeffe, S., Phatnani, H. P., Guarnieri, P., Caneda, C., Ruderisch, N., Deng, S., Liddelow, S. A., Zhang, C., Daneman, R., Maniatis, T., Barres, B. A. and Wu, J. Q. (2014), 'An RNA-Sequencing Transcriptome and Splicing Database of Glia, Neurons, and Vascular Cells of the Cerebral Cortex', *Journal of Neuroscience* **34**(36), 11929–11947.

Ziegler, G., Hauser, T. U., Consortium, N., Moutoussis, M., Bullmore, E. T., Goodyer, I. M., Fonagy, P., Jones, P. B., Lindenberger, U. and Dolan, R. J. (2019), 'Compulsivity and impulsivity traits linked to attenuated developmental frontostriatal myelination trajectories', *Nature Neuroscience* **22**(6), 992–999.

Ziv, Y. and Ghosh, K. K. (2015), 'Miniature microscopes for large-scale imaging of neuronal activity in freely behaving rodents', *Current Opinion in Neurobiology* **32**, 141–147.

Zonouzi, M., Berger, D., Jokhi, V., Kedaigle, A., Lichtman, J. and Arlotta, P. (2019), 'Individual Oligodendrocytes Show Bias for Inhibitory Axons in the Neocortex', *Cell Reports* **27**(10), 2799–2808.e3.

Zonouzi, M., Scafidi, J., Li, P., McEllin, B., Edwards, J., Dupree, J. L., Harvey, L., Sun, D., Hübner, C. A., Cull-Candy, S. G., Farrant, M. and Gallo, V. (2015), 'GABAergic regulation of cerebellar NG2 cell development is altered in perinatal white matter injury', *Nature Neuroscience* **18**(5), 674–682.

Zonta, B., Tait, S., Melrose, S., Anderson, H., Harroch, S., Higginson, J., Sherman, D. L. and Brophy, P. J. (2008), 'Glial and neuronal isoforms of Neurofascin have distinct roles in the assembly of nodes of Ranvier in the central nervous system', *The Journal of Cell Biology* **181**(7), 1169–1177.

Zottoli, S. J., Bentley, A. P., Prendergast, B. J. and Rieff, I, H. (1995), 'Comparative Studies on the Mauthner Cell of Teleost Fish in Relation to Sensory Input', *Brain, Behaviour and Evolution* **46**, 151–164.

Zottoli, S. J. and Faber, D. S. (2000), 'Review : The Mauthner Cell: What Has it Taught us?', *The Neuroscientist* **6**(1), 26–38.

Zottoli, S. J., Marek, L. E., Agostini, M. A. and Strittmatter, S. L. (1987), 'Morphological and physiological survival of goldfish Mauthner axons isolated from their somata by spinal cord crush', *The Journal of Comparative Neurology* **255**(2), 272–282.